The Axion Universe

Huangyu Xiao

A dissertation
submitted in partial fulfillment of the
requirements for the degree of

Doctor of Philosophy

University of Washington

2022

Reading Committee:
Stephen R. Sharpe, Chair
Matthew McQuinn
David B. Kaplan

Program Authorized to Offer Degree:
Physics

University of Washington

Abstract

The Axion Universe

Huangyu Xiao

Chair of the Supervisory Committee:
Professor Stephen R. Sharpe
Physics

The standard models of cosmology and particle physics have met enormous success. However, there are still a few big questions that remain to be answered. One of these outstanding questions is "what is the dark matter?". One of the most well-motivated dark matter candidates is the axion, as it provides a natural solution to another fundamental problem called the strong CP problem. Axions can also be motivated by various theories in high energy physics. A Universe with axion dark matter is very colorful as one expects many planetary-mass collapsed structures and potentially compact clumps such as axion stars. Astrophysical and cosmological observations can be sensitive to these structures, providing a unique window into the nature of dark matter. We will discuss recent progress in the evolution, formation and detectable signals of axion minihalos and axion stars.

TABLE OF CONTENTS

Page

ACKNOWLEDGMENTS

Huangyu's journey to physics would not be possible if his parents did not give him the ultimate freedom to choose his major. Huangyu's life in graduate school will be less sustainable without the support and understanding from his wife at all the difficult times. Huangyu would like to thank his parents and wife for their love and support all the time. Huangyu would like to thank Ann Nelson for teaching him how to do great physics, how to give talks, and how to survive in academia while being judged everyday. Huangyu would like to thank Matt Mcquinn for teaching him fun things about the Universe and advising him on the astrophysics side of his research. Huangyu would like to thank David B. Kaplan and Steve Sharpe for taking him under their wings since Ann's passing and making sure everything would function properly. Huangyu would also like to thank Paddy Fox, Neal Weiner, and Kathryn Zurek for co-advising him and guiding his way to exciting things in physics. There are so many people in the list that Huangyu could not thank enough. His journey with physics carries on and this would never come true without the support he received.

DEDICATION

to my dear wife, Miaoyuan

Chapter 1
INTRODUCTION

The standard models of particle physics and cosmology have been phenomenally successfully in describing our Universe. However, there are still big problems that remain to be answered. The Standard Model of particle physics provides a consistent quantum field theory (QFT) for the low energy interactions of the visible matter (baryons and photons), which only constitutes $\sim 5\%$ of the energy in the Universe. The rest of the Universe consists of dark matter and dark energy, whose existence has been confirmed from their gravitational effects, but how to incorporate them into a consistent model of particle physics remains unknown. The 'small' energy density in the dark energy is also known as the cosmological constant problem since the QFT predicts a number that is 120 orders of magnitude larger Weinberg [1989]. Perhaps the solution to this problem is that we only live in the part of the universe where the dark energy density is small enough so that collapsed structures like galaxies can form, an anthropic solution known as the multiverse Weinberg [1989]. The particle nature of dark matter, however, is likely addressable within the context of QFT itself. Another puzzle occurs in the the visible sector itself: The origin of the baryon asymmetry (the asymmetry between the density of matter and anti-matter) is unknown as one expects matter and antimatter to be initially equal to each other if they existed in thermal equilibrium in the early Universe Sakharov [1967]. The three big problems about baryonic matter, dark matter and dark energy have motivated myriad studies beyond the Standard Model of particle physics. In this thesis, we will focus on the question related to dark matter and show how astrophysical and cosmological observations can assist in probing the particle nature of dark matter. In particular, we are interested in a well-motivated dark matter candidate called the axion and study the Universe with the axion being dark matter.

The axion, originally proposed as a solution to the strong CP problem Peccei [2008], has received

renewed interest in recent years in the particle physics community as the second most popular, if not the most popular, dark matter candidate Weinberg [1978], Wilczek [1978], Kim [1979], Abbott and Sikivie [1983], Dine and Fischler [1983], Preskill et al. [1983], Peccei [2008]. The axion is a pseudo-Nambu–Goldstone boson arising from the spontaneously broken Peccei-Quinn symmetry and it accquires its mass through non-perturbative effects. Axions can be motivated from various high energy physics theories including the CP-violation in the Standard Model and theories with extra dimensions such as string theory Svrcek and Witten [2006], Marsh [2016], Hui et al. [2017], giving a broad landscape of axions and axion-like particles. Many experimental searches of axion dark matter has been proposed to detect axions either directly or indirectly. In particular, the Axion Dark Matter eXperiment (ADMX)Braine et al. [2020] has begun to constrain the axion-photon couplings predicted by QCD axion – the name for the axion that solves the strong CP problem – for some mass ranges. The QCD axion mass and couplings are determined by a single parameter, the axion decay constant f_a since the axion's mass m_a can be determined by f_a and the temperature of the QCD phase transition $\Lambda_{\rm QCD}$. On the other hand, if we do not need axions to solve the strong CP problem, m_a and f_a are independent of each other and we call them axion-like particles.

While there have been laboratory experiments that can directly detect axion dark matter, astrophysical and cosmological observations can provide an unique window onto axion physics. The axion Universe is colorful with even one type of particle since axion field fluctuations, if not homogenized by inflation, can enhance the matter power spectrum on extremely small scales, forming structures known as axion miniclusters or axion minihalos in the early Universe. While the matter power spectrum on galactic scales should remain consistent with current observations, smaller scale fluctuations are yet weakly constrained. Therefore, future searches for axion minihalos can provide a bridge between cosmological observations and fundamental physics. While microlensing is not sensitive to axion minihalos since they are not concentrated enough, there are two recent proposals that can detect axion minihalos with future observations. One uses the Shapiro time delays and Doppler shifts that these axion minihalos could impart on pulsar timing Dror et al. [2019], Ramani et al. [2020] and the other uses the effect of axion minihalos on the microlensing caustics of cosmological stars that are highly magnified both by a cluster lens and stellar microlens

Dai and Miralda-Escudé [2020].

Not only will an enhanced abundance of dark matter halos be potentially present in the Axion Universe, but also axion star formation owing to the bosonic nature of axions. Bose-Einstein condensation can occur inside axion minihalos, forming coherent objects called axion stars. The stable field configuration of axion stars have been studied extensively analytically, while there are also numerical simulations of the formation of axion stars Chen et al. [2021,], Levkov et al. [2018]. Since the self-interaction of axions are attractive, axion stars are balanced by the kinetic pressure and gravity. At some density self-interaction will overcome the kinetic pressure and axion stars will collapse, emitting relativistic axions. This process is called axinovae, which will significantly change the evolution of cosmological parameters since it is converting matter to radiation. The compactness of axion stars, as well as their nontrivial dynamics, offer potentially new avenues for observations.

Thus, axions have a rich phenomenology owing to gravitational interactions and self-couplings. However, axions are also expected to couple to photons and nucleons, which allows even more possibilities for exotic behaviors. Axion–photon couplings can induce radio emissions from axion minihalos or axion stars. Possible scenarios include axion stars that undergo parametric resonance into photons and axion stars or minihalos in the presence of a strong magnetic field (around neutron stars or the galactic center), both rapidly emitting radio photons Bai and Hamada [2018], Hertzberg and Schiappacasse [2018], Hertzberg et al. [2020], Prabhu [2020], Prabhu and Rapidis [2020], Carenza et al. [2020], Safdi et al. [2019], Battye et al. [2020], Foster et al. [2020], Hook et al. [2018], Caputo et al. [2019].

Given upcoming observations that will be sensitive to various aspects of axion phenomenology, studying the physics of the axion Universe is increasingly important. In the following subsections, we will review the theoretical motivation for the QCD axion, the unique production mechanism of axion as a dark matter candidate, and the formation of axion miniclusters. We will also discuss recent progresses in understanding the nonlinear evolution of axion miniclusters and the formation of axion stars.

1.1 *Axion as a solution to the Strong CP Problem*

That CP symmetry (the combination of charge symmetry and parity symmetry) is conserved in QCD is referred to as the strong CP problem. Our universe preferring CP symmetry might not be obviously problematic, especially for physicists back in the 1950s who used to believe that parity is strictly conserved in nature until Lee and Yang proposed experiments to look for parity violation in weak interactions Lee and Yang [1956] and Wu designed the experiment to test it Wu et al. [1957]. It was astonishing but then became a norm that parity or even CP may be violated in fundamental interactions. However, the neutron electric dipole moment, which quantifies the CP-violation in the strong interaction, is measured to be consistent with zero with extremely small error bars, suggesting CP is conserved in strong interactions. The strong CP problem is deepened as one studies more about the complicated structure of the vacuum in non-Abelian gauge theories, which contributes to the CP-violating term in the strong interaction. On the other hand, the phase of the quark mass matrix can also contribute to CP-violation. The real problem arises when two distinctly different physical mechanisms contribute to the same number that is measured to be very close to zero, which requires fine tuning. Different from other fine-tuning problems such as the cosmological problem, an anthropic solution is not likely as our Universe will behave very similarly with a slight CP-violation term. In the following, we show how axion can provide a natural solution to this problem.

For simplicity, we study an SU(2) gauge theory to reveal the vacuum structure of QCD. The result will still carry over to the SU(3) gauge theory as SU(2) is a subgroup of SU(3) (and SU(N) for N >3). The ground state of vacuum configurations will be studied in the context of the non-Abelian gauge theories. Using temporal gauge, $A^0 = 0$, and restricting ourselves to time independent gauge transformations, one obtains gauge fields with spatial components only, which transforms as

$$\frac{1}{2}\tau_a A^i_a \equiv A^i \rightarrow \Omega A^i \Omega^{-1} + \frac{i}{g}\nabla^i \Omega\Omega^{-1}, \tag{1.1}$$

where $\Omega(x) \in \mathrm{SU}(2)$. For the vacuum ground state, we have $F^a_{\mu\nu} = 0$, which implies vacuum configurations take the form $A^i = \frac{i}{g}\nabla^i\Omega\Omega^{-1}$. We impose the boundary condition that Ω approaches the same constant as $r \rightarrow \infty$ in all directions to ensure a finite energy, which gives the space the

topology of a 3-D sphere S^3. Since any SU(2) gauge transformation Ω can be parameterized by a euclidean four-vector of unit length, $\Omega(x)$ provides a mapping from spatial S^3 to the vacuum S^3. Such maps fall into topological classes labeled by integer n. The asymptotic behavior of Ω at infinity is described by the winding number which can classify these vacuum configurations

$$\Omega_n \to e^{2\pi i n} \quad \text{as} \quad r \to \infty \quad (n = 0, \pm 1, \pm 2, \pm 3, ...). \tag{1.2}$$

The winding number, which is related to the Jacobian of the mapping, can be expressed as:

$$n = \frac{ig^3}{24\pi^2} \int d^3x \mathrm{Tr}\ \epsilon_{ijk} A_n^i A_n^j A_n^k = \frac{g^2}{32\pi^2} \int d^4x F_a^{\mu\nu} \tilde{F}_{a\mu\nu}, \tag{1.3}$$

where

$$\tilde{F}_{\mu\nu} \equiv \frac{1}{2} \epsilon^{\mu\nu\sigma\tau} F_{\sigma\tau} \tag{1.4}$$

is the dual field strength and A_n is the gauge field configuration corresponding to Ω_n. The winding number is invariant under smooth deformations of Ω, and thus topologically invariant. Therefore SU(2) gauge theory has an infinite number of zero-energy field configurations labeled by n and different states are separated by energy barriers

$$\langle n+1|H|n\rangle \sim e^{-S}, \tag{1.5}$$

where H is the Hamiltonian and S is the instanton action that connects the vacuum state with winding number n at $t = -\infty$ to $n+1$ at $t = +\infty$. Due to the finite energy barrier, the n state is not the true vacuum state. One needs to diagonalize the Hamiltonian and obtain the *theta vacua*

$$|\theta\rangle = \sum_{n=-\infty}^{+\infty} e^{-in\theta} |n\rangle. \tag{1.6}$$

Ultimately, we would like to obtain the vacuum energy in *theta vacua*. Therefore we would like to compute the transition amplitude between different θ vacua, from $t = -\infty$ to $+\infty$, which can be expressed as

$${}_+\langle\theta'|\theta\rangle_- = \sum_{n_-,n_+} e^{i(n_+\theta' - n_-\theta)} {}_+\langle n_+|n_-\rangle_-, \tag{1.7}$$

The transition amplitude between different winding numbers ${}_+\langle n_+|n_-\rangle_-$ must depend on $n_+ - n_-$ only as the Hamiltonian is invariant under time-independent gauge transformations that carry a

nonzero winding number, which gives $\langle n_+|H|n_-\rangle = \langle n_+ + k|H|n_- + k\rangle$. Defining $n = n_+ - n_-$, one can rewrite the transition amplitude using the expression for the winding number in Eq. 1.3

$$\begin{aligned} {}_+\langle\theta'|\theta\rangle_- =& \delta(\theta' - \theta) \sum_n e^{in\theta} \int \mathcal{D}A_n e^{-S} \\ =& \delta(\theta' - \theta) \int \mathcal{D}A \exp \int d^4x \mathrm{Tr} \left(-\frac{1}{4} F^{\mu\nu} F_{\mu\nu} + \frac{ig^2\theta}{32\pi^2} F_a^{\mu\nu} \tilde{F}_{a\mu\nu} \right). \end{aligned} \tag{1.8}$$

Therefore, the complicated nature of the QCD vacuum reveals that one extra term should be added to the effective Lagrangian:

$$L_\theta = \theta \frac{g^2}{32\pi^2} F_a^{\mu\nu} \tilde{F}_{a\mu\nu}. \tag{1.9}$$

This term violates both Parity and Time reversal symmetry but conserves charge conjugation symmetry. The most stringent experimental bound for this term comes from the measurement of the neutron electric dipole moment, which is related to the θ parameter as $d_n \approx e\theta m_q / m_N^2$, which implies $|\theta| < 10^{-9}$ Baker et al. [2006].

As one considers the quark mass matrix, the complete coefficient of the $F\tilde{F}$ is

$$\bar{\theta} = \theta + \mathrm{Arg}\,\mathrm{det} M. \tag{1.10}$$

$\bar{\theta}$ is directly related to observables and is measured to be extremely small. Now we can clearly see how two physical parameters that have distinct origins (one from the quark mass matrix and the other from the vacuum structure) must cancel almost exactly to remain consistent with experimental data. This requires fine tuning to the physical parameters and one might consider it as unnatural in fundamental theories.

The axion, which is a Nambu-Goldstone boson of the broken symmetry $\mathrm{U}(1)_{\mathrm{PQ}}$ (The $\mathrm{U}(1)_{\mathrm{PQ}}$ symmetry corresponds to the shift symmetry of the axion field, which is spontaneously broken), provides a natural way out. The shift symmetry of the axion, $a \to a + \alpha f_a$, where f_a is the symmetry breaking scale, is essential for solving the strong CP problem as one wants to absorb the axion field into the QCD theta parameter:

$$\bar{\theta} = \theta + \mathrm{Arg}\,\mathrm{det} M + \frac{a}{f_a}. \tag{1.11}$$

The extra term can arise from effective field theory of the Standard Model that is $\mathrm{U}(1)_{\mathrm{PQ}}$ invariant:

$$\mathcal{L} \supset (\theta + \frac{a}{f_a}) \frac{g^2}{32\pi^2} F_a^{\mu\nu} \tilde{F}_{a\mu\nu}. \tag{1.12}$$

The shift symmetry of axions, $a \rightarrow a + 2\pi$ is protected from being broken during the symmetry breaking. Before acquiring its mass from instanton effects, the axion is massless, which guarantees that it only contributes to the vacuum energy as a function of $\theta + a/f_a$. Therefore, the vacuum energy is a periodic function of θ, and it gives the following axion potential if we ignore the effects from finite quark masses

$$V(a) \sim \Lambda_{\mathrm{QCD}}^4 \left(1 - \cos\left(\theta + \frac{a}{f_a}\right)\right). \tag{1.13}$$

The above formula will apply to a pure Yang-Mills theory. The complete expression should consider the quark masses and study the pion fields properly (See Hook [2019] for a review). Therefore, when the axion takes the vacuum expectation value to minimize the vacuum energy, the physical θ parameter automatically relaxes to zero, which successfully solves the strong CP problem. If there are other contributions to the axion potential, the vacuum expectation value will not guarantee the vacuum ground state has zero theta value. Therefore, the shift symmetry of axion is essential for solving the problem, as we mentioned.

There are concerns from quantum gravity breaks all global symmetries like the $U(1)_{\mathrm{PQ}}$. Gravity may breaks such symmetries in a manner that likely tilts the axion potential sufficiently so that it is difficult to satisfy $\theta < 10^{-10}$, a problem known as the axion quality problem Kamionkowski and March-Russell [1992], Barr and Seckel [1992], Ghigna et al. [1992]. There are a few possible solutions to the axion quality problem, including theories where $\mathrm{U}(1)_{\mathrm{PQ}}$ is an accidental symmetry Randall [1992] and theories where the $\mathrm{U}(1)_{\mathrm{PQ}}$ symmetry is promoted to be a gauge symmetry Choi [2004], Arkani-Hamed et al. [2003].

1.2 *Production Mechanism of Axion Dark Matter*

The production mechanism of the axions in the early Universe is very different from the thermal production of weakly interacting massive particles (WIMPs), perhaps the leading hypothesis for dark matter. While axions can also be thermally produced, their thermal contribution to the dark

matter relic density is negligible for viable parameters due to the small cross section (stellar cooling rules out the possibility of having a large cross section Masso and Toldra [1995]). The major mechanisms that produce axions is the vacuum misalignment mechanism as well as the decay of topological defects. If the axion field value is homogenized by inflation, which happens when the Peccei-Quinn symmetry breaking occurs before or during inflation, topological defects will not form and the vacuum misalignment mechanism alone is responsible for the production of axion dark matter. This is the so called the pre-inflationary scenario. On the other hand, the post-inflationary scenario, namely, where the symmetry is broken after inflation, a significant fraction of the the axions are likely produced by the decay of topological defects (mostly axion strings).

1.2.1 Vacuum Misalignment Mechanism of Axion Production

Vacuum misalignment is essentially a mechanism that converts vacuum energy to matter density when the particle mass is close to the Hubble parameter and starts to oscillate. So where is the vacuum energy coming from and why is it not relaxing to zero vacuum energy before the oscillation of axions? The answer is related to the solution of the strong CP problem we discussed previously. The axion potential only receives contributions from the non-perturbative QCD effect which is only turned on during the QCD phase transition. Therefore the vacuum is flat before the QCD phase transition and the axion field can take any values in the range of 0 to 2π in different horizon patches. During the QCD phase transition, the axion acquires its mass and the energy comes from the radiation plasma. Roughly at the same time, the axion mass is comparable to Hubble parameter and axions subsequently oscillate and act as matter-like particles. Therefore the axion relic abundance generated by the vacuum misalignment mechanism is determined by the time of axion oscillation as well as the initial vacuum energy density. In the following, we study the production of axions from vacuum misalignment more quantitatively.

We would like to study the equation of motion of the axion field in the early Universe to reveal its evolution during the QCD phase transition. The equation of motion is

$$\left(\partial_t^2 + 3\frac{\dot{R}}{R}\partial_t - \frac{1}{R^2}\nabla_x^2\right) a(x) + V'(a) = 0, \tag{1.14}$$

where R is the scale factor, the components of $\mathbf{x}$ are the co-moving spatial coordinates of the universe, and $V(a)$ is the potential of the axion field shown in Eq. 1.13. This potential comes from the non-perturbative contribution of instantons 't Hooft [1976]. Since the symmetry breaking scale f_a and the axion mass can be related by $m_a^2 f_a^2 = \Lambda_{\rm QCD}^4$, the equation of motion can be rewritten as

$$\left(\frac{d^2}{dt^2} + \frac{3}{2t}\frac{d}{dt}\right) a(t) + m_a^2(t) f_a \sin\left(\frac{a(t)}{f_a}\right) = 0, \tag{1.15}$$

where we have assumed the radiation era with $R(t) \propto \sqrt{t}$ and the homogeneity of axion fields. If the axion field is homogenized by inflation, the above equation captures all the physical information for the evolution of axion fields. However, this no longer holds if Peccei-Quinn symmetry breaking occurs after inflation and there are extra contributions from topological defects that cause spatial variance in the axion field. For the moment, we focus on the evolution of homogeneous axion fields. When the axion mass term is negligible compared to the Hubble parameter, the axion potential will behave as a dark energy term and the field value is

$$a(t) = a_0 + a_{1/2} t^{-1/2}, \tag{1.16}$$

where a_0 and $a_{1/2}$ are constants. Therefore the axion field will soon become constant during the expansion of the Universe. As t approaches the time when the axion starts to oscillate, t_1, which satisfies $m_a(t_1) = H(t_1) = 1/(2t_1)$, the axion field will evolve very differently. Solving the equation of motion, we will see axions will behave as matter. Assuming the initial field value is sufficiently small such that $f_a \sin(a/f_a) \approx a$, and defining a field ψ:

$$a(t) \equiv t^{-3/4} \psi(t), \tag{1.17}$$

the equation of motion can be rewritten as

$$\left(\frac{d^2}{dt^2} + \omega(t)^2\right) \psi(t) = 0, \tag{1.18}$$

where

$$\omega(t)^2 = m_a^2(t) + \frac{3}{16t^2}. \tag{1.19}$$

Once $t > t_1$, $\omega(t)$ rapidly reaches m_a and $\psi_0^2\omega(t)$ is adiabatically invariant. The solution can be written as

$$a(t) \approx A(t)\cos\left(\int^t dt'\omega(t')\right), \tag{1.20}$$

with

$$A^2(t)m_a(t) \propto t^{-3/2} \propto R(t)^{-3}. \tag{1.21}$$

This provides solutions to the zero mode axions, whose number per co-moving volume is conserved. This will hold as long as the changes in axion mass are adiabatic. The changes in axion mass are determined by the temperature in the radiation component, which can be modeled as Hertzberg et al. [2008]:

$$m_a(T) = \begin{cases} m_a(0) & T < 0.2 \text{ GeV}; \\ m_a(0)(\frac{0.2 \text{ GeV}}{T})^{6.5} & 0.2 \text{ GeV} \leq T \leq 1 \text{ GeV}; \\ bm_a(0)(\frac{0.2 \text{ GeV}}{T})^4 & T > 1 \text{ GeV} , \end{cases} \tag{1.22}$$

where $b = 0.018$ and $m_a(0) = (78 \text{ MeV})^2/f_a$, and $m_a(0)$ is the axion mass at zero-temperature. Therefore we expect the changes are adiabatic and axions shall behave as dark matter.

The energy density of dark matter relic abundance produced from the vacuum misalignment mechanism is

$$\rho_a^{\text{vc}} \sim \frac{1}{2}m_a(0)m_a(t_1)a(t_1)^2 = \frac{f_a^2 m_a(0)}{2t_1}\alpha_1^2, \tag{1.23}$$

where α_1^2 is the average axion field value before QCD phase transition. After t_1 the axion density will scale like matter

$$\rho_a^{\text{vc}}(t_0) \sim \frac{f_a^2 m_a(0)}{2t_1}\left(\frac{R_1}{R_0}\right)^3 \alpha_1^2. \tag{1.24}$$

In the pre-inflationary scenario, α_1 is just a number ranging from 0 to 2π and it should be considered as an input parameter to the model. On the other hand, it will be averaged over different horizons in the post-inflationary scenario and the relic abundance from the vacuum misalignment mechanism is fixed. Inserting the QCD scale, we can write the axion relic abundance from vacuum misalignment as

$$\Omega_a \sim 0.15\left(\frac{f_a}{10^{12}\text{GeV}}\right)^{7/6}\alpha_1^2. \tag{1.25}$$

1.2.2 Axions from topological defects

In the so called post-inflationary scenario, topological defects such as strings and domain walls can also form, and these will contribute to the axion relic abundance via emitting relativistic axions. The formation of domain walls is generically problematic as their energy density scales like $\rho_{\rm wall} \propto t^{-1}$ and they tend to overclose the Universe. So we will be focusing on the case where $N_{\rm DW} = 1$ to avoid the cosmological disaster ($Z(N_{\rm DW})$ is the subgroup of $U(1)_{\rm PQ}$ that is not broken by non-perturbative QCD effects, which implies a $N_{\rm DW}$ fold degeneracy of the vacuum). When $N_{\rm DW} = 1$, the domain walls bounded by strings can still form when axions accquire the mass but they will decay to axions. However, we assume this is not a cosmological problem here like everyone else. Therefore, the emission from topological defects like axion strings is the most important contribution to the axion relic abundance.

The evolution of axion strings and its contribution to dark matter density is a very difficult problem to solve though it has been studied numerically by many groups Vaquero et al. [2019], Gorghetto et al. [2021], Buschmann et al. [2022]. Different groups predict different axion relic density from strings, leaving it a open question for further discussion or debate. In this section, we will summarize the basic equations that govern the evolution of axion strings and the emission of axions. The current status of the study of axion strings will also be reviewed.

The axion string is a type of cosmic string that carries non-zero winding number under the $U(1)_{\rm PQ}$ symmetry. Its string tension is related to the Peccei-Quinn symmetry breaking scale

$$\mu = \pi f_a^2 \ln (f_a L), \tag{1.26}$$

where L is the infra-red cutoff which should equal the distance to the nearest neighbor string. Axion strings store a huge amount of energy within the string core and they strongly couple to axions. Therefore, the decay of strings is a very efficient way of producing axions. The exact relic density from string decay will sensitively depend on its evolution as well as the radiation spectrum, both of which can in principle be determined by numerical simulations.

Even though the axions emitted by strings are initially relativistic, the velocity will be redshifted and they soon become nonrelativistic in the early Universe, contributing to the relic density. When

the strings get unstuck from the plasma, they move freely at relativistic velocities and intersect with each other. The dynamics of this process is complicated as long strings that stretch across the horizon can reroute the topological flux and form string loops, which radiate axions, evolving in a way so that there is only a handful of strings per Hubble volume. Thus the, energy density in long strings can be estimated as

$$\rho_{\rm str}(t) \sim \xi\pi\frac{f_a^2}{t^2}\ln(f_a t), \tag{1.27}$$

where $\xi \sim 30$ characterizes the number of strings per horizon. Numerical studies find that it could be fitted as $\xi = \xi_0 + \xi_1 \ln(f_a/H)$, where H is the Hubble parameter Gorghetto et al. [2018, 2021], Buschmann et al. [2022]. The evolution of axion number density from the emission of strings, $n_a^{\rm str}$, can be described by the following equations

$$\begin{aligned}\frac{d\rho_{\rm str}}{dt} &= -2H\rho_{\rm str} - \frac{d\rho_{{\rm str}\to a}}{dt};\\ \frac{dn_{\rm str}}{dt} &= -3H\rho_{\rm str} + \frac{1}{\omega(t)}\frac{d\rho_{{\rm str}\to a}}{dt},\end{aligned} \tag{1.28}$$

where $\omega(t)$ is defined as

$$\frac{1}{\omega(t)} = \frac{1}{\frac{d\rho_{{\rm str}\to a}}{dt}}\int \frac{dk}{k}\frac{d\rho_{{\rm str}\to a}}{dt\,dk}. \tag{1.29}$$

Therefore, the spectrum of the string emission, $\frac{d\rho_{{\rm str}\to a}}{dt\,dk}(k,t)$, is crucial to determine the axion relic density from string emissions, with redder spectra leading to a more efficient conversion of the string energy into relic nonrelativstic axions. It is challenging to simulate the emission of axions from strings and the numerical results are controversial. The most challenging part concerns the dynamical range. While the string core has a physical size determined by $1/f_a$, the simulation box is a comoving volume and gradually loses sensitivity to small physical scales as the Universe expands. Therefore, one might need to use an adaptive mesh to maximize the dynamical range of simulations and this has been implemented in a recent work Buschmann et al. [2022]. The string contribution to the axion relic abundance has been found to be dominating over the misalignment contribution in Ref. Buschmann et al. [2022] and Gorghetto et al. [2021] while other groups found it to be subdominant Vaquero et al. [2019]. The study of axion string evolution and emission remains an active research direction and we hope to see more progress in the future.

1.3 *Axion Miniclusters and Minihalos*

In the post-inflationary scenario, as we discussed in the previous section, the axion field takes different values in different horizon patches. The axion field fluctuations will convert to matter density fluctuations if the axion is responsible for the dark matter relic density, enhancing the matter power spectrum on extremely small scales. Those order unity fluctuations will lead to the formation of the so-called axion miniclusters at matter-radiation equality. In the standard thermal history, assuming QCD axion parameters that give us the correct relic abundance (as we noted earlier, the contribution from axion strings may introduce some uncertainties here), axion miniclusters will have characteristic masses of $\sim 10^{-12} M_\odot$ and radii of $\sim 10^{12}$cm Hogan and Rees [1988], Kolb and Tkachev [1993, 1996]. (The mass and radii range can be modified by a nonstandard thermal history before big bang nucleosynthesis Nelson and Xiao [2018], Visinelli and Redondo [2020].)

These axion miniclusters, if they remain at their original density, might be detected in femto-, pico- Kolb and Tkachev [1996], and microlensing surveys as long as the concentration number is larger than $\sim 10^7$ at the characteristic mass Fairbairn et al. [2018]. However, initial miniclusters merged and formed bigger and less concentrated structures after matter-radiation equality, which makes them less detectable. As we will discuss later, the axion density perturbations have a white spectrum that extends to long wavelengths. Therefore, those longer-wavelength perturbations collapse and form more massive structures at progressively later times, which will be the dominant component of axion substructures. We call these late-time structures axion minihalos, and the low-redshift spectrum of structures that results is what is relevant for observations (by low here we really mean in comparison to the redshift of matter-radiation equality when axion miniclusters first formed). Even though axion minihalos at late times are not as dense as the initial axion miniclusters, many of these still form well before the halos of standard inflationary perturbations, and as such the axion minihalos can be much more compact and denser than the normal massive CDM halos that form from adiabatic fluctuations– making them less susceptible to disruption processes and also more detectable.

Axion minihalos have planetary masses but are much more diffuse than planets, though much

denser than normal CDM halos – which makes them more detectable. There are several recent proposals for detecting dark matter minihalos. One uses the Shapiro time delays and Doppler shifts that these minihalos could impart on pulsar timing Dror et al. [2019], Ramani et al. [2020]. A second proposal uses the effect of these minihalos on the microlensing caustics of cosmological stars that are highly magnified both by a cluster lens and stellar microlens Dai and Miralda-Escudé [2020]. Other proposals go beyond the gravitational effect and focus on the axion-photon coupling, including detecting radio emission from axion stars (which are likely to form in the central cusp of axion halos Kolb and Tkachev [1994, 1993], Kirkpatrick et al. [2020], Eggemeier and Niemeyer [2019], Levkov et al. [2018], Bai and Hamada [2018], Hertzberg and Schiappacasse [2018], Hertzberg et al. [2020], Prabhu [2020], Prabhu and Rapidis [2020], Carenza et al. [2020]), transients such as Fast Radio Bursts as a potential signal of the explosive decay of axion miniclusters Tkachev [2015], Iwazaki [2015], van Waerbeke and Zhitnitsky [2019], Dietrich et al. [2019], Sun and Zhang [2020], Buckley et al. [2020], and axion-photon conversion in neutron stars Safdi et al. [2019], Battye et al. [2020], Foster et al. [2020], Hook et al. [2018] or the Galactic Center Caputo et al. [2019]. Finally, the clumpiness of cosmic axions could affect direct detection efforts like the Axion Dark Matter eXperiment (ADMX)Braine et al. [2020], especially if a significant fraction of present-day axions are bound in minihalos. The direct detection is also related to the disruption of axion minihalos in the Milky Way galaxy, which may set some axions free from those bound objects Shen et al. [2022].

Given the current experimental proposals, it is crucial to accurately calculate the abundance and densities of axion minihalos, which will eventually determine the observability. One would naturally start from a semi-analytic method such as the Press & Schechter formalism to estimate the mass function of axion minihalos, which has been very successfully for normal CDM halos Press and Schechter [1974]. In Press & Schechter, the mass function is given by

$$\frac{m^2 dn/dm}{\bar{\rho}} \frac{dm}{m} = \nu f(\nu) \frac{d\nu}{\nu}, \tag{1.30}$$

where $\bar{\rho}$ is the comoving density of matter and ν, $f(\nu)$ are defined as:

$$\begin{aligned} \nu f(\nu) &= \sqrt{\frac{\nu}{2\pi}} \exp(-\nu/2), \\ \nu &\equiv \frac{\delta_c^2(z)}{\sigma^2(m)}, \end{aligned} \tag{1.31}$$

where δ_c is the critical density required for spherical collapse at z. In an Einstein-de Sitter cosmology, $\delta_c = 1.686$. $\sigma^2(m)$ is the variance in the initial density fluctuation field when smoothed with a tophat filter of scale $R = (3m/4\pi\bar{\rho})^{1/3}$, which can be determined as:

$$\sigma^2(m) \equiv \int \frac{dk}{k} \frac{k^3 P(k)}{2\pi^2} |W(kR)|^2, \tag{1.32}$$

where $W(x) = (3/x^3)[\sin(x) - x\cos(x)]$ is the spherical top-hat window function. Therefore, the primordial axion power spectrum $P(k)$ is crucial for calculating the axion minihalo mass function. At the critical time when the axion starts to oscillate, the energy stored in the vacuum will start to convert to matter, imprinting density fluctuations. Therefore, the size of the horizon at the oscillation time characterize the scale at which the fluctuation is order unity. The axion isocurvature fluctuations at wavenumbers with $k \ll \mathcal{H}_{\rm osc}$ follow a white noise power spectrum because different $\mathcal{H}_{\rm osc}^{-1}$ patches were not in communication and therefore uncorrelated. The axion density will be randomly distributed owing to the random field values ranging from 0 to 2π. Furthermore, because many horizon patches contribute to these scales, we assume the spectrum of fluctuations is Gaussian so that the power spectrum fully describes the fluctuations. The Gaussian nature of $k \ll \mathcal{H}_{\rm osc}$ axion perturbations is important, since otherwise one could not simply use the semi-analytic method to calculate the mass function. This assumption has been justified in N-body simulations as the lower wavenumbers are dominating the formation of axion minihalos that are relevant for observations Xiao et al. [2021]. Therefore, the initial axion perturbations can be well described by a white power spectrum until a sharp cutoff:

$$\Delta^2_{\mathcal{L}}(k) \equiv \frac{k^3}{2\pi^2} P_(k) = A_{\rm osc} \left(\frac{k}{k_{\rm osc}}\right)^3 \quad \text{at } k < k_{\rm osc}, \tag{1.33}$$

where $P_(k) \equiv V^{-1} |\tilde{\delta}_{\mathcal{L}}(\mathbf{k})|^2$, V is the volume, $\tilde{\delta}_{\mathcal{L}}$ is the Fourier transform of the configuration-space linear dark matter overdensity, $k_{\rm osc} \equiv \mathcal{H}_{\rm osc}$ and can be phrased in terms of the axion mass at low

temperatures, m_a, via Vaquero et al. [2019]

$$\frac{1}{k_{\rm osc}} = 0.036 \left(\frac{50\mu{\rm eV}}{m_a}\right)^{0.17} {\rm pc}, \tag{1.34}$$

and $A_{\rm osc}$ sets the normalization, with $A_{\rm osc} \sim 1$ resulting in order-unity fluctuations on the oscillation scale Simulations of the QCD axion field evolution in the early Universe find that values of the initial isocurvature variance are $A_{\rm osc} \sim 0.01 - 0.3$ Vaquero et al. [2019], Buschmann et al. [2020], where the large range of values depends on the importance of axion strings compared to the misalignment mechanism in establishing the density fluctuations. While the overall normalization appears to be smaller in the scenario of axion string formation, the power spectrum extends to even smaller scales which corresponds to the string structure inside horizon, which enhances the inhomogeneity on small scales. However, as shown in Ref. Xiao et al. [2021], the behavior of high k modes is the most relevant as minihalos will merge and form larger structures whose evolution is determined by the white-noise power spectrum at scales much larger than the horizon size. A wavenumber of $k_{\rm osc}$ can be define a characteristic mass scale which will be useful in the following Dai and Miralda-Escudé [2020]:

$$M_0 \equiv \frac{4\pi}{3}\left(\frac{\pi}{k_{\rm osc}}\right)^3 \bar{\rho}_{a,0} = 2.3\times10^{-10}\left(\frac{50\mu{\rm eV}}{m_a}\right)^{0.51} M_\odot, \tag{1.35}$$

where $\bar{\rho}_{a,0}$ is the mean density of axions in the present day. Integrating over the white-noise power spectrum, we can express the variance as:

$$\sigma(M) = \sqrt{\frac{3A_{\rm osc}}{2\pi^2}\frac{M_0}{M}}. \tag{1.36}$$

Now we have everything ready to compute the mass function of axion minihalos. Numerical studies find that while the Press & Schechter formalisim provides a good estimation to the mass function, a tweaked Sheth-Tormen mass function can fit the simulation results much better Xiao et al. [2021]. Since the white-noise spectrum is scale invariant (as we can see, the variance σ is a function of M/M_0 only), the simulation results apply to all scales and the fitting formula is generic as long as the power spectrum of density fluctuations is white-noise.

As one obtains the necessary information for the mass distribution of axion minihalos, one still needs to figure out the mass profile as well as its mass-concentration relation to obtain all the physical

information that will determine the observational signatures. While the mass-concentration relation has been studied quite extensively in the scenario of normal CDM halos, it is not well explored in the scenario early structure formation such as axion minihalos. Numerical studies find that a scaling law for certain mass ranges can well fit the mass-concentration relation Xiao et al. [2021], which can be motivated analytically by assuming the initial concentration of minihalos is 4 and then grows linearly with time as the background density drops. More studies will be needed to extend the conclusion to more mass ranges, quantify the impact of dense substructures of minihalos and estimate the scatter in the mass-concentration relation.

1.4 *Axion Stars*

The axion minihalos, being light, cold and dense, are ideal environments for axion star formation. The axion Universe is also more interesting given the possibility of axion star formation. Even though there is no dissipative force as in the visible sector, the bosonic nature of axions provides an extra window for star formation via Bose-Einstein condensation. Numerical studies have shown axion stars do form within a Hubble time in the presence of axion minihalos Levkov et al. [2017, 2018], Chen et al. [2021]. Therefore, understanding the formation and evolution of axion stars will be very important given the progress we have made in axion minihalos. Also, this can potentially provide more windows into the detection of physics in dark sector.

Axion stars, are stable axion-field configurations that are balanced by kinetic pressure, gravity and axion self-interactions. There are two branches of axion stars that have stable solutions, namely the dilute branch and the dense branch. The dilute branch is balanced by the kinetic pressure and gravity only while self-couplings are dominating over gravity in the dense branch. Since the self-interaction is attractive, the moment it turns on axion stars will collapse and emit relativistic axions, which makes them cosmologically unstable. There is a critical star mass that separates the two branches. Therefore, if they continue to accrete mass, the lighter dilute axion stars will eventually become unstable in a minihalo environment.

1.4.1 Axion Stars as Stable Configurations of Axion fields

The stable axion-field configuration for the gravitational bound-state of non-relativistic axions can be found by solving the Gross-Pitaevskii-Poisson equations, which must be done numerically. However, it has been shown that a good approximation of these solutions is obtained by using a Gaussian ansatz for the field profile Chavanis [2011], Chavanis and Delfini [2011], Chavanis [2016]. Doing so gives some insight into the competing effects driving the physicsVisinelli et al. [2018]. Expanding the axion potential to quartic order one finds an attractive self interaction

$$V = \frac{1}{2}m_a^2\phi^2 - \frac{\lambda}{4!}\phi^4 \,, \tag{1.37}$$

with $\lambda = (1-3c)m_a^2/f_a^2$. An axion star of mass M_* and radius R_* has energy

$$E_* = -\frac{G_N M_*^2}{R_*} + c_1\frac{M_*}{2\,m_a^2 R_*^2} - c_2\frac{\lambda M_*^2}{12\,m_a^4 R_*^3} \,. \tag{1.38}$$

In order, these terms correspond to the gravitational self energy, the gradient pressure, and the internal energy from self interactions. The numerical coefficients, c_i, depend upon the details of the field profile and are found numerically Ruffini and Bonazzola [1969], Membrado et al. [1989], Visinelli et al. [2018] to be $c_1 = 9.9$, $c_2 = 0.85$. The mass-radius relation for axion stars, found by minimizing E_*, has two solutions

$$R_*^{\pm} = \frac{c_1}{2\,G_N M_* m_a^2}\left(1 \pm \sqrt{1 - \frac{c_2}{c_1^2}\lambda G_N M_*^2}\right) \,. \tag{1.39}$$

The R_*^+ root corresponds to the so-called dilute branch in which the axion field value is small. On this branch gravitational attraction is balanced by gradient pressure leading to a stable configuration. As is typical for objects supported by uncertainty pressure the product of the radius and mass of the star is a constant

$$R_*^+ = 9.9\frac{M_{\rm pl}^2}{m_a^2 M_*} \,. \tag{1.40}$$

However, as one moves to larger axion star mass the self interactions cannot be ignored and if they are attractive (as assumed above) they destabilise the star. There is a maximal mass, beyond which axion stars are no longer stable

$$M_*^{max} = \frac{10.7}{\sqrt{\lambda}}M_{\rm pl} \,. \tag{1.41}$$

The two solutions meet at this maximal mass. The second solution is one where gravity can be ignored and the gradient pressure and the axion's attractive self interactions are in unstable equilibrium. On this branch $R_* \propto M_*$.

The value of the axion field at the center of the star scales as $a_0^2 \sim M_*/(m_a^2 R_*^3)$ so that at the low mass end of the R_*^- branch $a_0 \sim 1$ and the axion field is not dilute. The axions can no longer be thought of as non-relativistic and the solution is approximately constant density ($\rho \sim m_\pi^2 f_\pi^2$) and thus $R_* \sim M_*^{1/3}$. However, it is believed that this field configuration is also unstable, with a lifetime $\sim 10^3 m_a^{-1}$ Visinelli et al. [2018], although alterations to the axion potential can make these solutions long lived Cyncynates and Giurgica-Tiron [2021], Kawasaki et al. [2020], Olle et al. [2021].

The upshot of this is that if a dilute axion star with mass below $M_*^{\max}$ were to form and grow, by accumulation of additional axions, to the maximal mass it would then shrink in size and become a dense axion star which would survive for a short period. During this time the dense axion star goes through several oscillations and a density singularity develops in the central core and this dense region emits relativistic axions lowering the density Levkov et al. [2017]. This process repeats and $\sim 30\%$ of the initial star mass can be emitted, leaving a dilute remnant which may in turn grow to the maximal mass and emit more relativistic axions. Thus, maximal mass stars are an engine to turn substantial amounts of cold dark matter into radiation.

1.4.2 Condensation time for the formation of axion stars

Now we turn to the problem of the formation rate of axion stars. Once minihalos exist, gravitational interactions or self-interactions can subsequently lead to the formation of Bose-Einstein condensed axion stars at their center. The timescale for this formation, and subsequent growth, in an environment where the axions being captured have typical number density n and speed v is determined Levkov et al. [2018], Eggemeier and Niemeyer [2019], Chen et al. [2021], Kirkpatrick et al. [2020] by

$$\tau \sim (f_{\rm BE} n \sigma v)^{-1} \ . \tag{1.42}$$

With σ the total scattering cross section. This formation rate is Bose-enhanced from the naive expectation due to the large phase space density, $f_{\rm BE} = 6\pi^2 n (m_a v)^{-3}$. The gravitational Rutherford transport cross section is $\sigma_{\rm gr} = 8\pi (G_N m_a v^{-2})^2 \log(m_a v R)$, where the Coulomb logarithm has been cutoff at a characteristic length scale of the minihalo, R. Attractive self-couplings can also lead to formation and the scattering cross section is $\sigma_{\rm self} = \lambda^2 m_a^{-2}/128\pi$. The total condensation time, considering both gravity and self-interaction, is

$$\tau_{\rm total} = \frac{\tau_{\rm self}\tau_{gr}}{\tau_{\rm gr} + \tau_{\rm self}}. \tag{1.43}$$

With each individual process having a timescale of

$$\tau_{\rm gr} = \frac{b}{48\pi^3} \frac{m_a v^6}{G_N^2 n^2 \log\left(m_a v R\right)} \,, \tag{1.44}$$

for gravity, and

$$\tau_{\rm self} = \frac{64 d m_a^5 v^2}{3\pi n^2 \lambda^2} \,. \tag{1.45}$$

The parameters $b, d \sim O(1)$ are numerical coefficients that are extracted from numerical simulations Chen et al. [2021]. Comparing these two timescales, (6.9) and (6.10), we see that the self interactions will determine the axion star formation rate if $f_a \lesssim M_{\rm pl} v$. When determining the gravitational relaxation timescale for formation of axion stars in minihalos we take, as typical, the densities and speeds at the scale radius. Therefore, one can calculate the formation time of axion stars given the density and velocity in the axion minihalos, which can be obtained from halo parameters such as the halo concentration and the halo mass.

Chapter 2

AXION COSMOLOGY WITH EARLY MATTER DOMINATION

2.1 *Introduction*

The QCD axion, which was invented to solve the strong CP problem Peccei and Quinn [1977], Peccei [2008], is a well-motivated candidate for dark matter. The axion mass and couplings are determined by a single parameter, the axion decay constant f_a. Laboratory, astrophysical and cosmological bounds on f_a place it well above the weak scale. As the axion mass and couplings are inversely proportional to f_a, the axion must be extremely light, long lived, and weakly coupled.

If the axion exists, the misalignment mechanism produces axion dark matter, with an abundance that increases with f_a. It is often stated that there is an upper bound on f_a of 10^{12} GeV so as to not overproduce axions. This bound may be relaxed, e.g., if the axion exists during inflation and our patch of the universe happens to have a small misalignment, or with a new depletion mechanism Agrawal et al. [2018]. Without such tuning or depletion, the allowed value of f_a is in the window $10^9\text{GeV} < f_a < 10^{12}\text{GeV}$ Andriamonje et al. [2007], Ayala et al. [2014], Raffelt [2008], Preskill et al. [1983], Abbott and Sikivie [1983], Dine and Fischler [1983], Vysotsky et al. [1978], Visinelli and Gondolo [2009]. It has been argued that string theory favors a higher value of f_a Banks et al. [2003], Svrcek and Witten [2006], Conlon [2006] and lighter axion than this window allows.

We can detect axions directly through the couplings with SM particles, especially the axion-photon coupling (For some reviews, see Graham et al. [2015], Bradley et al. [2003]). However, there are other interesting strategies for axion indirect detection. The axion can form gravitational bound states on small scales at very early times. If the axion is produced after inflation, then the axion field has an alignment angle which varies over a scale on the order of the Hubble horizon size of the universe at the time of formation Kibble [1976]. Such inhomogeneities can grow and become gravitational bound states called axion miniclusters Tkachev [1986], Hogan and Rees

[1988], Sakharov and Khlopov [1994], Khlopov et al. [1998]. Axion miniclusters could grow to bigger structures or boson stars Kolb and Tkachev [1993], Seidel and Suen [1994], which could be detected by gravitational microlensing Fairbairn et al. [2017, 2018]. On the other hand, if the axion exists during inflation it is much more homogenous initially Kolb and Tkachev [1994], Hogan and Rees [1988], Kolb and Tkachev [1996], Chang et al. [1999], Hardy [2017]. For some references on possible consequences and observations connected with axion miniclusters and axion stars see refs. Barranco et al. [2013], Berezinsky et al. [2014], Tkachev [2015], Tinyakov et al. [2016], Marsh [2016], Braaten et al. [2017], Levkov et al. [2017], Bai et al. [2016], Davidson and Schwetz [2016], Visinelli et al. [2018], Enander et al. [2017], Bai and Hamada [2018], Iwazaki [2017], Eby et al. [2017], Hertzberg and Schiappacasse [2018], and for work on their structure and stability see refs Seidel and Suen [1994], Barranco and Bernal [2011], Braaten et al. [2016], Mukaida et al. [2017], Chavanis [2016], Eby et al. [2016], Helfer et al. [2017], Jackson Kimball et al. [2018], Bai and Hamada [2018], Michel and Moss [2018]. For work on the possible unique signatures of axion structure formation due to their quantum mechanical properties as light degenerate bosons see refs. Nambu and Sasaki [1990], Sikivie and Yang [2009], Rindler-Daller and Shapiro [2010, 2012], Rindler-Daller et al. [2012], Saikawa and Yamaguchi [2013], Noumi et al. [2014], Davidson and Elmer [2013], Davidson [2015], Guth et al. [2015].

The properties of axion miniclusters sensitively depend on the thermal history at the critical time when the axion starts to oscillate. For a radiation dominated universe, the corresponding temperature is typically about 1—10 GeV. This critical time is before big bang nucleosynthesis (BBN) and before the time when the big bang neutrinos decouple, and is during a time which is not connected to any established cosmological observable. If we consider a different thermal history for the universe prior to a temperature of a few MeV, we will see that the upper bound on f_a is relaxed, and there is a significant difference in the formation history of axion miniclusters. With early matter domination, axion miniclusters can form even if the axion field has been homogenized by inflation, due to the more rapid growth of small scale primordial perturbations of the axion. Such early growth of substructure during early matter domination has been considered for other candidate dark matter particles Erickcek and Sigurdson [2011]. The axion is special among dark

matter candidates because its free streaming effects are almost negligible, so very small structures can form and survive.

In this paper we will consider the early cosmology of the standard invisible QCD axion with a nonstandard thermal history, with a period of early matter domination prior to nucleosynthesis. Such matter domination can be due to a heavy, weakly coupled particle whose decays reheat the universe, as is required in some theories of low scale baryogenesis. We will briefly review the theory of the axion and its corresponding cosmology, including the axion relic density and the formation of axion miniclusters in section 2.2. In section 2.3 we will show how the axion window is opened by early matter domination. In section 2.4, a different story of axion minicluster formation with early matter domination is discussed. We will find that early matter domination potentially gives a larger initial characteristic mass of axion miniclusters.

2.2 *Axion Cosmology*

Here we review the axion and its cosmology. (For more details about axion cosmology, see Sikivie [2008], Marsh [2016], Arvanitaki et al. [2010], Grilli di Cortona et al. [2016], Visinelli [2017].) The axion is a pseudo Nambu-Goldstone Boson resulting from the spontaneous breaking of an approximate symmetry known as the Peccei-Quinn (PQ) symmetry, due to the vacuum expectation value of a complex field known as the PQ field. We consider the following Lagrangian for the PQ field, which we call ϕ:

$$\mathcal{L}_\phi = \frac{1}{2}\partial_\mu\phi^\dagger\partial^\mu\phi - \frac{\lambda}{4}(\phi^\dagger\phi - f_a^2)^2 + ... \tag{2.1}$$

where the dots represent possible interaction terms with other particles and f_a represents the vacuum expectation value of $\phi(x)$. The symmetry breaking will occur at a temperature $T_{\rm PQ}$ which is roughly at the scale f_a. Classically, because of the PQ symmetry, the phase of ϕ is undetermined by the potential. After the PQ symmetry breaking, the phase of the PQ field receives a small potential from nonperturbative QCD effects which is minimized at a value for which the strong CP violation vanishes. Fluctuations of the phase about the minimum are parameterized by the axion field $a(x)$.

Ignoring the energetically costly fluctations of the radial direction of ϕ, we may write

$$\langle \phi(x) \rangle = f_a e^{ia(x)/f_a}. \tag{2.2}$$

When the PQ transition occurs, the potential energy with different values of a is nearly degenerate, so a is expected to take on a random initial value. The expansion of the universe will smooth out spatial variations in $a(x)$ but the average value of $a(x)$ remains random until late times. We say the field is misaligned with respect to its minimum, and the energy stored in this misalignment will eventually become the dark matter. There are two different cases for the cosmological evolution. In case 1, the reheating temperature of inflation is less than $T_{\rm PQ}$ and the PQ symmetry is broken during inflation and never restored afterwards. In this case the axion field is smoothed during inflation and randomly obtain a spatially uniform vacuum expectation value αf_a, where α is known as the misalignment angle. Quantum fluctuations in a are small and proportional to the Hubble scale during inflation. As these fluctuations in $a(x)$ are isocurvature, and the cosmic microwave background observations place a strong limit on isocurvature fluctations, in case 1 there is a strong upper bound on the scale of inflation Linde [1985], Seckel and Turner [1985], Lyth [1990], Turner and Wilczek [1991], Lyth and Stewart [1992], Fox et al. [2004]. In case 2 the reheating temperature after inflation is greater than $T_{\rm PQ}$, and the PQ symmetry breaks after inflation. In this case the axion takes on random values uncorrelated over scales which are larger than the Hubble horizon at the time of PQ breaking. Topological axion strings and domain walls are then formed after inflation. Provided that there is no nontrivial unbroken discrete subgroup of the PQ symmetry, every domain wall ends on an axion string and the whole network of strings and domain walls will eventually disappear Sikivie [1982], Chang et al. [1999], Gorghetto et al. [2018]. The cosmological restriction that in case 2 the PQ symmetry must not have any exact discrete subgroup is a severe but achievable constraint on axion model building.

The evolution equation of the axion field in the early universe can be described by the equation

$$\left(\partial_t^2 + 3\frac{\dot{R}}{R}\partial_t - \frac{1}{R^2}\nabla_x^2 \right) a(x) + V'(a) = 0 \tag{2.3}$$

where R is the scale factor, the components of $\mathbf{x}$ are the co-moving spatial coordinates of the universe, and $V(a)$ is the effective potential energy density of the axion field. This potential comes

from non-perturbative QCD effects such as instantons 't Hooft [1976], which break the $U_{PQ}(1)$ symmetry to a $Z(N)$ discrete subgroup Sikivie [1982]. In case 2, we must have $N = 1$ in order to avoid overclosure of the universe by a frustrated network of axion strings and domain walls, while in case 1 any such defects are inflated away (however, see ref. Kaplan and Nelson [2008] for a conceivably observable effect of axion strings outside our horizon). We can write the instanton potential qualitatively as:

$$V_a = f_a^2 m_a^2(T) \left[1 - \cos\left(\frac{a}{f_a}\right)\right] \tag{2.4}$$

where m_a is the axion mass, which is a function of temperature T. The cosine form comes from the dilute instanton gas approximation and is not exact. The form of the axion potential at low temperatures may be found in reference Braaten et al. [2016]. At high temperature ($T >$1 GeV), $m_a(T)$ can be estimated by instanton effects and by lattice QCD. While there is disagreement between different approaches these disagreements will not significantly change our results Dine et al. [2017]. The axion mass is constant when T is below the QCD scale and the calculation at low energies is reliable due to chiral perturbation theory. However, we cannot reliably predict the axion mass when T is between 0.2 GeV and 1 GeV. In standard thermal history, this uncertainty will not affect our prediction of the axion relic density because the temperature at the critical time is higher than 1 GeV. However, we will see in the next section that early matter domination will decrease the critical temperature. We will assume the axion mass to be a continuous function of T, whose exact form will not change our main results. The full expression we will use for the axion mass follows ref. Hertzberg et al. [2008]:

$$m_a(T) = \begin{cases} m_a(0), & T < 0.2 \text{ GeV} \\ m_a(0)(\frac{0.2 \text{ GeV}}{T})^{6.5}, & 0.2 \text{ GeV} \leq T \leq 1 \text{ GeV} \\ b m_a(0)(\frac{0.2 \text{ GeV}}{T})^4, & T > 1 \text{ GeV} , \end{cases} \tag{2.5}$$

where $b = 0.018$ and $m_a(0) = (78 \text{ MeV})^2/f_a$, and $m_a(0)$ is the axion mass at zero-temperature. Given the thermal history of early universe, the axion mass is determined by cosmic time. The first three terms in Eq.(2.3) are proportional to t^{-2}, which are the dominant terms until late times.

We define the critical time t_1 at which the potential term becomes important relative to the Hubble expansion term to be:

$$H(t_1) = m_a(T(t_1)) \tag{2.6}$$

The mean value of the axion field does not evolve much before the time t_1. After t_1 the axion field begins to oscillate and its energy density behaves approximately like nonrelativistic matter. The energy density of a uniform oscillating axion field may be interpreted as the energy density of axion particles at rest. The number of axion particles per co-moving volume is adiabatically conserved because the axion mass changes slowly compared with the oscillation period. In case 1, where axions were homogenized by inflation, axions at rest are the dominate initial component of axions in the universe. In case 2, some spatial variation in the axion field remains which is interpreted as axions with non zero momentum, and also a substantial number of axions are produced via the decay of axion strings and domain walls. The number density of axions at rest is Preskill et al. [1983], Abbott and Sikivie [1983], Dine and Fischler [1983]:

$$n_a^{vac,0}(t) = \frac{1}{2} m_a(t) f_a^2 \alpha^2 \ . \tag{2.7}$$

In case 1, α is uniform throughout our universe and its random value introduces uncertainties in our prediction. We simply treat it as a $O(1)$ constant and do not consider the possible consequences of a small misalignment angle. In case 2, α is randomly distributed taking on many different values throughout our observable universe, and is roughly uniform on scales on the order of the Hubble horizon size at the time of PQ symmetry breaking. As there are many such volumes contained within our current horizon we may average over the different initial values. The dominant source of theory uncertainty for the axion density in case 2 is from the computation of the number of axions produced from the decay of axion strings and domain walls.

2.2.1 Axion Relic Density

In case 1, we can directly get the current energy density of the axion:

$$\rho_a^{\text{vac},0} = \frac{1}{2} m_a(0) m_a(t_1) f_a^2 \alpha^2 \left(\frac{R_1}{R}\right)^3 \tag{2.8}$$

where t_1 is the critical time when axion starts to oscillate and R_1/R is the ratio of the scale factor at the critical time to that at present. The number of axions is approximately conserved and the energy density is simply the number density multiplied by $m_a(0)$. Combined with a radiation dominated thermal history, we obtain the following energy density in case 1:

$$\Omega_a \sim 0.15 \left(\frac{f_a}{10^{12}\text{GeV}}\right)^{7/6} \left(\frac{0.7}{h}\right)^2 \alpha^2 \tag{2.9}$$

where h is defined to give the Hubble constant $H_0 = 100\text{km/s} \cdot h \cdot \text{Mpc}$.

Case 2 is more complicated because axion strings and domain walls will decay to axions and give an extra contribution to the axion relic density. There is a potential so-called domain wall problem when the PQ symmetry group $U_{PQ}(1)$ has non trivial discrete $Z(N)$ subgroup, as in this case there is an N fold degeneracy of the vacuum Sikivie [1982]. We assume in case 2 that $N = 1$ for viable axion cosmology Vilenkin and Everett [1982], Lazarides and Shafi [1982]. In this case the domain walls are unstable and bounded by strings. The string decay contribution to the axion relic density Gorghetto et al. [2018] is highly uncertain and we simply parameterize the uncertainty. Following ref. Hagmann and Sikivie [1991] we write:

$$\rho_a^{\text{str}} = m_a(0) n_a^{\text{str}}(t_1) \left(\frac{R_1}{R_0}\right)^3 \backsimeq Y m_a(0) \frac{f_a^2}{m_a(t_1)} \left(\frac{R_1}{R_0}\right)^3 \tag{2.10}$$

where $m_a(0)$ is the axion mass at zero temperature, $m_a(t_1)$ is the axion mass at the critical time when axion starts to oscillate, and Y is an order one factor which is determined by details such as the efficiency of string decay, the axion string number per horizon and average energy of the axions emitted in a string decay. We simply assume a value for Y here and study what will be different in a nonstandard thermal history.

The last step is to estimate the contribution from higher momentum modes. Assume that axion field varies by f_a from one horizon to the next, we can obtain the number density distribution of higher momentum modes of the axion:

$$\frac{n_a}{d\omega} \sim \frac{f_a^2}{2t^2\omega^2} \tag{2.11}$$

Only frequencies which enter the horizon are physically relevant for this work. Integrating over $\omega > 1/H(t_1)$ in Eq.(2.11) gives us the contribution from vacuum realignment of higher momentum

modes:

$$\rho_a^{\text{vac},1} \sim \frac{m_a(0) f_a^2}{2m_a(t_1)} \left(\frac{R_1}{R_0}\right)^3 \tag{2.12}$$

So the contribution from higher momentum modes is roughly the same as that of the zero momentum mode. Including an estimate of the contribution from higher momentum modes and string decays, the relic density could be written as:

$$\Omega_a \sim 0.6 \left(\frac{f_a}{10^{12}\text{GeV}}\right)^{7/6} \left(\frac{0.7}{h}\right)^2 \tag{2.13}$$

Notice that the axion relic density in case 2 is generally greater than in case 1 for a given f_a.

From Eqs.(2.9),(2.13), we see an upper bound for f_a in order to avoid overproduction of axion dark matter. The upper bounds for case 1 and case 2 with standard thermal history are respectively $\sim 1.4 \times 10^{12}$ GeV and $\sim 4.4 \times 10^{11}$ GeV, with order one uncertainties in both cases. Combined with other constraints, we obtain the so-called axion window, 10^9 GeV $< f_a < 10^{12}$ GeV.

2.2.2 Axion Miniclusters

In case 2, where inflation happens before the PQ phase transition, the initial misalignment angle will not be homogenized by inflation. Therefore, its value will vary randomly from one horizon to another. An inhomogeneity with $\delta\rho_a/\rho_a = O(1)$ is produced when the axion mass turns on. If not erased by the free-streaming effect, gravitationally bound objects , which are called axion miniclusters, may form at the time t_{eq} when energy density of radiation and matter are equal Hogan and Rees [1988], Kolb and Tkachev [1993, 1996], Chang et al. [1999].

Because axions are typically very cold, free-streaming effects will not restrain the form of axion miniclusters Kolb and Tkachev [1996], Chang et al. [1999]. In case 1, only zero mode axions due to vacuum misalignment are produced and there is no velocity dispersion. In case 2, there are higher momentum modes produced by vacuum realignment axions produced by wall decay and string decay. They will give us some non-zero velocity dispersion but it can still be shown that free-streaming will not homogenize the axions.

The characteristic minicluster mass is given by the total mass of axions contained within the

horizon at the critical time when the axion starts to oscillate:

$$M_{mc} = \frac{1}{2} m_a(0) m_a(t_1) f_a^2 \, \frac{4\pi}{3} \left(\frac{1}{H(t_1)} \right)^3 \tag{2.14}$$

Since the number of axions per co-moving volume is conserved, we must take the evolution of the axion mass into consideration in computing the mass of axion miniclusters. If we assume a standard thermal history where the early universe is dominated by radiation, the corresponding temperature of the critical time is:

$$T_1 \simeq 1 \text{ GeV} \left(\frac{10^{12}\text{GeV}}{f_a} \right)^{1/6} \tag{2.15}$$

Thus we obtain the mass of axion miniclusters in a standard thermal history:

$$M_{mc} = 3.7 \times 10^{-10} M_\odot \left(\frac{f_a}{10^{12}\text{GeV}} \right)^{5/3} \tag{2.16}$$

where $M_\odot$ is the solar mass. Note that there are various strategies to estimate the mass of axion miniclusters, such as calculating the axions contained within the horizon at t_{eq}. A detailed study requires the calculation of the mass function of axion minicluster through its power spectrum. The evolution of axion miniclusters in the nonlinear region should be also included, which allows for the possibility of larger axion stars. Such evolution is outside the scope of this paper. Our main goal is to find what will be changed during a nonstandard thermal history. Therefore, we focus on the linear region and give the estimate of the change in the initial axion minicluster mass with early matter domination.

2.3 *Opening the Axion Window*

Nothing so far has been directly detected from the epoch after inflation and before nucleosynthesis. The "standard" assumption about that period is that the inflationary energy density decayed to a hot thermal relativistic plasma containing all the particles in the standard model and possibly some extension Albrecht et al. [1982], Turner [1983], Traschen and Brandenberger [1990], Kofman et al. [1994], reheating the universe, and the universe remained radiation dominated until the temperature dropped below about 1 eV. However, the inflationary energy density could also decay

to some nonstandard massive particles, which could be long lived and come to dominate the energy of the universe, as the energy density of nonrelativistic particles evolves with the scale factor R as R^{-3} while that of radiation evolves as R^{-4}. The success of standard nucleosynthesis implies that any such massive long lived particles have decayed and brought the universe to radiation domination before a temperature of order a few MeV. A pre-nucleosynthesis epoch with energy dominated by nonrelativistic massive particles is called an Early Matter Dominated Epoch (EMDE). Such a scenario is favored by some baryogenesis models as a way to satisfy the out of equilibrium Sakharov condition for producing the asymmetry between matter and anti-matter. One top down motivated example of an EMDE is motivated by stabilized moduli in string theory de Carlos et al. [1993], Banks et al. [1994], Acharya et al. [2014]. Another motivation is to produce curvature perturbations in the curvaton model Mollerach [1990], Linde and Mukhanov [1997], Lyth and Wands [2002], Moroi and Takahashi [2001]. There are other cosmological consequences of a EMDE scenario, such as boosting the thermal dark matter annihilation rate Khlopov and Polnarev [1982], Erickcek et al. [2016], Erickcek [2015], Choi and Takahashi [2017].

An EMDE will affect the axion relic density and expand the allowed range of f_a. The co-moving entropy density will increase during the decay of the massive particles, which will decrease the ratio of axions to photons Giudice et al. [2001], Grin et al. [2008], Visinelli and Gondolo [2010], Kane et al. [2015], Lazarides et al. [1990]. We may calculate the abundance of relic axions with an EMDE by solving Boltzmann equations. We will use the example of matter domination by a particle Φ, whose spin is irrelevant. In the three-fluid model for reheating, the evolution of energy density is give by:

$$\begin{aligned} \frac{d\rho_\Phi}{dt} + 3H\rho_\Phi &= -\Gamma_\phi \rho_\Phi \\ \frac{d\rho_r}{dt} + 4H\rho_r &= \Gamma_\phi \rho_\Phi \end{aligned} \tag{2.17}$$

where ρ_Φ is the energy density of Φ, ρ_r is the energy density of radiation, Γ_Φ is the decay rate of the massive particle and H is the Hubble parameter. We have neglected the contribution from the axion field because it contributes only a minor energy density to the early universe. Combined with the Friedmann equations we can solve the exact energy density of the massive particle and radiation

as a function of cosmic time. We assume that the radiation plasma reaches its equilibrium state instantaneously after Φ decays. This is reasonable since the decay rate is relatively slow compared with the thermalization rate of the light particles. In this way we can also obtain the temperature in terms of cosmic time, which also gives us the mass of the axion as a function of time. Once we know the axion mass as a function of time, the critical time t_1 when the axion starts to oscillate can be estimated from $H(t_1) = m_a(t_1)$. We then use the adiabatic approximation with the co-moving number density of axions conserved after the critical time, which gives the evolution of axion number density at time $t > t_1$:

$$n_a(t) = \frac{1}{2} m_a(t_1) f_a^2 \left(\frac{R(t_1)}{R(t)} \right)^3 . \tag{2.18}$$

When the universe is dominated again by radiation, the entropy density behaves exactly like R^{-3} and n_a/s is conserved. The entropy of universe is dominated by radiation. We can thus obtain the current axion density. The axion energy density must be less than the dark matter relic density. We can therefore obtain an upper bound on the axion decay constant f_a as a function of the reheat temperature T_{rh}. The reheat temperature is directly determined by the decay rate of oscillating scalar field.

$$\frac{\pi^2}{30} g_*(T_{rh}) T_{rh}^4 = \frac{3 E_{pl}^2 \Gamma_\phi^2}{8} \tag{2.19}$$

where g_* is the effective number of degrees of freedom, and E_{pl} is the planck energy. The upper bound on f_a does not depend on the EMDE unless the reheat temperature is below the temperature at the critical time when the axion field begins to oscillate. Thus, only a reheat temperature greater than about 1 MeV (So it happens before nucleosynthesis) and less than about 1 GeV is relevant for a new story of axion cosmology.

2.4 *Axion Miniclusters with Early Matter Domination*

Since the axion window is widened by early matter domination, it is straightforward to show that the possible mass of axion miniclusters increases with a greater axion decay constant. A nontrivial result is that the formation of axion miniclusters is even allowed in case 1, which is not

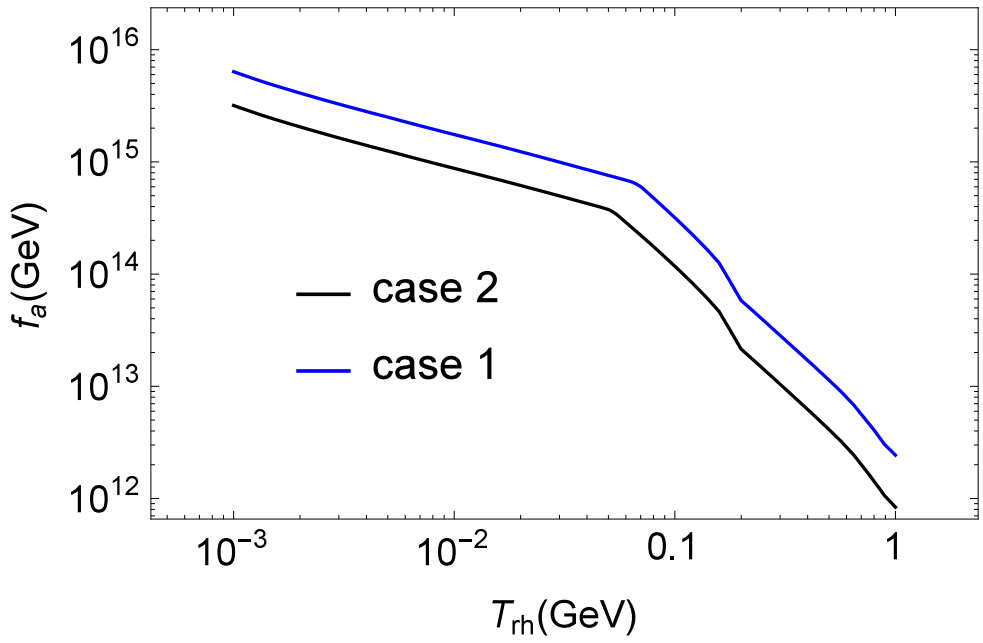

Figure 2.1: New upper bound on the axion decay constant under early matter domination with reheating temperature T_{rh}, assuming the various undetermined constants are of order 1. The blue curve is for case 1 and black curve is for case 2.

expected with a standard thermal history. The formation of miniclusters results because matter density perturbations will grow linearly with the scale factor during the EMDE while they only grow logarithmically during radiation domination. Generally an EMDE allows for an increase in small scale dark matter structure formation Erickcek and Sigurdson [2011], Fan et al. [2014]. But axion miniclusters are especially sensitive to such a period because axions are extremely cold. Free streaming effects are negligible for axions which allows for tiny structures.

For miniclusters in case 2, the correction to the axion minicluster mass from early matter domination is straightforward. We simply estimate the critical time with early matter domination and use the same formula Eq.(2.14). However, in case 1 with standard thermal history axion miniclusters do not generally form. In contrast, the primordial perturbations of axion field that enter the horizon during the EMDE can grow linearly, and form an axion minicluster. If such structures form during the EMDE then they are dominated by the massive particles which will decay to reheat the universe, and when those particles decay the structures will be erased. But structures that form during and after the radiation dominated epoch persist. We estimate the initial size of such structures as follows. We assume a nearly scale invariant primordial perturbation of about 10^{-4} Komatsu et al. [2011]. Axions are frozen before the critical time at which axion oscillations begin. When there is a period of EMDE and the reheating time is later than the critical time, initial inhomogeneities which are inside the horizon will grow linearly with the scale factor. We therefore find the scale at which perturbations of a given scale size enter the horizon during the EMDE, and grow to $\delta\rho/\rho$ of order 1 at the end of the early matter domination epoch. Continued logarithmic growth of these structures will allow for axion minicluster formation at the end of radiation domination. Only specific combinations of f_a and T_{rh} will allow the formation of axion miniclusters in case 1. In general larger axion decay constants lead to a later critical time at which the axion starts to oscillate, and these structures grow linearly with the scale factor only during the EMDE. In case 1, formation of axion miniclusters implies a reheating temperature dependent upper bound on f_a.

2.4.1 Cosmological Perturbations

In order to obtain the axion minicluster mass in case 1, we need to find the perturbation growth during early matter domination. Generally the perturbations will grow linearly with the scale factor if the universe is dominated by matter. In principle the situation is more complicated for the axion because its mass is also changing with time, however the term from the changing mass is negligible compared with the linear growth term for the following reasons: 1. The temperature is typically less than 1 GeV at the critical time when the axion perturbation starts to grow. The axion mass will not change much at that time. 2. The axion mass is temperature dependent and gives perturbations proportional to $\dot{T}/T$, which is actually a logarithmic growth term. We can treat the oscillating scalar field, the radiation and cold axions as perfect fluids with energy momentum tensors Kodama and Sasaki [1984], Malik et al. [2003], Lemoine and Martin [2007]:

$$T^{\mu\nu} = (\rho + p)u^{\mu}u^{\nu} + pg^{\mu\nu} \tag{2.20}$$

Where $u^{\mu} \equiv dx^{\mu}/d\lambda$ is the four-velocity. For cold axions and Φ particles, the pressure is zero and for radiation $p = \rho/3$. Due to the decay of Φ particles, different fluids exchange energy covariantly:

$$\nabla({}^{(i)}T^{\mu}_{\nu}) = Q^{(i)}_{\nu} \tag{2.21}$$

Where i denotes different fluids. For the energy exchange vector:

$$\begin{aligned} Q^{\phi}_{\nu} &= {}^{(\phi)}T_{\mu\nu}u^{\mu}_{\phi}\Gamma_{\phi} \\ Q^{r}_{\nu} &= -Q^{\phi}_{\nu} - Q^{a}_{\nu} \\ Q^{a}_{\nu} &= -{}^{(a)}T_{\mu\nu}u^{\mu}_{a}\frac{\dot{m}_a}{m_a} \end{aligned} \tag{2.22}$$

During the early matter domination, $Q^a \ll Q^{\phi}$. So the the perturbation in axions should not change the evolution of the radiation perturbation. To obtain the perturbation equations, we start with the perturbed metric

$$\mathrm{d}s^2 = -(1 + 2\Psi)\mathrm{d}t^2 + a^2(t)\delta_{ij}(1 - 2\Psi)dx^i dx^j \tag{2.23}$$

Thus we have the perturbation of the four-velocity:

$$\begin{aligned} u^0 &= 1 - \Psi \\ u_i^j &= (1 - \Psi) V_{(i)}^j \end{aligned} \tag{2.24}$$

where $V_{(i)}^j \equiv \mathrm{d}x^j/\mathrm{d}t$ is the fluid velocity of the ith fluid. With the perturbation of energy density of each fluid $\rho_i = \rho_i^0(1+\delta_i)$, we can write the dominant term and the first order perturbation term of Q

$$\begin{aligned} Q_0^{(\phi)} &= \Gamma_\phi \rho_\phi^0 (1 + \delta_\phi + \Psi) \\ Q_j^{(\phi)} &= -\Gamma_\phi \rho_\phi^0 a^2 \delta_{kj} V_\phi^k \\ Q_0^{(a)} &= -\frac{\dot{m}_a}{m_a} \rho_a^0 (1 + \delta_a + \Psi) \\ Q_j^{(a)} &= \frac{\dot{m}_a}{m_a} \rho_a^0 a^2 \delta_{kj} V_a^k \end{aligned} \tag{2.25}$$

Γ_ϕ and $\frac{\dot{m}_a}{m_a}$ are significantly different. One is a constant and the other has perturbation determined by the temperature perturbation of the radiation. Compared with the Hubble parameter, Γ_ϕ is usually negligible but $\frac{\dot{m}_a}{m_a}$ may be important for the perturbation function.

Expressing Q_ν with in terms of the zero-order and first-order perturbations, we can combine equation (1) and (2) to get simple results that determine the perturbation:

$$\begin{aligned} &\frac{\mathrm{d}\delta}{\mathrm{d}t} + (1+w)\frac{\theta}{a} + 3(1+w)\frac{\mathrm{d}\Psi}{\mathrm{d}t} = \frac{1}{\rho^0}[Q_0^{(0)}\delta - Q_0^{(1)}] \,, \\ &\frac{\mathrm{d}\theta}{\mathrm{d}t} + (1-3w)H\theta + \frac{\nabla^2\Psi}{a} + \frac{w}{1+w}\frac{\nabla^2\delta}{a} \\ &= \frac{1}{\rho_0}\left[\frac{\partial_i Q_i}{a(1+w)} + Q_0^{(0)}\theta\right] \,, \end{aligned} \tag{2.26}$$

where $w = p/\rho$ is the fluid's equation of state parameter, and $\theta = a\partial_i V^i$ is the divergence of fluid's conformal velocity. $Q_0^{(0)}$ and $Q_0^{(1)}$ are respectively the zero-order and first-order components of Q.

It can be generally shown that the metric perturbation is frozen in a matter-dominated universe. We define the beginning of early matter domination as $a = 1$ and its corresponding Hubble parameter is H_0. For convenience, we also define dimensionless parameter $\widetilde{\theta_\phi} \equiv \theta_\phi/H_0$, $\widetilde{k} \equiv k/H_0$. Therefore

we can represent our equations during early matter domination in the following way:

$$\begin{aligned}
&a^{-1/2}\delta_\phi^{'}(a) + \widetilde{\theta}_\phi(a) = 0 \,, \\
&a^{1/2}\widetilde{\theta}_\phi^{'}(a) + a^{-1/2}\widetilde{\theta}_\phi(a) + \widetilde{k}^2\Psi = 0 \,, \\
&a^{1/2}\widetilde{\theta}_a^{'}(a) + a^{-1/2}\widetilde{\theta}_a(a) + \widetilde{k}^2\Psi = 0 \,, \\
&a^{-1/2}\delta_a^{'}(a) + \widetilde{\theta}_a(a) = \frac{a\dot{m}_a}{m_a H(t_1)}\Psi \,,
\end{aligned} \tag{2.27}$$

where a prime represents the derivative to scale factor, and $H(t_1)$ is the Hubble parameter at the critical time. It is not hard to show that the term $\frac{a\dot{m}_a}{m_a H(t_1)}$ only causes a logarithmic growth, which could be neglected compared with the linear growth. Eventually the perturbation for modes that have already entered horizon before the critical time is:

$$\delta_a(a,k) = 2\Psi_0 + \frac{2k^2}{3H(t_1)^2}a\Psi_0 \tag{2.28}$$

where Ψ_0 represents the primordial perturbation of quantum fluctuation during inflation, which is about 10^{-4}. Now it is clear that perturbations grow linearly with scale factor a during early matter dominated epoch. To form axion miniclusters efficiently at the end of radiation domination, δ_a must be grow up to about 1. Actually the formation of axion minicluster is complicated here because the growth depends on momentum. We can actually obtain the transfer function for axion generally and calculate the mass function of axion minicluster with Press-Schechter formalism. However, axion perturbation grows to the nonlinear region very early and it is hard to predict its later evolution. In this paper we just estimate the original axion minicluster mass and leave its evolution for future research.

2.4.2 Formation of Axion Miniclusters

A perturbation $\delta_a(a,k)$ will start to grow when k enters the horizon. The momentum modes which have already entered the horizon at the critical time ($k > H(t_1)$) will grow the largest. Typically large k represents smaller axion miniclusters so we only care about $k < H(t_1)$. Therefore the criterion for axion miniclusters formation in case 1 is if $\delta_a(a_e, H(t_1))$ is larger than 1, where a_e is the scale factor at the end of early matter domination. It can be drawn together with the upper

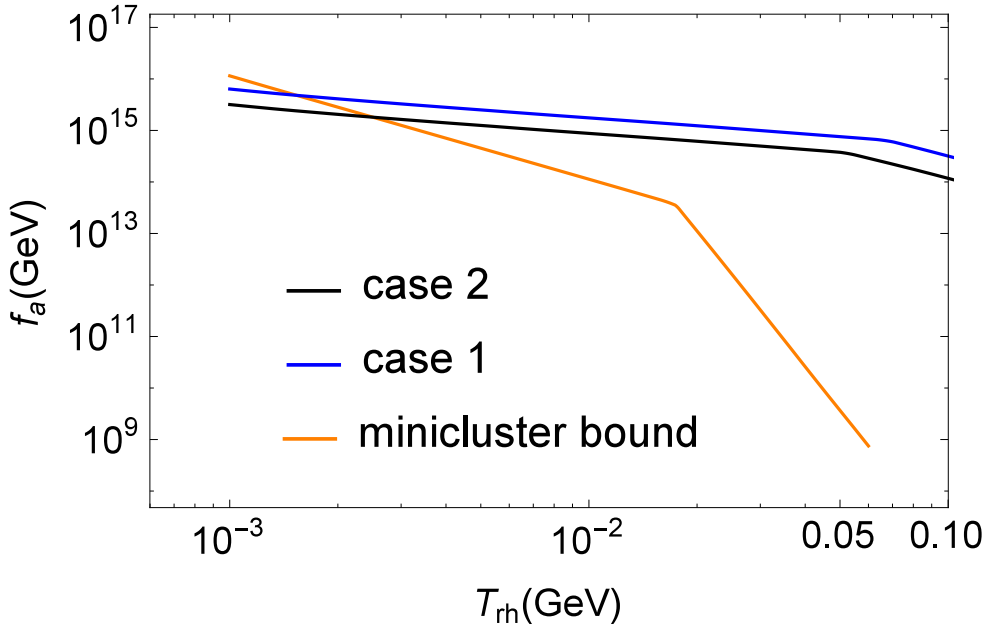

Figure 2.2: The blue and black curve which indicate the bound on f_a from the relic axion density is part of FIG.(2.1). The orange curve represents the upper bound for axion decay constant if growth is sufficient for formation of axion miniclusters in case 1. (In case 2, due to larger initial inhomogeneity on small scales, axion miniclusters can generally form.) The axion density increases with the axion decay constant. When the reheating temperature is sufficiently low, dark matter axions can comprise all of the dark matter as well as form axion miniclusters in case 1, because the blue curve is below the orange curve.

bound for allowed axion density (See FIG.(2.2)). Parameters must be below the bound from axion density to not overproduce axions. To form axion miniclusters, the parameters must be below the orange curve. For case 1, if all the dark matter is axions, the reheating temperature must be below about 60 MeV in order to obtain axion miniclusters.

The final step of this chapter is to determine the mass of axion miniclusters with early matter domination. In case 2 it is can be straightforwardly done by substituting the new critical time. In

case 1, suppose that we have some $k_c < H(t_1)$ which satisfies:

$$\delta_a(a_e, k_c) = 1 \tag{2.29}$$

where a_e is the scale factor at the end of early matter domination. k_c represents the characteristic modes that eventually grow to axion miniclusters. Suppose that k_c enters the horizon at time t_c, $H(t_c) = k_c$. The corresponding axion number density at t_c is:

$$n_{ac} = \frac{1}{2} m_a(t_1) f_a^2 \left(\frac{R(t_1)}{R(t_c)}\right)^3 \tag{2.30}$$

where t_1 is the critical time and R is the scale factor of universe. Therefore axion minicluster mass mass could be estimated by:

$$M_{mc} = \frac{4}{3}\pi m_a(0) \left(\frac{1}{k_c}\right)^3 n_{ac} \tag{2.31}$$

As an example, we calculate how the axion minicluster mass changes with the axion decay constant at a reheating temperature of 3 MeV, as shown in FIG.(2.3). From FIG.(2.3) we can see that the upper limit on the axion minicluster mass has increased to $10^{-8} M_\odot$, where $M_\odot$ is the solar mass. In comparison, from Eq.(2.16), with the standard thermal history the maximum minicluster mass is $\sim 3.7 \times 10^{-10} M_\odot$. It is worth noting that the initial axion minicluster mass is typically less than the critical mass at which an axion star becomes unstable to either a Bosenova or gravitational collapse into a black hole Visinelli et al. [2018], Helfer et al. [2017], Chavanis [2016], Michel and Moss [2018]. The order of magnitude for the minicluster mass at which a gravitational collapse instability sets in is $\sim M_p^2/m_a \sim 10^{-5} M_\odot f_a/(10^{12}$ GeV) which is much larger than the initial minicluster mass.

2.5 *Conclusions*

We have shown that the axion window is wider and the formation history of axion miniclusters is significantly affected by a period of matter domination prior to nucleosynthesis. The axion can be lighter, and the maximum mass of axion miniclusters is increased. Furthermore axion miniclusters can form even in the case where the PQ symmetry breaking occurs before inflation. In this work we

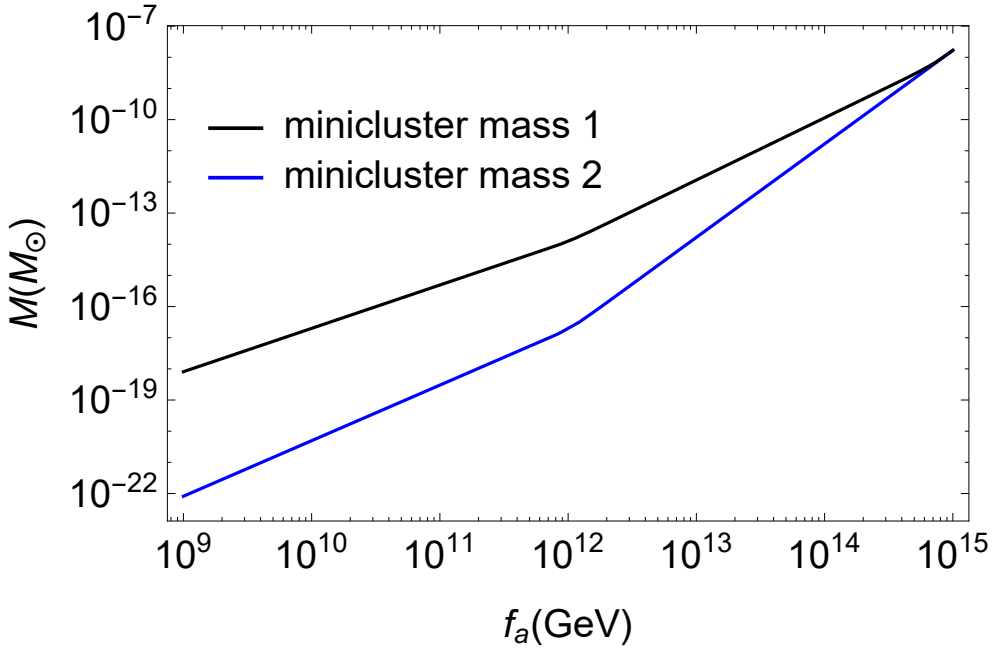

Figure 2.3: The black curve and the blue curve respectively represent the axion minicluster mass in case 1 and case 2 when the reheating temperature is 3 MeV.

have estimated the characteristic mass of axion miniclusters at the time of formation. More detailed numerical study about the evolution of axion miniclusters is needed to obtain the information about axion miniclusters at present, including the mass function of axion miniclusters, the percentage of axions that form axion miniclusters, and the percentage of axion miniclusters that form boson stars or black holes. The evolution of axion miniclusters after their formation and the fraction of axions that finally become gravitationally bound objects requires detailed numerical study, which is beyond the scope of this paper. Such work would be important, as indirect detection of axion miniclusters could possibly provide evidence for both the existence of the axion and for a nonstandard thermal history of the very early universe.

Chapter 3

SIMULATION OF AXION MINIHALOS

3.1 *Introduction*

The QCD axion, a leading solution for the strong CP problem, can also be the dark matter if its mass falls in the range $1 - 100\mu$eV Weinberg [1978], Wilczek [1978], Kim [1979], Abbott and Sikivie [1983], Dine and Fischler [1983], Preskill et al. [1983], Peccei [2008], and possibly smaller masses still with anthropic tuning Wilczek [2004] or a low inflation scale Graham and Scherlis [2018]. In the post-inflationary scenario where Peccei-Quinn symmetry Peccei and Quinn [1977] is broken after inflation, axion dark matter has enhanced small-scale structure that may make it more observable. This enhanced structure occurs because the axion field is coherent over the Hubble horizon when Peccei-Quinn symmetry is broken. Afterwards, the axion field is smoothed by its dynamics on scales up to the horizon size, plus additional discontinuities from topological defects Kibble [1976]. The axion then acquires its mass during QCD era and starts to act as nonrelativistic matter. The local number density of axions when the axion acquires its mass is directly determined by the axion field value there, leaving primordial inhomegeneity at the horizon scale. Topological defects from the symmetry breaking like axion strings also introduce inhomogeneities, extending axion perturbations to even smaller scales Vaquero et al. [2019], Gorghetto et al. [2021].

After the axion becomes nonrelativstic, gravity takes over as the dominant force. Axions residing in $\gtrsim 1$ fractional density perturbations will collapse at matter-radiation equality and form 'axion miniclusters' with characteristic masses of $\sim 10^{-12} M_\odot$ and radii of $\sim 10^{12}$cm Hogan and Rees [1988], Kolb and Tkachev [1993, 1996]. (The mass and radii range can be modified by nonstandard thermal history before big bang nucleosynthesis Nelson and Xiao [2018], Visinelli and Redondo [2020].) In the standard thermal history, the mass range of axion substructures might be detected in femto-, pico- Kolb and Tkachev [1996], and microlensing surveys if the concentration number is

larger than $\sim 10^7$ at the characteristic mass Fairbairn et al. [2018]. Those initial miniclusters merged and formed bigger and less concentrated structures after matter-radiation equality. As the axion density perturbations have a white spectrum that extends to long wavelengths, at progressively later times longer wavelength perturbations collapse and form more massive structures. We call these late-time structures axion minihalos, and the low-redshift spectrum of structures that results is what is relevant for proposed observables. Many of these still form well before the halos of standard inflationary perturbations, and as such the axion minihalos can be much more compact and denser – making them more hardy to disruption processes and also more detectable.

There are several proposals for detecting axion minihalos. One uses the Shapiro time delays and Doppler shifts that these axion minihalos could impart on pulsar timing Dror et al. [2019], Ramani et al. [2020]. Pulsar timing signal of dark matter substructures in mass range 10^{-11}-$10^3 M_\odot$ Dror et al. [2019], Ramani et al. [2020] can be detected in the future by pulsars detected with the Square Kilometer Array (SKA) Rosado et al. [2015]. A second proposal uses the effect of these minihalos on the microlensing caustics of cosmological stars that are highly magnified both by a cluster lens and stellar microlens Dai and Miralda-Escudé [2020]. Such highly-magnified stars have been discovered recently with the Hubble Space telescope Kelly et al. [2018], Chen et al. [2019], Kaurov et al. [2019], and the James Webb Space Telescope (JWST) is projected to find more of these extreme events Dai et al. [2018]. Other proposals include detecting radio emission from axion stars (which are likely to form in the central cusp of axion halos Kolb and Tkachev [1994, 1993], Kirkpatrick et al. [2020], Eggemeier and Niemeyer [2019], Levkov et al. [2018], Bai and Hamada [2018], Hertzberg and Schiappacasse [2018], Hertzberg et al. [2020], Prabhu [2020], Prabhu and Rapidis [2020], Carenza et al. [2020]), transients such as Fast Radio Bursts as a potential signal of the explosive decay of axion miniclusters Tkachev [2015], Iwazaki [2015], van Waerbeke and Zhitnitsky [2019], Dietrich et al. [2019], Sun and Zhang [2020], Buckley et al. [2020], and axion-photon conversion in neutron stars Safdi et al. [2019], Battye et al. [2020], Foster et al. [2020], Hook et al. [2018] or the Galactic Center Caputo et al. [2019]. Finally, the clumpiness of cosmic axions could affect direct detection efforts like the Axion Dark Matter eXperiment (ADMX)Braine et al. [2020], especially if a significant fraction of present-day axions are bound in minihalos.

To place meaningful constraints on axion minihalos and the post-inflation axion scenario requires an understanding of the mass spectrum of these minihalos. Several works have used semi-analytic models that were developed for the inflationary fluctuations to compute the mass function and concentration of axion minihalos Dai and Miralda-Escudé [2020], Enander et al. [2017], Fairbairn et al. [2018], Ellis et al. [2020], Blinov et al. [2020]. It is important to test these semi-analytic models using numerical simulations for the much different case of white isocurvature fluctuations that arise for post-inflationary axions. In addition, the fraction of axion dark matter that collapsed into axion minihalos can only accurately be estimated by numerical simulations. The spectrum of axion density perturbations prior to the QCD epoch has been numerically simulated Vaquero et al. [2019], Buschmann et al. [2020]. Starting from the predictions of these early universe simulations Zurek et al. [2007], Eggemeier et al. [2019], the subsequent nonrelativistic phase in which the evolution is mainly gravitational has also been simulated, and this work follows this program. We compute the (subhalo) mass function and density profiles of axion minihalos at all redshifts to $z = 0$. Even though our simulation is designed for QCD axions, the initial density power spectrum in our numerical experiments is scale-invariant, which makes generalizing some of our results to other axion-like particles (such as fuzzy dark matter Arvanitaki et al. [2010], Hui et al. [2017]) straightforward.

This paper is organized as follows: In section 3.2, we discuss the initial conditions of axion perturbations and other simulation setup. In section 5.5.1, we present the halo mass function obtained from simulation data and fit it with a semi-analytic formula. In section 3.4, we present the density profiles and the mass-concentration relation obtained from our simulation data. In section 3.5, we discuss the observations that will be sensitive to those objects. Our simulation is run with a ΛCDM cosmology with h=0.697, $\Omega_{\rm m} = 0.2814$, and $\Omega_\Lambda = 0.7186$, and some of our semi-analytic calculations further adopt $n_s = 0.9667$, which are consistent with Planck cosmic microwave background results Aghanim et al. [2020]. The radiation component is included in the background evolution with a present-day CMB temperature 2.7255 K and we treat the neutrinos/antineutrinos as massless particles with 3.045 effective degrees of freedom.

3.2 *Simulation of Axion Minihalos*

We follow the nonlinear gravitational evolution of the initial axion perturbations with the MP-Gadget code Feng et al. [2018], which is based on GADGET-2 Springel [2005]. Our simulations focus on larger axion minihalos than previous simulations (such as Eggemeier et al. [2019]). This choice is motivated by our finding that most of the mass at low redshifts is in relatively massive $\sim 10^{-7} M_\odot$ minihalos. This mass is much greater than the mass of the first axion minicluster halo that forms, which are smaller than the mass within the horizon when the axion becomes nonrelativistic ($\sim 10^{-12} M_\odot$). This motivates a simulation box size that is much greater than this horizon. A second motivation is that the axion isocurvature perturbations are white on these super-horizon scales, whereas on smaller scales is set by complicated dynamics that requires evolving the relativistic sine-Gordon equation.

Our simulations start at $z = 30,000$ with radiation background included in the expansion. The evolution of axion isocurvature perturbations is dominated by the matter density and the radiation component can be approximated as a uniform background. The comoving size of our fiducial simulation is 50 pc$/h$, and the simulation follows the gravitational dynamics of 1024^3 dark matter particles each with a mass of $1.3 \times 10^{-11} M_\odot$. We also run a smaller 10pc$/h$ box with 512^3 particles to test a different power spectrum cutoff at high k, as well as a series of 50 pc$/h$, 512^3 simulations to test convergence in force softening and time stepping (Appendix 3.9). However, as our simulations are largely scale invariant with structure formation occurring in a self-similar manner during matter domination, they can essentially be remapped to other mass scales to study other axion-like scenarios. All simulations are run to $z = 19$. By this point, larger scales than captured in our box start to collapse and so it is not motivated to run the simulation further. However, we devise semi-analytic tools to predict the subsequent evolution of minihalos in and outside of more massive halos.

Our results only sensitively depend on the spectrum of density fluctuations on separations larger than the comoving Hubble scale when the axion starts to oscillate in its potential and act as nonrelativistic matter, $\mathcal{H}_{\rm osc}^{-1}$, where $\mathcal{H} = aH$ and a is the scale factor and H is the Hubble function.

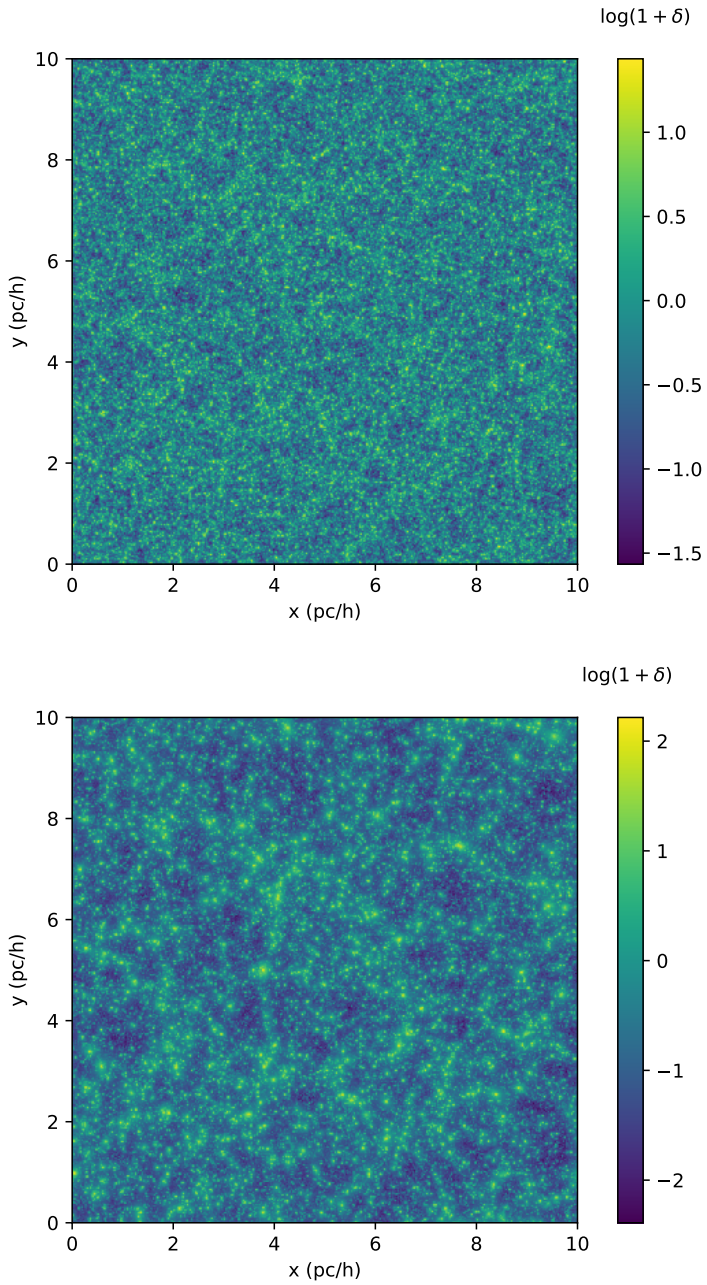

Figure 3.1: Visualization of a projection through the $10/h$ pc simulation at $z = 99$ (top panel) and z=24 (bottom panel). The color scale indicates the logarithm of the projected density field, $\log(1 + \delta_P)$, where δ_P is the projected overdensity. The size of axion minihalos grow significantly between these two redshifts, yet they do not inhabit as distinctive a cosmic web as lower redshift halos that form from the adiabatic perturbations from inflation.

Resolving the initial perturbations on smaller scales would not change our results significantly, as the collapse on larger scales effectively erases the smaller collapsed structures that initially form. However, these smaller structures, if sufficiently segregated in mass and collapse redshift, would likely be subhalos in the larger axion minihalos that later form.

The axion isocurvature fluctuations at wavenumbers with $k \ll \mathcal{H}_{\rm osc}$ follow a white noise power spectrum because different $\mathcal{H}_{\rm osc}^{-1}$ patches were not in communication and so there can be no correlation. Furthermore, because $\gg 1$ horizon patches contribute to these scales, we assume the spectrum of fluctuations is Gaussian so that the power spectrum full describes the fluctuations, although we further justify this approximation later. We initialize our simulation with a white power spectrum until a sharp cutoff:

$$\Delta^2_{\mathcal{L}}(k) \equiv \frac{k^3}{2\pi^2} P_{\mathcal{L}}(k) = A_{\rm osc} \left(\frac{k}{k_{\rm osc}}\right)^3 \quad \text{at } k < k_{\rm osc}, \tag{3.1}$$

where $P_{\mathcal{L}}(k) \equiv V^{-1}|\tilde{\delta}_{\mathcal{L}}(\mathbf{k})|^2$, V is the volume, $\tilde{\delta}_{\mathcal{L}}$ is the Fourier transform of the configuration-space linear dark matter overdensity, $k_{\rm osc} \equiv \mathcal{H}_{\rm osc}$ and can be phrased in terms of the axion mass at low temperatures, m_a, via Vaquero et al. [2019]

$$\frac{1}{k_{\rm osc}} = 0.036 \left(\frac{50\mu{\rm eV}}{m_a}\right)^{0.17} {\rm pc}, \tag{3.2}$$

and $A_{\rm osc}$ sets the normalization, with $A_{\rm osc} \sim 1$ resulting in order-unity fluctuations on the oscillation scale [1]. Simulations of the QCD axion find that values of the isocurvature variance at initial conditions are $A_{\rm osc} \sim 0.01 - 0.3$ Vaquero et al. [2019], Buschmann et al. [2020], where the large range of values we think owes to the importance of axion strings over the misalignment mechanism in establishing the density fluctuations. (There is some controversy in the importance of radiation from axion strings, as discussed later. Our results are applicable regardless.) Though we start our simulation well after the time when the field has become nonrelativistic (at $z = 30,000$), Eq. 3.1 still holds to good approximation at subsequent times during radiation domination Iršič et al. [2020].

[1] In contrast to the small scale limit of ΛCDM model at late times, the dimensionless initial (post QCD-epoch) linear dark matter power spectrum $\Delta^2_{\mathcal{L}}$ in our axion cosmology can reach $O(1)$ at high wavenumbers, indicating that small scales will collapse as early as matter-radiation equality. However, for the mass scales we consider, the collapse occurs generally well after matter-radiation equality

Eq. 3.1 has an artificially sharp cutoff in the spectrum at $k_{\rm osc}$. In the misalignment mechanism for density perturbations, a somewhat sharp cut-off is expected for the modes that entered the horizon when the axion behaved relativistically, as the field homogenize at higher wavenumbers. Defects such as axion strings can result in an even weaker cutoff. However, for the mass scales probed by pulsar timing and microlensing lensing observables that we focus on, the precise wavenumbers and spectral shape of the cut-off are irrelevant since our results will not be sensitive to the affected scales. Therefore, our power spectrum is effectively scale-invariant for the dynamical range of interest. One may also worry about the axion Jeans scale, $k_{\rm J}$, where density and pressure are in equilibrium. Modes can grow only when $k < k_{\rm J}$ otherwise it will be smoothed by pressure. The Jeans scale is given by $k_{\rm J} \approx 2 \times 10^4 a^{1/4} \sqrt{m/(10^{-5}{\rm eV})} {\rm pc}^{-1}$ if the axion is the dark matter Marsh [2016]. Therefore, the modes resolved in our simulation box satisfy $k < k_{\rm J}$.

The initial conditions of our simulations are generated with the parameters $A_{\rm osc} = 0.1$ and the momentum cutoff to be $k_{\rm osc} = 19.8$ pc^{-1}, corresponding to axion mass $m_a = 6.9\mu$eV and decay constant $f_a \approx 10^{12}$GeV. Note that the axion decay constant plays no role in our simulation. The only parameter that matters for structure formation on most mass scales is the amplitude of the power spectrum, $A_{\rm osc}/{k_{\rm osc}}^3$. There are some uncertainties on axion mass due to the production of axions from axion string decay, leading to different m_a and $k_{\rm osc}$ Gorghetto et al. [2021]. We use our simulations to calibrate a semi-analytic model in § 3.2, which allows us to model a broad class of post-inflation axion scenarios.

All modes in our simulation are well within the Horizon at the starting time of the simulation and have a growing and decaying component. We only include the growing mode because of the following justification: The comoving scale of perturbations that contribute to the halos we focus on is larger than $1/k_{\rm osc}$. On such scales the isocurvature fluctuations are much smaller than one ($\Delta^2_{\mathcal{L}}(k) \ll 1$), meaning that the formation of axion structures occurs after matter-radiation equality when the decaying mode is being redshifted away. The picture for isocurvature fluctuations contrasts with adiabatic fluctuations, where the overdensity contrast grows outside the Horizon, at least in the Newtonian gauge, and then its growth freezes if it enters the horizon during radiation domination, leading to additional scale dependence depending on when a mode enters the horizon. This

growth outside the horizon is not present for our isocurvature fluctuations. Once our isocurvature perturbation is within the horizon so that the perturbations in radiation and baryons have been damped, the growing mode of the dark matter in radiation- and matter-dominated epochs can be well described by a solution of the Mészáros equations:

$$D = \frac{2}{3} + \frac{a}{a_{\rm eq}}, \tag{3.3}$$

where D is the growth function of cosmological perturbations. At late times when the dark energy starts to dominate, there are corrections to this growth function that are included in this study. In Iršič et al. [2020], the scale-independent linear evolution given by Eq. 3.3 was checked against a full Boltzmann calculation with isocurvature perturbations and found to agree well. (See this footnote for additional discussion: [2]) We tested the power spectrum in the simulation at early times and found that its behavior is well described by this growth factor in the linear regime.

The initial condition of our simulation is generated with the MP-GenIC code included in MP-Gadget which uses linear order Lagrangian Perturbation Theory (1LPT). Displacements and velocities are generated assuming the power spectrum given by Eq. 3.1 with all the power growing as Eq. 3.3. We justify this perturbative approach because $\Delta^2_{\mathcal{L}}(k) \ll 1$, reaching a maximum of $\Delta^2_{\mathcal{L}}(k_{\rm osc}) = 0.1$. Since the initial time we start the simulation is way after the QCD era, axions are already nonrelativistic at the scale of interest and the velocity is only slightly nonzero in the 1LPT treatment. The initial conditions in Ref. Eggemeier et al. [2019] are generated with zero initial velocity.

The simulation then evolves the linear axion perturbations from $z = 30,000$ to where they become nonlinear and form of axion minihalos. Substructure forms at much earlier times than in the standard ΛCDM cosmology. A visualization of our simulation at $z = 24$ and $z = 99$ is shown in Fig. 3.1.

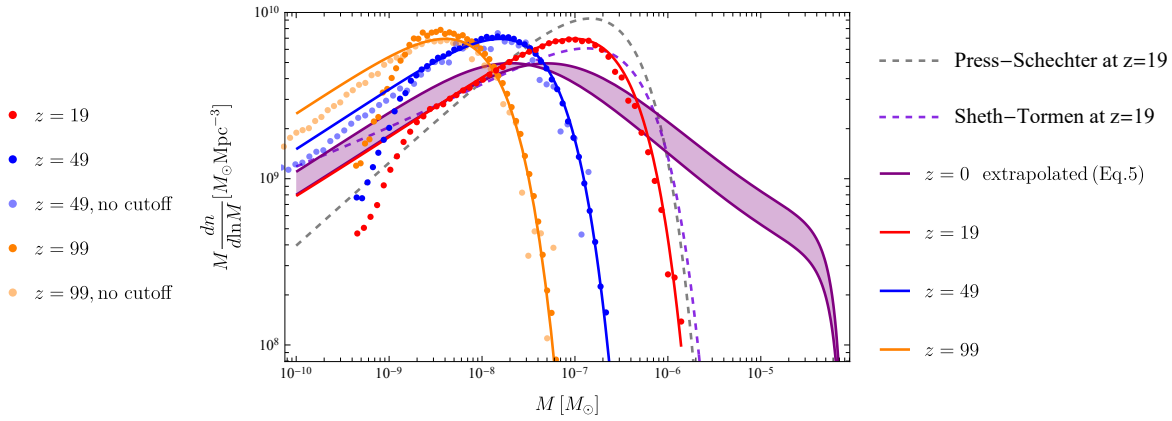

Figure 3.2: The mass function of axion minihalos at select redshifts for a white power spectrum plus cutoff specified by $A_{\rm osc} = 0.1$ and $k_{\rm osc} = 19.8$ pc^{-1}. We compare mass functions obtained from two set of simulations to those in semi-analytic models. The data points are from simulations, and the solid curves are the semi-analytic formula discussed in Appendix 3.8, which recalibrates the barrier parameters of the Sheth Tormen mass function. We also plotted the Press-Schechter and Sheth-Tormen mass functions at $z = 19$. The recalibrated model agrees with the original simulation with a cutoff in the power spectrum except for the high mass end. Another simulation that does not have a cutoff in the power spectrum, denoted by "no cutoff", agrees more broadly with the semi-analytical prediction. The solid "z=0 extrapolated (Eq. 5.1)" band is our model for the present-day number density of axion minihalos. It is our estimate for the mass function of minihalos that resides in most dark matter halos, including those that exist as subhalos. We assume axion minihalos will fall into larger CDM halos (that are too large to be captured in our simulation) and stop merging. The width of the purple band is set by whether the growth of axion minihalos is terminated by when the larger host halo collapses or when it is at turnaround.

3.3 *Mass Function of Axion Minihalos*

We use the Friends-of-Friends (FOF) algorithm Davis et al. [1985] to identify groups of particles in the simulation, demanding any particle that finds another particle within a linking-length distance of l is linked to it to form a group. We choose $l = 0.2\,d$, where d is the mean separation of dark matter particles in the simulation. The minimum number of dark matter particles in each FOF groups is chosen to be $N_g = 32$. This N_g corresponds to a minimum halo mass of $4 \times 10^{-10} M_\odot$ in our fiducial simulation. These choices of l and N_g are standard in cosmological studies, as they approximately select groups that are large enough to be reliably captured in the simulation and link regions with overdensity greater than 80 Knebe et al. [2011], characteristic of the outskirts of dark matter halos. (Minihalos that form during matter domination have a characteristic overdensity of ~ 200 at the time of formation.)

Studies of dark matter halos in the standard CDM cosmology have found great success at explaining the mass function of halos with semi-analytic models developed in the excursion set formalism Bond et al. [1991]. It is unclear how well these models should work in our case, where the density perturbations have a much bluer spectrum, but success for other nonstandard cosmologies gives reason to believe these models may work for our blue spectrum as well Bagla et al. [2009]. We use these semi-analytic formulas to fit the mass function obtained from the simulation. In particular, we consider Press-Schechter Press and Schechter [1974], Sheth-Tormen Sheth and Tormen [1999], and a tweaked mass function that changes the barrier parameters in Sheth-Tormen. See Appendix 3.8 for the relevant formulae. We note that in the standard CDM cosmology, Press-Schechter is able to explain the halo mass function at the factor of ~ 2 level (crudely speaking, as the differences are exponentially enhanced at the highest masses), whereas Sheth-Tormen has been tuned to give percent-level agreement. For the post-inflation axion scenario, both disagree with the simulation at the factor of ~ 2 level, whereas our tweaked Sheth-Tormen mass function fits well the simulated mass function, except for the masses influenced by our wavenumber

[2]An approximation is that our simulations are in the standard limit where all the matter is dark matter, there is a factor of $\Omega_{\rm DM}/\Omega_m \approx 0.8$ suppression over the growth rates relatively to our simulation. The large uncertainty in $A_{\rm osc}$ justifies omitting this factor.

cutoff at $k_{\rm osc}$ ($M \lesssim 10^9 M_\odot$).

The halo mass function of axion minihalos computed from our fiducial simulation is shown in Fig. 3.2. The y-axis shows the comoving number density of axion minihalos per logarithmic mass interval and, then, multiplied by halo mass, such that the integral over this quantity in $\ln M$ gives the total mass in minihalos. As time evolves, the mass function shifts towards higher masses as halos grow and merge. At all redshifts there is a peak halo mass around which much of the mass in axion minihalos lies (e.g. $M \sim 10^{-7} M_\odot$ at $z = 19$), although there is a substantial fraction of lower mass halos.

The shape of the mass function at $M \lesssim 10^{-9} M_\odot$ is affected by the cutoff in our (input) linear power spectrum at $k_{\rm osc}$. A wavenumber of $k_{\rm osc}$ can be turned into a characteristic mass scale Dai and Miralda-Escudé [2020]:

$$M_0 \equiv \frac{4\pi}{3}\left(\frac{\pi}{k_{\rm osc}}\right)^3 \bar{\rho}_{a,0} = 2.3 \times 10^{-10}\left(\frac{50\mu{\rm eV}}{m_a}\right)^{0.51} M_\odot, \tag{3.4}$$

where $\bar{\rho}_{a,0}$ is the mean density of axions in the present day. For our initial conditions, $M_0 = 6.3 \times 10^{-10} M_\odot$, corresponding to axion mass $m_a = 6.9\mu$eV. We have run simulations without a cutoff at $k_{\rm osc}$ ('no cutoff' in Fig. 3.2, with 10pc and 512^3 particles). Comparison of the simulations with and without a cutoff shows that the break in the small-scale power-law scaling of the mass function manifests at several times larger scales than M_0. Interestingly, the semi-analytic model only shows a break around M_0 (a feature that falls off the left-hand side of the plot), so the effect of a cutoff in the power spectrum on the mass function is not well captured in these excursion set models for the mass function. However, as the bulk of the mass in dark matter halos at $z < 100$ resides in halos more massive than are affected by this break, the mass scales around where the break manifests are not important for our primary results. Indeed, a scale-invariant power spectrum is a sufficient description at almost all scales we study: the only relevant parameter is the power spectrum amplitude $A_{\rm osc}/k_{\rm osc}^3$.

Finally, we calculate the total amount of bound structure in axion minihalos. This fraction is important for direct detection efforts, which are sensitive to the unbound component. The fraction of axion dark matter in these bound structures is found to be 0.8 at z=19, growing from 0.6 at $z = 100$.

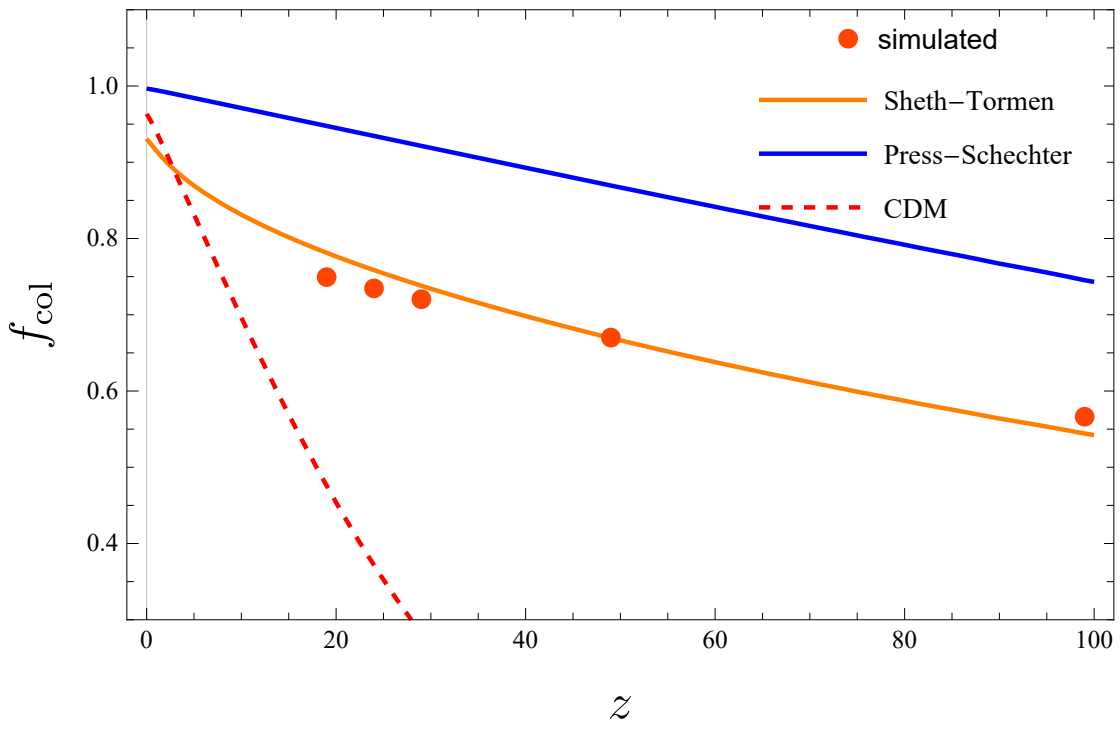

Figure 3.3: The collapsed fraction of axion dark matter as a function of redshift for $A_{\rm osc} = 0.1$ and $k_{\rm osc} = 19.8$ pc^{-1}. The orange data points are the collapsed fraction computed as the mass fraction in our FOF groups from our fiducial white-noise simulation, while the orange and blue curves are the collapse fraction of white noise perturbations in the Sheth-Tormen model and Press-Schechter model, respectively. The collapsed fraction in the Sheth-Tormen and the Press-Shechter models is obtained by intergrating over our white noise mass functions from $M_0 = 7 \times 10^{-10} M_\odot$ to $10^{-4} M_\odot$. The red dashed curve is the Press-Schechter collapse fraction in 'CDM halos' that form from adiabiatic fluctuations (which are calculated by cutting off to include only masses of $M > 10^{-3} M_\odot$ halos for which adiabatic fluctuations dominate). This collapse fraction which appears in our forward-evolution model (Eqs. 5.1 and 5.2).

This is smaller than in Press-Schechter but comparable to the Sheth-Tormen mass function (see Fig. 3.3). We expect that this estimate for the total mass in minihalos is an upper bound, especially in a Milky Way-like environment where stellar disruption processes are important (see § 3.6).

3.3.1 Comparison with mass function calculated from early universe axion simulations

Previous N-body simulations have attempted to start from the initial conditions calculated from solving the sine-Gordon equation for the axion Zurek et al. [2007], Eggemeier et al. [2019]. Unlike our simulations, which are of the white spectrum that occurs at $k \ll \mathcal{H}_{\rm osc}$, their concentration was on $k \gtrsim \mathcal{H}_{\rm osc}$, scales shaped by the early universe axion dynamics. Such a study was recently reported in Eggemeier et al. [2019], whose halo mass function at different masses is shown by the dashed lines in Fig. 3.4. We use their results here to understand whether the tools we develop are applicable for understanding axion structure formation on the scales they studied.

In particular, we have evaluated our semi-analytic model, calculated using the input power spectrum for the simulations (solid curves in Fig. 3.4). At late times, this model is generally able to reproduce the evolution seen in their N-body simulation. The model errs most for the highest redshift Eggemeier et al. [2019] reported, $z = 2507$. Our semi-analytic model is motivated by matter-dominated spherical collapse calculations that do not apply during radiation domination and need some modification. For example, in Press-Schechter, the barrier $\delta_{\rm c}$ is no longer 1.686 once radiation is important. While our model should not be used when radiation is important in the universe, improving our model to extend into radiation domination would further enhance the differences. Rather, the mass function found in Eggemeier et al. [2019] at these times is likely driven by the collapse of small-scale non-Gaussian structures that our Gaussian model does not capture (the formalism from which these semi-analytic models are built is based on Gaussian random walks). We surmise that the agreement of the simulations of Eggemeier et al. [2019] and our model at later times occurs for two reasons. First, for smaller mass scales than the our peak-scale, the model is less sensitive to deviations from Gaussianity since the minihalos that are collapsing are not the rare peaks for which non-Gaussianity has its largest effect. Further, as time progresses, the mass scale at which halos are rare (exponentially suppressed) moves to larger and larger masses.

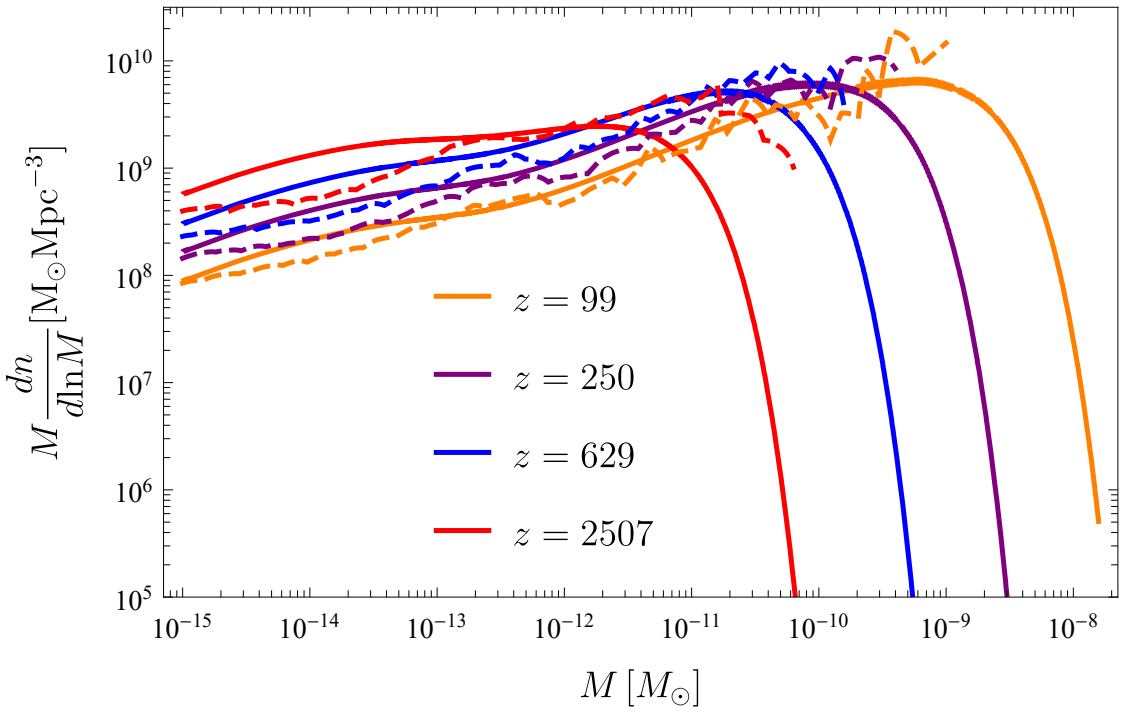

Figure 3.4: Comparison of the mass function of axion minihalos from Eggemeier et al. [2019] with the prediction of our semi-analytic halo model using the same initial density power spectrum. The semi-analytic model is tuned to fit our simpler white-noise simulations, but still describes reasonably the simulated mass function of Eggemeier et al. [2019]. The N-body simulations in Eggemeier et al. [2019] evolve the density field predicted from detailed early universe simulations of the relativistic axion field, which results in the initial conditions for their N-body simulations having a less abrupt cutoff in the power spectrum at high wavenumbers than in our simulations. However, our analytic model broadly agrees, especially at lower redshifts (we suspect because the non-gaussianty in the field matters less at these times). This agreement allows us to forward model their predictions, which yields at late times curves similar to our white noise model shown in Fig. 3.8.

Many small-scale contributions sum to determine the perturbations on these larger scales, making the fluctuations on these scales more Gaussian (although note that the model is not well tested by the simulations of Eggemeier et al. [2019] at these high masses).

Finally, we remark that even though our analytic model is able to capture the mass function of Eggemeier et al. [2019] at early times, at late times the amplitude of the white noise power at $k \ll \mathcal{H}_{\rm osc}$ shapes the mass function – this study presents precise simulations in this regime. We use the normalization of Eggemeier et al. [2019] at these scales as our fiducial model when we analyze observations in § 3.5. The complex spectrum of fluctuations on $k \gtrsim \mathcal{H}_{\rm osc}$ that were simulated by Eggemeier et al. [2019] should largely affect the subhalo distribution in the larger axion minihalos.

3.3.2 Extrapolating the mass function to the present day

Our simulation boxes, with our largest containing in total a cosmologically minuscule mass of $10^{-2} M_\odot$, are far from capturing the scales needed to follow cosmological structure formation, which results in most of the dark matter being incorporated galactic mass halos of $\gtrsim 10^{10} M_\odot$ today. Thus, we need a way of incorporating the effects of these large scales. Fortunately, the separation of mass scales between what later collapses and our axion minihalos suggests a reasonable approach.

An axion halo will stop growing once it falls into CDM halo. We distinguish "CDM halos" as the halos that form from the standard adiabatic perturbations from inflation. The spectrum of adiabatic density perturbations is such that a large range of masses collapse at around the same time: few CDM halos have formed at $z \sim 50$, but most have collapsed by $z \sim 10$. Thus, most of the axion minihalos are incorporated into the larger CDM halos at these redshifts. However, because the host CDM halos are generally much larger, most axion minihalos do not spiral inward from dynamical friction and merge into a single halo. Furthermore, once subsumed in the larger halo, they stop growing via accretion because of the high velocities in the host halo.

Therefore, we estimate the mass function at a given redshift of axion minihalos, *including those*

incorporated into massive CDM halos, as

$$\frac{dn_f}{dM}(z) = \int_{z_{\rm eq}}^{z} dz' \frac{df_{\rm col}^{\rm CDM}(z')}{dz'} \frac{dn_{\rm WN}}{dM}(z') + \left[1 - f_{\rm col}^{\rm CDM}(z)\right] \frac{dn_{\rm WN}}{dM}(z), \tag{3.5}$$

where $dn_{\rm WN}/dM$ is the mass function computed from our white noise–only simulations and $f_{\rm col}^{\rm CDM}(z)$ is the collapse fraction of CDM halos at redshift z into halos (shown with the dashed curve in Fig. 3.3), which goes from near zero to near unity over $z \sim 10-50$ – freezing the spectrum of axion minihalos. The second term on the right hand side, which comes from axion minihalos unbound to any CDM halos, becomes small at low redshifts. While this estimate provides the global mass function of axion minihalos, including those that are subhalos in CDM halos, Eq. 5.1 likely approximates the mass function of axion minihalos at $z = 0$ within any Milky Way-like or cluster-scale CDM halo because the $f_{\rm col}^{\rm CDM}$ history of the matter within these much larger halos is not be significantly different than the mean history. This estimate is a different approach from previous studies where the mass function is calculated using the power spectrum from the sum of isocurvature and adiabatic fluctuations Dai and Miralda-Escudé [2020], Lee et al. [2020]. In our estimate, we tracked all the minihalos arising from isocurvature fluctuations even though they may have fallen into CDM halos formed from adiabatic fluctuations. We contrast the two methods in the conclusions.

The estimate given by Eq. 5.1 may overestimate the fraction of axion minihalos that exist today because it does not account for destruction processes. Destruction owing to encounters with stars and other minihalos are discussed in § 3.6. We argue that in galactic environments stellar destruction can remove an O(1) fraction, but it's likely many still remain. Another process is the tidal stripping of the host macro-halo itself on the minihalo. See this footnote for discussion [3]. While beyond the

[3]The tidal radius of a minihalo sitting ~ 1 scale radius from the center of the host macro-halo is roughly the scale radius of the minihalo times the ratio of the concentrations of the macro halo and minihalo. (Tidal stripping is further enhanced by the radial biased nature of orbits in CDM halos.) Thus more concentrated minihalos are more likely to survive in their host halo. Because axion minihalos form much earlier than CDM halos, making them more concentrated, one might think we are safe to ignore tidal stripping. However, our most massive minihalos are our least concentrated, forming at a time similar to CDM halos. Thus, we expect some tidal stripping will be important, particularly for the most massive minihalos.

scope of this study, techniques that have been developed for the standard cosmology to evaluate the tidal stripping and survival of subhalos should be applied to evolve axion minihalos Taylor and Babul [2001], Errani and Navarro [2020].

With these caveats in mind, to evaluate Eq. 5.1, we use the Press-Schechter model for the collapse fraction of CDM halos, which yields

$$f_{\rm col}^{\rm CDM}(z) = \mathrm{erfc}\left(\frac{\delta_c}{\sqrt{2}\sigma_{\rm CDM}(M_{\rm min})D(z)}\right), \tag{3.6}$$

where $\sigma_{\rm CDM}(M)^2$ is the variance in the initial density fluctuation field, and $M_{\rm min}$ is the smallest halo we are counting in the tally of collapsed structures. We take $M_{\rm min}$ to be $10^{-2}M_\odot$, corresponding to a scale where CDM power spectrum starts to dominate and axion perturbations becomes subdominant. Our results are insensitive to this choice owing to the roughly logarithmic dependence of $\sigma_{\rm CDM}(M)$ on M at relevant masses. While the Press-Schechter mass function is known to error, the simplicity of our model does not motivate more sophisticated prescriptions for $f_{\rm col}^{\rm CDM}(z)$. We evaluate δ_c at two values: Its formal spherical collapse value of 1.69 and the value for turnaround of 1.06 (both of these are matter-dominated values, but including dark energy has a percent-level effect by $z = 0$). The two choices quantify some uncertainty in our estimate, as it is unclear whether turnaround or collapse better encapsulates the time when subhalos stop growing owing to tidal effects. Furthermore, choosing turnaround segregates the time of formation of the host CDM halo from the axion minihalos and, thus, chooses the denser minihalos that form by the earlier turnaround epoch that are more likely to survive. However, these choices for δ_c yield results that are within a factor of two of each other.

The solid purple band in Fig. 3.2 shows our estimate using Eq. 5.1 for the final mass function in axion minihalos. The upper edge of the purple band at high mass uses $\delta_c = 1.69$ and lower $\delta_c = 1.06$. The peak occurs at the peak location of the individual snapshots when much of the mass is incorporated in the standard CDM halos and stop growing (at $z \sim 30$). However, the mass function extends over a broader range of masses than the mass functions from individual snapshots in our simulations (compare with this curve with, e.g., the $z = 19$ curve). We use this estimate in § 3.5 to compare with observations. Since we have an analytic model, we can further take into

account uncertainties in the initial spectrum of axion fluctuations.

3.4 *Density profile of axion minihalos*

The density profile of axion minihalos is important for their detectability. The more dense and concentrated these halos, the more detectable they generally are and the longer they are able to survive in galactic environments. We study the angular-averaged density profiles at $z = 19$ and $z = 49$. Much of our discussion uses the famous Navarro-Frenk-White (NFW) profile and so we start off by defining it and related quantities. In particular the NFW profile is given by Navarro et al. [1996]:

$$\rho(r) = \frac{\rho_s}{r/r_s(1 + r/r_s)^2}, \tag{3.7}$$

where ρ_s is the characteristic density of the halo and r_s is the scale radius. The scale radius determines the concentration number via $c \equiv r_{\rm vir}/r_s$, where $r_{\rm vir}$ is the virial radius of dark matter halo. The virial radius is defined here by the matter density $\bar{\rho}(z)$ and halo mass M as $4\pi(200)r_{\rm vir}^3\bar{\rho}/3 = M$, i.e. the region that encloses an overdensity of 200. This standard choice is motivated by spherical collapse, and it means that the concentration number, c, of a static halo (i.e. one with a fixed density profile) increases with time as $r_{\rm vir} \propto (1 + z)^{-1}$.

We plot NFW density profiles at z=19 and z=49 in Fig. 3.5 and Fig. 3.6 respectively and compare them with the density profiles of 10 halos taken from the simulation that fall nearest the specified mass. The NFW profile is fully determined by the halo mass M and scale radius in Eq. 3.8 as $\rho_s = M/[4\pi r_s^3(\log(1+c) - c/(1+c))]$, while the colored curves are computed from the simulation data, representing density profiles of 10 halos around the same halo mass M. Many of the density profiles of small halos agree with solid NFW profile reasonably. However, some of the halo density profiles do not agree with the NFW profile, with a flatter density profile in the central region. This occurs more often for our most massive halos ($M \sim 10^{-6}M_\odot$). We do not expect this to be a gravitational softening effect because the flat density profile starts on a scale much larger than the softening scale (and is most common in our massive halos). Rather, it owes to halos with multiple components that have not merged: The largest minihalos – like galaxy clusters today –

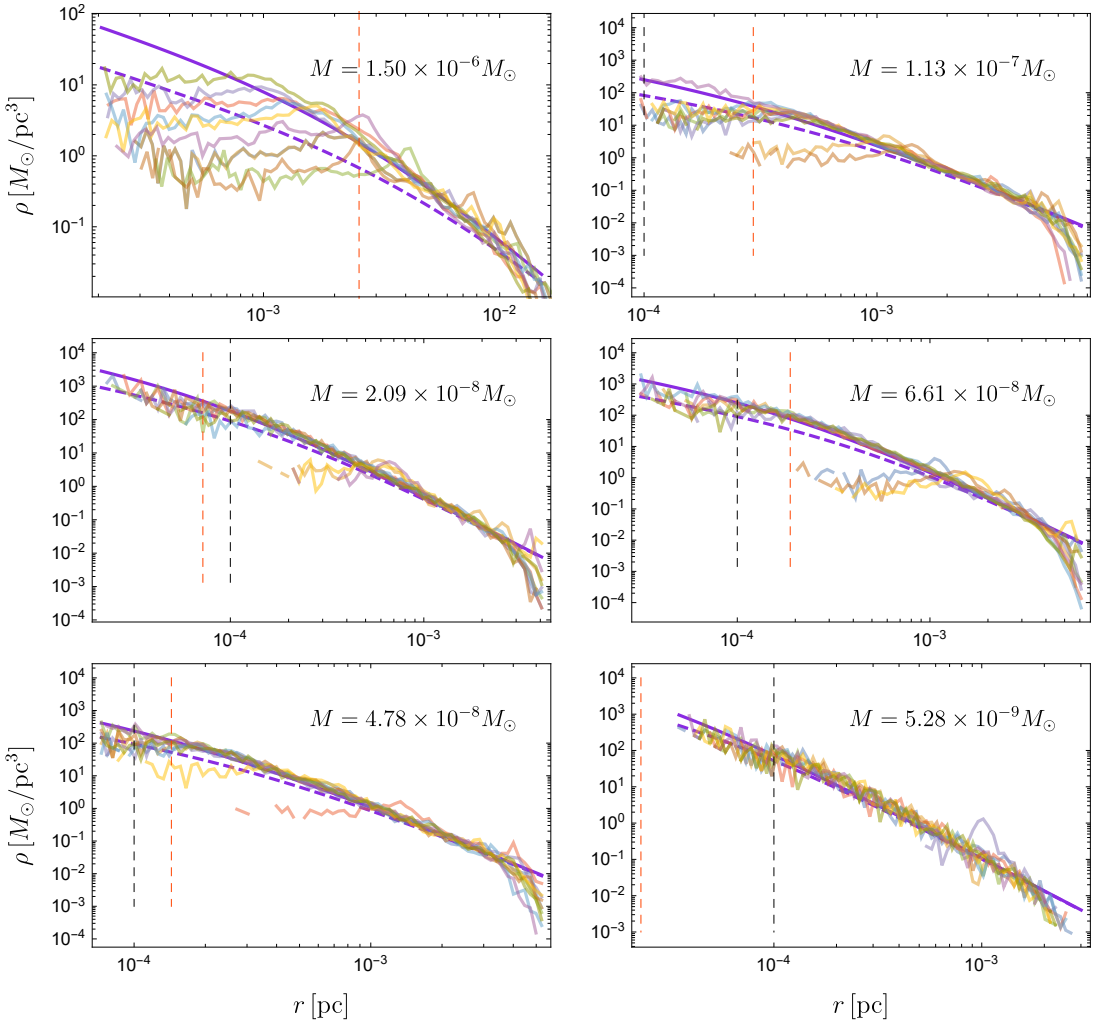

Figure 3.5: Density profile of halos with different masses at $z = 19$ from our fiducial simulation interpreted with $A_{\rm osc} = 0.1$ and $k_{\rm osc} = 19.8$ pc^{-1}. The colored curves with less opacity represent the density profile of 10 halos around the same mass obtained from our simulation data. The purple solid curve represents the NFW density profile with a mass-dependent scale radius given by Eq.3.8, whereas the dashed purple curve is re-scaled to a factor of two smaller values for the scale radius (Eq. 3.8), which suggests how well the scale radius can be determined from the simulation. The vertical black and orange-red dashed line are indicating the gravitational softening length and scale radius of the halo respectively. The density profiles from simulations broadly agree with the predicted NFW profiles at different masses, except for a contingent of halos that are unrelaxed at their center. This contingent is especially present the higher masses, and owes to incomplete merging of two halos (Fig. 3.7 shows some examples). An NFW profile with the model for the scale radius in Eq. 3.8 agrees reasonably with the more relaxed profiles.

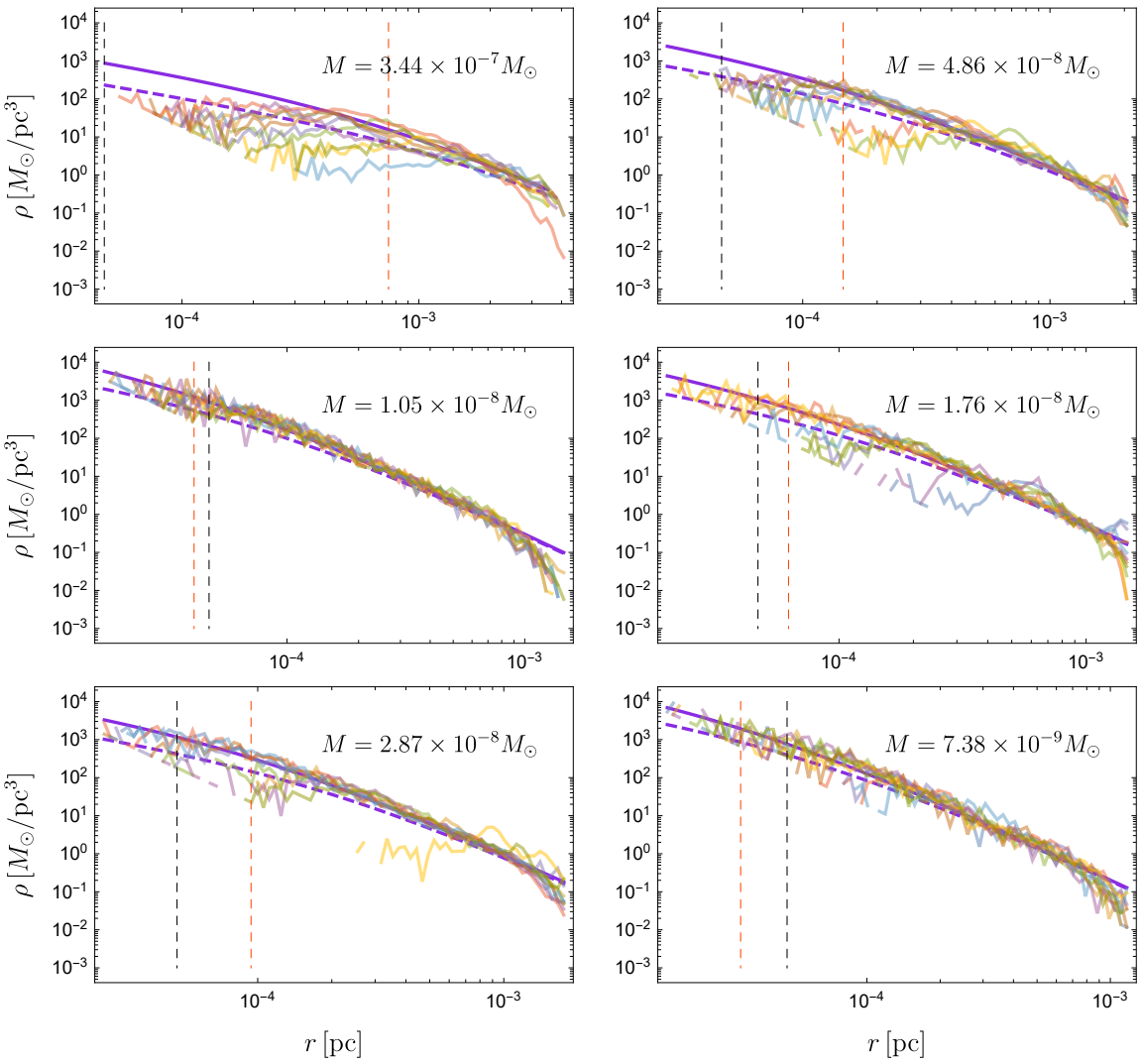

Figure 3.6: The same as Figure 3.5 except showing the density profile of halos with different masses at $z = 49$ rather than $z = 19$. The colored curves with less opacity represent the density profile of 10 halos around the same mass obtained from our simulation data. The purple solid curve represents the NFW density profile with a scale radius described in Eq. 3.8, and the purple dashed curve has a scale radius that is a factor of two smaller than the solid curve. The vertical black and orange-red dashed line are indicating the gravitational softening length and scale radius of the halo respectively. The NFW model predictions broadly agrees with the simulation data except for the high mass end where halos have substructures. The main conclusion is the same as what we found in Fig. 3.5. In combination the two figures support that the density profile of axion halos do not change over time (at trait that holds also for the NFW model curves).

are the least merged and relaxed systems. The large amount of structure in our massive halos can be seen in Fig. 3.7, which plots the projected density distribution of four $M \sim 10^{-7} M_\odot$ halos at different redshifts and four different mass halos at $z = 19$. For instance, the distance between the substructures for the axion minihalo with $M = 10^{-7} M_\odot$ at $z = 49$ is roughly 200 AU (10^{-3}pc) as shown in Fig. 3.7, which matches with the size of the flat central region of high mass halos in Fig. 3.6. More generally, in our white noise cosmology, halo formation for a given range of halo masses is spread over a larger range in scale factor than in the standard cosmology. This enhances the density contrast of substructures and makes them more able to survive in their parent halo.

In the picture that the axion halo forms early and then sits undisturbed, one might expect the characteristic scale radius, r_s, is only a function of halo mass M and does not depend on redshift Dai and Miralda-Escudé [2020]. (The virial radius as defined, however, does depend on the redshift because it is determined by the mean density of the Universe. Therefore, c grows linearly with scale factor a in this picture.) Dai & Miralda-Escudé Dai and Miralda-Escudé [2020] assumed that the axion minihalos form with a relatively small concentration of $c = 4$ and that the collapse at a given minihalo mass that can be characterized by when a 1σ perturbation at that mass collapses. These assumptions are sufficient to predict r_s and c analytically as a function of halo mass Dai and Miralda-Escudé [2020]. If we calibrate the analytical prediction with a prefactor and compare it to the average density profiles in the simulation, we found they are in good agreement for different halo masses at different redshifts. Therefore, this picture seems to be roughly obeyed by our simulations. The solid curves in Fig. 3.5 and Fig. 3.6 show

$$\begin{aligned} r_s(M) \approx & 3.7 \times 10^{-3} h^{-1} \mathrm{pc} \left(\frac{A_{\rm osc} M_0}{10^{-11} M_\odot / h} \right)^{-1/2} \\ & \times \left(\frac{M}{10^{-6} M_\odot / h} \right)^{5/6}, \end{aligned} \tag{3.8}$$

or equivalently

$$c(z) \equiv \frac{r_{\rm vir}}{r_s} = \frac{1.4 \times 10^4}{(1+z)\sqrt{M/(A_{\rm osc} M_0)}}, \tag{3.9}$$

where M_0 is the characteristic mass of axion minihalos at power spectrum cutoff, which is defined in Eq. 6.4, and $A_{\rm osc}$ is the amplitude in Eq. 3.1. The only relevant parameter in our simulation

is $A_{\rm osc}/k_{\rm osc}^3$, which is proportional to $A_{\rm osc}M_0$. The dependencies of Eqns. 3.8 and 3.9 are from the model of Dai and Miralda-Escudé [2020], discussed shortly. In Ref. Eggemeier et al. [2019], characteristic concentration parameters for axion minihalos at $z = 99$ for certain mass ranges are discussed. Their concentration parameter varies with mass more slowly than our relation at the low mass end, which is still reasonably consistent with our model because their power spectrum is also more flat at smaller scales. At highest masses they study of $\sim 10^{-8}M_\odot$, their concentration parameters roughly agree with what we found.

Figures 3.5 and 3.6 show respectively $z = 19$ and $z = 49$ four four halo mass bins that span $2-3$ orders of magnitude in mass. The solid curve is the $r_s(M)$ given by Eq. 3.8, and the dashed is a factor of two smaller. The former values of r_s and c appear to describe most of the relaxed halo profiles, and the outer profile of of the unrelaxed.

We also note that these concentrations are much larger and have a stronger mass dependence than standard CDM halos Okoli [2017]. We expect CDM halos only to have a similar concentration if they form at the same redshift as our minihalos. Finally, it is well known that CDM halos have a lognormal distribution of concentrations with a full width at half maximum (FWHM) of ≈ 1 dex at $z \approx 0$. For our relaxed axion minihalos, there is no clear evidence for such significant scatter in their concentrations although we did not study it quantitatively.

Our simulated minihalos halos have r_s values that are smaller than the analytic prediction in Dai and Miralda-Escudé [2020] by a factor of four. We think that some of this difference comes from the fact that they defined the halo mass when its concentration number is four. The scale radius of a halo will remain a constant as time evolves, but the 'boundary' at $r_{\rm vir}$ will expand due to the less dense Universe. Therefore, dark matter halos will go through 'pseudo-growth' as the boundary expands and encompasses more mass Diemer et al. [2013]. For the NFW profile that describes halos in our simulations, a halo with $c = 100$ at late times is about four times heavier than it was at formation with $c = 4$ simply owing to this effect.

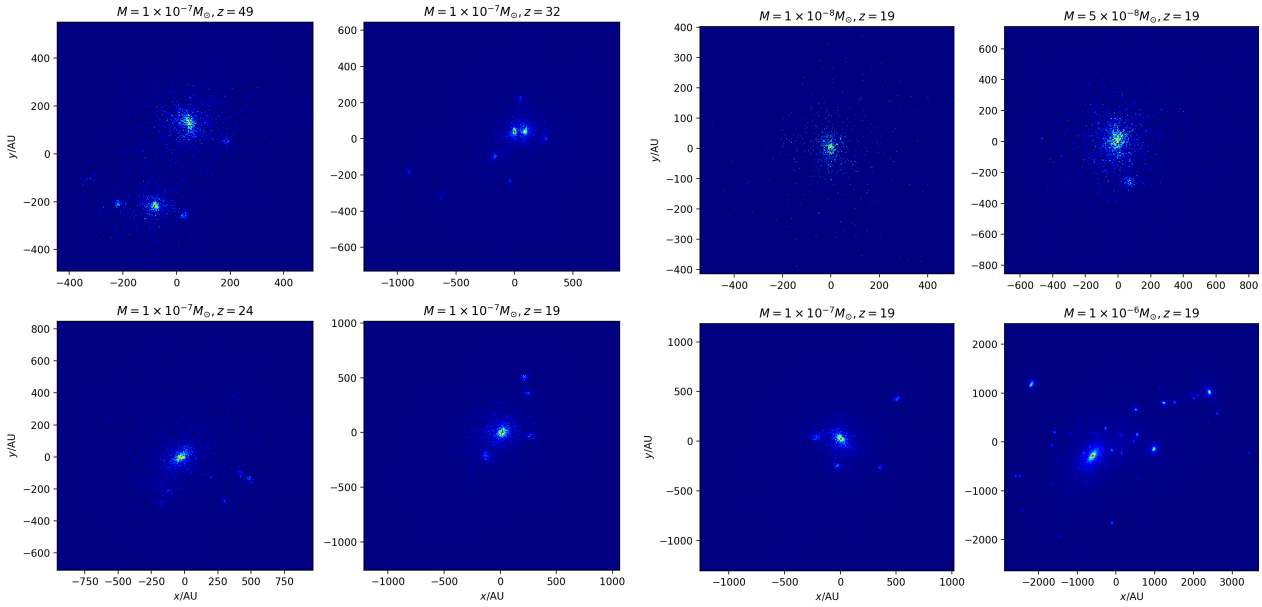

Figure 3.7: The visualization of halos that have different masses and redshifts from our simulation interpreted with $A_{\rm osc} = 0.1$ and $k_{\rm osc} = 19.8$ pc^{-1}. Left panels are showing halos with the same mass $10^{-7} M_\odot$ at different redshifts. Right panels are showing halos with different masses at the same redshift. The density profile is supposed to be the same for halos that have the same masses. However, we show that the halo at $z = 49$ has more substructures than other halos with the same mass. This is because $M = 10^{-7} M_\odot$ is at the high mass end of the mass function at $z = 49$ and the high mass end shifts to larger masses at lower redshifts. Halos at high mass end just formed very recently and did not go through enough merger events. Therefore they may have a lot of substructures than other halos. In summary, a larger value of $\nu = \delta_c / \sigma(M, z)$ is corresponding to more substructures.

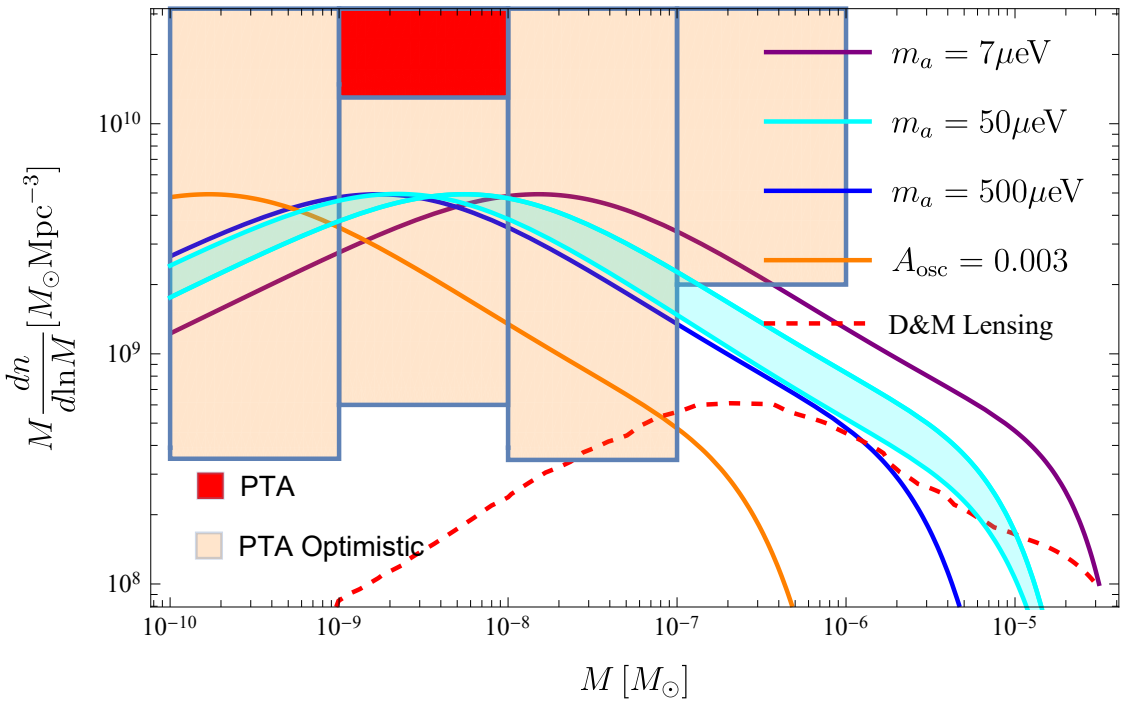

Figure 3.8: Model prediction of axion halo mass function at the present time with different choice of axion masses (solid curves) compared against forecasts for the observational sensitivity for a future pulsar timing array (PTA) observations and gravitational lensing in the scenario proposed in Dai and Miralda-Escudé [2020]. Disruption is neglected for reasons discussed in § 3.6. Different axion particle masses are shown computed assuming $A_{\text{osc}} = 0.03$ for the power spectrum normalization, and our amplitude parameter can be deduced from the masses m_a via Eq. 3.2 and we show one string-dominated case with $A_{\text{osc}} = 0.003$ and $m_a = 500\mu eV$ (orange curve). The power spectrum with mass $m_a = 50\mu$eV and $A_{\text{osc}} = 0.03$ agrees with the white scaling of the early universe axion simulations used in Eggemeier et al. [2019]. We show with the yellow band for our middle-of-the road 50 μeV mass the range of estimates using the turnaround and collapse δ_c for when axion minihalo growth is terminated. The red region represents the PTA sensitivity with SKA parameters, while the orange region assumes more optimistic PTA parameters (see main text). The dashed curve presents the mass function in Dai et al. Dai and Miralda-Escudé [2020], which owing to the size of an effect it creates on this observable, we interpret as (very roughly) a lower bound on what can be probed by lensing of magnified stars (see text).

3.5 *Axion Minihalo Observables*

The previous sections obtained the mass function and density profile of axion minihalos from simulations and developed a semi-analytic model to extrapolate to the present day. We can now use this model to evaluate the prospects for detecting axion minihalos in the post-inflation scenario. We will show that pulsar timing arrays and the gravitational lensing of highly magnified stars both show promise for constraining our mass spectrum of axion minihalos.

Figure 3.8 is the key figure on which we will place our constraints. It shows our semi-analytic model's prediction for the present time axion minihalo mass function compared to forecasts for the observational sensitivity for future pulsar timing array (PTA) observations and the gravitational lensing in the scenario proposed in Dai and Miralda-Escudé [2020]. Different axion masses are shown assuming $A_{\rm osc} = 0.03$ (and for one curve $A_{\rm osc} = 0.03$) for the power spectrum normalization. The power spectrum amplitude $A_{\rm osc}/k_{\rm osc}^3$ can be deduced from the masses m_A via Eq. 3.2. The range of axion masses reflects the uncertainty in how much axion strings contribute to the production of early universe axions. The blue and solid curves take $m_A = 500\mu eV$ and represent the scenario of axion strings radiating mostly in the infrared and dominating over misalignment production by the factor $\log(f_A/m_A) \sim 60$. We note that $A_{\rm osc} = 0.03$ is calibrated to match the low wavenumbers of the simulations of Vaquero et al. [2019] where strings provide a middle-of-the-road enhancement. Pure misalignment production of axions likely has a larger value for $A_{\rm osc}$. However, even a string dominated spectrum should have a significant $A_{\rm osc}$ owing to the expectation that there are a handful of strings per Hubble patch.

We now compare these model predictions to the forecast sensitivities of pulsar time arrays and gravitational lensing observables.

3.5.1 Pulsar timing array

Due to the stability of pulsar pulse phases observed over at least several year durations, dark matter structures around the Earth-pulsar system can imprint discernible signatures in these phases via gravitational Doppler and Shapiro delays. Using pulsar timing arrays (PTAs), individual transiting

subhalos can be detected in the future by Square Kilometer Array (SKA) Rosado et al. [2015]. Constraints for a single 'subhalo' mass for dark matter substructure are presented in Ramani et al. [2020], which Carr et al. [2017] found can be extended to non-monochromatic mass functions within a mass bin of $M_1 < M < M_2$ using the following inequality:

$$\int_{M_1}^{M_2} dM \frac{dn}{d\ln M} \frac{1}{\bar{\rho}_{\rm dm} f_{\rm max}(M, c)} \leq 1. \tag{3.10}$$

Here, $f_{\rm max}$ is the maximum mass fraction of dark matter in substructures of a *single* mass presented in Ramani et al. [2020], which is a function of halo mass and concentration number, $\bar{\rho}_{\rm dm}$ is the mean density of dark matter in the Universe, and $dn/d\ln M$ is the mass function of axion minihalos. We consider the two observational scenarios for $f_{\rm max}$ presented in Ramani et al. [2020]. One is an optimistic case based on the futuristic PTA parameters $N_P = 1000$, $T = 30\,{\rm yr}$, $t_{\rm rms} = 10\,{\rm ns}$, $\Delta{\rm t} = 1\,{\rm week}$, where N_P is the number of pulsars, T is the observing duration, $t_{\rm rms}$ is the residual timing noise and Δt is the cadence. The second is a somewhat less futuristic PTA sensitivities based on the estimated capability of the PTA with the Square Kilometer Array: $N_P = 200$, $T = 20\,{\rm yr}$, $t_{\rm rms} = 50\,{\rm ns}$, $\Delta{\rm t} = 2\,{\rm weeks}$. The parameter choices in both cases are motivated further in Ramani et al. [2020].

With our mass function and concentration numbers of axion minihalos at present day, we use Eq. 3.10 to determine whether PTA observations with future instruments may be sensitive to axion minihalos. We present our results in Fig. 3.8, where the current mass function of axion minihalos and the threshold mass function that will lead to a detectable signal in PTA observations are plotted. As shown in Fig. 3.8, our estimate for the current mass function of axion halos lives well above the threshold that would be detectable for future PTA observations with optimistic PTA parameters. This conclusion holds for each of the axion mass scenarios we consider. However, our estimate for the current mass function is not large enough to produce a detectable in PTA observations with SKA parameters. We need more futuristic observations to detect axion minihalos with PTAs. (See this footnote for a caveat on our PTA bounds on the most massive halos that pertains to their lower concentrations: [4])

[4]The PTA bounds in Fig. 3.8 assume $c \gtrsim 1000$, which we find applies at $10^{-8} M_\odot$ (Eq. 3.9). When the halo mass

In § 3.6 we consider disruption by encounters with stars. We argue that this process is not efficient enough to suppress by the order of magnitude required to be below the 'PTA Optimistic' limits.

3.5.2 Gravitational lensing of highly magnified stars

The usual microlensing signatures of axion minihalos requires the concentration number to be ultrahigh in order to exceed the critical surface density for lensing ($c \gtrsim 10^7$ for typical masses). Our minihalos do not come anywhere near such high concentrations (Eq. 3.9). However, recently another lensing diagnostic was suggested. Caustic transiting stars behind a galaxy cluster lens can reach extreme magnifications of $\mu \gtrsim 10^3 - 10^4$ as the lensed stars cross microlensing caustics induced by intracluster stars Diego et al. [2018], Venumadhav et al. [2017]. The perturbations from dark matter structure can add additional structure to these lensing caustics, changing their profile Dai and Miralda-Escudé [2020]. Indeed, Dai and Miralda-Escudé [2020] argued that this effect is sensitive to the minihalos in the post-inflationary axion scenario.

In particular, Dai et al. Dai and Miralda-Escudé [2020] showed that this diagnostic is sensitive to convergence fluctuations are at the level of $\Delta_\kappa \sim 10^{-4} - 10^{-3}$ on scales $10 - 10^4\,\mathrm{AU}/h$ (corresponding to mass scales $10^{-8} - 10^{-5} M_\odot$). Motivated by the fact that axion minihalos have r_s in this interesting range of scales, they modeled the abundance of axions using the $z \sim 1$ Press-Schechter mass function calculated with both axion isocurvature and inflationary adiabatic fluctuations. (This is likely a conservative model as it predicts most of the mass is in large halos that form from the adiabatic fluctuations. Others have also adopted this model, which we contrast with in the conclusions.) They concluded that the post-inflation axion scenario can produce sufficient level of fluctuations, although their results suggest that their QCD axion model is near the minimum of what might feasibly be detected. Our simulation results suggest a larger amplitude for the mass function at all masses except the scenario where axion mass is 500μeV, indicating that axion minihalos likely lead to a larger lensing signature than in their fiducial model. In Fig. 3.8, we show the comparison

is larger than $10^{-7} M_\odot$, axion minihalos have lower concentration numbers and so the bound shown in Figure 3.10 are not applicable and a more detailed study is required.

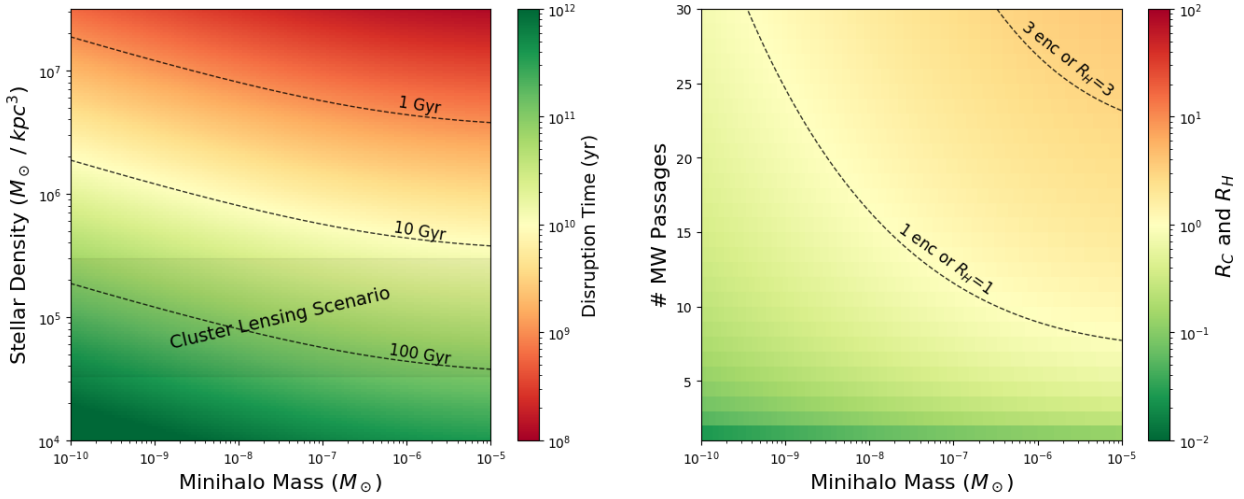

Figure 3.9: Disruption of axion minihalos from stellar encounters, assuming NFW density profiles with concentrations calculated for $A_{\rm osc} = 0.03$ and $m_a = 50\mu$eV. The left panel shows the average time taken for one catastrophic ($\Delta E > |E_b|$) encounter to occur, which is also the approximate time taken for dynamical heating from smaller encounters to add up to $|E_b|$. Most minihalo should survive in the environment needed for the gravitational lensing observable. The right panel shows both disruption effects as a function of passages through the Milky Way disk.

between the mass function used for the lensing calculations in Dai and Miralda-Escudé [2020] (dashed red curve) against our mass functions.

We also find in § 3.6 that stellar disruption is unlikely to destroy the axion minihalos in the cluster environment envisioned in Dai and Miralda-Escudé [2020], verifying simpler estimates they present. This may not be the case for a similar diagnostic involving a galactic macro-lens rather than a cluster.

3.6 *Disruption of Axion Minihalos*

The primary mechanism for disrupting minihalos is high speed encounters with stars and other minihalos. Here we present estimates of the disruption from these encounters. We use the NFW profiles discussed in § 3.4, and the impulsive analytic framework developed in Spitzer [1958],

Gerhard and Fall [1983], Moore [1993], Carr and Sakellariadou [1999], Binney and Tremaine [2008], Green and Goodwin [2007]. The associated energy change from an encounter is Green and Goodwin [2007]:

$$\Delta E = \frac{4\alpha^2}{3}\frac{G^2 M_p^2 M r_{\rm vir}^2}{V^2 b^4}, \tag{3.11}$$

where M_p is the perturber mass, b is the impact parameter, M is the subject axion minihalo mass, and α^2 is the root mean square radius ($0.1 \lesssim \alpha^2 \lesssim 0.4$; the exact expression can be calculated from the definitions in Green and Goodwin [2007]).

Once minihalos fall onto a CDM halo, we assume they stop accreting mass and evolving in any significant way. Thus, for the purposes of our disruption analysis, we evaluate $r_{\rm vir} = cr_s$ as a static quantity at $z = 20$ using Eq. 3.9. This has the effect of cutting off the NFW halo at the $z = 20$ virial radius, which makes the axions more bound than a NFW halo that extends out to the $z = 0$ virial radius.

To consider the disruption from an encounter, we compare the energy imparted to the binding energy of the subject minihalo: $|E_b| = f_c GM^2/2r_{\rm vir}$, where f_c is computed for an NFW profile and ranges in value from 0.75 for $10^{-4}M_\odot$ to 12 for $10^{-10}M_\odot$ minihalos using our fitted value for the concentration. There are two important limits: 1) catastrophic encounters where $\Delta E/|E_b| > 1$, and 2) dynamical heating from the cumulative effect of many small encounters. The catastrophic regime occurs at impact parameters satisfying this condition, the largest of which we define to be b_c.

Over its lifespan, a minihalo will have many encounters with other minihalos and stars. Minihalo-minihalo interactions occur in a larger macro halo, and are negligible in galactic halos or cluster halos, where high encounter speeds and low perturber masses prevent catastrophic encounters entirely and suppress the heating rates. However, in the early stages of structure formation the minihalos inhabit halos with velocities not much larger than their virial velocities, and so these effects could be important. While preliminary calculations suggest this process is less important than stellar disruptions (aided by fact that often axion minihalos accrete onto much larger CDM halos), we plan further study of minihalo interactions in future work.

We now focus on stellar encounters. Assuming Maxwellian velocity distributions, an estimate for the catastrophic encounter rate is (Appendix 3.10):

$$R_c = \sqrt{\frac{8G\alpha^2}{3f_c M}}\pi\rho_p r_{\rm vir}^{3/2}. \tag{3.12}$$

This rate does not depend on the velocity dispersion nor the distribution of perturbers masses, just the overall perturber mass density, $\rho_p \equiv M_p n_p$, and subject mass. A power law fitting can approximate this result when $M < 10^{-5} M_\odot$:

$$\begin{aligned} R_{\rm c}^{-1} \approx 40\ {\rm Gyr} &\left(\frac{\rho_p}{10^5 M_\odot {\rm kpc}^{-3}}\right)^{-1} \\ &\left(\frac{M}{10^{-6}M_\odot}\right)^{-0.16}\left(\frac{A_{\rm osc}}{0.03}\right)^{0.11}, \end{aligned} \tag{3.13}$$

The M and $A_{\rm osc}$ dependence is weak.

The next consideration is the cumulative heating of smaller encounters, with $b > b_c$. Successive smaller encounters continue to add energy, leading to disruption when the total energy added is $\sim |E_b|$. We estimate that the heating rate is (Appendix 3.10):

$$R_H \equiv \frac{\dot{E}}{|E_b|} = \sqrt{\frac{8\alpha^2 G}{3f_c M}}\pi\rho_p r_{\rm vir}^{3/2} = R_c. \tag{3.14}$$

Curiously our estimate for the heating rate is equal to our estimate for the catastrophic destruction rate, Eq. 3.12. The average time for one catastrophic encounter to occur is also the average time needed for cumulative heating to add up to the binding energy. Details on this interesting equivalence can be found in Appendix 3.10.

At small impact parameters of $b \lesssim r_s$, Eq. 3.11 overpredicts the energy imparted Carr and Sakellariadou [1999], Green and Goodwin [2007]. Simulations exploring this in Green and Goodwin [2007] determined that the transition is well-fit by a sharp cutoff between these two regimes, located at $b_s \equiv (4\alpha^2/9\beta^2)^{1/4} r_{\rm vir}$, where β^2 is the is the root mean square inverse radius and is $6 < \beta^2 < 14$ for our minihalos (see Green and Goodwin [2007] for details). We find that, for the minihalos in this work, $b_s = [0.25 - 0.41] r_{\rm vir}$. For encounters with $b_s > b_c$, catastrophic encounters are impossible. We calculate b_c and b_s and find that, for speeds characteristic of the

cluster lensing scenario ($V = 1500$ km s^{-1}), minihalo of mass $10^{-5}M_\odot$ or larger have $b_s > b_c$ for encounters with stars as high as $1.6M_\odot$. This implies that the largest minihalos are immune to the majority of would-be-catastrophic encounters in this environment; the encounters contribute to heating instead. We neglect this in the following computations and note that the net effect is longer disruption times for $\gtrsim 10^{-5}M_\odot$ minihalos in galaxy clusters. This consideration is even less relevant in Milky Way-like environments, where the vast majority of minihalos predicted by our simulations are nearly unaffected by this correction.

Using R_H and R_c, we estimate the disruption of axion minihalos in environments relevant for the Milky Way and cluster environments. For the Milky Way, we calculate the expected catastrophic encounters and total heating in terms of the number of passages through the Milky Way's disk. This parameterization allows for the fact that some minihalos will have encountered the disk a handful of times if they were accreted late and had a low angular momentum orbit that takes it far out into the halo. Other minihalos at the Solar Circle likely pass through the disk many tens of times. We neglect stars in the bulge and stellar halo, estimate the stellar surface density at 8 kpc to be $10^8 M_\odot$ kpc^{-2} and $V = 200$ km/s. Results are shown in right panel of Figure 3.9.

In the Milky Way, relevant to the PTA observable, our estimates show that $\sim 10^{-6}M_\odot$ minihalos experience a catastrophic encounter and disruptive heating after ~ 10 disk passages, with stellar impacts becoming somewhat less important for less massive minihalos. The minihalos accreted many Gyr ago likely would have had 1-3 catastrophic encounters, and those that avoided one would have had significant heating. Material that has fallen onto the Milky Way more recently or that is on an orbit with rare disk passages is likely to retain its axion minihalos, even the larger ones. More detailed calculations are required to make a better estimate. Our results suggest disruption patterns similar to Kavanagh et al. [2020], despite differences in the modeling of the minihalos.

Detecting the perturbations from axion minihalos from gravitational lensing of highly magnified stars (§3.5) depends on whether minihalos are disrupted in the centers of galaxy clusters (although minihalos outside of the cluster can contribute non-negligibly). Galaxy clusters are a less stellar rich location than the Milky Way and, thus, survival is more likely. We calculate the expected disruption time for this cluster environment; results are shown in the left panel of Figure 3.9.

At these lower densities, our estimates indicate that many minihalo do not experience a single catastrophic encounter and collective heating should not significantly alter the axion minihalos, in agreement with the estimates in Dai and Miralda-Escudé [2020].

Authors studying the effects of these disruptive mechanisms on dark halos and stellar systems have made the case that the result from $\Delta E > E_b$ encounters is not full disruption, but mass loss Gieles and Renaud [2016], Kavanagh et al. [2020], van den Bosch et al. [2018]. The energy imparted from a catastrophic encounter is mostly carried off by particles in outer layers, leaving behind dense cores. More detailed simulations would be required to understand the masses of these cores for the minihalos that are most impacted by encounters.

3.7 *Conclusions*

We have run N-body simulations that study the formation of axion minihalos on mass scales where the initial spectrum of axion perturbations is described by Gaussian white-noise. The exact spectrum of axion perturbations will be damped below the white noise scaling at high momentum, and high-wavenumber modes can be shaped by non-gaussianities. However, lower momenta modes where the spectrum is white and that limit to being Gaussian are likely to be most relevant for observations, as they shape the late-time minihalo mass function.

We simulated the mass function and density profiles of axion minihalos. Our results show that the standard Press-Schechter and Sheth-Tormen mass functions only err at the factor of ~ 2 level. We further showed that a tweaked version of the Sheth-Tormen mass function and the NFW profile with a physically motivated scale radius (adapting the model of Dai and Miralda-Escudé [2020]) accurately describe the simulated halo properties at different redshifts. We further showed that our mass function, developed on our Gaussian white noise simulations, is also able to roughly describe the evolution of the mass function found in the simulations of Eggemeier and Niemeyer [2019] that start from the outputs of early universe simulations to the sine-Gordon equation.

Our cosmologically minute simulations do not capture the range of structures that collapse in the real universe. We developed a model which allows us to extrapolate our results to the current time and make connection to observations. Namely, we assume that axion minihalos stop merging

and growing once they fall into the much larger halos sourced by the adiabatic fluctuations from inflation, but that they are able to survive intact. This extension of our model allowed us to make predictions for pulsar timing arrays and microlensing of highly magnified cosmological stars. The abundance of axion minihalos we find appear to be above the threshold that can be probed by PTA observation with futuristic parameters, modulo uncertainty in the amplitude of the density fluctuations when cosmic strings dominate the axion production. Our predictions for halo mass function and concentration are also greater than an estimate for the threshold sensitivity of the microlensing scenario.

However, these predictions ignore processes that potentially disrupt axion minihalos within larger dark matter halos. We investigated the disruption of minihalos by stellar encounters. While we found that such disruption is unlikely to be important within galaxy clusters (applicable for the microlensing observable), we found that it is more important in a galactic environment relevant to PTAs; however, they are likely not disruptive enough to suppress our predictions by more than an $O(1)$ factor. Semi-analytic techniques that better approximate stellar encounters as well as other disruptions processes, such as tides from the parent halo, have been developed Taylor and Babul [2001], Green and Goodwin [2007], Errani and Navarro [2020]. We aim to apply these to improve our estimates for the abundance of axion minihalos in future work. In lieu of these calculations, our primary result for the mass function (without disruption) in Fig. 3.8 should perhaps be considered an upper bound for the axion minihalo abundance. To further complicate the story, axion minihalos have more substructure than CDM halos, which is not included in our model and would enhance the signals.

Our estimates for the abundance of minihalos in present-day systems contrast with previous studies Dai and Miralda-Escudé [2020], Lee et al. [2020] where minihalos that merged into other halos before they were subsumed into the Milky Way or galaxy cluster halos were effectively excluded. In particular, Dai and Miralda-Escudé [2020], Lee et al. [2020] computed the mass function results from axion isocurvature plus adiabatic fluctuations at the time of formation of the Milky Way or cluster, which results in the mass function of axion halos being shifted to considerably higher masses and less concentrated halos compared to our estimates (compare the dashed ‘D&M

Lensing' curve in Fig 3.8 with the solid curves). Our estimates include the less massive more concentrated minihalos that merge earlier with CDM halos. We argued that many of these should survive.

Our simulations are scale-invariant except on the smallest scales, and most collapse occurs during matter domination when the evolution is self-similar. In these limits, the only relevant parameter is the variance on any mass scale $\sigma^2(M)$. Our semi-analytic halo mass function naturally incorporates this symmetry. Thus, it is straightforward to apply our results to other axion-like particles (ALP), where the axion decay constant f_a and axion mass m_a are two potentially independent model parameters unlike for the QCD axion. Our simulations apply to the white noise formation for all ALP scenarios by only matching the mass scale that has the same variance as in our calculations. Disruption processes do depend on halo mass and so unfortunately our results there do not generalize. Of course, the observables will change with mass as well. For example, much more massive halos may exceed to the critical density to act as a strong gravitational lens Fairbairn et al. [2018].

Our calculations also have relevance to much different dark matter scenarios. Primordial black holes (PBHs) should have a white spectrum much like the post-inflation axion, with $O(1)$ fluctuations on the mass scale of the black holes, $M_{\rm PBH}$ Inman and Ali-Haïmoud [2019]. Our simulations and calculations also apply to the case where these comprise the dark matter for halos comprised of PBHs with $M \gg M_{\rm PBH}$ (although the center of PBH halos could be cored by two body interactions). Indeed, there is still a window at $M_{\rm PBH} = 10^{-17} - 10^{-11} M_\odot$ where PBHs could be a substantial fraction of the dark matter Montero-Camacho et al. [2019], one of the few windows left. Our calculations suggest that microlensing and PTAs may be able to constrain the more massive end of this window. Finally, our white spectrum of perturbations is closer to the blue spectrum anticipated from scenarios with early matter domination Erickcek [2015] or a light vector whose abundance is set by inflationary fluctuations Graham et al. [2016], suggesting that the standard semi-analytic mass functions will apply there as well.

3.8 *Appendix*: *Fitting the Halo Mass Function*

The halo mass function from our simulation does not agree with the prediction by Press & Schechter Press and Schechter [1974] or Sheth & Tormen Sheth and Tormen [1999] computed with power spectrum in Eq.3.1. However, we can calibrate our mass function with these analytic models and extrapolate the result of our simulation to present time. A simple model of collapsed halos by Press & Schechter Press and Schechter [1974] gives the following halo mass function:

$$\frac{m^2 dn/dm}{\bar{\rho}} \frac{dm}{m} = \nu f(\nu) \frac{d\nu}{\nu}, \tag{3.15}$$

where $\bar{\rho}$ is the comoving density of matter and ν, $f(\nu)$ are defined as:

$$\begin{aligned} \nu f(\nu) &= \sqrt{\frac{\nu}{2\pi}} \exp(-\nu/2), \\ \nu &\equiv \frac{\delta_c^2(z)}{\sigma^2(m)}, \end{aligned} \tag{3.16}$$

where δ_c is the critical density required for spherical collapse at z. In an Einstein-de Sitter cosmology, $\delta_c = 1.686$. $\sigma^2(m)$ is the variance in the initial density fluctuation field when smoothed with a tophat filter of scale $R = (3m/4\pi\bar{\rho})^{1/3}$, which can be determined as:

$$\sigma^2(m) \equiv \int \frac{dk}{k} \frac{k^3 P(k)}{2\pi^2} |W(kR)|^2, \tag{3.17}$$

where $W(x) = (3/x^3)[\sin(x) - x\cos(x)]$ is the spherical top-hat window function. The variance of white-noise power spectrum from axion can be expressed as:

$$\sigma(M) = \sqrt{\frac{3A_{\rm osc}}{2\pi^2} \frac{M_0}{M}}. \tag{3.18}$$

The Sheth-Tormen mass function provides a better fit to the number density of halos in simulations, which gives:

$$\nu f(\nu) = A(p) \left(1 + (q\nu)^{-p}\right) \left(\frac{q\nu}{2\pi}\right)^{1/2} \exp(-q\nu/2), \tag{3.19}$$

where $p \approx 0.3$, $q \approx 0.75$ and $A(p) = [1 + 2^{-p}\Gamma(1/2 - p)/\sqrt{\pi}]^{-1} \approx 0.3222$ Sheth and Tormen [1999]. The functional form of this mass function is motivated by the impact of large-scale tidal fields on delaying collapse relative to the (spherical) Press-Schechter prediction.

We can fit the halo mass function from our simulation by tuning the parameters $A,\ p,\ q$ in the Sheth-Tormen mass function. We treat model parameter A as a free parameter rather than expressing it in terms of p. We find the best fitting parameters to be $A = 0.374, p = 0.19, q = 1.2$. Given these parameters, we can make predictions in halo mass function at different redshifts. As shown in Fig. 3.2, the fitted halo mass function broadly agrees with the mass function obtained from simulation, except at low mass end where halo mass $M \lesssim 10^{-9} M_\odot$. See the main text for discussion of the differences at low masses.

3.9 *Appendix*: *Convergence Testing*

This appendix investigates whether our primary results are sensitive to our choice of gravitational softening length and time stepping. A worry is that the axion cosmology is so much different than the standard cosmology that simulations may require much different accuracy parameters. We find that this is not the case.

To test convergence, we have run a reference simulation that uses the same box size, gravitational softening parameter and time-stepping parameter as the simulations in Sec.3.2. We compare it to a simulation with half the gravitational softening length and one with twice as small time steps. All simulations considered in this appendix take $N = 512^3$ particles and are run in a box size of 50 pc/h.

In particular, the reference gravitational softening length is equal to 1/30 in units of the mean separation of N-body particles. (The mean separation can be estimated as $L/N_{\rm grid}$, where L is the box size and $N_{\rm grid}$ is the cube root of the number of particles.) In the reference run, the time stepping parameter η is taken to be 0.02, which is the default time-stepping parameter in MP-Gadget. The time-stepping criterion Power et al. [2003] used in MP-Gadget:

$$\Delta t = \sqrt{2\eta\epsilon/a}, \tag{3.20}$$

where ϵ is the gravitational softening length, $\eta = \textit{ErrTolIntAccuracy}$ is a dimensionless parameter and a is the local acceleration. The error of MP-Gadget's leap-frog integration scheme scales quadratically in Δt. Both the softening and time stepping parameters are set to half their reference

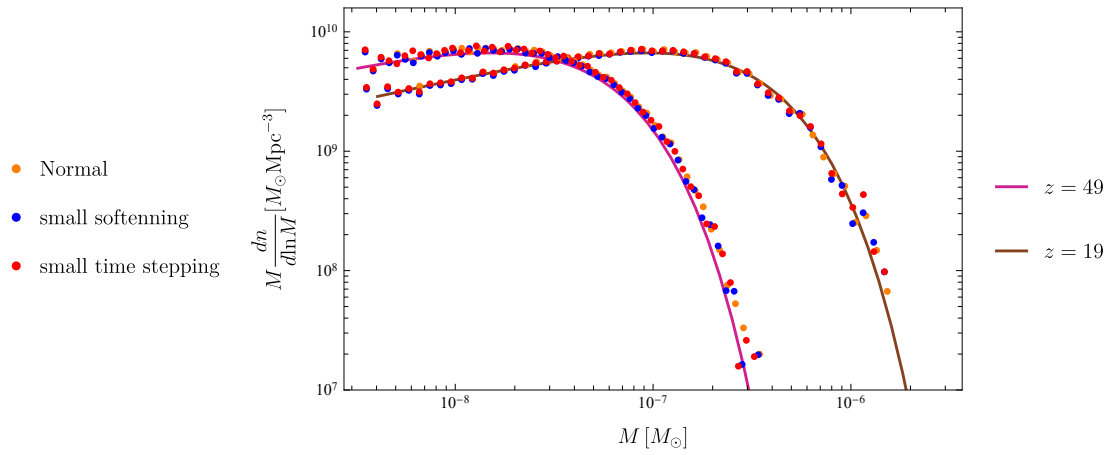

Figure 3.10: Simulated FOF mass function at $z = 49$ and $z = 19$. Data points with different colors are from simulations run with different force softening and timestepping parameters, in addition to the fiducial simulation. See the appendix for more information on the different parameter values. The solid curves are the semi-analytic prediction discussed in Appendix 3.8. The simulated mass functions all agree with each other, suggesting that the halo mass function is converged in softening and time stepping.

values in our two additional simulations to test for convergence.

We compare the mass function and the density profile in the reference run and the convergence-testing runs, as shown in Fig. 3.10 and Fig. 3.11. We plot the mass functions at $z = 19$ and $z = 49$, as shown in Fig. 3.10 and the mass functions of all the simulations agree well and with our semi-analytic model.

The $z = 19$ density profiles in Figure 3.11 are obtained by averaging 20 halos around the specified mass (points) as well as the NFW halo profile with scale radius given by Eq. 3.8 (solid curves). We show density profiles of halos at four different masses, and they all agree well with the NFW profile. There are some differences at smaller radii, although the differences do not notably go in one direction or the other. We suspect this owes to slight differences in the properties of halos being used in the average. Overall, the halo mass function and density profile appear to be

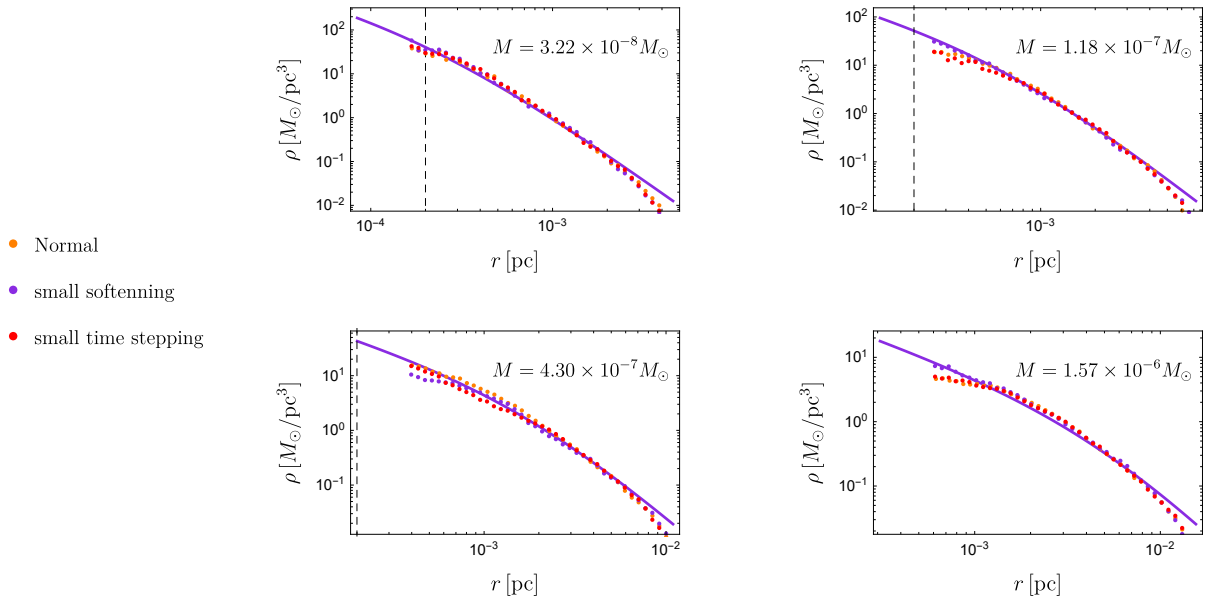

Figure 3.11: Density profiles at $z = 19$ for halos with different masses. These plots are obtained by averaging 20 halos around the specified mass. The orange, purple and red data points are from the reference simulation, the simulation with a smaller gravitational softening length, and the simulation with a smaller time-stepping parameter, respectively. The solid curves are the NFW halo profile with scale radius given by Eq. 3.8. The vertical dashed line indicates the fiducial gravitational softening length in our simulation.

convergence. In Fig. 3.2, we also compared the mass function with simulation that has a different box size 10 pc and particle number 512^3, which shows good convergence as well. We also note that Fig. 3.11 is showing the lowest redshift in our simulation, where the comoving softening length subtends the largest physical scale.

3.10 *Appendix*: *Equivalence of Disruption Timescales*

When the encounter velocity V is much greater than the minihalo's internal dispersion, the impulse approximation may be used. For minihalos, all encounters are in this regime. When the impact

parameter $b \gg r_s$, the characteristic radius of the minihalo, the distant-tide approximation is valid, allowing the perturbing potential to be expanded and higher order terms dropped. This introduces error in the low b regime which generally must be investigated with simulations. For minihalos, Green and Goodwin [2007] investigated this and found that a good approximation to the energy imparted from a high speed encounter with stars is:

$$\Delta E = \frac{4\alpha^2}{3}\frac{G^2 M_p^2 M r_{\rm vir}^2}{V^2 b^4} \qquad (\mathrm{b} > \mathrm{b_s}); \tag{3.21}$$

$$\Delta E = 3\beta^2 \frac{G^2 M_p^2 M}{V^2 r_{\rm vir}^2} \qquad (\mathrm{b} < \mathrm{b_s}). \tag{3.22}$$

where $b_s \equiv (4\alpha^2/9\beta^2)^{1/4} r_{\rm vir}$. As discussed in § 3.6, we find that for all but the largest minihalos in cluster environments, the $b > b_s$ expression applies. Here we show the derivation of the $R_H = R_c$ equivalence under this assumption.

We assume the perturber and subject have velocities drawn from Maxwellian distributions, so that the relative encounter velocities are also Maxwellian, with dispersion $\sigma_{\rm rel}$. The average rate of encounters with perturbers of number density n_p, encounter speed V, and impact parameter b is Binney and Tremaine [2008]:

$$\dot{C} = \frac{2\sqrt{2\pi} n_p}{\sigma_{\rm rel}^3} \exp\left\{ -\frac{V^2}{2\sigma_{\rm rel}^2} \right\} V^3 \mathrm{d}V b \mathrm{d}b. \tag{3.23}$$

The catastrophic encounter rate is then obtained from integrating Eq. 3.23 over all encounter velocities and impact parameters from 0 to b_c:

$$\begin{aligned} R_c &\equiv \frac{2\sqrt{2\pi} n_p}{\sigma_{\rm rel}^3} \int_0^\infty V^3 \mathrm{d}V \exp\left\{ -\frac{V^2}{2\sigma_{\rm rel}^2} \right\} \int_0^{b_c} b \, \mathrm{d}b \\ &= \sqrt{\frac{8G\alpha^2}{3 f_c M}} \pi \rho_p r_{\rm vir}^{3/2}, \end{aligned} \tag{3.24}$$

where the maximum catastrophic impact parameter b_c is found by setting the ratio of the energy impacted over the binding energy to unity:

$$b_c = \left(\frac{8\alpha^2 G M_p^2 r_{\rm vir}^3}{3 f_c M V^2} \right)^{1/4}. \tag{3.25}$$

The remaining encounters, $b > b_c$, are in the diffusive regime. Each encounter creates some small $|\Delta \boldsymbol{v}| \ll \boldsymbol{v}$ impulse on the particles, changing the energy per unit mass by $\boldsymbol{v} \cdot \Delta \boldsymbol{v} + |\frac{1}{2}\Delta \boldsymbol{v}|^2$. The first term is much larger, but we assume there is no preferred angle and so it cancels out, leaving the heating term. The average rate of energy added from non-catastrophic encounters is $\dot{E} = \dot{C}\,\langle \Delta E \rangle$. We use Eq. 3.23 and the high b expression for ΔE (Eq. 3.11) and integrate over all encounter velocities and from b_c upwards:

$$\begin{aligned} \dot{E} = \dot{C}\,\langle \Delta E \rangle &= \frac{8\alpha^2}{3}\sqrt{2\pi}\frac{G^2 M M_p^2 n_p r_{\rm vir}^2}{\sigma_{\rm rel}^3} \\ &\int_0^\infty V \mathrm{d}V \exp\left\{ -\frac{V^2}{2\sigma_{rel}^2} \right\} \int_{b_c}^\infty \frac{\mathrm{d}b}{b^3}, \\ &= \sqrt{\frac{\alpha^2 |E_b| M}{3}} 2\pi G \rho_p r_{\rm vir}. \end{aligned} \tag{3.26}$$

Finally, we obtain the fractional heating rate by dividing by the binding energy:

$$R_H \equiv \frac{\dot{E}}{|E_b|} = \sqrt{\frac{8G\alpha^2}{3 f_c M}} \pi \rho_p r_{\rm vir}^{3/2} = R_c. \tag{3.27}$$

We arrive at the surprising conclusion that, so long the use of the high b expression for ΔE is justified, the expected time for one catastrophic encounter is the same as the average time taken for cumulative encounters to impart energy equal to the binding energy.

Previous heating estimates in the literature using the impulsive encounter framework often use a low b cutoff of $\sim r_{\rm vir}$, which introduces dependencies on $\sigma_{\rm rel}$ and the mass distribution of perturbers. This is justified when $b \sim r_{\rm vir}$ encounters are generally not catastrophic, and when penetrative encounters should impart negligible energy. However, when the catastrophic regime exists, the heating calculation should begin at b_c, where the catastrophic encounters ended, to correctly count all encounter impact parameters. This leads to the equivalence of the disruption timescales.

Chapter 4

EARLY STRUCTURE FORMATION CONSTRAINTS ON THE ULTRA-LIGHT AXION

4.1 *Introduction*

The nature of the dark matter remains one of the biggest unsolved puzzles in particle physics and cosmology. We think that the dark matter is a particle produced in the early universe via one of several established mechanisms. The foremost has it thermally produced and its abundance freezing out when non-relativistic, which can result in the observed dark matter density if it has a weak-scale mass and interaction cross section – the so-called 'WIMP miracle' Jungman et al. [1996]. After decades of searching for the WIMP, the limits on this scenario are becoming more stringent. Perhaps our second most favored mechanism is the misalignment mechanism, discovered for the axion of quantum chromodynamics Weinberg [1978], Wilczek [1978], Kolb and Turner [1990]. At early times when Hubble rate is greater than axion mass – a mass that is acquired by non-perturbative effects such as instantons–, the axion field is stuck outside of the minimum of its potential. However, when the Hubble rate later becomes smaller than axion mass, the axion field begins to oscillate coherently, behaving like non-relativistic matter with energy density set by its initial potential energy Preskill et al. [1983], Abbott and Sikivie [1983], Dine and Fischler [1983], Marsh [2016].

The misalignment mechanism is also how the early universe could create dark matter in the form of ultra-light axion-like particles (ALPs; also known as fuzzy dark matter). The misalignment mechanism may naturally produce an ALP relic abundance of order the dark matter abundance if the ALP is the Goldstone Boson arising from a broken GUT to Planck scale symmetry and if it later acquires a mass of $m_A \sim 10^{-20}$eV Hui et al. [2017]. The non-perturbative mass generation can also naturally explain such ultralight masses, with $m_A \sim 10^{-20}$eV motivated by the estimated

size of non-perturbative effects for the GUT coupling constant Marsh [2016].

Our study focuses on such ultra-light ALPs in the limit where the Peccei-Quinn symmetry breaking that establishes this particle (re)occurs after inflation. For string theory-motivated models, the anticipated ranges for the symmetry breaking scale, f_A, are GUT to Planck scales Marsh [2016], Hui et al. [2017], although models that allow a lower scale have been devised Svrcek and Witten [2006]. Too low of a symmetry breaking scale would not generate the dark matter abundance: As our constraints probe, $m_A = 10^{-16} - 10^{-20}$eV, this requires f_A just below the GUT scale with $\sim 10^{15} - 10^{16}$ GeV to generate the relic abundance. These high values for f_A (which are far above the Hubble scale during inflation so that this symmetry must be broken during this epoch) may be strained by CMB B-mode observations, which limit the energy scale of inflation to $V(\phi) \lesssim 1.7 \times 10^{16}$GeV Planck Collaboration et al. [2018]. Our mechanism requires the symmetry to be re-established after inflation. This reestablishment can occur if the maximum post-inflation thermalization temperature is greater than f_A [1] or instead during preheating where larger effective temperatures can naturally arise from the non-thermal distribution of resonantly produced particles Tkachev [1996], Kofman et al. [1996].

We further consider models with an asymptotically-free strongly interacting sector that mimics the behavior of the QCD axion (in which the particle mass increases after the ALP behaves behaves like dark matter). Such models allow a somewhat lower f_A to match the dark matter abundance (down to $f_A \sim 10^{13}$GeV), at the cost of introducing a sub-MeV confinement scale. The cosmological constant problem can be solved by hundreds of ALPs connected with strongly coupled sectors (as such sectors allow non-degenerate vacuum minima owing to higher instanton contributions), possibly with several hidden sectors per decade in energy Arvanitaki et al. [2010]. (See this endnote [2] for more discussion of the strongly interacting 'Axiverse' scenario, as there are

[1]The maximum temperature is larger (in some models by orders of magnitude) than the reheat temperature [e.g. Kolb et al., 2003].

[2]In this strongly interacting 'axiverse' scenario, any post-inflation ALP likely cannot have multiple non-degenerate vaccua to avoid a domain wall catastrophe. Thus, the ALPs with non-degenerate vaccua would come into existence before inflation and have a small misalightment angle coherent over the cosmological volume so that they do not overclose the Universe, which perhaps could occur because of the anthropic principle Wilczek [2004]. For our results to apply of course, the ALPs that dominate the dark matter density would have to come into existence after

some challenges to this scenario in our post-inflationary picture.)

Just like with the QCD axion in this post inflation limit, different causally disconnected patches will acquire different energy vaccua depending on the random angle $\theta \in [-\pi, \pi]$ the field rolled to after symmetry breaking in a given patch, with the Horizon scale setting the coherence length until $m_A \sim H$ Kibble [1980], Kolb and Turner [1990]. At this time, the vacuum energy is then converted into non-relativistic axions with number density $\propto \theta^2$, leading to order unity fluctuations in the abundance of axions on the horizon scale when $m_A \sim H$ Hogan and Rees [1988]. The lighter the axion, the later this occurs, the larger the horizon-scale coherence length of the fluctuations.

These isocurvature perturbations are potentially observable. For the QCD axion Preskill et al. [1983], the mass contained in the horizon $M_{H(m_A)}$ when $m_A \sim H$ – which is also the scale where there are order unity density fluctuations – is $M_{H(m_A)} \sim 10^{-10} M_\odot$ Efstathiou and Bond [1986], Hogan and Rees [1988], Vaquero et al. [2019] (and axion self interactions can lead to larger enhancements on even smaller scales; Kolb and Tkachev [1994]). This leads to the collapse of 'axion miniclusters' near this mass scale at matter radiation equality, resulting in much denser dark matter structures than would be produced by the scale-invariant potential fluctuations from inflation. Still, there is no smoking gun observable for verifying whether these minute structures exist, although see Dai and Miralda-Escudé [2020] for a promising possibility. In contrast, for ultra-light axions that are relevant for small-scale structure problems, $M_{H(m_A)}$ can approach the sizes of dwarf galaxies, and the RMS fluctuations produced via these isocurvature fluctuations scale as M^{-1}, where M is the average mass contained within a spherical volume. These fluctuations are still larger than the inflationary perturbations even on mass scales of $M \gg M_{H(m_A)}$. This property has been used to place constraints on the ultralight ALPs via the cosmic microwave background [CMB; Marsh et al., 2013, Feix et al., 2019].

This paper shows that other observables are much more constraining than the CMB. We first focus on the the Lyα forest, which is the quasi-linear 'large-scale' structure formation probe sensitive to the smallest scales. In addition, we show that such isocurvature perturbations could

inflation.

significantly affect the formation of the first stars and galaxies in the redshift of $z \sim 6-20$ Universe, and discuss potential constraints. Since these ioscurvature perturbations lead to the formation of dark matter halos at much higher redshifts than would occur in the standard cosmology, we also consider whether the shocks from these supersonic dense structures could ionize and heat the post-recombination universe. Figure 4.1 summarizes our constraints on the fractional amplitude of isocurvature fluctuations $f_{\rm iso}$ (defined shortly) and axion mass m_a, where dashed lines represent existing constraints and dotted represent forecasts for future efforts.

This paper is organized as follows. Section 4.2 describes the character of ALP isocurvature fluctuations. Then, we discuss the limits from several observables: the Lyα forest (§4.3), the high-redshift galaxy luminosity function (§4.4), measurements that constrain early universe star formation from the electron scattering optical depth through reionization (§4.5), and finally from future 21cm observations and the potential shock heating of cosmic gas (§4.6). While some of these observables are inherently very astrophysical and hence the constraints dependent on modeling, we show that isocurvature fluctuations can result in qualitatively different trends. Our numerical calculations take $\Omega_m = 0.308, \Omega_\Lambda = 0.692, \Omega_b = 0.0484, h = 0.678, \sigma_8 = 0.815$, and $n_s = 0.968$, consistent with the results of Planck Collaboration et al. [2016]. When convenient, our calculations will use natural units where $c = \hbar = k_b = 1$. Cosmological distances and wavenumbers are given in comoving units. All mass function calculations use the mass function of Sheth and Tormen [2002]. Even though we are considering non-standard cosmologies, the well-tested universality of the mass function means that Sheth and Tormen [2002] still holds at the 10% fractional level [Bagla et al., 2009, and some of us have also have been involved in running simulations testing this].

4.2 *Isocurvature power from post-inflation axions*

After perturbative effects break the degeneracy between different θ-vacua, the vacuum misalignment of the ALP translates into a component that behaves like non-relativistic matter with local density Weinberg [1978], Wilczek [1978], Kolb and Turner [1990]

$$\rho_a(T, \theta_{\rm ini}) = \frac{1}{2} f_a^2 m_a(T) m_a(T_{\rm osc}) \theta_{\rm ini}^2 \left(\frac{a(T_{\rm osc})}{a(T)} \right)^3 , \tag{4.1}$$

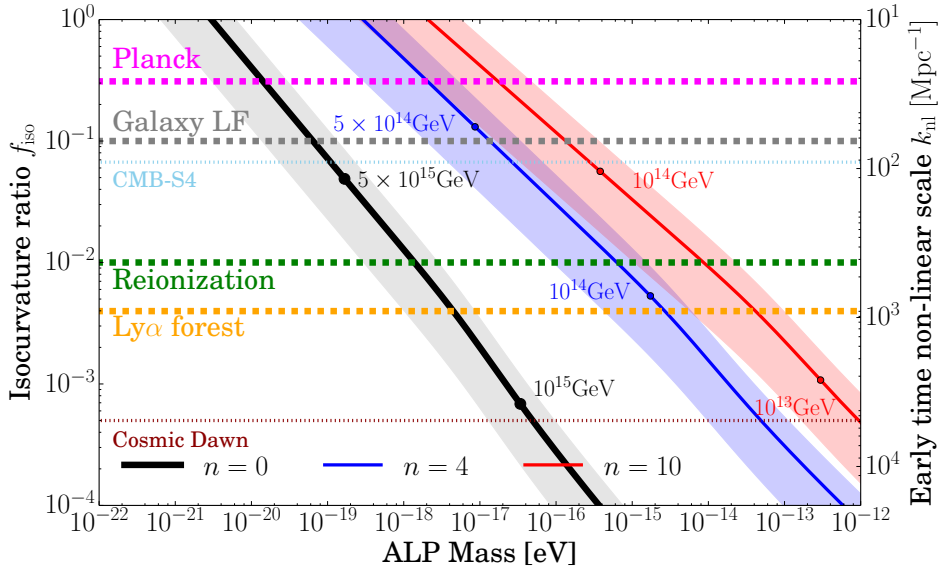

Figure 4.1: The $f_{\rm iso} - m_a$ constraints for the ALP dark matter in the post-inflation scenario, assuming the ALP is all of the dark matter. The isocurvature to adiabatic ratio $f_{\rm iso}$ applies at the pivot scale of $k_\star = 0.05$ Mpc^{-1}, and the second y-axis gives the nonlinear scale defined by $\Delta^2_{\rm iso} \equiv (k/k_{\rm nl})^3$ at early times. The solid lines show this mapping for our fiducial choice of $A_{\rm osc} = 0.1$ and the shaded bands span $0.01 \leq A_{\rm osc} \leq 0.3$. The horizontal dashed lines correspond to current upper limits on $f_{\rm iso}$ obtained using different data sets: the Planck 2018 CMB measurements in magenta from Feix et al. [2019], Hubble Space Telescope galaxy luminosity function measurements in grey (§ 4.4), a combination of constraints on the reionization history in green (§ 4.5), and finally Ly-α forest in orange (§ 4.3). The horizontal dotted line in light blue is a forecast for CMB-S4 Feix et al. [2019], while the horizontal dotted line in dark red is a rough forecast for where shock-heating should qualitatively change the $z \sim 20$ 21cm signal (§ 4.6). The labeled dots give the value of the symmetry breaking scale f_a.

where $\theta_{\rm ini}$ is the initial vacuum misalignment angle after symmetry breaking, $a(T)$ is the scale factor, and $m_a(T)$ the axion mass. This formula holds after the axion starts oscillating at an oscillation temperature that we define as $m_a = 3H(T_{\rm osc})$. Eqn. (4.1) allows for the possibility that the axion temperature is also evolving at $T_{\rm osc}$ as could occur in strongly interacting sectors (as discussed later). We average $\rho_a(T, \theta_{\rm ini})$ over space, noting that we use the simple relation for the spatial average $\langle\theta_{\rm ini}^2\rangle = \pi^2/3$, to calculate the average dark matter abundance. The axion decay constant f_A (which we also refer to as the "symmetry breaking scale") will be adjusted to match the observed dark matter abundance.

Because different causal horizons have different $\theta_{\rm ini}$, this translates into a white spectrum of isocurvature fluctuations in the matter overdensity at times after the field behaves like non-relativistic matter but well into the radiation era with growing mode dimensionless power spectrum of (e.g. Feix et al. [2019])

$$\Delta^2_{\mathcal{S}}(k) \equiv \frac{k^3}{2\pi^2} P_{\mathcal{S}}(k) = A_{\rm osc} \left(\frac{k}{k_{\rm osc}}\right)^3 \quad \text{at } k < k_{\rm osc}, \tag{4.2}$$

where $P_{\mathcal{S}}(k) \equiv V^{-1}|\tilde{\delta}_{\mathbf{k}}|^2$, V is the volume, and $\tilde{\delta}_k$ is the Fourier transform of the configuration-space dark matter matter overdensity $\delta(\mathbf{x})$ (which we assume to be entirely composed of ALPs such that $\delta(\mathbf{x}) = \rho_a(\mathbf{x})/\langle\rho_a\rangle - 1$), $k_{\rm osc} = a\,H\,|_{T_{\rm osc}}$ is the size of the Horizon when the APL starts to oscillate in its potential Kolb and Turner [1990], and $A_{\rm osc}$ sets the normalization for which the order-unity fluctuations on the oscillations scale mean $A_{\rm osc} \sim 1$. While irrelevant for this study, at scales $k \gtrsim k_{\rm osc}$ a sharp cut-off is expected as the vacuum misalignment fluctuations have been smoothed out by the Kibble Mechanism Kibble [1980]. Typical values of $k_{\rm osc}$ are between 100 and 1000 Mpc^{-1} for the ALP masses of 10^{-19} and 10^{-17} eV, respectively. The signatures we study are sourced by structures that are coming from an order of magnitude smaller wavenumbers.

Simulations of the QCD axion find that values of the isocurvature variance at initial conditions are $A_{\rm osc} \sim 0.01 - 0.3$ Feix et al. [2019], Vaquero et al. [2019], somewhat smaller than unity because some of the misalignment power is not in the zero mode and because this signal is diluted by relativistic axions radiated by axionic strings. However, for our ALP we expect the details that shape $A_{\rm osc}$ to depend on the specific model. When we connect our results to the axion mass m_a,

we take as a fiducial value $A_{\rm osc} = 0.1$, but our results are easily re-scaled to other values.

We use the standard growth and transfer function parameterization to model the subsequent evolution of the isocurvature fluctuations (as well as the standard inflationary adiabatic fluctuations). We parameterize the ioscurvature fluctuations as

$$\Delta^2_{\rm iso}(k,z) = D^2_{\rm iso}(z) T^2_{\rm iso}(k,z) A_{\rm iso} \left(\frac{k}{k_\star}\right)^3 , \tag{4.3}$$

where $D_{\rm iso}(z)$ is the growth function that tends to a constant deep in the radiation era, and $T^2_{\rm iso}(k,z)$ is the transfer function that is normalized to unity at high-k [3]. This transfer function is approximately constant for modes that enter the horizon during radiation domination. We take $k_\star = 0.05$ Mpc^{-1} for the pivot scale. Similarly, for the adiabatic fluctuations from inflation

$$\Delta^2_{\rm ad}(k,z) = D^2_{\rm ad}(z) T^2_{\rm ad}(k,z) A_s \left(\frac{k}{k_\star}\right)^{n_s-1} , \tag{4.4}$$

with analogous definitions as for $\Delta^2_{\rm iso}$ except that the adiabatic transfer function is normalized to unity at low k. For our chosen value of σ_8, $A_s = 2.054 \times 10^{-9}$. The total matter power at redshift z is the sum of the isocurvature and adiabatic contributions, $\Delta^2_{\rm iso} + \Delta^2_{\rm ad}$. The transfer functions at late times were calculated using `CAMB` Boltzmann code solver Lewis and Bridle [2002]. Following convention, we define $f_{\rm iso}$ to be the ratio of isocurvature to adiabatic fluctuations at $k_\star = 0.05$ Mpc^{-1}:

$$f^2_{\rm iso} = \frac{A_{\rm iso}}{A_s} = \frac{A_{\rm osc}}{A_s} \left(\frac{k_\star}{k_{\rm osc}}\right)^3 , \tag{4.5}$$

where the second equation uses that deep into the radiation dominated universe $A_{\rm iso}/{k_\star}^3 = A_s/k^3_{\rm osc}$ since $D_{\rm iso}T_{\rm iso} \to 1$. In the late time matter power, the ratio of isocurvature-sourced to adiabatic-sourced fluctuations is highly scale dependent, scaling approximately as k^3 at high wavenumbers. This is illustrated in Fig. 4.2, where different colours represent different values of $f_{\rm iso}$, with highest value of $f_{\rm iso}$ resulting in highest small scale power. Dashed vertical lines show the mass scale at which the adiabatic and isocurvature contributions to the power spectrum are equal. The contribution of isocurvature fluctuations becomes important at different mass scales, following the

[3] That the isocurvature transfer function limits to unity at high-k is true for the dark matter/ALP transfer function. Whereas the total matter transfer function will be lower due to the effects of Jeans smoothing on the baryons.

approximate scaling of $f_{\rm iso}$ with mass as $M^{1/2}$. This is a direct consequence of the definition of $f_{\rm iso}$ which is fixed on large scales ($k_\star$), and leads to a natural expectation that observables probing smaller mass scales will result in tighter constraints on $f_{\rm iso}$.

We also specify the level of isocurvature by its early time nonlinear scale $k_{\rm nl}$, where $k_{\rm nl} \equiv k_{\rm osc} A_{\rm osc}^{-1/3}$ such that deep into the radiation era $\Delta^2_{\rm iso} = (k/k_{\rm nl})^3$. The nonlinear scale represents a more straightforward quantification of the white noise power because it does not convolve in the well-understood amplitude of adiabatic fluctuations and because it does not single out a specific $k_\star$.

One likely scenarios is that the m_a does not exhibit strong temperature dependence in the early Universe. This limit applies to ALPs whose mass is acquired by nonperturbative effects associated with the perturbative gauge couplings in GUT theories Hui et al. [2017]. In this case, the non-perturbative mass is exponentially suppressed relative to the symmetry breaking scale and the ALP field obtains its zero-temperature mass at $T \gg T_{\rm osc}$. We also consider a QCD-like case of a asymptotically-free strongly interacting sector where the non-perturbative effects increase with decreasing temperature until the temperature reaches the confinement scale, Λ; evolution of the mass occurs even after the ALP behaves like non-relativistic matter if $\Lambda < T_{\rm osc}$, with the final mass equal to $m_A = \Lambda^2/f_a$. The ALP mass evolution can be characterized at $T \lesssim T_{\rm osc}$ by

$$m_a(T) = m_a \left(\frac{\Lambda}{T}\right)^n \quad \text{for } T > \Lambda, \tag{4.6}$$

$$m_a(T) = m_a \quad \text{otherwise}, \tag{4.7}$$

where we use the notation that m_a without an argument is the zero temeprature mass and where n parameterizes the temperature dependence of the instanton effects. The case $n = 4$ mimics the scaling found for the QCD axion, but the details of this scaling will depend on the strong sector. For $n = 0$ perturbative case, we note that this parameterization still holds (trivially).

With this parameterization,

$$T_{\rm osc} = 3\left(\frac{10}{\pi^2 g_{\rm eff}}\right)^{1/4}[m_A(T_{\rm osc})M_P]^{1/2} \tag{4.8}$$

$$\propto \langle\theta_{\rm ini}^2\rangle^{-\frac{n}{8+3n}} m_a^{\frac{4+n}{8+3n}}, \tag{4.9}$$

$$k_{\rm osc} = a_{\rm osc}H(T_{\rm osc}) = \frac{T_{\rm cmb,0}}{T_{\rm osc}}\frac{m_A(T_{\rm osc})}{3} \propto T_{\rm osc}, \tag{4.10}$$

$$f_A \propto \langle\theta_{\rm ini}^2\rangle^{-2/(8+3n)} m_a^{-(2+n)/(8+3n)}, \tag{4.11}$$

where $M_P = 1/\sqrt{8\pi G}$ is the reduced Planck mass, and $T_{\rm osc}$ evaluates to $1-100$keV for m_A of interest, indicating $g_{\rm eff} \approx 3.4$. For the proportionality relations, we have eliminated the Λ dependence in favor of m_a and f_A. We note that at fixed $m_A(T_{\rm osc})$ the amplitude of isocurvature fluctuations does not depend on n, and our constraints in Fig. 4.1 translate to $m_A(T_{\rm osc}) = 10^{-20} - 10^{-17}$eV. For our $n = 4, 10$ models in Fig. 4.1, the particle mass increases by $3, 4$ orders of magnitude to reach m_a at $T = \Lambda$.

Fig. 4.1 foreshadows the constraints we find in the following sections in the $m_a - f_{\rm iso}$ plane. The different horizontal limits show the upper limit on $f_{\rm iso}$, bounding the viable parameter space to be below the curves. The $n = 0$ corresponds to the most likely case where the mass is established well before the particle commences oscillations, and the QCD axion yields a scaling with $n = 4$. The dots on the lines correspond to the values of the decay constant f_A for those models (colour coded to match the lines), while the shaded regions around the lines correspond to the uncertainty in the value of $A_{\rm osc}$. The sold lines themselves were evaluated at the value of $A_{\rm osc} = 0.1$.

4.3 *Lyman-α forest*

The Lyman-α forest is used to infer the initial conditions using significantly smaller comoving scales than other large-scale structure observables, to 3D wavenumbers of $k \approx 10 - 100{\rm Mpc}^{-1}$ Meiksin [2009], McQuinn [2016]. The Lyman-α forest circumvents many of the difficulties of modeling structure formation at these nonlinear scales by being sensitive exclusively to low-densities ($\Delta \sim 1$ as the absorption of higher densities is saturated; Iršič and McQuinn [2018]) where our nonlinear models for the cosmic web appear to be under control Cen et al. [1994], Miralda-Escudé et al.

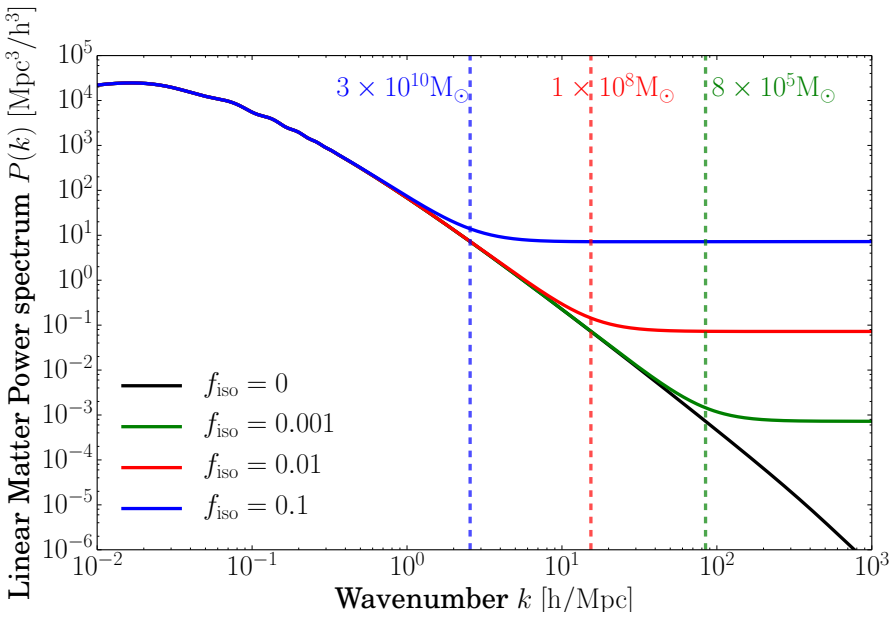

Figure 4.2: The linear matter power spectrum at $z = 0$ for different values of $f_{\rm iso}$. The scales where isocurvature contribution become important, relative to the adiabatic power spectrum, are marked with vertical dashed lines and labeled by their $M = 4\pi/3\rho_m(z = 0)k_c^{-3}$, where k_c is the wavenumber where adiabatic and isocurvature fluctuations are equal.

[1996], Hernquist et al. [1996] and where astrophysical processes appear to be less of a contaminant McQuinn [2016]. Indeed, the forest has been used to place the tightest constraints on small-scale cutoff in the spectrum of primordial matter fluctuations, which may owe to the free streaming of warm dark matter and the de-Broglie wavelength of fuzzy dark matter Seljak et al. [2006], Viel et al. [2005], Iršič et al. [2017]. In the context of ALPs, combining the Lyα constraints with the limits on the isocurvature fluctuations from the CMB can lead to interesting bounds on the tensor-to-scalar ratio Kobayashi et al. [2017].

A typical Lyα forest analysis is sensitive to 1D wavenumbers between 0.1 and 10 Mpc/h, which would naively lead to a typical mass of 10^8 $M_\odot$ (see Fig. 4.2). However, The non-linear mapping from the 3D density field to the 1D flux field in the quasar spectra makes the Lyα forest sensitive to even smaller wavenumbers (see e.g. Murgia et al. [2019]). Additionally, the non-linearity of the

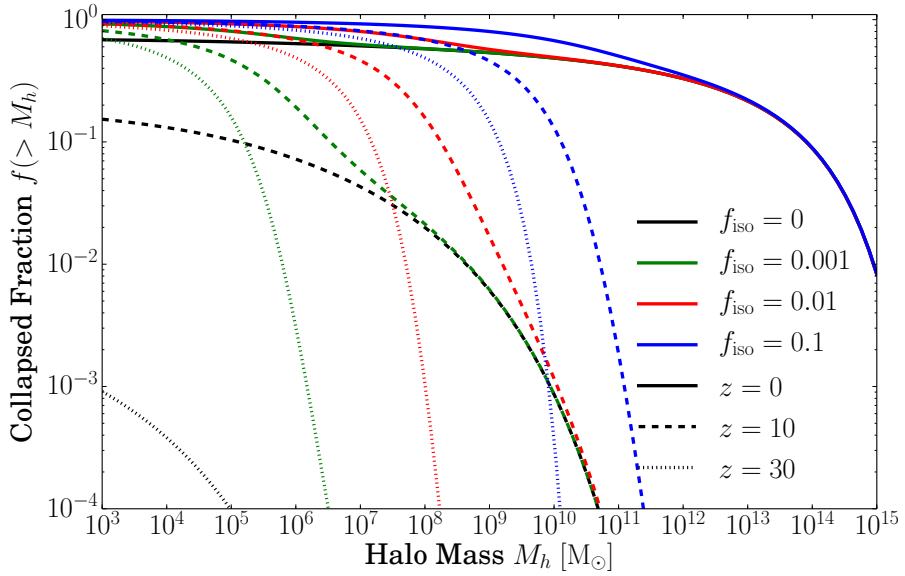

Figure 4.3: The collapsed fraction in halos above a mass of M_h. Different colours show the collapsed fraction for isocurvature fractions of $f_{\rm iso} = 0.1$ (blue), $f_{\rm iso} = 0.01$ (red), $f_{\rm iso} = 0.001$ (green) and $f_{\rm iso} = 0$ (black). The line styles differentiate redshifts.

gravitational evolution does not dominate over the clustering signal at high redshifts, which helps to better constrain cosmology at a given scale.

The forest is also sensitive to an enhancement in power as would occur from the white isocurvature fluctuations from axions in the post-inflation scenario. Indeed, the allowed level of enhancement has been constrained in the context of primordial black holes, which also may have a white spectrum Afshordi et al. [2003], Murgia et al. [2019]. Conveniently, the adiabatic plus white-noise simulations run for the primordial black holes in Murgia et al. [2019] are the same as would be run in the context of ALP isocurvature perturbations, the difference comes in the interpretation of the isocurvature amplitude and how it is linked to the actual physical model. In particular, Murgia and coworkers Murgia et al. [2019] find that the isocurvature fraction of $f_{\rm iso} = \sqrt{A_{\rm iso}/A_s}$ at the pivot scale of $k = 0.05$ Mpc^{-1}, should be lower than 0.004 at 2σ confidence level when adopting conservative priors on the thermal history. This constraint can be remapped to our models by

solving Eqs. 4.5 and 4.11 for a given ALP mass evolution model. The relation between f_A and m_a is fixed by assuming that all of dark matter is composed of the axion-like particle. This gives a lower bound on the mass of the ALP of $m_A > 2 \times 10^{-17}$ eV for the most natural case of no mass evolution after the axion starts oscillating ($n = 0$). This constraint further shows that the forest is effectively able to probe structure in the dark matter to mass scales as small as $\sim 3 \times 10^7$ $M_\odot$ (using Fig. 4.2); a number that is helpful for putting the forest in context with the other constraints we discuss.

Figure 4.1 shows the constraints from the forest. A primary result of this paper is that we find the Lyα forest is more constraining than other probes, although future observations of the high-redshift universe using redshift 21cm radiation may ultimately be more constraining.

4.4 *Galaxy luminosity function*

Small galaxies are a second observable that has been used to constrain the primordial fluctuations on small scales, with observations both probing them as satellite galaxies to the Milky Way Bullock and Boylan-Kolchin [2017] and at high redshifts when they are forming the bulk of their stars Barkana et al. [2001], Pacucci et al. [2013]. Since the white-noise isocurvature fluctuations in our ultra-light axion models dramatically increase fluctuations on small scales, such scenarios may predict a large increase in the number of low-luminosity galaxies. Foreshadowing the result of this section: For galaxies that are directly observable in the future, we find that this enhancement is small for the $f_{\rm iso}$ allowed by the forest, although in § 4.5 we show that for smaller galaxies (whose effects can only be indirectly probed via their ionization and enrichment) the enhancement can be more substantial.

To model the enhanced number of small galaxies, we use a simple but successful model for star formation where the predicted number density of galaxies n_g per UV luminosity between L and $L + dL$ is related to the halo mass function dn_h/dM_h by

$$\phi(L) \equiv \frac{dn_g}{dL} = \frac{dn_h}{dM_h}\frac{dM_h}{dL}, \tag{4.12}$$

This model assumes the common one-to-one mapping between halo mass and observed UV lumi-

nosity described by dM_h/dL. As this function has significant astrophysical uncertainty, we will use qualitatively different shapes for the galaxy luminosity function, dn_g/dL, as a signature that a given axion cosmology is excluded.

To calculate the terms in eqn. 4.12, we use the Sheth-Tormen mass function Sheth and Tormen [2002] to model dn_h/dM_h [4] The 'universality' of the halo mass function makes it likely that the same mass function should be a good approximation to cases with isocurvature fluctuations Lukić et al. [2007], Bagla et al. [2009]. Additionally, we adopt a common assumption that a galaxy's star formation rate is proportional to its gas accretion rate, $\dot{M}_b$, with proportionality constant $f_\star(M_h, z)$ called stellar efficiency. Note that the star formation rate directly maps to the UV luminosity of the galaxy. We follow Furlanetto et al. [2017] to calculate $f_\star$, who calculate it from an analytic model that considers energy regulated stellar feedback process plus virial shocking. In this model, the stellar efficiency of the baryons peaks at around $M_h = 10^{11.5}$ $M_\odot$, where it reaches the values of just below 0.05. This efficiency has a steep tail towards smaller masses, reaching 10^{-3} by $M_h = 10^8$ $M_\odot$. One worry, which we will address, is that this efficiency depends on uncertain astrophysics and so any differences we find may not be distinguishable.

To model the gas accretion rate $\dot{M}_b$, numerical results are typically obtained from cosmological simulations (e.g. McBride et al. [2009]), but for the isocurvature case, $\dot{M}_b$ has not been determined using simulations. However, the time evolution of the halo accretion rate is driven largely by the time evolution of the mass variance $\sigma(M)$ (see e.g. Correa et al. [2015]). We set

$$\frac{d\ln M_b}{dt} = \left|\frac{d\ln\sigma}{d\ln M_h}\right|^{-1} \frac{d\ln D}{dt}, \tag{4.13}$$

and D is the growth function. This allows us to build a consistent approach to calculating the gas accretion for any $f_{\rm iso}$. Our results on the gas accretion are in good agreement Correa et al. [2015] in the limit they consider of $f_{\rm iso} = 0$.

Fig. 4.4 shows the resulting comparison of the galaxy luminosity function. Our model is compared to the measurements of McLure et al. [2013], Bowler et al. [2017], Bouwens et al. [2015,

[4]We have checked that the results are not sensitive to the choice of the mass function by also investigating a mass function specifically calibrated to simulations at high redshift Trac et al. [2015].

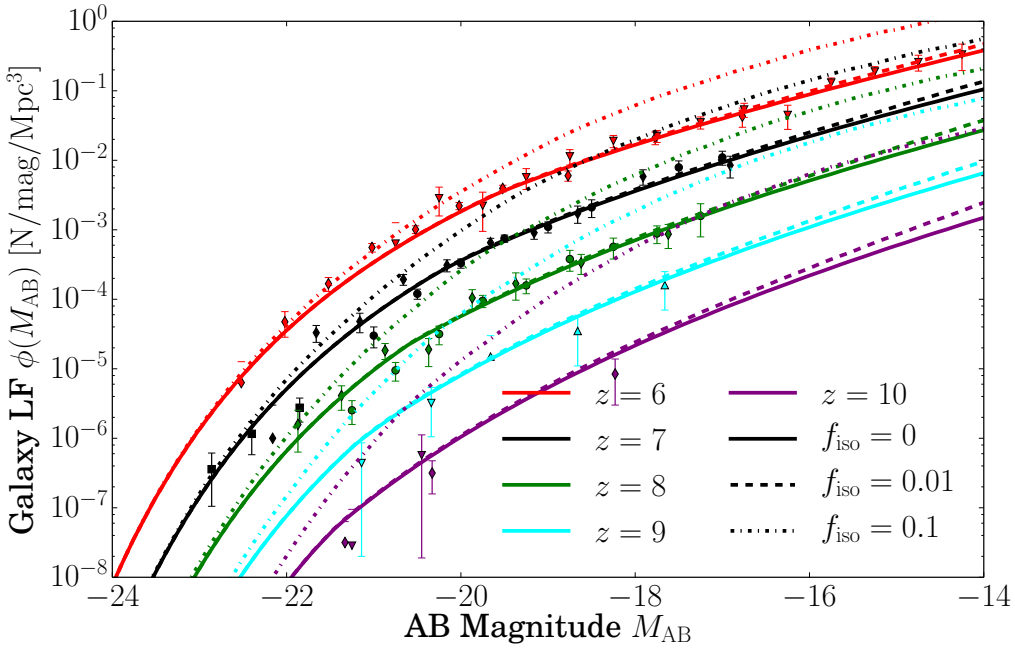

Figure 4.4: The effect of white-noise isocurvature fluctuations on the galaxy luminosity function. The various linestyles shows different levels of isocurvature fluctuations, with colour indicating redshift. Overplotted is a compilation of observational data ranging over typical redshifts probed by the future surveys. We consider $f_{\rm iso} = 0.1$ to be ruled out by these observations as by this value the luminosity function has a qualitatively different behavior, especially at the highest redshifts probed.

2016], but also include the $z = 6$ lensed galaxy sample of Bouwens et al. [2017] that extend the measurement to fainter immensities. We use the standard convention of writing the UV luminosity in terms of absolute AB magnitude where $M_{\rm AB} = -2.5 \log_{10}(L_{\rm UV}) + M_{\rm ref}$ where $M_{\rm ref}$ is a constant. We have not performed any dust correction at this stage, as the typical corrections Smit et al. [2012] are only significant for the higher mass systems, and leads to a shallower relation between the halo mass and the UV magnitude [5].

[5]This effect may weaken our constraints from the galaxy luminosity function if lower mass galaxies are substantially dust absorbed.

However, including isocurvature fluctuations, even at level already excluded by Lyα forest of $f_{\rm iso} = 0.01$, only results in a small signal at a lower end of the luminosity function. This is mainly due to the fact that even the observed high-redshift galaxies behind cluster lenses reside in $> 10^9 M_\odot$ halos in our models. In contrast, the Lyα forest is sensitive to scales of $M \sim 10^8\ M_\odot$, as illustrated in Fig. 4.2. We find that current observations of the high-redshift luminosity function rule out $f_{\rm iso} > 0.1$, as this leads to a large qualitative change that likely cannot be mimicked by the large astrophysical uncertainty in our star formation efficiency model. One can already start to see this large effect for the $f_{\rm iso} = 0.05$ model in Fig. 4.2. These limits translate into a lower bound on the ALP mass to be $m_a > 10^{-19}$ eV.

Future observations at higher redshifts would help in discriminating between different isocurvature models, and could potentially provide constraints comparable to the ones derived from the small scale structure of the Lyα forest. Namely, the James Webb Space Telescope (JWST) is able to go a few magnitudes deeper at $z \approx 6$, and more importantly has the infrared sensitivity that allows better constraints at higher redshifts. With lensed galaxy samples, JWST should be able to place similar constraints to HST at $z = 6$ (reaching to absolute magnitudes of $M_{\rm AB} = -14$) but all the way to $z = 10$, constraining $f_{\rm iso} \sim 0.01$. Unfortunately, astrophysical uncertainties require a qualitative change in behavior, making it difficult to probe beyond $f_{\rm iso} = 0.01$. Thus, the Lyα forest is likely to always provide a more sensitive probe than direct measurements of galaxy luminosity functions.

4.5 *High-redshfit star formation rate and reionization*

Though we find that the galaxy luminosity function is not competitive with the Lyα forest, the collapsed fraction of halos that can form stars can be orders of magnitude larger than the $f_{\rm iso} = 0$ prediction at $z = 10$, and this difference is even larger at higher redshifts, if we take $f_{\rm iso} = 0.01$ – comparable to the constraint coming from Lyα. This is illustrated in Fig 4.3, noting that stars can only form in halos with $M_h \gtrsim 10^{7-8} M_\odot$ if the gas condenses by cooling via atomic transitions and $M_h \gtrsim 10^{5-6} M_\odot$ halos if instead by molecular ones. Unfortunately, the direct luminosity function measurements with HST (and in the future with JWST) are not sufficiently sensitive to detect the stars/galaxies that likely lie in these diminutive halos. However, the enhanced extremely

high-redshift star formation from an increased abundance of these small halos could also heat and ionize the cosmic gas (and their UV photons can pump the 21cm line) in a manner that may allow constraints on $f_{\rm iso}$. There is also some indirect evidence that the smallest galaxies contribute disproportionately to the ionizing photons that escape into and hence ionize the IGM Haardt and Madau [2012], which would make our mass-independent escape in what follows conservative.

To illustrate just how much isocurvature fluctuations could change the mass in halos that are massive enough to host stars, we calculate the fraction of mass that is collapsed in halos with masses above M_h using Extended Press-Schechter theory Press and Schechter [1974], Bond et al. [1991]. This yields $f_{\rm coll}(>M_h) = {\rm erfc}\left(\nu(M_h)/\sqrt{2}\right)$, where ${\rm erfc}(x) \equiv \pi^{-1/2}\int_x^\infty dx\,\exp[-x^2]$ and $\nu \equiv \delta_c/\sigma(M,z)$ and $\sigma(M,z)$ is the standard deviation of the density in a spherical top-hat Lagrangian volume with mass M. The virial temperature of halo (the characteristic temperature the gas can shock heat) is the property of a halo that sets whether its gas can cool and form stars rather than the halo mass. The two are related by $M_h \propto [aT_{\rm vir}]^{3/2}$ – at higher redshifts the same virial $T_{\rm vir}$ halo has smaller M_h. The isocurvature fluctuations with constant power spectrum on small scales during the matter dominated epoch this leads to $\sigma^2(M) \propto a^2 M^{-1}$, whereas for $f_{\rm iso} = 0$ we have $\sigma^2(M) \propto a^2\log[M]$. The result is that the redshift evolution of the collapsed fraction at fixed virial radius is *much* flatter for masses where isocurvature fluctuations dominate, with the difference given by

$$\begin{aligned} f_{\rm coll}(>T_{\rm vir}) &= {\rm erfc}\,[1.7\,Z_{10}] && \text{for adiabatic;} \\ f_{\rm coll}(>T_{\rm vir}) &= {\rm erfc}[1.0\,f_{\rm i,-2}^{-1}Z_{10}^{1/4}T_{\rm vir,4}^{3/4}] && \text{isocurvature,} \end{aligned}$$

where $f_{\rm i,-2} \equiv f_{\rm iso}/10^{-2}$, $Z_{10} \equiv (1+z)/10$ and $T_{\rm vir,4} \equiv T_{\rm vir}/10^4$ K.[6]

The former function falls off exponentially with increasing redshift for rare (large ν) objects noting asymptotic form $\sqrt{\pi}{\rm erf}(x) = \exp[-x^2](x^{-1} + O(x^{-3}))$, whereas the latter (while still exponentially sensitive once the argument becomes greater than unity) is much flatter, allowing halos

[6]The full dependence on redshift and virial temperature for the adiabatic case is roughly $f_{\rm coll}(>T_{\rm vir}) = {\rm erfc}\left[2.04\times Z_{10}\left\{\ln\left(4.6\times Z_{10}T_{\rm vir,4}^{-1}\right)\right\}^{-1/2}\right]$, but the logarithmic dependence only adds a small correction to the redshift evolution.

that can cool at much higher redshifts.

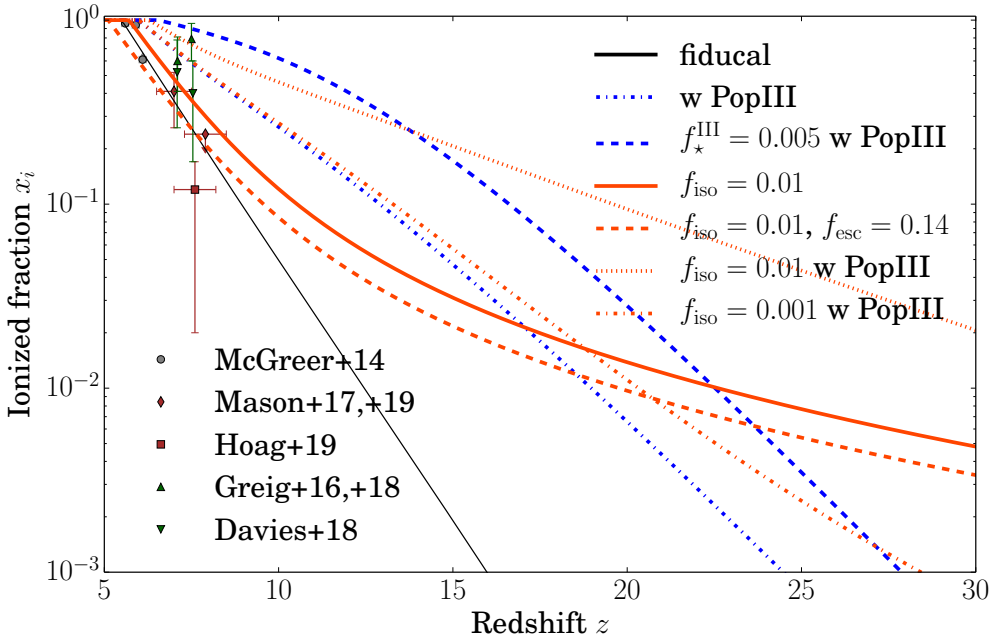

Figure 4.5: The evolution of the ionized fraction of the intergalactic gas during reionization. The fiducial model assumes a given stellar efficiency described in Sec. 4.4. The effect of axion isocurvature fluctuations is shown for various values of $f_{\rm iso}$ and also varying assumptions about the escape fraction of Pop-II stars (orange dashed) or including a contribution from Pop-III stars (blue and orange dot-dashed). Overplotted is a compilation of observational constraints on the ionized fraction coming from Lyα dark pixels (grey), Lyα emitters (brown) and QSO damping wings (green).

An enhancement in the number of star forming halos in the manner of our white isocurvature fluctuations should lead to an enhanced number of hydrogen ionizing photons, causing the reionization of the Universe to start earlier and be a much more prolonged process. Such a reionization history would be constrained by direct estimates of the ionized fraction using quasar spectra and Lyman-α emitters. The ionized state of the intergalactic gas can be measured through the time evo-

lution of the volume-averaged ionized fraction, that depends on the balance between recombination and ionization due to photo-ionization Sun and Furlanetto [2016],

$$\frac{dx_{\rm i}}{dt} = \frac{d\left(\zeta f_{\rm coll}\right)}{dt} - \bar{n}_H(t)\,\alpha_{\rm re}(T_e)\,C_{\rm HII}\,x_{\rm i}, \tag{4.14}$$

where $\zeta = A_{\rm He} f_\star f_{\rm esc} N_\gamma$ is the ionizing efficiency: a product of the correction factor for singly ionized helium, $A_{\rm He} \approx 1.22$; the star formation efficiency, $f_\star$; the escape fraction of ionizing photons, $f_{\rm esc}$; and the average number of ionizing photons produced per stellar baryon, N_γ. In the recombination term, the number density of hydrogen, $\bar{n}_H$, is time dependent as $\bar{n}_H = \bar{n}_H(z = 0)\,(1+z)^3$ at redshift z; the recombination rate, $\alpha_{\rm re}$, is temperature dependent such that $\alpha_{\rm re}(T_e) = 2.6 \times 10^{-13}\left(T_e/10^4\ {\rm K}\right)^{0.76}\ {\rm cm^3\,s^{-1}}$, at the electron temperature T_e; and the volume-averaged clumping factor is defined to be $C_{\rm HII} \equiv \langle n_e^2\rangle/\langle n_e\rangle^2$.

A rough approximation during HI reionization Shull et al. [2012], Sun and Furlanetto [2016] is to fix $C_{\rm HII} = 3$, and $T_e = 10^4$ K. It would be naturally to expect a redshift evolution of the clumping factor (see e.g. Haardt and Madau [2012]), which might change the reionization history. In our simple scenario, chaning the value of the clumping factor to 5 (1) leads to a largely redshift-independent change in the ionized fraction in our calculations by a factor of 0.8 (1.4) (at least at high redshifts). The value of the mean number of ionizing photons produced, N_γ, depends in the initial mass function and metalicity of the stellar population. We use $N_\gamma = 4,000$ for Population II (Pop-II) stars, assuming Salpeter IMF and 5% of the solar metalicity (although the results are weakly sensitive to these choices at least assuming empirically motivated IMFs). Pop-II stars are the second generation of stars that are born in metal enriched gas and likely have properties similar to stars observed at low-redshifts. Unless otherwise stated we use the escape fraction of 20% for the Pop-II stars. In the fiducial Pop-II model we assume all halos above $M_{\rm min}$ form stars, and at each redshift the value of $M_{\rm min}$ is fixed to the mass at the virial temperature of $T_{\rm vir} = 10^4$ K. The basic photo-ionization rate can be evaluated using the halo mass accretion rates discussed in (§4.4),

$$\frac{d\left(\zeta f_{\rm coll}\right)}{dt} = A_{He}\,N_\gamma\,f_{\rm esc}\int_{M_{\rm min}}^{\infty}\frac{dM_h}{\bar{\rho}_m}n(M_h)f_\star\dot{M}_h, \tag{4.15}$$

where $f_\star$ is the mass-dependent stellar efficiency and $n(M_h)$ is the halo mass function.

In the context of the early star formation, a Population III (Pop-III) stellar contribution is often discussed, which is the first generation of stars which are born metal free and expected to be more massive. Since this contribution is at present largely unconstrained Visbal et al. [2015], we adopt a toy model to characterize their effect on the progression of the reionization. In this case an additional photo-ionization term is added, mimicking the structure of $d\left(\zeta_{\rm III} f_{\rm coll}\right)/dt$, but with the ionizing efficiency characteristic of the Pop-III models. Namely, following Eqn. (4.15) we write down the Pop-III photo-ionization rate as

$$\frac{d\left(\zeta_{\rm III} f_{\rm coll}\right)}{dt} = A_{He}\, N_{\gamma}^{\rm III} \int_{M_{\rm min}^{\rm III}}^{M_{\rm min}} \frac{dM_h}{\bar{\rho}_m} n(M_h) f_{\star}^{\rm III} \dot{M}_h. \tag{4.16}$$

The integration is only over halos where molecular cooling is efficient and atomic is not (as atomic leads to our normal mode of star formation), i.e. between $T_{\rm vir} = 500$ K ($M_{\rm min}^{\rm III}$), warm enough to excite rotational transitions of molecular hydrogen, and the mass at the virial temperature of 10^4 K ($M_{\rm min}$). We use $N_{\gamma}^{\rm III} = 40,000$ as anticipated for the hotter photospheres of these metal free starsBromm et al. [2001], and assume that all ionizing photons escape as anticipated for star formation in these diminutive halos. We also take a stellar efficiency of $f_{\star}^{\rm III} = 5 \times 10^{-4}$, although the escape of ionizing photons can be pulled into this parameter. This efficiency is on the lower end of what is typically used in the literature Trenti and Stiavelli [2009], Visbal et al. [2018], with most commonly used values being $10^{-3} - 10^{-2}$. However, in our simplifed model, our fiducial value of $f_{\star}^{\rm III}$ leads to the star formation rate density of Pop-III stars comparable to that of Visbal et al. [2015] (see our endnote [7]).

Once enough stars form in the Universe, the $\sim$ 11eV Lyman-Werner radiation they produce dissociates molecular hydrogen, turning off cooling in molecular cooling halos and preventing the formation of further Pop-III stars Haiman et al. [1997, 2000]. To model this we follow McQuinn and

[7]The star formation rate density in our model peaks at around 2×10^{-4} $M_{\odot} yr^{-1} Mpc^{-3}$ at redshift of 15, and falls off towards higher redshifts (e.g. 10^{-6} $M_{\odot} yr^{-1} Mpc^{-3}$ at redshift of 35), behaviour quantitatively very similar to that found in Visbal et al. [2015]. This is true despite different star formation efficiency assumed in our model compared to Visbal et al. [2015], because the minimum mass in which molecular cooling can lead to Pop-III star formation is lower in our model, compared to the that of Visbal et al. [2015]. In Visbal et al. [2015] the numeric value of the minimum mass is obtained from CDM simulations and corresponds to roughly $T_{\rm vir} = 1000$ K. See Eqn. 4.17 as the minimum does not just set the absolute minimum but also what halos are affected by the Lyman-Werner background.

O'Leary [2012], Visbal et al. [2015], Mebane et al. [2018], where we modify the lower integration limit ($M^{\rm III}_{\rm min}$) in Eqn. (4.16) to also include self-regulations due to Lyman-Werner background. The numerical calculations of Machacek et al. [2001], Wise and Abel [2007] found that the gas is able to cool in halos with mass

$$M^{\rm III}_{\rm min} = M_h \left(T_{\rm vir} = 500 \text{ K}\right) \left[1 + 6.69\, F^{0.47}_{LW,21}\right], \tag{4.17}$$

where $F_{LW,21}$ is the Lyman-Werner intensity integrated over solid angle in units of 10^{-21} erg s^{-1} Hz^{-1} cm^{-2}. To estimate the Lyman-Werner intensity given a star formation rate ($\dot{\rho}_{\rm SFR}$), we use the relations of Visbal et al. [2015], Mebane et al. [2018]

$$F_{LW,21} = 7.22\, \frac{(1+z)^3}{H(z)}\, e^{-\tau_{LW}} \left(N^{\rm II}_{\rm LW}\dot{\rho}^{\rm II}_{\rm SFR} + N^{\rm III}_{\rm LW}\dot{\rho}^{\rm III}_{\rm SFR}\right), \tag{4.18}$$

where $H(z)$ is the Hubble rate of expansion, and τ_{LW} is the intergalactic opacity for the Lyman-Werner photons which can be $1-2$ in the absence of dissociations Ricotti et al. [2001] and can be larger once the first HII regions have formed Johnson et al. [2007]. We use $\exp\left(-\tau_{LW}\right) = 0.5$, however we note that in the isocurvature model the value of τ_{LW} might increase due to more small scale structure obscuring the Lyman-Werner background.

The number of Lyman-Werner photons produced per baryon in stars is taken to be $N^{\rm II}_{\rm LW} = 9,690$ for Pop-II stars, and $N^{\rm III}_{\rm LW} = 100,000$ for Pop-III stars Mebane et al. [2018]. The value of $\dot{\rho}_{\rm SFR}$ is modelled through Eqns. (4.15) and (4.16), such that $\dot{\rho}_{\rm SFR} = f_\star d\left(f_{\rm coll}\right)/dt$. We use an iterative process to determine the value of $\dot{\rho}^{\rm III}_{\rm SFR}$ that satisfies Eqns. (4.16), (4.17) and (4.18).

We also multiply Eqn. (4.16) by $(1 - x_i)$ to account for the photo-heating. This term only becomes important towards the end of reionization at lower redshifts, but prevents the Pop-III photo-ionization term from resulting in overly large optical depth contribution in the range of $10 - 15$. The functional form of the above model is an approximate way to characterize the self-regulation of the Pop-III stellar population in the early Universe. Simpler models regulated by the average ionized fraction (e.g. Miranda et al. [2017]) give very similar results. We would also comment that relations in Visbal et al. [2015], Mebane et al. [2018] that we use to derive Eqns. (4.17) and (4.18) were empirically determined from CDM simulations. An approach based

on simulations is most likely required to model the details of the Pop-III star formation history in the presence of the isocurvature fluctuations.

However not including any self-regularization leads to larger ionized fractions earlier in its evolution, which violate the observational constraints shown in Fig. 4.5, as well as the integrated optical depth from Planck (see below). Thus some form of self-regularization is important to implement, but the exact details of the model do not change the quantitative picture that including the isocurvature fluctuations leads to a slower decrease of the ionized fraction at higher redshifts, compared to just Pop-III star formation, which is illustrated in Fig. 4.5.

Fig. 4.5 shows how the ionized fraction evolves in the redshift range probed by the measurements. Current observations from a variety of sources are plotted on Fig. 4.5: Lyα dark pixels (McGreer et al. [2015] in grey), Lyα emitters (Mason et al. [2018], Hoag et al. [2019], Mason et al. [2019] in brown), and QSO damping wings (Greig et al. [2017, 2019], Davies et al. [2018] in green). The fiducial model (black solid line), uses only Pop-II photo-ionization rates, with $f_{\rm esc} = 0.2$ and no isocurvature fluctuations ($f_{\rm iso} = 0$). The effect of including axion isocurvature fluctuations (red lines) exhibits a distinctly longer tail of reionization, where the ionized fraction starts to increase much earlier and at a steadier rate than for the no iosocurvature case. At lower redshift, where the ionized fraction can be currently estimated, the effect of the isocurvature fluctuations is slightly degenerate with the escape fraction of Pop-II stars (red dashed line).

On the other hand, the effect of Pop-III stars is prominent at higher redshifts (green dot-dashed line), and in tandem with the isocurvature fluctuations (dot-dashed red line) can create a boost to the ionized fraction such that it evolves much slower between redshifts of 25 and 10, potentially creating a strong observable signal of the isocurvature modes in the future observations. However, enhancing the star formation efficiency for Pop-III stars to 0.005 as used in Visbal et al. [2018] increases the ionized fraction evolution even without isocurvature fluctuations (green dashed line in Fig. 4.5), making it not obvious that the astrophysics of star formation can be robustly disentangled from $f_{\rm iso}$. Nevertheless, at high enough redshift all our isocurvatore models cross the green-dashed line in Fig. 4.5 that corresponds to this extreme case of Pop-III stellar efficiency. This is the unique signal of the isocurvatore models in the ionization history, resulting from the nearly redshift-independent

collapse fraction in such models.

Future observations by ground based surveys (e.g. UKIDSS Lawrence et al. [2007]; VIKING Edge et al. [2013]; VHS McMahon et al. [2013]; UHS Dye et al. [2018]) and wide-field surveys (e.g. Euclid, WFIRST, WEAVE, J-PAS) in combination with high signal-to-noise spectra from JWST would be more sensitive to the differences between the models. In particular measuring the ionized fraction during the cosmic dawn epoch ($z > 15$) can lead to stronger constraints on the isocurvature fluctuations.

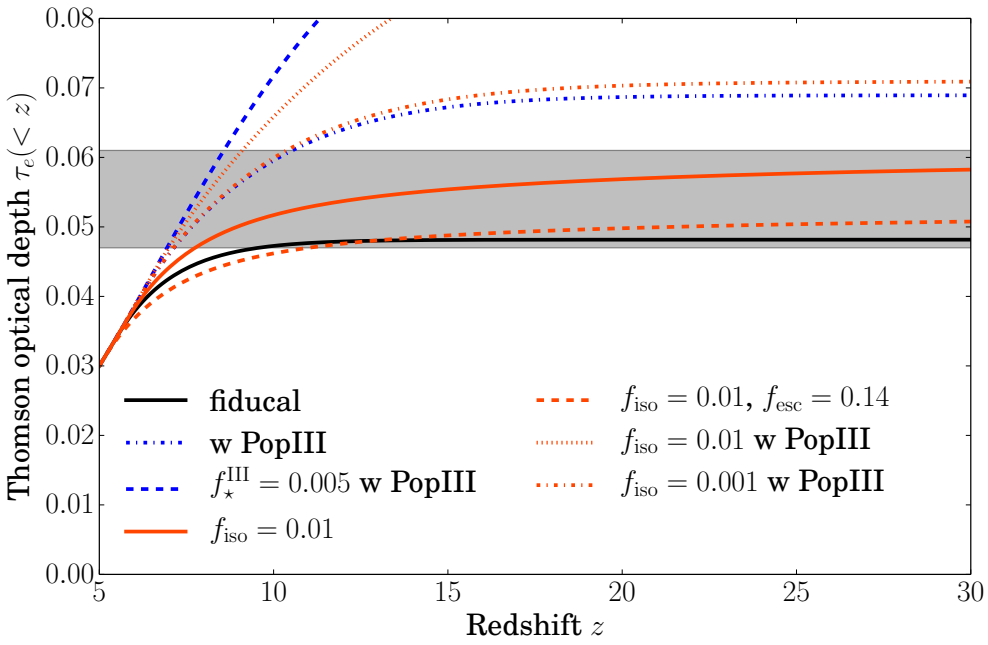

Figure 4.6: Thomson optical depth to recombination, τ_e. The grey band shows the Planck 2018 constraints on τ_e. The models plotted are the same as in Fig. 4.5, with the black solid line respresenting the fiducial case using the stellar efficiency described in Sec. 4.4 and $f_{\rm iso} = 0$, while the orange lines show the contribution for varying $f_{\rm iso}$. The models that are clearly discrepant by the current CMB constraints have either (1) Pop-III photo-ionization and $f_{\rm iso} = 0.01$ or (2) high Pop-III star formation efficiency and no isocurvature fluctuations (blue dashed).

Another possibility of constraining the reionization process is utilizing the measurements of the CMB anisotropy, in particular the effect of the CMB Thomson scattering off of free electrons. Since the redshift where this would occur ($z < 20$) are relatively closer than the surface of last scattering, this physical process affects predominantly large scales of the CMB fluctations. The CMB constraints from the Planck satellite on the τ_e are very strong Aghanim et al. [2020], as is show by the grey band in Fig. 4.6. The axion isocurvature model has a different signal in the Thomson scattering optical depth, which primarily reflects the prolonged redshift evolution of the reionization process seen in Fig. 4.5. However, we note that that reionization affects on the CMB are not just as a single number, τ_e, as an earlier tail ionization creates polarization anisotropies at smaller scales Hu and Holder [2003], Heinrich et al. [2017]. An extended reionization is constrained by the Planck satellite to be $\tau_e(15, 30) < 0.007$, where this notation indicates the optical depth contributed between $z = 15$ and $z = 30$ Aghanim et al. [2020]. (The Planck limits on the tail of reionization vary only slightly with the assumed priors, and can lower the bound to $\tau(15, 30) < 0.006$ if flat priors are chosen on the positions of the knots on which τ is interpolated.)

The limits on the tail of reionization are most constraining for models with an earlier star formation, in particular if the contribution of Pop-III stars is included. Of the models plotted in Fig. 4.6 the models with $f_{\rm iso} = 0.01$ and including Pop-III star formation is clearly excluded, with $\tau_e(15, 30) = 0.018$ (dotted red line) as shown in Fig. 4.7. On the other hand, with the typical Pop-III star formation rate, the current data is not excluding a lower value of $f_{\rm iso} = 0.001$, suggesting that lower $f_{\rm iso}$ values are more degenerate with astrophysical uncertainties of early star formation. Along this lines, increasing the star formation efficiency of Pop-III stars to $f_{\rm star}^{\rm III} = 0.005$ (0.05)[8] leads to $\tau_e(15, 30) = 0.007$ (0.017) for $f_{\rm iso} = 0$. While tangential to the focus of this paper, this interestingly suggests that Planck is already constraining Pop-III star efficiencies in some of the range typically used. The limits on the tail of reionization are most constraining for models with an earlier star formation, in particular if the contribution of Pop-III stars is included. Apart from the stellar efficiency, changing the escape fraction of photons from Pop-II stellar

[8]This is the efficiency one expects from assuming that each 10^5 $M_\odot$ halo hosts one (ten) 100 $M_\odot$ stars, and it further takes the efficiency to scale with halo mass.

population ($\tau_e(15,30) = 0.002$ - dashed red line) can also lower the predicted optical depth, making isocurvature models similar to the fiducial adiabatic dark matter model (solid black line). This effect can also lower the optical depth in Pop-III models that have slightly higher τ_e compared to the CMB data (green and red dot-dashed lines).

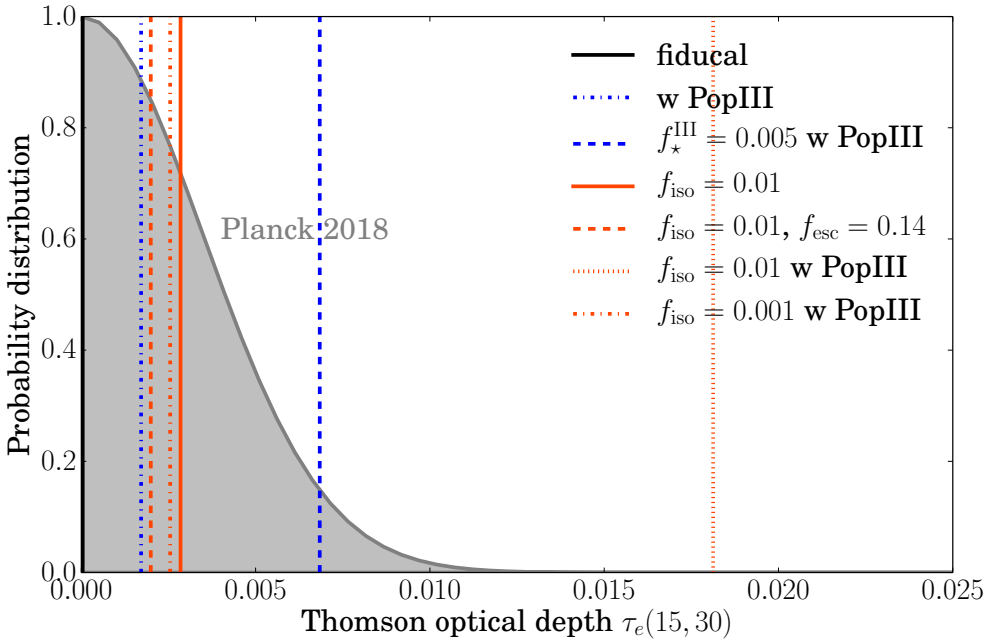

Figure 4.7: Thomson optical depth contributed in redshift interval $15 < z < 30$, $\tau_e(15,30)$, in both models and observations. The grey posterior shows the Gaussian that yields the Planck 2018 2σ upper bound of $\tau_e(15,30) < 0.007$. The vertical lines show $\tau_e(15,30)$ values for the same models that are plotted in Fig. 4.6: the fiducial case using the stellar efficiency described in Sec. 4.4 and $f_{\rm iso} = 0$ (black solid line), adding Pop-III photo-ionization rates (blue dot-dashed), and varying $f_{\rm iso}$ (orange lines with differing linestyles). Including even small Pop-III star formation efficiencies can result in detectable $\tau_e(15,30)$ for $f_{\rm iso} = 0.01$.

The enhanced contribution to τ_e from the isocurvature fluctuations can be mimicked by astrophysical uncertainties: Similar effects can be observed by keeping $f_{\rm iso} = 0.01$ fixed, but switching

off the Pop-III star formation (solid red line); or switching off isocurvature contribution, but adding Pop-III photo-ionization with the stellar efficiency of $f_\star^{\rm III} = 5 \times 10^{-4}$ (green dot-dashed line). However, differences may show up in the tail of the reionization, where the aforementioned two models differ by a factor of ≈ 2 in $\tau_e(15, 30)$. In particular, further increasing Pop-III stellar efficiency by another order of magnitude to $f_\star^{\rm III} = 0.05$ results in too much ionization at early times – $\tau_e(15, 30) = 0.018$ – which is ruled out by Planck CMB constraints. Such a high $\tau_e(15, 30)$ is similar to that for the case with low Pop-III stellar efficiency and non-zero $f_{\rm iso}$ (see red dot-dashed line in Fig. 4.7). However, the contribution to the ionization fraction comes from $z < 20$ in the case of high Pop-III stellar efficiency, while the signal in isocurvature models is dominated by the contribution at $z > 20$.

On the other hand, further increasing the amount of isocurvature power by a factor of 5 ionizes the Universe to 10% early on ($z \sim 29(46)$ for $f_{\rm iso} = 0.05(0.1)$), leading to large values of $\tau_e(15, 30) \sim 0.04(0.09)$. Such models are clearly ruled out by the current CMB data, despite the astrophysical uncertainties. At a high enough level of $f_{\rm iso}$ the statement that such models are excluded by the CMB holds over the range of Pop-III efficiencies considered. In our models this transition happens in the range of $f_{\rm iso} = 0.01 - 0.1$.

Neglecting Pop-III contribution also lowers the effect of isocurvature modes. This occurs because the minimal mass ($M_{\rm min}$) that contributes to the Pop-II photo-ionization rates (Eqn. 4.15) is typically $\sim 10^8$ M$_\odot$, requiring a large $f_{\rm iso}$ to have an appreciable effect on these mass scales (see Fig. 4.2). On the other hand the minimal mass for Pop-III photo-ionization rates ($M_{\rm min}^{\rm III}$) is generally two orders of magnitude lower than for Pop-II stars ($\sim 10^6$ M$_\odot$), and thus more sensitive to smaller values of $f_{\rm iso}$.

Since some contribution from the Pop-III star formation is expected, values of $f_{\rm iso}$ of the order of 10^{-2} are excluded with the current measurements already, which corresponds to ALP mass limit of $m_a > 10^{-18}$ eV. Current and future CMB observations (e.g. CLASS, LiteBIRD) aim to put more stringent constraints on τ_e approaching the cosmic variance limit of $\sigma_\tau = 0.002$ Di Valentino et al. [2018], Watts et al. [2019]. The sensitivity of measurements of the tail of reionization via statistics like $\tau_e(15, 30)$ likely can be improved even more significantly over Planck with future missions

than this improvement in σ_τ Watts et al. [2019], although we expect measuring even higher redshift contributions like $\tau_e(25, 40)$ would be needed to be able to disentangle astrophysics and improve constraints on $f_{\rm iso}$.

Finally, we note that early ionization (which is likely also associated with X-ray and ultraviolet backgrounds) would shape the high-redshift 21cm emission signal Furlanetto et al. [2006]. The 21cm signal is potentially sensitive to much lower star formation rate densities via these emissions than the ionizing emissions this section has focused on McQuinn and O'Leary [2012]. The next section discusses another effect that may be even more constraining for this signal.

4.6 *CMB recombination and the dark ages thermal history*

As illustrated in Fig 4.3, the presence of white noise isocurvature fluctuations leads to the formation of dark matter halos much earlier than in the standard scenario. These early dark matter halos are moving supersonically relative to the gas, with an RMS Mach number of ≈ 2 and with a Maxwellian distribution Tseliakhovich and Hirata [2010]. Some regions can even be moving hypersonically at $z \gtrsim 500$ (i.e. with relative velocities of $\gtrsim$ 10km s^{-1} so that the shocks can ionize the gas). Furthermore, a $10^4 M_\odot$ dark matter halo will lose its velocity relative to the dark matter within a Hubble time O'Leary and McQuinn [2012], potentially ionizing and heating the gas in the Universe if enough of these halos are present.

We first investigate the effect of shock ionization on the cosmic microwave background from such hypersonic motion. Even percent level differences in the global $z \sim 500$ recombination history that result from this ionization could have a detectable effect on the cosmic microwave background Slatyer et al. [2009]. However, while we found that the shocks in a large fraction of the Universe at $z > 500$ would often heat the gas sufficiently for it to start to collisionally ionize, ionization would quickly sap out the thermal energy of the gas, leaving it at insufficient temperatures to collisionally ionize further. We found that because of this cost to ionization, even the strongest shocks would only ionize the gas to $\sim 1\%$. This small ionization, coupled with the fact that (for viable $f_{\rm iso}$) only a fraction of dark matter has collapsed into the $M_h \gtrsim 10^3 M_\odot$ at $z \gtrsim 500$ halos that generate significant shocks, results in the recombination history being negligibly affected.

We next turn to the heating imparted by such shocks. If the heating occurs early enough, it could also affect the recombination history, as the recombination rate depends inversely on the temperature. Our calculations suggest that such heating does not occur at early enough times to be relevant for Recombination. Another observable is the cosmological 21cm signal. When the 21cm signal is in absorption as is anticipated $15 \lesssim z \lesssim 30$, its amplitude is inversely proportional to the gas temperature Furlanetto et al. [2006]. We show below that this shock heating could be important for this 21cm signal.

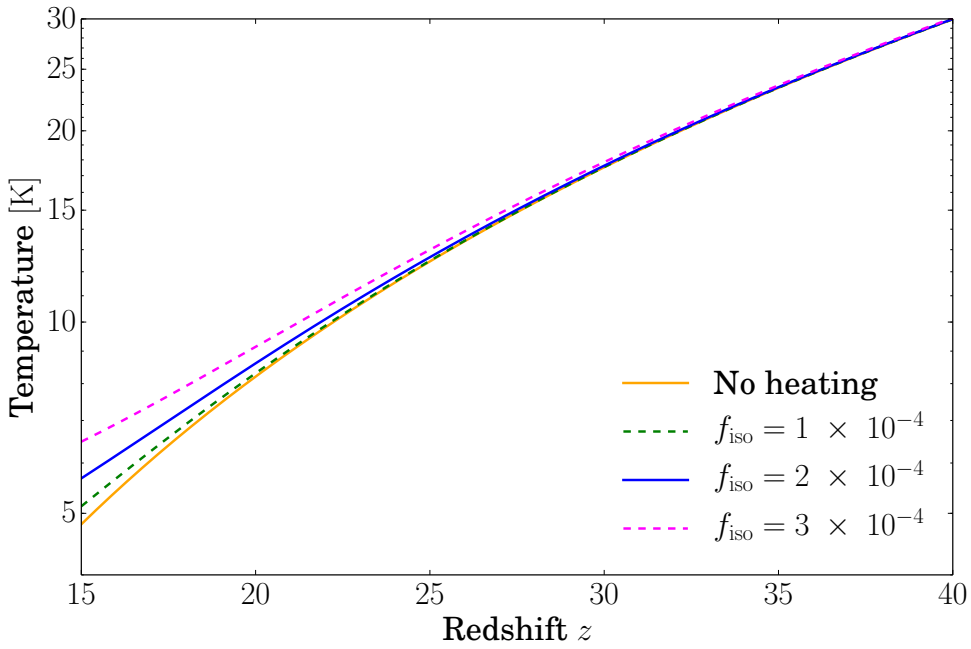

Figure 4.8: Rough estimates for the evolution of gas temperature at different $f_{\rm iso}$, with larger $f_{\rm iso}$ leading to more shock heating. Our estimates suggest that $f_{\rm iso} \sim 10^{-4}$ lead to percent-level or greater shock heating. Percent level heating would manifest in a qualitatively different high-redshift 21cm signal, with significant BAO peaks.

A simple estimate for the amount of shocking uses that we know how much energy is dissipated into the gas via dynamical friction, a frictional force from the gas that acts to decelerate the

supersonicly streaming dark matter halos. Namely, halos more massive than $\sim 10^5 - 10^6 M_\odot$ should lose all of their relative velocity to the baryons in a Hubble time at $z \sim 20$ McQuinn and O'Leary [2012]. Some of this dynamical energy should go into shocks (and if all of the energy goes into shocks we would expect to heat the Universe by $\langle \mathcal{M}^2 \rangle \sim 4$). We estimate the effect of shock heating on the thermal history by solving

$$\begin{aligned} \frac{dT}{dt} &= \overbrace{-2HT}^{\text{adiabatic}} + \overbrace{\frac{8\pi^2 x_i T_\gamma^4 \sigma_T (T_\gamma - T)}{45 m_e (1+x_i)}}^{\text{Compton}} \\ &- \underbrace{\frac{\mu m_p}{3 M_P^4} \langle \zeta_s (v_{\text{b-dm}}) v_{\text{b-dm}}^{-1} \rangle \int_{M_{\min}}^{M_{\max}} dM_h M_h^2 \frac{dn}{dM_h}}_{\text{shock heating}}, \end{aligned} \tag{4.19}$$

where σ_T is the Thomson cross section, m_p is the mass of hydrogen atom, $v_{\text{b-dm}}$ is the velocity difference between dark matter and baryons, M_h is the halo mass and ρ_{dm} is the density of dark matter. The Compton cooling term owes to the scattering of CMB photons, which is negligible below redshift $z = 200$. The "shock heating" term in Eqn. 4.19 follows from the power generated from dynamical friction; taking the expression in Ostriker [1999] but dropping the factor of the Coulomb logarithm. The motivation for dropping this logarithm is that the resulting expression accounts only for gas that intersects within the Bondi-Hoyle radius for accretion ($r_{\text{BH}} = 2GM/v_{\text{b-dm}}^2$; Bondi and Hoyle [1944] and see this endnote [9]), which is the gas whose trajectory would be deflected to the origin (in the absence of pressure) and hence is most likely to shock. We conservatively assume the shock heating has efficiency ζ_s at thermalizing its energy, and we take $\zeta_s = 0.1$ motivated by entropy increase calculated in planar shocks with Mach numbers of $\mathcal{M} = 2$. Finally, $M_{\max}$ is set to the halo mass whose timescale to lose its energy by dynamical friction in much less than the age of the Universe, as once a halo reaches this mass, it will likely have decelerated and no longer contribute to the heating. We take $10^6 M_\odot$ as the maximum mass. The minimum mass is set by where the halo viral radius equals r_{BH}, which we find is $M \approx 10^4 M_\odot$. It is worth stressing that the shock heating effect is most sensitive to the maximum mass. If we make the maximum

[9] Our expression for the heating power from each halo is equal to the cross section for Bondi-Hoyle accretion times the kinetic energy density of the accreted gas times the velocity offset.

mass a factor of 10 smaller ($10^5 M_\odot$), the temperature difference will be about three times smaller in Fig. 4.8, which we think reflects the level of uncertainty.

Our simple estimates show that the shock heating effects from axion halos starts to become significant around redshift $z = 20$ as shown in Fig. 4.8 for $f_{\rm iso} \gtrsim 10^{-4}$. Models predict a global 21cm absorption feature at $\sim$ 80MHz, corresponding to absorption at $z \sim 15 - 20$ Furlanetto et al. [2006], the same signal purported to be detected by EDGES Bowman et al. [2018]. This absorption dip is inversely proportional to the gas temperature. Thus, a detection of the full amplitude of this dip should at a minimum be used to discern shock heating at the $O(1)$ level, requiring for us $f_{\rm iso} \sim 5 \times 10^{-4}$. Such heating would be hard to disentangle from X-ray heating from the first supernovae and black holes Furlanetto et al. [2006]. However, efforts to detect fluctuations in the 21cm have a potentially smoking gun signal for this heating. Since change in temperature is tied to the relative velocity between the baryons and the dark matter ($v_{\rm b\text{-}dm}$), and this relative velocity is modulated by the acoustic physics in the early Universe, any heating could result in large acoustic oscillations in the signal. McQuinn and O'Leary [2012] showed that even just $\sim$ 3% changes in the temperature that are tied to $v_{\rm b\text{-}dm}$ would lead to order-unity acoustic features in the 21cm signal at $k \sim 0.1{\rm Mpc}^{-1}$ McQuinn and O'Leary [2012], qualitatively changing the 21cm signal. Our estimates in Fig. 4.8 suggests that heating at the few percent level occurs for $f_{\rm iso} \gtrsim 10^{-4}$, although we illustrate the rough constraint in Fig 4.1 at $f_{\rm iso} = 3 \times 10^{-4}$. These acoustic features are quite distinct from the smoother continuum of fluctuations from the extra star formation would create, which were referenced as a potential observable in § 4.5.

4.7 *Conclusions*

One possible candidate for the dark matter is that it is an ultra-light scalar field that is generated in the early universe in a similar manner to that for the QCD axion, making it an 'axion like particle' (ALP). Most previous studies have concentrated on how the ultralight ALP's quantum pressure suppresses the small-scale growth of the adiabatic fluctuations from inflation or on how its relaxation can lead to solitonic cores Schive et al. [2014], Veltmaat et al. [2018], Mocz et al. [2019]. However, if the symmetry breaking that establishes the axion-like particle (ALP) occurs

after inflation ends, this leads to white isocurvature fluctuations in the ALP energy density. The parameter space where the post inflationary scenario can occur are for symmetry breaking scales of $10^{13} - 10^{16}$GeV for the particle mass ranges that are probed by the large scale structure observables considered here ($m_A \sim 10^{-13} - 10^{-20}$eV). The higher values for the symmetry breaking scale (and lower values for the mass) push against limits from searches for inflationary B-modes. This paper focused on how these isocurvature fluctuations could influence various observations of early structure formation.

Fig. 4.1 summarizes our resulting constraints on the ALP mass m_a and isocurvature fluctuation amplitude $f_{\rm iso}$ – defined in the traditional manner as their ratio with adiabatic fluctuations at a wavenumber of $0.05{\rm Mpc}^{-1}$ (but we also report constraints in terms of the more natural nonlinear wavenumber $k_{\rm nl}$). The solid lines show the relation between the axion mass and $f_{\rm iso}$. Different colours represent different parameterizations of the evolution of the axion mass with temperature after it commences oscillations. The simplest model, and also most conservative in terms of mass constraints, is the $n = 0$ case where the mass was set at early times. For an ALP coupled to an asymptotically free sector (in analogy to the QCD axion), leading to a mass that increases in size until the cosmic temperature falls below the sector's confinement scale, the value of n is nonzero (with $n = 4$ approximating the evolution of the QCD axion). As n increases above 4, the sensitivity of our results to n becomes weak.

The cosmological observables presented in this paper are sensitive to different axion masses m_A or equivalently different levels of $f_{\rm iso}$, with the smaller scale the observable is sensitive to the stronger the constraint. Our strongest present constraint comes from the Lyα forest power spectrum measurements at high redshifts (orange dashed line). The lower bound on the ALP mass from the Lyα forest is $m_A > 2 \times 10^{-17}$ eV for $n = 0$ (and $m_A > 10^{-13}$ eV for $n = 4$). Apart from being currently most constraining bound, the Lyα analysis is also the least affected by uncertainties in the astrophysics of the existing probes we investigated.

Another potential probe is high-redshift galaxy observations. We find that only for m_A already ruled out by the Lyα forest is the observed luminosity function qualitatively changed in a manner that could potentially be disentangled from more mundane astrophysical explanations. However,

smaller mass (and higher redshift) galaxies than can be observed directly are more substantially boosted by isocurvature fluctuations. Such diminutive galaxies may be observable via their effect on the ionized fraction evolution during the Reionization Epoch. We find that a particularly interesting observable is the CMB, which is sensitive to the high-redshift tail of reionization. This tail can be substantially more extended in models with white isocurvature fluctuations. While we find that the ionization fraction in models where galaxies form via the traditional route (in halos massive enough that the gas can cool atomically) only show qualitatively different trends for m_A already ruled out by the forest, models that include Pop-III stars (even for much lower efficiencies for their formation than is commonly assumed) could lead to a small residual ionization to extremely high redshifts. Thus, future CMB efforts could potentially probe m_A range similar to that of the Lyα forest.

Finally, the shock-heating of the gas due to supersonically moving axion minihalos during the Cosmic Dark Ages and Cosmic Dawn could lead to even stronger constraints, potentially excluding ALP masses of $m_A < 10^{-16}$ eV for $n = 0$. This shocking would suppress the depth of the absorption trough in the global 21cm signal (as probed by e.g EDGES and PRIZM). The caveat is that X-ray heating could have a similar effect Barkana [2018], Fialkov and Barkana [2019]. However, even percent-level changes in the mean temperature from shock-heating will manifest in distinct baryon acoustic oscillation features in the 21cm brightness temperature fluctuations that trace the relative baryon-dark matter velocity field. These oscillations are potentially a smoking gun of shock heating from a dramatic enhancement in the number of minihalos.

Some low redshift small-scale structure probes could complement the probes discussed here. First, local observations of Milky Way tidal streams could lead to detection of small sub halos in the mass range $10^8 - 10^5$ $M_\odot$ Bovy et al. [2017], Bonaca et al. [2019], with some uncertainty in whether the lowest values of 10^5 $M_\odot$ can be disentangled from astrophysical uncertainties, as encounters with these subhalos open up gaps in these streams. This places the sensitivity of the galactic streams somewhere in the range of isocurvature amplitudes of $f_{\rm iso} = 0.001 - 0.01$, potentially pushing the constraints lower than the current Lyα bound and comparable to our most optimistic reionization constraints.

In addition, Dai and Miralda-Escudé [2020] recently showed that the micro-lensing caustics of

stars on a cluster macro-lens could even be sensitive to the minute value of $M_{H(m_A)}$ for the QCD axion of $\sim 10^{-12} M_\odot$, where $M_{H(m_A)}$ is the mass within the Horizon at $T_{\rm osc}$. In particular, these micro-lensing caustics are perturbed by these axion structures, deviating from the smooth profile otherwise expected. This constraint can also be translated to our scenario. Dai and Miralda-Escudé [2020] showed this method is sensitive to $10^{-13} < M_{H(m_A)} < 10^{-6}$ $M_\odot$, which translates to the bounds on the ALP mass of $10^{-15} < m_A < 10^{-11}$ eV for $n = 0$ ($10^{-11} - 10^{-6}$ eV for $n = 4$). Since the sensitivity falls off on both sides of the ALP mass range, this makes the microlensing of stars complementary to the signatures of early structure formation considered in this paper. Future observations with HST or JWST should be able to push forward this exciting science Chen et al. [2019], Kaurov et al. [2019].

Lastly, a post-inflation ALP may affect the properties of black holes. Studies of black hole superradiance Arvanitaki et al. [2015], Baryakhtar et al. [2017], Stott and Marsh [2018], Davoudiasl and Denton [2019] – the gravitaional production of a ALP halo from the free energy in black hole spin – have excluded the existence of ALPs with $10^{-14} < m_A < 10^{-11}$ eV from measurements of finite stellar black hole spins. The measurements of super massive black hole spin can potentially exclude a wide mass range $m_A < 10^{-16}$ eV Stott and Marsh [2018], but inferring the black hole masses over a broad mass range. The bounds from superradiance are also only valid in the limit of $f_A > 10^{14}$ GeV and no self-interaction Stott and Marsh [2018]. Furthermore, the earlier structure formation sourced by a post-inflation ALP could potentially produce the seeds that grow into the highest mass black holes, ameliorating somewhat the difficulty in having sufficient time for these seeds to grow into the highest redshift quasars (e.g. Latif and Ferrara [2016]).

Chapter 5

DISRUPTION OF DARK MATTER MINIHALOES IN THE MILKY WAY ENVIRONMENT

5.1 *Introduction*

The gravitational clustering of dark matter has been well measured on galactic scales and super-galactic scales, and is consistent with a nearly scale-invariant spectrum of primordial fluctuations [e.g. Aghanim et al., 2020]. However, the matter power spectrum on extremely small scales ($k \gtrsim \mathrm{pc}^{-1}$), which corresponds to sub-planetary-mass structures, is still weakly constrained, and is sensitive to both the nature of dark matter and the thermal history of the early Universe. There have been proposals to detect small scale structures in the mass range $\sim 10^{-13} - 10^{2}\,\mathrm{M}_{\odot}$ in the future with Pulsar Timing Arrays [PTAs; e.g. Siegel et al., 2007, Baghram et al., 2011, Dror et al., 2019, Ramani et al., 2020, Lee et al., 2020, 2021] and Femto/Micro-lensing [e.g., Kolb and Tkachev, 1996, Fairbairn et al., 2018, Katz et al., 2018].

Many well-motivated dark matter theories can leave unique fingerprints on the primordial perturbations on small scales [1] ($k \gtrsim \mathrm{pc}^{-1}$), such as quantum chromodynamics (QCD) axion/axion-like particles (ALPs) with the Peccei-Quinn (PQ) symmetry breaking [Peccei and Quinn, 1977] after inflation [e.g., Hogan and Rees, 1988, Kolb and Tkachev, 1993, 1994, Zurek et al., 2007], Early Matter Domination [EMD; e.g., Erickcek and Sigurdson, 2011, Fan et al., 2014] and vector dark matter produced during inflation [e.g. Nelson and Scholtz, 2011, Graham et al., 2016]. Therefore, the search and constraints for small dark matter substructures would provide unique insights to the microphysics of dark matter. The model space of interest here is quite different from that in more common WIMP-like collisionless cold dark matter (CDM) models. In those models, adiabatic

[1] We note that the "small scale" here is fundamentally different from the small-scale problem of CDM (at kpc scale) discussed in astrophysical studies [see review by Bullock and Boylan-Kolchin, 2017].

fluctuations produced at the end of inflation can also seed small CDM subhaloes down to the kinetic decoupling and free-streaming limit ($k \sim O(\mathrm{pc}^{-1})$), roughly corresponding to the Earth mass [$\sim 10^{-6}\,\mathrm{M}_{\odot}$; e.g., Hofmann et al., 2001, Berezinsky et al., 2003, Green et al., 2005, Loeb and Zaldarriaga, 2005]. The evolution of these subhaloes in the Milky Way environment has been studied in the past [e.g., Angus and Zhao, 2007, Goerdt et al., 2007, Green and Goodwin, 2007, Zhao et al., 2007, Schneider et al., 2010, Berezinsky et al., 2014, Delos, 2019, Facchinetti et al., 2022]. However, the WIMP-like CDM formed the first non-linear structures at relatively late times (e.g. $z \sim 60 \ll z_{\mathrm{eq}}$ as shown in Green et al. 2005), and the minihaloes formed are subject to significant disruption due to tidal stripping and disk shocking after falling into their host haloes [e.g., Ostriker et al., 1972, Gnedin et al., 1999, Goerdt et al., 2007, Zhao et al., 2007, Schneider et al., 2010]. The typical minihaloes of WIMP-like CDM are out of reach for PTAs and other observations we discuss here [e.g., Lee et al., 2020].

On the other hand, dark matter minihaloes in the theories we consider here formed in very early Universe and therefore are much denser than WIMP-like CDM subhaloes and are less likely to be disrupted by tidal forces. For instance, a (pseudo)scalar field (*e.g.* the QCD axion) with PQ symmetry breaking after inflation [e.g., Hogan and Rees, 1988, Zurek et al., 2007, hereafter called the "post-inflationary axion"] can induce order-unity isocurvature fluctuations on the horizon scale during the symmetry breaking. Regions with order-unity overdensities tend to collapse gravitationally very soon, even prior to average matter-radiation equality ($z_{\mathrm{eq}} \sim 3000$), into small axion miniclusters (AMCs). The miniclusters went through subsequent hierarchical clustering the large scale adiabatic perturbations intervene. As another example, EMD models can introduce a non-standard thermal history that is not constrained by any current data, but adiabatic fluctuations within the horizon can grow during this early period of matter domination. The characteristic mass of dark matter minihaloes formed in early matter domination models is determined by the reheating temperature of this period. In vector dark matter models, the longitudinal modes of the vector DM produced at the end of inflation give rise to a peak in the matter power spectrum on small scales, with the scale directly determined by the dark matter particle mass [Graham et al., 2016, Lee et al., 2020]. Those models have interesting dynamics in the early Universe, which are difficult to directly

probe. However, the remnants of those early Universe dynamics, dark matter minihaloes, may be detectable in local observations [e.g., Dror et al., 2019, Ramani et al., 2020, Lee et al., 2020].

While the evolution of (some versions of) these dark matter minihaloes in the non-linear regime have been studied both semi-analytically with the Press-Schechter model [Zurek et al., 2007, Fairbairn et al., 2018, Enander et al., 2017, Blinov et al., 2020, Lee et al., 2020, Blinov et al., 2021] and numerically with N-body simulations [Zurek et al., 2007, Buschmann et al., 2020, Eggemeier et al., 2019, Xiao et al., 2021], the gravitational interactions between dark matter minihaloes and large scale dark matter structures or baryonic structures are not well studied, due to the large dynamic range and non-linear behaviors involved. Dark matter minihaloes formed from nonstandard early universe physics can be as light as $\sim 10^{-12}\,M_\odot$, while the Milky Way has a halo mass of $\sim 10^{12}\,M_\odot$. Therefore it is challenging to resolve these small structures while simultaneously simulating the dynamics of the largest structures. However, it is critical to study the survival probability of minihaloes in the Milky Way and to determine the prospects of detecting such structures in the local environment.

Recently, [Kavanagh et al., 2020] made a preliminary analytic estimate of the effects of stellar disruption on minihaloes, and argued that $\sim 46\%$ of dark matter minihaloes akin to AMCs could survive in the Solar neighborhood after stellar disruptions. But this neglects many nonlinear effects, a realistic minihalo concentration distribution and some other channels for disruption. In this paper, we improve on these estimates by detailed numerical simulations and semi-analytic treatment to combine all of the expected dominant disruption terms. To deal with the enormous dynamic range involved, our strategy is to numerically simulate the dynamics of the dark matter minihaloes in individual encounters (varying *e.g.* halo parameters and impact parameters), using these to build detailed semi-analytic models which can be used to treat the large-scale behavior. This allows us to capture the key nonlinear physics on small scales while making realistic predictions for the overall behavior of dark matter minihaloes in the Milky Way galaxy (in ways that can be generalized, in principle, to a broad class of minihalo-like models). Broadly speaking, the disruption of dark matter minihaloes in the Milky Way can be divided into two parts: stellar disruption and tidal disruption. The stellar disruption term is sensitive to close encounters with individual stars, while the tidal term

only depends on the gradient of the collective gravitational potential on large scales. We study each of these separately using our N-body simulations, and then combine them nonlinearly to show that they have non-trivial mutual effects.

This paper is organized as follows. In Section 5.2 we discuss the analytic model for the minihalo mass function, stellar disruptions due to individual stellar encounters and tidal disruptions. In Section 5.3, we present our numerical results from a series of idealized N-body simulations for isolated minihaloes encountering a star, and simulations of tidal stripping. In Section 5.4, we apply the results of our idealized simulations to a realistic Milky Way environment and combine both stellar disruption and tidal disruption. In Section 5.5, we study the survival fraction of dark matter minihaloes by applying the results to different physical models.

We assume a ΛCDM cosmology with parameters given as h=0.697, $\Omega_{\rm m} = 0.2814$, and $\Omega_\Lambda = 0.7186$, and adopt scalar spectral index $n_s = 0.9667$. These are consistent with the recent Planck results [Aghanim et al., 2020], and our conclusions are relatively insensitive to variations in these parameters (compared to the much larger uncertainties in e.g. minihalo properties from different physical models).

5.2 *Analytic model*

5.2.1 Initial mass functions and concentrations of small-scale structures

To be specific, two of the models discussed in the introduction that lead to the formation of dense minihaloes in the early Universe are: (pseudo)scalars (*e.g.* the QCD axion) with symmetry breaking after inflation [Hogan and Rees, 1988, Zurek et al., 2007] and the EMD model as studied in [Erickcek and Sigurdson, 2011]. These two models are physically well-motivated and are also representative of models that can enhance the matter power spectrum at small scales. Although the cosmological perturbations in those models have different origins, they share common features. These perturbations are generated at extremely small scales before matter-radiation equality, forming dark matter substructures as light as $10^{-12}\,{\rm M}_\odot$ ubiquitously, decoupled from the usual adiabatic fluctuations. The model parameters are the axion mass $m_{\rm a}$ for the AMC model and the reheating

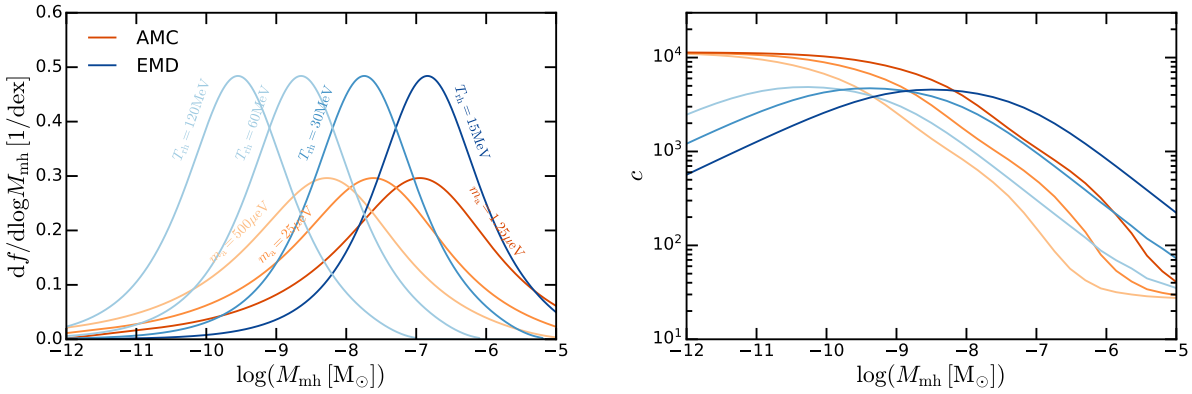

Figure 5.2.1: *Top*: Initial (pre-disruption) mass function of minihaloes in different physics models (f is mass fraction with respect to the total dark matter mass in the Universe). Here we show the mass functions for the AMC models with axion mass $m_{\rm a} = 1.25, 25, 500\,\mu$eV and the EMD models with reheating temperature $T_{\rm rh} = 15, 30, 60$ MeV. The model parameter variations manifest as constant horizontal shifts of the mass function (see Appendix 5.7 for details). The EMD models have sharper peaks than the AMC models. *Bottom*: Mass concentration relation of minihaloes in different models shown in the top panel. The mass-concentration in the AMC model is peaked due to the peaked matter power spectrum. Generically the halo concentration hits a floor at the high mass end as the CDM power spectrum starts to take over. One would not expect minihalos to form before matter-radiation equality, which applies a cap to the concentration at the low mass end.

temperature $T_{\rm rh}$ for the EMD model. We vary the axion mass from 1.25 μeV to 500 μeV which is roughly the mass window that can produce the correct dark matter relic abundance, given uncertainties introduced by the axion emission from strings as shown in Buschmann et al. [2022], Gorghetto et al. [2021]. We choose the fiducial value $m_{\rm a} = 25\mu$eV and $T_{\rm rh} = 30\,$GeV correspondingly such that minihalos in the EMD model will have a similar mass range to those in the AMC model. It is worth noting that the reheating temperature $T_{\rm rh}$ cannot be below a few MeV otherwise the big bang nucleosynthesis will be spoiled (Kawasaki et al. [1999]).

The formation of dense substructures from these small-scale perturbations occurs at early times (see Lee et al. 2020 for an analytic study and Xiao et al. 2021 for simulations of axion miniclusters). After initial formation with a redshift-dependent initial mass function $\mathrm{d}n_0/\mathrm{d}M(z)$, they will then fall onto CDM substructures formed from adiabatic perturbations. The redshift of infall, $z_{\rm c}$, which occurs after the initial minihalo formation, defines the average density of minihaloes since they fall into WIMP-like CDM haloes and stop merging, owing to the high virial velocities in the normal CDM haloes.

The final mass function including minihaloes falling into the CDM structures can be expressed as

$$\frac{\mathrm{d}n_f}{\mathrm{d}M}(z) = \int_{z_{\rm eq}}^{z} \mathrm{d}z_{\rm c} \frac{\mathrm{d}f_{\rm col}^{\rm CDM}(z_{\rm c})}{\mathrm{d}z_{\rm c}} \frac{\mathrm{d}n_0}{\mathrm{d}M}(z_{\rm c}) \tag{5.1}$$

where $f_{\rm col}^{\rm CDM}(z)$ is the collapse fraction of normal CDM haloes formed from adiabatic fluctuations. The probability of infall at $z = z_{\rm c}$ is $\propto \frac{\mathrm{d}f_{\rm col}^{\rm CDM}(z_{\rm c})}{\mathrm{d}z_{\rm c}}$. We can use the Press–Schechter model [Press and Schechter, 1974] to compute the collapse fraction

$$f_{\rm col}^{\rm CDM}(z) = \mathrm{erfc}\left(\frac{\delta_{\rm c}}{\sqrt{2}\sigma_{\rm CDM}(M_{\rm min})D(z)}\right), \tag{5.2}$$

where $D(z)$ is the growth function, $\sigma_{\rm CDM}(M)^2$ is the variance of the adiabatic fluctuations calculated using the Code for Anisotropies in the Microwave Background [2] [CAMB; Lewis et al., 2000, Howlett et al., 2012, Lewis], and $M_{\rm min}$ is the smallest CDM structure we consider formed from adiabatic fluctuations. There might be even smaller CDM haloes that can be formed, which will increase the

[2] CAMB documentation

collapse fraction $f_{\rm col}^{\rm CDM}(z)$, especially at high redshifts. However, below a certain mass the normal CDM haloes may have comparable masses to the enhanced substructures and our assumptions will no longer hold. A detailed study of this infall process will be ultimately needed for more detailed predictions and we leave it for future study (treating the mass function as somewhat uncertain below). We take $M_{\rm min}$ to be $10^{-2}\,{\rm M}_\odot$, corresponding to a scale where the CDM power spectrum dominates while the enhanced small scale perturbations become subdominant. The result is insensitive to $M_{\rm min}$ as $\sigma(M)$ depends logarithmically on M at small scales. This allows us to analytically compute the collapse fraction at various redshifts and obtain the final mass function for the enhanced substructures. This will also give us the distribution of the infall redshift $z_{\rm c}$, $\mathcal{P}(z_{\rm c}) \propto {\rm d}f_{\rm col}^{\rm CDM}(z)/{\rm d}z$, which determines the time where the structural changes of minihaloes halt and thus the average density of minihaloes. Including minihaloes falling into CDM haloes, we obtain the minihalo mass function at $z = 0$ given the initial mass function from different models, as shown in Figure 5.2.1.

Regarding the concentration of minihaloes, we use the model in [Lee et al., 2020] to calculate the concentration from the power spectra of different models. In Figure 5.2.1, we show the initial (pre-disruption) mass functions and the mass-concentration relations of minihaloes in different physics models. Minihalos form earlier tend to have a higher concentration. At the high mass end, CDM power spectrum will dominate and one should reproduce the mass-concentration relation of normal CDM halos. At the low mass end, there is a cap in the concentration since one will not expect minihalo formation before matter-radiation equality. The axion mass for the AMC models or the reheating temperature of the EMD models only creates constant mass shifts in the mass function and the mass-concentration relation. For reference, the typical concentration of WIMP-like CDM haloes studied in [Green and Goodwin, 2007] and [Delos, 2019] are $c \sim 1$ - 20 at the redshift when minihaloes are initialized. They are much more dilute than the minihaloes studied here.

5.2.2 Disruption in late-time evolution

Owing to the ultra-compact structure of the minihaloes, they are largely immune to external perturbations through their evolutionary history after decoupling from the Hubble flow. However,

after falling into a massive host systems like the Milky Way, non-linear gravitational interactions with the host halo and the dense baryonic structures in the host halo can lead to significant disruption of minihaloes. The two leading disruption mechanisms are tidal disruption from the host halo (and baryon disk) and close encounters with stars (referred to as stellar disruption). The relevant spatial and time scales on which these two mechanisms operate are drastically different. In this section, we will review the analytic model developed.

Stellar disruption

First, we consider the consequence of the encounter between a minihalo and a star. The virial radius of minihaloes with a mass of interest ($\sim 10^{-10}\,\mathrm{M}_\odot$) is of the order of 0.01 pc, which is still much larger than the radius of main sequence stars even though we are considering very small structures. Therefore, for simplicity, stars can be treated as point-like objects during encounters. In addition, after a stellar encounter, the structure of the minihalo cannot immediately react to the energy imparted during the encounter. It takes roughly a dynamical time for the minihaloes to relax to the final state after disruption, which is given by

$$\begin{aligned} t_{\rm dyn} &= \sqrt{\frac{3\pi}{16 G \bar{\rho}_{\rm mh}}} \\ &\approx 0.78\,\mathrm{Gyr}\left(\frac{1+z_{\rm c}}{3}\right)^{-3/2}, \end{aligned} \tag{5.3}$$

where $\bar{\rho}_{\rm mh}$ is the average density of the minihalo. The dynamical time $t_{\rm dyn}$ will be comparable to the Hubble time scale for $z_{\rm c} = 0$ but much shorter than that if the minihaloes fall into CDM structures at a high redshift. The duration of the star-minihalo encounter ($\propto b/v_*$), however, is at least five orders of magnitude shorter than $t_{\rm dyn}$. Therefore, the impulse approximation holds and the encounter can be treated as an instantaneous interaction [Spitzer, 1958]. In the distant-tide approximation (when the impact parameter is much larger than the size of the minihalo), the imparted energy from a single encounter with a star can be be expressed as [Spitzer, 1958]

$$\Delta E \approx \frac{4}{3}\frac{G^2 m_*^2 M_{\rm mh}\langle R^2\rangle}{v_*^2 b^4} = \frac{4\alpha^2}{3}\frac{G^2 m_*^2 M_{\rm mh} R_{\rm mh}^2}{v_*^2 b^4}, \tag{5.4}$$

where ΔE is the increase of internal energy of the minihalo, $M_{\rm mh}$ ($R_{\rm mh}$) is the virial mass (radius) of the minihalo, $\langle R^2 \rangle$ represents the mean-squared radius of the minihalo. m_*, b, and v_* are the mass, impact parameter, and relative velocity of the stellar object, respectively. The mean-squared radius of the minihalo can be parameterized as $\langle R^2 \rangle = \alpha^2 R_{\rm mh}^2$, where α is a dimensionless parameter determined by the density profile $\rho(r)$ of the dark matter minihalo

$$\alpha^2 = \frac{\langle R^2 \rangle}{R_{\rm mh}^2} = \frac{1}{M_{\rm mh} R_{\rm mh}^2} \int_0^{R_{\rm mh}} {\rm d}^3\mathbf{r}\, r^2 \rho(r). \tag{5.5}$$

Assuming that the minihalo has the NFW profile [Navarro et al., 1996, Navarro et al., 1997], one obtains

$$\alpha^2(c) = \frac{c(-3 - 3c/2 + c^2/2) + 3(1+c)\ln(1+c)}{c^2(-c + (1+c)\ln(1+c))}, \tag{5.6}$$

where c is the concentration number of dark matter minihaloes.

However, when the impact parameter becomes comparable to the size of the minihalo, the distant-tide approximation made by Equation 5.4 breaks down. The strong b^{-4} dependence of ΔE will disappear once the star passes through the minihalo and the disruption effect is suppressed [e.g., Gerhard and Fall, 1983, Moore, 1993, Carr and Sakellariadou, 1999, Green and Goodwin, 2007]. For a single encounter, [Green and Goodwin, 2007] proposed a more general treatment of the imparted energy calibrated using simulations

$$\Delta E = \begin{cases} \dfrac{4\alpha^2(c)}{3} \dfrac{G^2 m_*^2 M_{\rm mh} R_{\rm mh}^2}{v_*^2} \dfrac{1}{b^4} & (b > b_{\rm s}) \\ \dfrac{4\alpha^2(c)}{3} \dfrac{G^2 m_*^2 M_{\rm mh} R_{\rm mh}^2}{v_*^2} \dfrac{1}{b_{\rm s}^4} & (b \le b_{\rm s}) \end{cases} \tag{5.7}$$

where $b_{\rm s} = f_{\rm b}\,(2\alpha/3\beta)^{1/2} R_{\rm mh}$ is the transition radius, which is close to the physical size of the minihalo up to a factor determined by structure parameters, and $f_{\rm b}$ is an order-unity correction factor we introduce [3] to be determined by our simulations, which will be discussed in Section 5.3.

[3]The original formula proposed in [Green and Goodwin, 2007], who were studying low concentration haloes, does not have the correction term (equivalently $f_{\rm b} = 1$). However, minihaloes with higher concentrations are studied in this work and we find the correction term is necessary empirically to fit the simulation results.

β is another structural parameter defined as

$$\begin{aligned}\beta = \langle r^{-2}\rangle R_{\rm mh}^2 &= \frac{R_{\rm mh}^2 \int_{r_{\rm c}}^{R_{\rm mh}} {\rm d}^3\mathbf{r}\; r^{-2}\,\rho(r)}{M_{\rm mh}} \\ &\simeq \frac{c^2\,\ln\left(r_{\rm s}/r_{\rm c}\right) + c^2/2 - 1/2}{\ln\left(1+c\right) - c/(1+c)},\end{aligned} \tag{5.8}$$

where the NFW profile is assumed and $r_{\rm c}$ is the smallest radius that the profile extends to, which we assume to be $0.01\,r_{\rm s}$. In principle, a boson star can form in the center of a minihalo, which provides a natural physical scale for $r_{\rm c}$. However, the size of an axion star sensitively depends on particle physics parameters as well as the growth rate of axion stars [e.g., Visinelli et al., 2018, Helfer et al., 2017, Chen et al., 2021]. We note that the choice of $r_{\rm c}$ has weak effects since i. it only appears in the logarithm; ii. the uncertainty of $r_{\rm c}$ and β has been effectively captured by the free parameter $f_{\rm b}$; iii. β in fact only matters for close encounters which are rare in reality.

Compared to full analytic calculations under the impulse and distant-tide approximations, Equation 5.7 gives better agreement with simulations in the transitional regime. Roughly speaking, disruption of a minihalo is expected to occur when the increase in internal energy of the minihalo given by Equation 5.4 exceeds the binding energy of the minihalo

$$E_{\rm b} = \gamma G M_{\rm mh}^2/2R_{\rm mh}. \tag{5.9}$$

Here γ is a dimensionless parameter again determined by the mass profile of the dark matter halo. For the NFW profile, it takes the form [Mo et al., 1998]

$$\gamma(c) = \frac{c}{2}\frac{1 - 1/(1+c)^2 - 2\ln(1+c)/(1+c)}{[c/(1+c) - \ln(1+c)]^2}. \tag{5.10}$$

Utilizing Equation 5.7 and 5.9, we obtain the normalized energy input to the minihalo as

$$\frac{\Delta E}{E_{\rm b}} = \begin{cases} \dfrac{4\alpha^2(c)}{3\gamma(c)}\dfrac{Gm_*^2}{v_*^2 b^4}\dfrac{R_{\rm mh}^3}{M_{\rm mh}} = \dfrac{\alpha^2(c)}{\pi\gamma(c)}\dfrac{Gm_*^2}{v_*^2 b^4}\dfrac{1}{\bar{\rho}_{\rm mh}} & (b > b_{\rm s}) \\ \dfrac{4\alpha^2(c)}{3\gamma(c)}\dfrac{Gm_*^2}{v_*^2 b_{\rm s}^4}\dfrac{R_{\rm mh}^3}{M_{\rm mh}} = \dfrac{3\beta^2(c)}{f_{\rm b}^4\,\gamma(c)}\dfrac{Gm_*^2}{v_*^2}\dfrac{1}{M_{\rm mh}R_{\rm mh}} & (b \le b_{\rm s}) \end{cases} \tag{5.11}$$

where $\bar{\rho}_{\rm mh} = M_{\rm mh}/(4\pi\, R_{\rm mh}^3/3)$ is the average density of the minihalo. Assuming the minihaloes are in virial equilibrium with respect to the background density at redshift $z_{\rm c}$ (the infall redshift), we obtain $\bar{\rho}_{\rm mh} = \Delta_{\rm c}\, \rho_{\rm crit}(z_{\rm c})$, where $\rho_{\rm crit}(z_{\rm c})$ is the critical density of the Universe at $z_{\rm c}$ and $\Delta_{\rm c} = 200$ is the critical overdensity of collapsed objects (we can neglect corrections from e.g. Ω_Λ to $\delta_{\rm c}$ at the $z_{\rm c}$ of interest). Since $\bar{\rho}_{\rm mh}$ is independent of minihalo mass, the energy input in the large-b case in Equation 5.11 will be independent of minihalo mass while having a strong dependence on the impact parameter. The only free parameter that is left to be determined by simulations in Equation 5.11 is the correction factor $f_{\rm b}$.

From Equation 5.11, we can compute a characteristic impact parameter when $\Delta E/E_{\rm b} = 1$

$$
\begin{aligned}
b_{\rm min} &= \sqrt{\frac{m_*}{v_*}} \left(\frac{\alpha^2(c) G}{\pi \gamma(c) \bar{\rho}_{\rm mh}} \right)^{1/4} \\
&\approx 0.027\,{\rm pc} \left(\frac{\alpha^2(c)}{\gamma(c)} \right) \left(\frac{m_*}{1\,{\rm M}_\odot} \right)^{1/2} \left(\frac{v_*}{200\,{\rm km/s}} \right)^{-1/2} \left(\frac{1+z_{\rm c}}{20} \right)^{-3/4} ,
\end{aligned}
\tag{5.12}
$$

which gives a crude estimate of the condition for destruction of minihaloes. It is worth noting that the average density of a virialized halo is much larger when formed at higher redshifts, given as $\bar{\rho}_{\rm mh} \propto (1+z_{\rm c})^3$. Minihaloes that collapsed and fell into the host halo earlier in cosmic time should be less vulnerable to stellar disruptions due to higher central densities.

Although $b_{\rm min}$ serves as a good indicator for significant disruption of the minihalo, the actual mass loss of the minihalo (as a function of $\Delta E/E_{\rm b}$) after a single encounter will be calibrated by numerical simulations presented in the following section.

Tidal disruption

Another important disruption mechanism for minihaloes is tidal disruption. After the minihaloes falling into the Milky Way halo, they experience tidal forces from the Milky Way dark matter halo and the galactic disk. In contrast to the stellar disruption, which sensitively depends on close encounters with stars, the tidal forces are determined by gravity at galactic scales, dominated by the collective effects of the smooth gravitational potential rather than the fluctuating component from individual particles and/or stars. Moreover, rather than an impulsive event, tidal disruption is

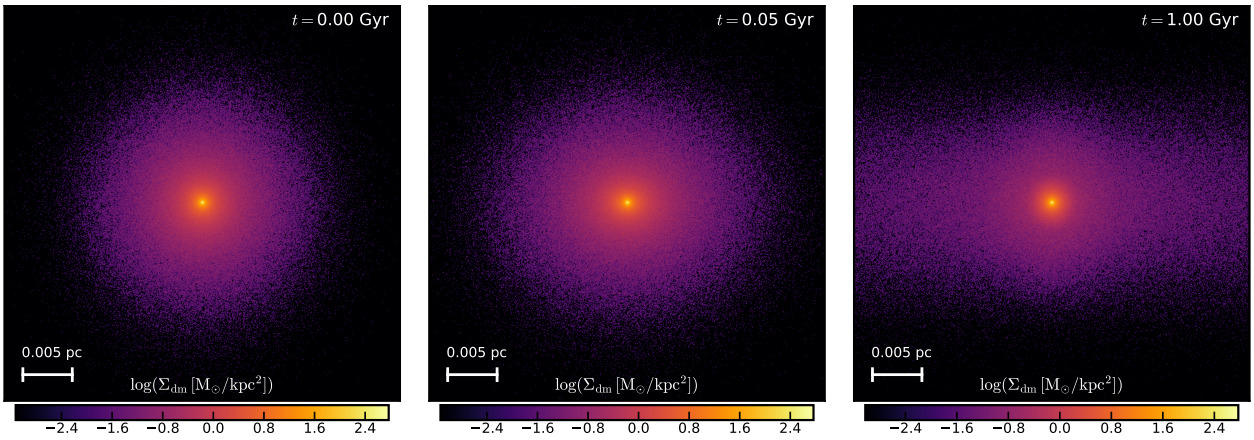

(a) (b) (c)

Figure 5.2.2: The evolution of a minihalo during stellar disruption visualized. This is a simulation of an encounter between a minihalo of mass $M_{\rm mh} = 10^{-10}\,{\rm M}_\odot$ and a star of mass $m_* = 1\,{\rm M}_\odot$, with the impact parameter $b = 10^{-4}$kpc. The star passed by in the y direction of the image. We show the dark matter surface density distribution of the minihalo. Figure 5.2.2a shows the initial dark matter distribution. Right after the encounter, a large fraction of dark matter has been heated up from the gravitational interaction with the passing star and become unbounded. Although this energy is transfered impulsively, it requires roughly the minihalo dynamical time ($t_{\rm dyn} \gtrsim 1\,{\rm Gyr}$) for the the disruption to be reflected in the minihalo density distribution, as shown in Figure 5.2.2b and Figure 5.2.2c.

secular, and is therefore usually treated differently from stellar disruptions.

In a sufficiently strong and smooth external tidal field, the outskirts of the minihalo will be stripped away where the tidal force exceeds the self-gravity of the minihalo. This tidal radius is given by [e.g., King, 1962, Taylor and Babul, 2001, Zentner and Bullock, 2003]

$$r_t = R \left[\frac{M_{\rm mh}(r < r_t)/M_{\rm MW}(r < R)}{2 - \frac{d\ln M_{\rm MW}}{d\ln R}\Big|_R + \frac{V_{\rm t}(\mathbf{R})}{V_{\rm c}(R)}} \right]^{1/3} , \tag{5.13}$$

where R is the galactocentric distance of the minihalo, $M_{\rm MW}(r < R)$ is the mass of the Milky Way (including both dark and baryonic matter) enclosed within radius R and $M_{\rm mh}(r < r_{\rm t})$ is the minihalo mass enclosed within r_t. $V_{\rm t}(\mathbf{R})$ is the instantaneous tangential speed of the minihalo, which equals the circular velocity $V_{\rm c}(R)$ when the minihalo is on a circular orbit. The minihalo mass outside the tidal radius will be stripped away roughly over a dynamical time scale of the host, and the instantaneous mass loss rate is often expressed as [e.g., Taffoni et al., 2003, Zentner and Bullock, 2003, Oguri and Lee, 2004, Pullen et al., 2014]

$$\dot{M}_{\rm mh}(r > r_{\rm t}) = -\frac{M_{\rm mh}(r > r_{\rm t})}{t_{\rm ts}(R)}, \tag{5.14}$$

where $t_{\rm ts}$ is the characteristic time scale of tidal stripping, which is proportional to the dynamical time scale of the host halo (not the minihalo)

$$\begin{aligned} t_{\rm ts}(R) &= A\, t_{\rm dyn}^{\rm host}(R) \\ &\approx 93\,{\rm Myr} \left(\frac{A}{1}\right) \left(\frac{\bar{\rho}_{\rm host}(R)}{1.6\times10^7 {\rm M}_\odot\,{\rm kpc}^{-3}}\right)^{-1/2} \end{aligned} \tag{5.15}$$

where $\bar{\rho}_{\rm host}(R)$ is the averaged density of the host halo within radius R and A is a constant fudge factor of order unity that is found to be $\sim$ 0.5 - 3 in several previous studies [e.g., Zentner and Bullock, 2003, Zentner et al., 2005, Pullen et al., 2014, van den Bosch et al., 2018, Green et al., 2021]. If the tidal stripping occurs in the Solar neighborhood, the time scale will be much shorter than the lifetime of minihalo in the Milky Way environment. As a simple estimation, the characteristic formation time (defined as when $\mathrm{d}\log M/\mathrm{d}\log a$ falls below a threshold as proposed in Wechsler

et al. 2002) of a Milky Way-mass halo is about $a_c = 0.3$ (corresponding to $z_c \sim 2.5$ and lookback time $\gtrsim 10\,\mathrm{Gyr}$). If the minihaloes are dynamically coupled to the smooth dark matter content accreted by the Milky Way halo, the typical lifetime of minihaloes in the Milky Way environment will be of the same order. Therefore, a reasonable assumption is that the minihalo outskirts will be tidally disrupted immediately after infall and before any form of stellar disruptions takes place.

5.3 *Idealized simulations for stellar encounters and tidal stripping*

We next use N-body simulations to systematically study the stellar disruption and tidal stripping effects for isolated minihaloes initialized with the NFW profile. The goal is to test the analytic models described in Section 5.2 and calibrate them with various minihalo parameters.

5.3.1 Stellar encounters

A suite of N-body simulations is performed for minihaloes initialized with the NFW profile by varying minihalo concentrations, masses and impact parameters of the encountering stars. The simulations adopt the code Gizmo [4] [Hopkins, 2015], which has been widely used in cosmological N-body or hydrodynamical simulations [e.g., Hopkins et al., 2014, 2018, Feldmann et al., 2022]. The goal of these simulations is to test and calibrate analytic predictions of the minihalo mass fraction disrupted in stellar encounters. The relaxation process of minihaloes and the evolution of density profiles are also studied, which provides important insights in modelling the disruption effects under multiple encounters.

In these simulations, an isolated minihalo (composed of collisionless N-body dark matter particles) is initialized at $z = 0$ [5] with a star (represented by a single point-mass particle) having mass $m_* = 1\,\mathrm{M}_\odot$ at a large distance (10 pc) moving towards the minihalo with a relative velocity of $200\,\mathrm{km\,s^{-1}}$. Since the code is Lagrangian, it makes no difference whether the star or the minihalo

[4] Gizmo documentation

[5] The simulations are not cosmological, but the redshift value is required for initializing the NFW halo. The response of minihaloes to encounters we test in this section is not sensitive to the density normalization or at what redshift we set up the minihalo.

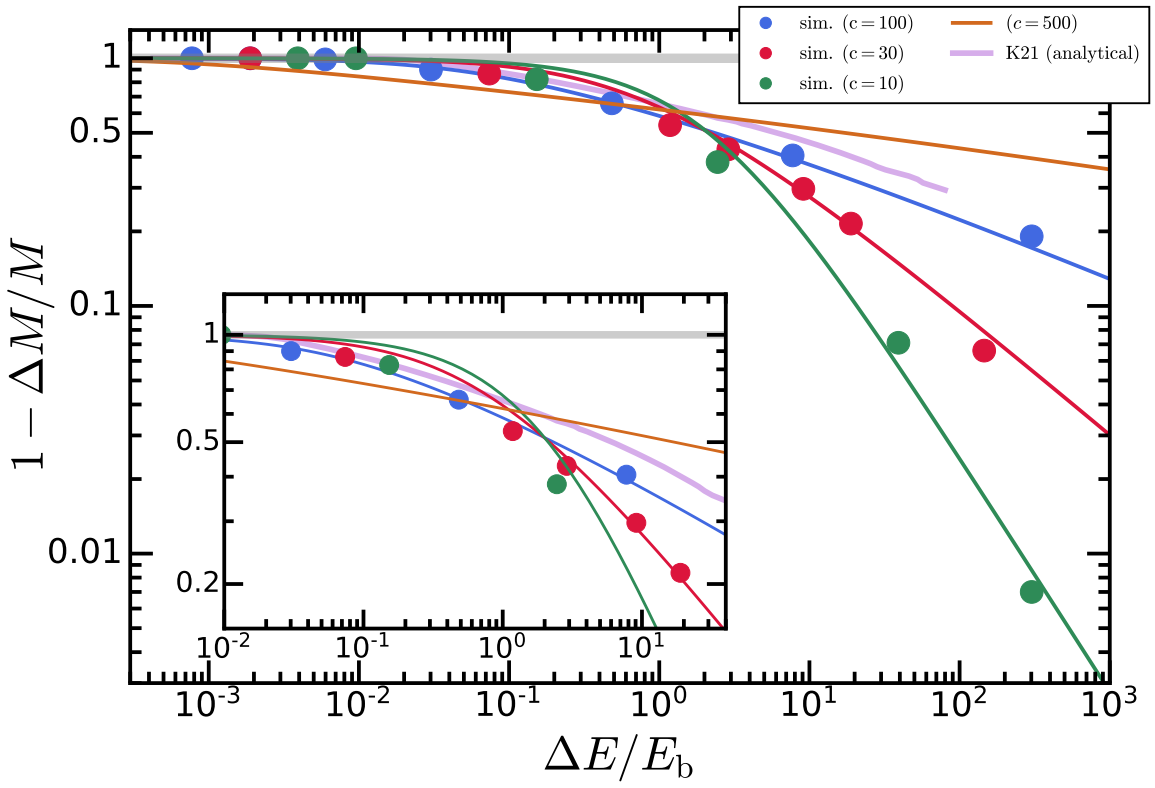

Figure 5.3.3: Fractional mass loss as a function of the normalized imparted energy for stellar encounters with minihaloes with $c = 10, 30, 100, 500$. The simulation results are shown in solid points and the best-fit model is shown in solid lines. For reference, the purple curve is the analytic prediction from [Kavanagh et al., 2020] for $c = 100$ minihaloes. The zoom-in subplot shows the transitional regime around $\Delta E/E_{\rm b} \sim 1$. The response curves calibrated from our simulations are in good agreement with results in [Kavanagh et al., 2020]. However, the asymptotic behaviour of the response curve at large $\Delta E/E_{\rm b}$ has a significant concentration dependence, which has not been revealed in previous studies.

is moving and in which frame we solve the dynamics equations. In Figure 5.2.2, the evolution of a minihalo during disruption is visualized. The encounter with a star will impart a certain amount of energy into the minihalo, disrupting the halo outskirts at roughly a minihalo dynamical time. Our default simulations resolve the minihalo with 10^6 dark matter particles initialized in an equilibrium NFW halo following the method in [Springel, 2005]. We generate the initial condition using the package PyICs [6][Herpich et al., 2017]. We vary the impact parameter of the star, the minihalo mass, and the minihalo concentration (or equivalently scale radius), to systematically study stellar disruption effects. The gravitational softening length of the dark matter particles is taken to be 10^{-9} kpc, which is small enough to resolve the dense core of those minihaloes with a mass $10^{-10}\,M_\odot$ and concentration $c = 100$, which have a scale radius $r_s = 9.6 \times 10^{-8}$kpc. The time-stepping in the simulation requires more careful consideration, since most disruption occurs when the distance between the star and the minihalo is around its minimum. We choose the maximum size of the timestep to be 10^{-8}Gyr even when the star is still at a large distance (10 pc) from the minihalo and study the subsequent disruption as the star moves closer towards the minihalo. It is worth noting that this timestep is about an order of magnitude smaller than the crossing time of the star, $\sim R_{\rm mh}/v_*$, so that the trajectory of the star around the minihalo can be well resolved. After the close encounter, we can relax the upper limit on the timestep to integrate the relaxation of the minihalo after the stellar disruption to arbitrarily long times (at a fairly low computational cost). A detailed discussion of numerical convergence is given in Appendix 5.8. Experimenting with the maximum timestep and/or gravitational softening shows that smaller values produce essentially identical results (with larger computational cost), but order-of-magnitude larger values of softening length can risk allowing the simulation to "oversmooth" gravity or take excessively large timesteps for some particles, which "overshoot" the very brief duration of the encounter (for detailed numerical tests, see Hopkins et al. 2018 and Grudić and Hopkins 2020).

[6] PyICs documentation

Disruption under different impact parameters and calibration of the response function

We first run three sets of simulations for encounters with fixed minihalo mass and concentration but different impact parameters. In all these simulations, we set a fixed minihalo mass $M_{\rm mh} = 10^{-10}\,{\rm M}_\odot$, star mass $m_* = 1\,{\rm M}_\odot$ and initial star-minihalo relative velocity $v_* = 200\,{\rm km/s}$. The halo concentration has been fixed to be $c = 10, 30, 100$ for each set of simulations respectively. The goal is to characterize the relation between the mass loss of the minihalo after a stellar encounter and the normalized energy input. The imparted energy can be related to the impact parameter with Equation 5.11. After the minihalo become fully relaxed after the stellar encounter (at $t = 1\,{\rm Gyr} > t_{\rm dyn}(z = 0)$), dark matter particles, with kinetic energy (in the center-of-momentum frame) larger than the absolute value of their gravitational potential energy, are identified as unbound and disrupted. The remaining mass of the minihalo is measured as the fraction of bound dark matter particles after minihalo relaxation, and we have verified that the remaining minihalo mass has converged at the time of measurement.

In Figure 5.3.3, we show the minihalo mass loss as a function of the normalized imparted energy for different choices of halo concentrations. The imparted energy is calculated using Equation 5.11 (for the minihalo and impact parameters tested here, the transition radius $b_{\rm s}$ is always smaller than the impact parameters, so the free parameter $f_{\rm b}$ does not affect the results). The mass loss is negligible when $\Delta E/E_{\rm b} \ll 1$, and quickly increases in a power-law fashion with respect to $\Delta E/E_{\rm b}$. In this regime, minihaloes with low concentrations are more vulnerable to stellar encounters with steeper power-law slopes. In the following, the mass loss as a function of the imparted energy and halo concentration will be referred to as the response curve, $\mathcal{F}(\Delta E/E_{\rm b}, c)$. We propose the following functional form to fit the response curve

$$\frac{M_{\rm mh} - \Delta M_{\rm mh}}{M_{\rm mh}} \equiv \mathcal{F}(\Delta E/E_{\rm b}, c) = \frac{2}{1 + \left(1 + \dfrac{\Delta E/E_{\rm b}}{p(c)}\right)^{k(c)}}, \tag{5.16}$$

where $\Delta E/E_{\rm b}$ should be evaluated using Equation 5.11 (the free order-unity parameter $f_{\rm b}$ is yet to be determined, but the calibration here is done in the $b \gg b_{\rm s}$ regime, so $f_{\rm b}$ does not have any real impact). After exploring the response curve of each choice of minihalo concentration, we propose

the following fitting formula for the parameters $p(c)$ and $k(c)$

$$\log p(c) = a_1 (\log c - \eta) + a_2 (\log c - \eta)^2 + a_3 (\log c - \eta)^3$$
$$\log k(c) = b_0 + b_1 (\log c - 2) \tag{5.17}$$

Then we perform the least-square fits jointly to the results of all sets of simulations. The best-fit parameters are $\eta = 0.98, a_1 = -0.8(\text{fixed}), a_2 = -0.59, a_3 = -0.034, b_0 = -0.58, b_1 = -0.56$. The best-fit model is also shown in Figure 5.3.3 and is in good agreement with the simulation results of minihaloes with various concentrations.

This best-fit model of the response curve will be the foundation we use to understand the disruption of minihaloes with different masses or concentrations. We now relax our assumption of a fixed concentration or mass ratio and test this fitted response curve for a wide range of encounters. In Figure 5.3.3, we show our best-fit model of the response curve for minihaloes of concentration $10 - 500$, and show that the model agrees well with the simulation results.

Disruption under different halo concentrations

Given the calibrated response function, we next run an additional set of simulations with a fixed impact parameter $b = 0.05$ pc but for minihaloes with different concentrations. The goal is to further validate this semi-analytic model (the analytic calculation of imparted energy plus simulation calibrated response function) for minihaloes with various of compactness. The minihalo mass is still fixed to $M_{\rm mh} = 10^{-10}\,{\rm M}_\odot$ and the properties of the encountering star are the same as in Section 5.3.1.

The halo concentration will affect the mass loss from stellar encounters in two ways. First, the structural parameters α, β and γ all have explicit dependence on minihalo concentration, which will propagate to the calculation of energy imparted (*i.e.* $\Delta E/E_{\rm b} \propto \alpha^2(c)/\gamma(c) \sim \ln(c)/c$ when $b \gg b_{\rm s}$ and $c \gg 1$). Secondly, the response function also has a strong dependence on concentration (see Equation 5.16), especially when $\Delta E/E_{\rm b} \gg 1$. Less concentrated minihaloes will become increasingly vulnerable to disruptive stellar encounters. Therefore, it is non-trivial for the semi-analytic model to correctly capture the concentration dependence of minihalo mass loss.

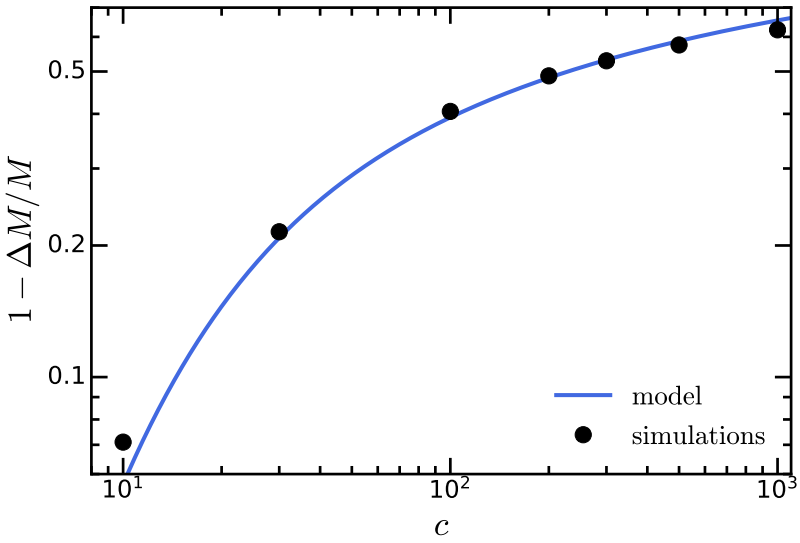

Figure 5.3.4: Fractional mass loss as a function of concentration at impact parameter $b = 0.05\,\mathrm{pc}$. The blue solid curve is the semi-analytic model prediction while the data points are obtained from simulations.

In Figure 5.3.4, we show the mass loss of minihalo versus minihalo concentration. The best-fit semi-analytic model agrees with the simulation results over a wide range of concentrations, even extrapolating into regimes not covered in our original calibration step above.

Disruption under different minihalo masses

One remaining ingredient of the semi-analytic model that needs to be calibrated is the disruption behavior in the $b \lesssim b_{\mathrm{s}}$ regime. According to Equation 5.11, the imparted energy will stop rising as b decreases when a characteristic scale b_{s} is reached. The free, order-unity correction factor is calibrated by simulations. We fix the impact parameter $b = 0.05\mathrm{pc}$ and concentration $c = 100$, and run another set of simulations for minihaloes of different masses ranging from 10^{-10} to $10^{-3}\,\mathrm{M}_{\odot}$. In low-mass minihaloes, b_{s} is small enough that the encounter is in the $b > b_{\mathrm{s}}$ regime, where mass loss is independent of minihalo mass. As minihalo mass increases (and b_{s} increases), test cases

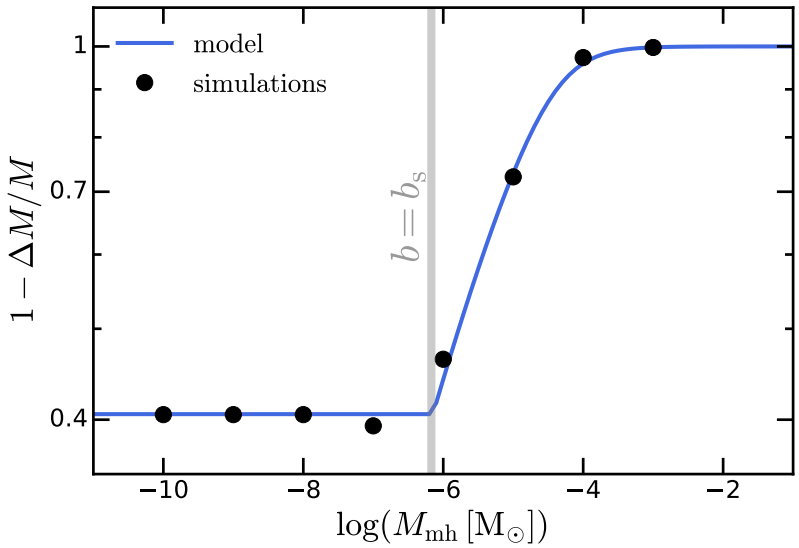

Figure 5.3.5: Fractional mass loss as a function of minihalo mass with concentration $c = 100$ and impact parameter $b = 0.05$ pc. The black solid points are simulation results. The blue curve is the semi-analytic prediction using the best-fit response curve.

with massive minihaloes enter the $b < b_s$ regime, where stellar disruptions are suppressed. In Figure 5.3.5, we show the mass loss as a function of minihalo mass. A transition of the response of the minihalo occurs, and we use the mass of this transition to calibrate the free parameter to be $f_b = 5$. The predicted mass loss using the best-fit response curve for $c = 100$ haloes is shown in the figure the solid line. In general, the semi-analytic model gives the correct location and shape of the transition at $b \sim b_s$. The mass loss remains a constant at low minihalo masses as indicated by Equation 5.11 in the $b \gg b_s$ regime. A sharp transition occurs at $b \simeq b_s$ such that the mass loss rate reduces to almost zero at high minihalo masses.

Density profiles

The density profile will not immediately change after the close encounter with stars, but will gradually relax to the final minihalo profile within a few minihalo dynamical times [Delos, 2019].

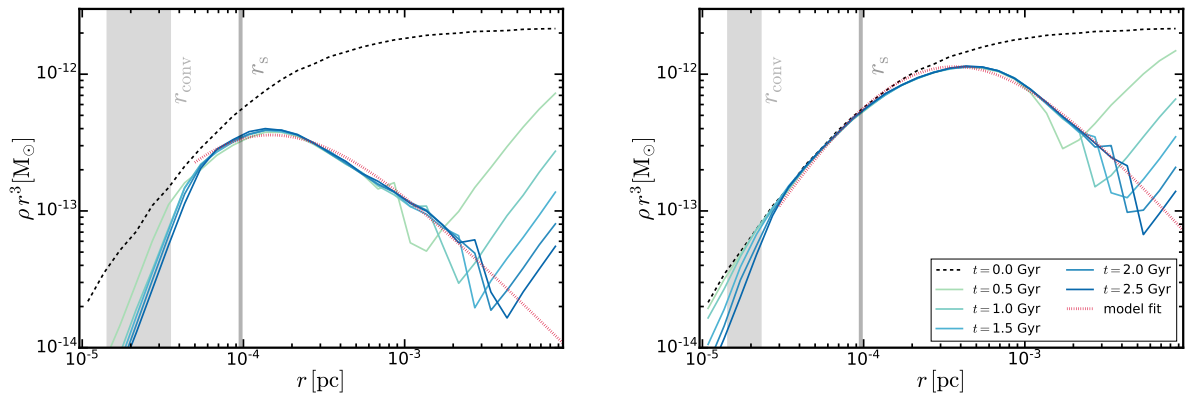

Figure 5.3.6: The evolution of minihalo density profiles after a close encounter with a star. For the tests here, the minihalo mass is set as $10^{-10}\,{\rm M}_\odot$ initialized with the NFW profile at redshift zero, with virial radius $R_{\rm mh} \sim 0.01$ pc and dynamical time scale $t_{\rm dyn} \sim 2.2$ Gyr. The halo concentration is $c = 100$. The impact parameter is $b = 2 \times 10^{-5}$ kpc in the top panel and $b = 5 \times 10^{-5}$ kpc in the bottom panel. After the close encounter with the star, the outskirts of the minihaloes are dominantly disrupted in less than a dynamical time. Eventually 81% (60%) of the minihalo mass is disrupted for the $b = 2 \times 10^{-5}$ kpc ($b = 5 \times 10^{-5}$ kpc) case. The density profile of minihalo after disruption can be well-fitted by a broken power-law profile with best-fit asymptotic slopes ($k = 3.2$ for $b = 2 \times 10^{-5}$ kpc, $k = 3.3$ for $b = 5 \times 10^{-5}$ kpc) analogous to that of the Hernquist profile. The "model fit" curve provides an asymptotic limit of the density profile after infinite time. The upturn at the outskirt of the minihalo represents a propagating shell of unbound particles. As this upturn propagates towards the outer part of the minihalo, the density profile gradually converges to the asymptotic limit.

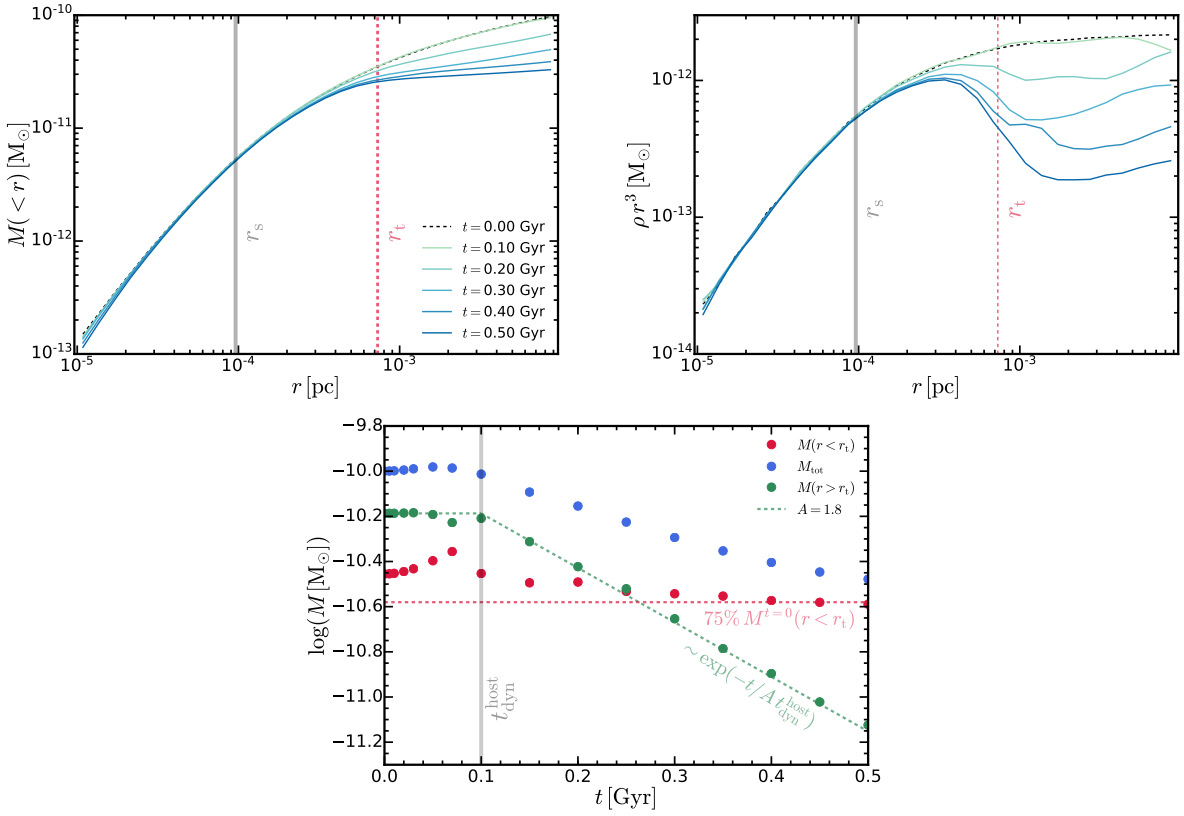

Figure 5.3.7: *Upper Left*: The enclosed mass profile of a minihalo with $M = 10^{-10}\,\mathrm{M}_\odot$ at $t = 0 - 0.5\,\mathrm{Gyr}$. The minihalo is on a circular orbit at $R = R_\odot = 8\,\mathrm{kpc}$ in a Milky Way-mass dark matter halo. For reference, the dynamical time of the host halo within this radius is about 0.1 Gyr. The gray vertical line indicates the scale radius of the minihalo and the red vertical dashed line indicates the tidal radius analytically calculated using Equation 5.13. The mass outside the tidal radius is stripped away at roughly the dynamical time scale of the host halo while the mass inside is marginally perturbed. *Upper Right*: The density profile of the dark matter halo at the same time as the top panel. The plot is to illustrate the behavior of the matter distribution at the outskirts of the minihalo during tidal stripping. *Bottom*: Mass evolution history of the minihalo. The total mass here is the sum of halo mass within the initial virial radius of the minihalo. In addition, we show the mass inside and outside the tidal radius as a function of time. After approximately a dynamical time of the host halo, the mass outside the tidal radius starts an exponential decay as described by Equation 5.14 with the fudge factor $A \simeq 1.8$. The mass inside the tidal radius is marginally affected.

This is mainly because the close encounter with a star occurs on a timescale much shorter than the minihalo dynamical time. In Figure 5.3.6, we show the evolution of minihalo density profiles for minihaloes with mass $10^{-10}\,\mathrm{M}_\odot$ and concentration $c = 100$. In the top (bottom) panel, we show the case with impact parameter $b = 2 \times 10^{-5}$ pc (5×10^{-5} pc). The density profile is shown as $\rho\, r^3$ which is proportional to $\Delta M/\Delta \log r$, the contribution to total mass per unit logarithmic interval of radius. The vertical shaded region shows the convergence radius for collisionless particles based on the [Power et al., 2003] criterion (this is roughly the radius interior to which the numerical two-body relaxation time drops below the Hubble time, a conservative indication of where N-body integration error could be significant). In the $b = 5 \times 10^{-5}$ pc case, the outskirts of the halo are predominantly disrupted while the core of the halo remains relatively unperturbed, leaving approximately 60% of the halo disrupted. Although the central density exhibits a small decrease, its contribution to the total mass loss is negligible and the scale of this decrease is close to the convergence radius of dark matter properties, which makes it hard to distinguish the decrease from a numerical artifact. At the outskirts of the minihalo, the density profile turns up, corresponding to a shell of unbound particles (heated by the encounter) propagating outward. For $b = 2\times10^{-5}$ pc, due to higher imparted energy, the disruption is more significant with over 80% disrupted. However, the behavior of the final density profile is rather similar to the previous case.

It is worth noting the remaining minihaloes never relax to a new NFW profile. Instead, the final density profile (after the shell of unbound particles escapes) can be well described by a broken power-law of the form

$$\rho(r) = \frac{\rho_0}{\frac{r}{r_0}\left(1 + \frac{r}{r_0}\right)^k}, \tag{5.18}$$

with the best-fit asymptotic slope $k = 3.2$ for $b = 2 \times 10^{-5}$ kpc and $k = 3.3$ for $b = 5 \times 10^{-5}$ kpc. This slope implies that the density profile is close to a [Hernquist, 1990] profile ($k = 3$), or in a more general sense, the η-profile family [Dehnen, 1993, Tremaine et al., 1994] with a asymptotic slope of -4. Unsurprisingly, given the scale-free physics involved, this is similar to well-studied simulations of impulsive high-mass ratio galaxy-galaxy encounters [e.g. Hernquist and Quinn, 1988, Barnes and Hernquist, 1992, Hopkins et al., 2008, 2009, Boylan-Kolchin et al., 2005], particularly the structure

of shell galaxies [Hernquist and Quinn, 1987, Hernquist and Spergel, 1992] and the closely-related slopes of the marginally-bound layer of particles at apocenter in cosmological simulations defined as the halo "splashback" radius [e.g., Diemer and Kravtsov, 2014, More et al., 2015]. Generically, this slope arises from relaxation after dynamical mass ejection events which (by definition) excite some material to a broad distribution of energies crossing a specific binding energy $\mathcal{E} = 0$, as the outer slope $k+1 = 4$ corresponds to the only finite-mass asymptotic power-law distribution function which is continuous through $\mathcal{E} = 0$ [Hernquist et al., 1993].

Therefore, we cannot apply the single-encounter prediction multiple times for an NFW profile in the scenario of multiple encounters. After the first close encounter with stars, the halo profile is no longer well-described by an NFW profile and the subsequent analysis will be invalid. Instead, one can compute the accumulated injected energy $\Delta E_{\rm tot}$ for successive encounters and use the response function $\mathcal{F}(\Delta E_{\rm tot}/E_{\rm b})$ to obtain the total disruption fraction. This will lead to an additional disruption fraction after the first encounter whose magnitude is determined by the slope of the response function at large $\Delta E_{\rm tot}/E_{\rm b}$. This method is reasonable because the next encounter in general will occur before the halo relaxes to an NFW profile. In the scenario where the second encounter occurs after the relaxation, the relaxed density profile is effectively more concentrated since the outskirts are dominantly disrupted and thus the minihalo is less susceptible to subsequent disruptions. One could recompute the structure parameters as well as the concentration number of the relaxed profile and evaluate the disruption fraction of the second encounter. On the other hand, the response curve also has the feature that subsequent encounters with the same energy injection will rapidly become less important (the particles which would be unbound by such an energetic encounter have already been unbound), and the accumulated injected energy method can reasonably accurately approximate the disruption fraction from the relaxed profile.

5.3.2 Simulation of tidal stripping

To validate the semi-analytic description of tidal disruptions of minihaloes in Section 5.2.2, we perform an idealized simulation of a minihalo traveling through the analytic gravitational potential of a Milky Way-mass host halo. The host halo profile is modelled as an NFW profile with mass

$M_{\rm vir} = 10^{12}\,{\rm M}_\odot$ and concentration $c = 12$ [e.g., Klypin et al., 2002, McMillan, 2011, Deason et al., 2012, Bland-Hawthorn and Gerhard, 2016]. For simplicity, we ignore the baryon content. The minihalo is assumed on a circular orbit with $R = R_\odot \simeq 8\,{\rm kpc}$. In the top and middle panel of Figure 5.3.7, we show the evolution of the enclosed mass profile and density profile of the minihalo. The tidal radius calculated using Equation 5.13 is shown as the red vertical dashed line. After evolving for about 0.5 Gyr (for reference, the dynamical time scale of the host halo at $R = 8$kpc is $t_{\rm dyn}^{\rm host} \sim 0.1\,{\rm Gyr}$, see Equation 5.15), the enclosed mass profile starts flattening and eventually plateaus outside the analytically evaluated tidal radius. In the bottom panel of Figure 5.3.7, we show the mass evolutionary history of this minihalo, and specifically the mass inside and outside the tidal radius. The mass within the tidal radius is almost immune to tidal stripping, with 75% of the mass remaining after 0.5 Gyr. On the other hand, the mass outside the tidal radius exhibits an exponential decay after about $1\,t_{\rm dyn}^{\rm host}$. The mass loss of the minihalo can be well represented by Equation 5.14, implying $M(r > r_{\rm t}) \sim e^{-t/A\,t_{\rm dyn}^{\rm host}}$ with a fudge factor A close to 1.8 for the minihalo tested, in broad agreement with previous numerical studies of more massive CDM subhaloes [e.g., Zentner and Bullock, 2003, Pullen et al., 2014, van den Bosch et al., 2018]

The simulation presented in this section demonstrates that the semi-analytic treatment of tidal disruption works reasonably well in predicting the mass loss and tidal stripping time scale. Given the fudge factor A found here, the tidal stripping time scale $t_{\rm ts}$ in Equation 5.15 is an order of magnitude smaller than the Hubble time. Therefore, in modelling the cosmic evolution of minihaloes, tidal stripping can be treated as an instantaneous process.

5.4 *Disruptions in the realistic Milky Way environment*

In the sections above, we described the physical process and consequence of a single stellar encounter and the effects of tidal fields. Next, we will discuss how the impact of successive encounters with an ensemble of stars accumulates and how stellar and tidal disruption affect each other.

5.4.1 Multiple encounters in the Milky Way disk

Disk stars are the dominant component of the stellar populations in the Milky Way, and thus will be the main contributor to the disruption of dark matter substructures. When a minihalo passes through the stellar disk, it will encounter a slab of stars within a short timescale

$$t^{\rm x}_{\rm disk} \simeq 2\,{\rm Myr}\left(\frac{H_{\rm d}}{400\,{\rm pc}}\right)\left(\frac{V^{\perp}_{\rm mh}}{200\,{\rm km/s}}\right)^{-1}, \tag{5.19}$$

where $H_{\rm d}$ is the scale height of the Milky Way thin disk and $V^{\perp}_{\rm mh}$ is the relative velocity of the minihalo perpendicular to the disk plane. Since this disk passage time is much shorter than the dynamical time of dark matter minihaloes, the internal structure of the minihaloes will not have enough time to relax between successive stellar encounters during a single passage. Therefore, a series of encounters with disk stars can be considered as effectively one encounter with the injected energy accumulated over the passage.

Back-of-the-envelope model

First, we will consider a simplified model assuming that a minihalo will be disrupted after a single encounter with impact parameter smaller than $b_{\rm min}$ given by Equation 5.12, and it will remain unperturbed if the impact parameter is larger than $b_{\rm min}$. Note that we aim for a back-of-the-envelope estimate with this simplified model. Consider a minihalo with mass $M_{\rm mh}$ and an average density $\bar{\rho}_{\rm mh}$, moving through a field of stars with differential number per unit mass $n_{m_*} = {\rm d}N_*/({\rm d}m_*{\rm d}^3\mathbf{x})$ characterized by the stellar present-day mass function (PDMF), one can choose a normalization such that the total stellar mass density is $\int m_*\, n_{m_*}\, {\rm d}m_* = \rho_*$. We assume that an encounter with impact parameter b has a probability $p = p(b,\, M_{\rm mh},\, c,\, m_*,\, \mathbf{v},\, ...)$ to disrupt the minihalo, where $\mathbf{v} = \mathbf{v}_{\rm mh} - \mathbf{v}_*$, and that the stars have a locally Maxwell-Boltzmann velocity distribution function with velocity dispersion σ_* which is independent of stellar mass. The disruption rate of the cluster is

$$R = \int {\rm d}^3\mathbf{v}_* \int 2\pi b\, {\rm d}b \int {\rm d}m_*\, |\mathbf{v}| \\ ({\rm d}N_*/{\rm d}m_*\, {\rm d}^3\mathbf{x}\, {\rm d}^3\mathbf{v}_*)\, p(b,\, \bar{\rho},\, m_*,\, \mathbf{v}). \tag{5.20}$$

Taking the disruption probability p to be a step function between $p = 0$ for $b \gg b_{\rm min}$ and $p = p_0 \sim 1$ for $b \ll b_{\rm min}$ as assumed by this simplified model, after the integration, we obtain

$$R = \left(\frac{\alpha^2(c)G}{\gamma(c)\bar{\rho}_{\rm mh}}\right)^{1/2} \rho_* . \tag{5.21}$$

Integrating this over time for a given minihalo gives a survival fraction $f_{\rm survive} = \exp(-\tau)$ where $\tau \equiv \int R\, dt = \int R{\rm d}\ell/v_{\rm mh}$ along the minihalo trajectory. The time-integrated destruction probability τ is dominated by the minihalo time in the disk. If a minihalo stayed in the disk over the entire Hubble time, then

$$\tau = \left(\frac{\alpha^2(c)G}{\gamma(c)\bar{\rho}_{\rm mh}}\right)^{1/2} \rho_* \, \frac{1}{H_0} \tag{5.22}$$

$$\sim 1.3 \times 10^4 \left(\frac{\langle \rho_{*,\,\rm disk}\rangle}{1\,{\rm M}_\odot/{\rm pc}^3}\right) c_{100}^{-1/2}\,(1+z_{\rm c})^{-3/2}\,, \tag{5.23}$$

where $c_{100} = c/100$. This implies total disruption of the minihalo if it is always in the disk. On the other hand, if a minihalo only has a single passage through the disk, then

$$\begin{aligned}
\tau_{\rm single} &= \int R\,{\rm d}t \\
&\simeq \left(\frac{\alpha^2 G}{\gamma\bar{\rho}_{\rm mh}}\right)^{1/2} \int \rho_*\,{\rm d}h/v_{\rm mh}^{\perp} \\
&\sim 0.02\, c_{100}^{-1/2} \left(\frac{1+z_{\rm c}}{20}\right)^{-3/2} \left(\frac{\Sigma_*}{70\,{\rm M}_\odot\,{\rm pc}^{-2}}\right) \left(\frac{v_{\rm mh}^{\perp}}{200\,{\rm km\,s}^{-1}}\right)^{-1},
\end{aligned} \tag{5.24}$$

where Σ_* is the stellar surface density of the Milky Way disk, which is reasonably well-fit by an exponential profile $\Sigma_* \approx \Sigma_0 \exp(-R/R_{\rm d})$ with $\Sigma_0 = 816.6\,{\rm M}_\odot\,{\rm pc}^{-2}$ and $R_{\rm d} = 2.9\,{\rm kpc}$ ($\Sigma_0 = 209.5\,{\rm M}_\odot\,{\rm pc}^{-2}$ and $R_{\rm d} = 3.31\,{\rm kpc}$) for the thin (thick) disk of the Milky Way [e.g., McMillan, 2011, 2017]. If we are only interested in the Solar neighborhood ($R_\odot \approx 8\,{\rm kpc}$, see Bland-Hawthorn and Gerhard 2016 for a review of measurements on $R_\odot$), the total surface density of both the thin and thick disks is $\Sigma_*^\odot \sim 70\,{\rm M}_\odot\,{\rm pc}^{-2}$. Therefore, the impact of a single passage through the disk is not significant for reasonably high halo concentrations.

Besides the two extreme cases above, the more realistic scenario is successive passages through the disk, where the number of passages of a minihalo through the disk is a critical factor. Assuming circular orbits, the number of disk passages for minihaloes in the Solar neighborhood is

approximately $t_{\rm Hubble}/t_{\rm circ} \sim 60$, leading to an $O(1)$ effect. Therefore, those minihaloes in the Solar neighborhood should experience significant disruption. To make a quantitative prediction for the remaining mass and structure of minihaloes, we need a more complete model which will be studied in the following.

General response model

In general, the mass loss of minihaloes in single (or multiple successive) encounters characterized by the response curve $1 - \Delta M_{\rm mh}/M_{\rm mh} = \mathcal{F}(\Delta E_{\rm tot}/E_{\rm b}, c)$ was found in Section 5.3. Assuming the surface density of stars in the disk is large enough so that we can neglect stellar shot noise (discussed further below), the total energy injection $\Delta E_{\rm tot}/E_{\rm b}$ when crossing a localized slab of stars can be calculated by integrating over all possible impact parameters, masses and velocities of stars

$$\begin{aligned}\frac{\Delta E_{\rm tot}}{E_{\rm b}} &= \int \mathrm{d}^3\mathbf{v}_* \int \mathrm{d}\ell \int 2\pi b\,\mathrm{d}b \int \mathrm{d}m_* \\ &\qquad\qquad (\mathrm{d}N_*/\mathrm{d}m_*\,\mathrm{d}^3\mathbf{x}\,\mathrm{d}^3\mathbf{v}_*)\,\frac{\Delta E}{E_{\rm b}} \\ &= G\int \mathrm{d}\ell \int \mathrm{d}^3\mathbf{v}_* f(\mathbf{v}_*)\frac{1}{|\mathbf{v}_* - \mathbf{v}_{\rm mh}|^2}\int \mathrm{d}m_*\, n_{m_*}\, m_*^2 \\ &\times\left(\int_{b_{\rm s}}^{\infty}\frac{\alpha^2(c)}{\pi\gamma(c)\bar{\rho}_{\rm mh}}\frac{2\pi b\,\mathrm{d}b}{b^4} + \int_0^{b_{\rm s}}\frac{3\beta^2(c)}{f_{\rm b}^4\gamma(c)}\frac{2\pi b\,\mathrm{d}b}{M_{\rm mh}R_{\rm mh}}\right) \\ &\simeq \frac{G m_\kappa \Sigma_*}{\sigma_*^2 + v_{\rm mh}^2}\frac{2\,\alpha^2(c)}{\gamma(c)\bar{\rho}_{\rm mh}b_{\rm s}^2},\end{aligned} \tag{5.25}$$

where $\Delta E/E_{\rm b}$ is evaluated using Equation 5.11, σ_* is the *one-dimensional* velocity dispersion of stars and $f(\mathbf{v}_*)$ is the Maxwell-Boltzmann velocity distribution function. m_κ is a characteristic mass that depends on the PDMF of stars in the Milky Way,

$$m_\kappa \rho_* = \int \mathrm{d}m_*\, n_{m_*}\, m_*^2. \tag{5.26}$$

A simple approximation which gives a good fit to the Milky Way data is to take the Kroupa IMF [Kroupa, 2001] as the PDMF at $M_* \leq 1\,\mathrm{M}_\odot$ (since the evolutionary effects are small at low masses)

with a power-law cutoff $n_{m_*} \sim m_*^{-4.5}$ at $M_* > 1\,\mathrm{M}_\odot$ [e.g., Scalo, 1986, Kroupa et al., 1993, Sollima, 2019]. After the integration, we obtain $m_\kappa \simeq 0.6\,\mathrm{M}_\odot$, which is insensitive to the minimum or maximum star mass assumed. m_κ can be viewed as the characteristic mass of the most effective disruptor, which can vary in different kinds of environments For example, a clumpy medium may have significantly higher m_κ and thus stronger disruption effects.

The integration in Equation 5.25 is carried out to infinite distance, where in principle the localized quantities we define in a disk patch no longer apply. This will not affect the results significantly since the contribution from distant stars is suppressed by the $1/b^4$ dependence of energy imparted. We note that when the galactic disk is dominated by stars, our treatment integrating the cumulative perturbations from disk stars to large distances (rather than considering only close encounters like in the back-of-the-envelope model) is physically equivalent to the disk shocking effect [e.g., Ostriker et al., 1972, Binney and Tremaine, 1987, Gnedin et al., 1999, Stref and Lavalle, 2017] studied in the depletion of substructures in the Milky Way [e.g., D'Onghia et al., 2010, Stref and Lavalle, 2017, Facchinetti et al., 2022].

It is, however, still important to note that Equation 5.25 will no longer be valid if the stellar surface density is small enough that shot noise becomes important, *i.e.* when $\pi b_\mathrm{c}^2 \Sigma_* / m_\kappa \sim 1$. If we take $m_\kappa = 0.6\,\mathrm{M}_\odot$ as estimated above, we obtain the cut-off impact parameter as

$$b_\mathrm{c} = 0.044\,\mathrm{pc} \left(\frac{m_\kappa}{0.6\,\mathrm{M}_\odot}\right)^{1/2} \left(\frac{\Sigma_*}{100\,\mathrm{M}_\odot/\mathrm{pc}^2}\right)^{-1/2}. \tag{5.27}$$

If shot noise becomes dominant, $b_\mathrm{c} \gg b_\mathrm{s}$, the total energy injection becomes [7]

$$\frac{\Delta E_\mathrm{tot}}{E_\mathrm{b}} = \frac{G m_\kappa \Sigma_*}{\sigma_*^2 + v_\mathrm{mh}^2} \frac{\alpha^2(c)}{\gamma(c)\bar{\rho}_\mathrm{mh} b_\mathrm{c}^2}. \tag{5.28}$$

Connecting the behavior at $b_\mathrm{c} \ll b_\mathrm{s}$, the general solution of the accumulated energy injection during one disk passage can be written as

$$\frac{\Delta E_\mathrm{tot}}{E_\mathrm{b}} = \frac{G m_\kappa \Sigma_*}{\sigma_*^2 + v_\mathrm{mh}^2} \frac{\alpha^2(c)}{\gamma(c)\bar{\rho}_\mathrm{mh}} \frac{2}{b_\mathrm{s}^2 + 2b_\mathrm{c}^2} \tag{5.29}$$

[7] More accurately, we can calculate b_c *at each value of the stellar mass* m_*, using the same PDMF and $\pi\, b_\mathrm{c}'(m_*)\, \mathrm{d}N_*(>m_*)/\mathrm{dArea} = 1$, insert this into Equation 5.25, and then integrate over all masses numerically to define an appropriately-weighted b_c. Doing so, we find that this gives an "effective" b_c which is only $\sim 8\%$ larger than what we obtain using $\pi\, b_\mathrm{c}\, \Sigma_* / m_\kappa = 1$.

Typically, $b_{\rm s} > b_{\rm c}$ for massive minihaloes with low concentrations and $b_{\rm s} < b_{\rm c}$ for low-mass minihaloes with high concentrations. It is also worth noting that m_κ will cancel out when $b_c \gg b_s$, implying that clumpiness of the medium only matters for objects with physical sizes comparable to or larger than the typical spacing of the disruptors.

Depending on the orbit of the minihalo, it can pass through the stellar disk multiple times after falling into the host. When the orbital time is much smaller than the relaxation time of the minihalo, the combined effect can again be modeled as one single passage with the accumulated injected energy. The total number of passages and stellar surface densities at the encounter point should take an ensemble average of all possible stellar orbits passing the location of the detector. In Appendix 5.9, with a simple orbital model, we calculate the relevant correction factors from the ensemble average of all possible orbits. The accumulated injected energy will ultimately be fed to the response function $\mathcal{F}(\Sigma\Delta E_{\rm tot}/E_{\rm b})$ to calculate the mass loss.

If the time between passages is comparable to the minihalo relaxation time, the density profile of minihaloes can be relaxed to the asymptotic profile shown in Figure 5.3.6. However, as discussed in Section 5.3.1, we can still use the accumulated injected energy and the response curve to determine the disruption fraction. The slope of the response function in Figure 5.3.3 at high $\Delta E/E_{\rm b}$ suggests that a much larger injected energy does not necessarily correspond to a much more significant disruption, which is expected as the remaining core of the minihalo is less sensitive to subsequent disruption events.

5.4.2 Semi-analytic model to combine stellar and tidal disruptions

As the minihalo moves closer to the galactic center, both $r_{\rm t}$ (Equation 5.13) and $t_{\rm ts}(R)$ (Equation 5.15) will decrease sharply. Therefore, the total mass loss of an infalling minihalo is dominated by its pericenter passages. For minihaloes of interest for detection (e.g. in the Solar neighborhood $R_\odot \simeq 8$kpc), the tidal-stripping time scale during a pericenter passage at $R_\odot$ is $O(100)$ Myr, which is much shorter than the lifetime of the minihalo in the host ($\sim t_{\rm H}$). We assume that the mass of an infalling minihalo outside the tidal radius will be quickly stripped away during the first few pericenter passages before the impact of stellar disruptions start to accumulate.

For simplicity, we evaluate the tidal radius at the target radius $r_{\rm obs}$ of observation assuming a circular orbit

$$r_t = r_{\rm obs}\left[\frac{M_{\rm mh}(r<r_t)/M_{\rm MW}(r<r_{\rm obs})}{3-\frac{d\ln M_{\rm MW}}{d\ln R}\big|_{r_{\rm obs}}}\right]^{1/3}. \tag{5.30}$$

where the Milky Way halo mass distribution is modelled as an NFW profile for dark matter plus a Hernquist profile [Hernquist, 1990] for the stellar content

$$M_{\rm MW}(<r) = M_{\rm dm}\frac{f^{\rm nfw}(r/r_{\rm s})}{f^{\rm nfw}(c)} + M_{\rm b}\frac{r^2}{r^2+a^2}, \tag{5.31}$$

where $f^{\rm nfw}(x) \equiv \ln(1+x) - x/(1+x)$, the host halo parameters are $c = 12$, $M_{\rm dm} = 10^{12}\,{\rm M}_\odot$ [e.g., Klypin et al., 2002, McMillan, 2011, Deason et al., 2012, Bland-Hawthorn and Gerhard, 2016]. For baryon properties, abundance-matching studies have shown that a Milky-Way mass system typically has a stellar-to-total-mass ratio of $M_{\rm b} \simeq 0.01\,M_{\rm dm}$ [e.g., Moster et al., 2013] and the half mass radius $r^*_{1/2} \simeq 0.02\,R_{\rm vir}$ [e.g., Somerville et al., 2018]. The scale radius of the Hernquist profile is related to the stellar-half-mass-radius as $a = 0.414 r^*_{1/2}$ [Hernquist, 1990].

The post-stripping density profile of the minihalo is assumed to be a truncated NFW profile at $r_{\rm t}$, which is equivalent to a normal NFW profile with effective virial radius, concentration and overdensity as

$$\begin{aligned} R^{\rm eff}_{\rm vir} &= r_{\rm t}, \\ c_{\rm eff} &= c\frac{r_{\rm t}}{R_{\rm vir}}, \\ \Delta_{\rm eff} &= \frac{\log(1+c_{\rm eff}) - c_{\rm eff}/(1+c_{\rm eff})}{\log(1+c) - c/(1+c)}\frac{c^3}{c^3_{\rm eff}}\Delta_{\rm c}, \end{aligned} \tag{5.32}$$

The mass loss due to the tidal disruption is

$$1 - \Delta M_{\rm mh}/M_{\rm mh} = \frac{\log(1+c_{\rm eff}) - c_{\rm eff}/(1+c_{\rm eff})}{\log(1+c) - c/(1+c)}. \tag{5.33}$$

We assume that the tidal stripping happens before the minihalo settles to its current day bound orbit with respect to the host, and before any form of stellar encounters happen. The stripped minihalo forms the initial condition for the following stellar disruptions. Therefore, for a minihalo observed

at $r_{\rm obs}$, the energy accumulated from stellar encounters can be written as (following Equation 5.29 but considering multiple passages through the disk during the lifetime of the minihalo)

$$\begin{aligned}\frac{\Delta E_{\rm tot}}{E_{\rm b}}(r_{\rm obs}) &= \left\langle N_{\rm p}\left\langle \frac{G m_\kappa \Sigma_*}{\sigma_*^2+v_{\rm mh}^2}\frac{\alpha^2(c_{\rm eff})}{\gamma(c_{\rm eff})\Delta_{\rm eff}\rho_{\rm crit}(z_{\rm c})}\right.\right. \\ &\qquad \left.\left.\frac{2}{b_{\rm s}^2(c_{\rm eff},R_{\rm vir}^{\rm eff})+2b_{\rm c}^2(\Sigma_*)}\right\rangle_{\rm x}\right\rangle_{\rm o} \\ &= \overline{N_{\rm p}}\, f_\theta\, f_{\Sigma_*}\frac{G m_\kappa \Sigma_*(r_{\rm obs})}{\sigma_*^2+v_{\rm mh}^2}\frac{\alpha^2(c_{\rm eff})}{\gamma(c_{\rm eff})\Delta_{\rm eff}\rho_{\rm crit}(z_{\rm c})} \\ &\qquad \frac{2}{b_{\rm s}^2(c_{\rm eff},R_{\rm vir}^{\rm eff})+2b_{\rm c}^2(\Sigma_*(r_{\rm obs}))}, \\ \overline{N_{\rm p}} &= f_{\rm N_p}\, N_{\rm p}^{\rm circ}, \quad N_{\rm p}^{\rm circ} = T_{\rm lb}(z_{\rm c})/T_{\rm circ}(r_{\rm obs})\end{aligned} \tag{5.34}$$

where $N_{\rm p}$ is the number of passages through the stellar disk, $\langle\rangle_{\rm o}$ denotes averaging over an ensemble of minihaloes observed at $r_{\rm obs}$ with all possible orbits. Therefore, $\overline{N_{\rm p}}$ represents the averaged number of passages over all possible orbits. $N_{\rm p}^{\rm circ}$ is the number of passages assuming the minihalo is on a circular orbit with radius $r_{\rm obs}$ calculated based on the lookback time $T_{\rm lb}(z_{\rm c})$ at the infall redshift $z_{\rm c}$ and the circular orbit period $T_{\rm circ}(r_{\rm obs})$. $f_{\rm N_p}$ characterizes the deviation of $\overline{N_{\rm p}}$ from this circular orbit estimation. In Equation 5.34, Σ_* is the stellar surface density where the minihalo crossed the disk (the surface density profile $\Sigma_*(r)$ is given below Equation 5.24). $\langle\rangle_{\rm x}$ denotes averaging over all past disk crossings given the orbit of the minihalo. The correction factor f_{Σ_*} characterizes the deviation of the averaged Σ_* at all past encounter locations for all possible orbits from $\Sigma_*(r_{\rm obs})$. f_θ accounts for the increased effective stellar surface density when the minihalo is not passing perpendicular to the disk, see Appendix 5.9 for details). In Appendix 5.9, $f_{\rm N_p}$ and f_{Σ_*} are estimated based on the orbital model of an isothermal halo. For simplicity, $\sigma_*^2+v_{\rm mh}^2$ is assumed to be the constant value $(250\,{\rm km/s})^2$. We note that $b_{\rm c}$ has an implicit dependence on the surface density at the encounter. When $b_{\rm c} \gg b_{\rm s}$ (when Σ_* is large or $M_{\rm mh}$ is small), $\Delta E_{\rm tot}/E_{\rm b}$ will be proportional to Σ_*^2 and the correction factor f_{Σ_*} should be replaced with $f_{\Sigma_*^2}$ (see the calculation in Appendix 5.9). To properly account for this, we model the transition from f_{Σ_*} to $f_{\Sigma_*^2}$ as

$$f = f_{\Sigma_*} + (f_{\Sigma_*^2} - f_{\Sigma_*})\frac{1}{1+e^{-k\log(\sqrt{2}b_{\rm c}/b_{\rm s})}} \tag{5.35}$$

where $k = 3$ is assumed. The value of k or the detailed form of the transition does not affect the post-disruption mass function.

5.4.3 Monte Carlo sampling of the minihaloes

Now we are ready to implement all the physics of disruption discussed above to a sample of minihaloes and track their mass loss. We model the evolution of the minihalo population in the Milky Way halo following the steps below:

- We initialize a Monte Carlo sample of minihaloes. The masses of minihaloes are sampled over the dynamical range 10^{-14} to $10^{-3}\,\mathrm{M}_\odot$ following the initial mass function given in Section 5.2.1 and Appendix 5.7. The minihalo concentrations are calculated following the mass-concentration relation in Section 5.2.1 and the redshifts of infall are calculated using the matter power spectrum from adiabatic fluctuations on small scales (see the discussion in Section 5.2.1). These physical properties sampled represent the initial status of the minihaloes upon falling into the Milky Way host.

- Tidal stripping and structural corrections are applied to the sampled minihaloes as described in Equation 5.32 and 5.33. Since the r_t solved from Equation 5.30 after normalizing over r_s is independent of minihalo mass, we calculate $r_\mathrm{t}/r_\mathrm{s}$ on a grid of c and z_c for several different choices of r_obs and prepare them as lookup tables for efficient interpolation of the tidal radius.

- After the tidal stripping and the implementation of relevant structural corrections, we apply the stellar disruption with the mass loss given by $\mathcal{F}(\Delta E_\mathrm{tot}/E_\mathrm{b}, c)$. $\Delta E_\mathrm{tot}/E_\mathrm{b}$ is evaluated using the structural parameters corrected after tidal disruptions (see Equation 5.34).

5.5 *Results*

5.5.1 Post-disruption mass functions

In Figure 5.4.8, we show the mass function of minihaloes (from AMC with the fiducial $m_\mathrm{a} = 25\,\mu$eV as an example) at Solar neighborhood ($r_\mathrm{obs} = 8\,$kpc). We have assumed the axion gives the correct

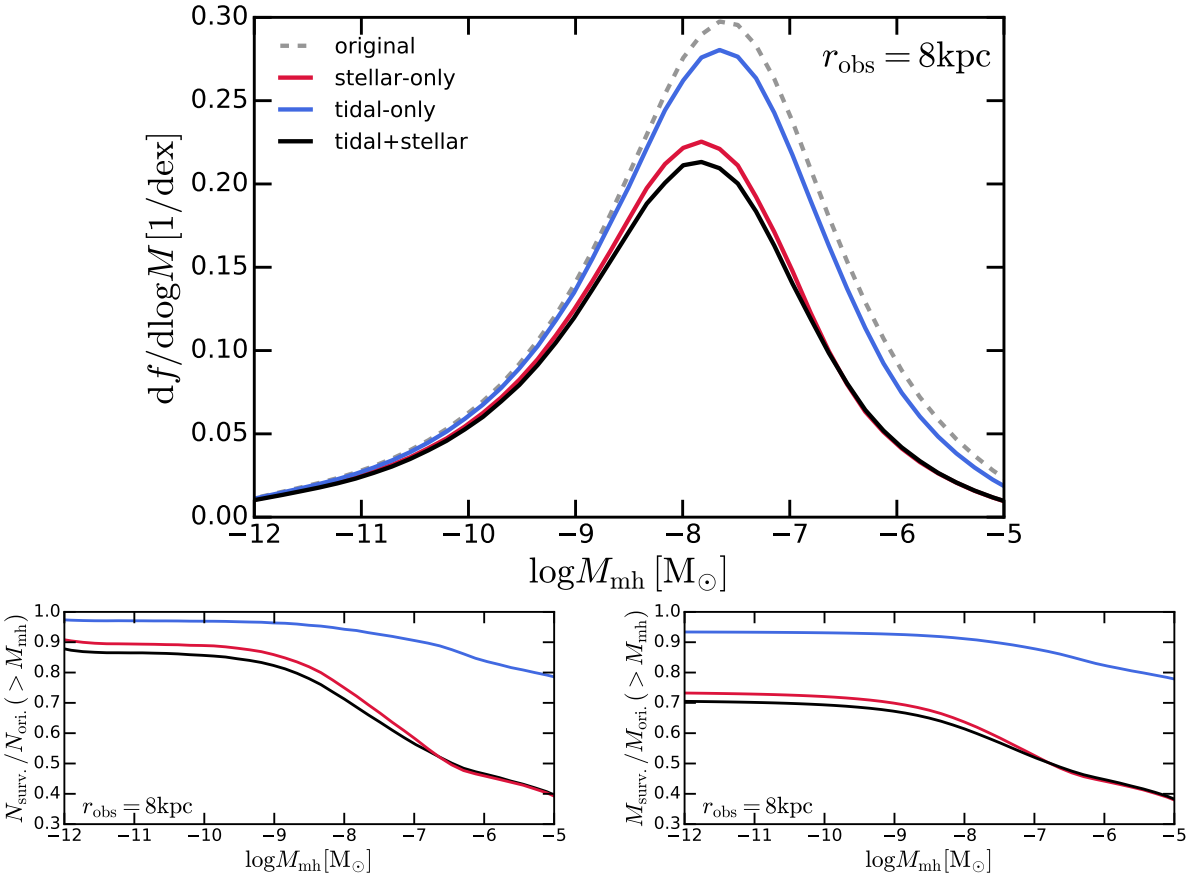

Figure 5.4.8: *Top*: Mass function of minihaloes (from axion miniclusters) at the Solar neighborhood ($r_{\rm obs} \simeq 8$kpc). We assume tha AMC model with $m_{\rm a} = 25\,\mu$eV. The mass function prior to disruption is shown as the gray dashed line. The mass function after processing only tidal (or stellar) disruption is shown as the blue (red) solid line. The mass function post-disruption, combining both tidal and stellar disruption, is shown as the solid black line. In general, the disruptions taken together induce approximately a 30% decrease in the peak value of the mass function and shift the mass of the peak by roughly half an order of magnitude. The massive end is more strongly affected by disruption than the low mass end. *Bottom*: We show the integrated number (left) and mass (right) of minihaloes prior to and after disruption. The typical survival fraction of minihaloes with $M_{\rm mh} \geq 10^{-12}\,{\rm M}_\odot$ is 87% in term of number and about 70% in term of mass. The stellar disruption is the dominant disruption mechanism through the entire mass range of interest.

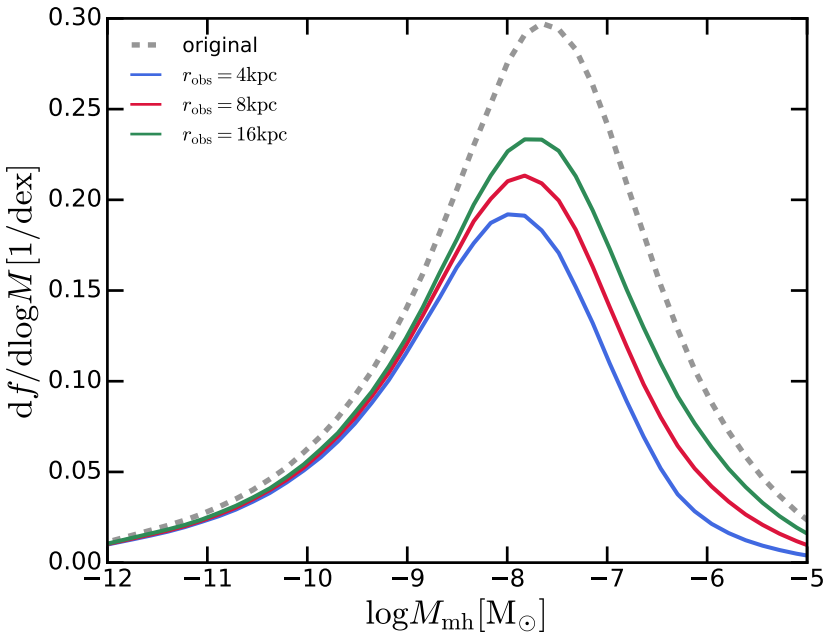

Figure 5.5.9: Mass function of minihaloes (from AMC with $m_{\rm a} = 25\,\mu$eV) observed at three galactocentric distances ($r_{\rm obs} = 4, 8, 16\,$kpc). A similar reduction pattern in the mass density of minihaloes is found at each distance, with stronger disruption at smaller radius and at the massive end of the mass function. We also compare the mass function after tidal disruption with the mass function after both tidal and stellar disruption, and again stellar disruption is found to be strongly subdominant. It is the enhancement of minihalo density after tidal disruption that reduces the energy imparted in subsequent stellar encounters to a regime where disruption becomes totally insignificant.

dark matter relic abundance. The mass functions are presented as the matter mass fraction (with respect to the total dark matter mass) in minihaloes per unit logarithm interval (dex) of minihalo mass. We present the initial (pre-disruption) mass function, the post-tidal/stellar disruption mass functions and the mass function considering the combined effect of tidal and stellar disruptions. With both tidal and stellar disruption, the peak of the mass function is reduced by about 30% accompanied by roughly half an order of magnitude mass shift of the peak. The low mass end

of minihaloes is less disrupted than the massive end because lighter minihaloes generically form earlier in these models and are more concentrated. Comparing the two disruption mechanisms, the stellar disruption dominates over the entire mass range, which agrees with the conclusion of previous studies of AMC [e.g., Kavanagh et al., 2020, Lee et al., 2020]. It is worth to note that tidal disruption can altered the structural parameters and enhance the average density of minihaloes, which could lead to non-linear effects on the following stellar disruption. However, in our experiments, the effect is weak enough that one can simply combine the mass loss from stellar and tidal disruption linearly. In the bottom panels of Figure 5.4.8, we show the integrated disruption fraction of minihaloes in number and total mass respectively. The overall survival fraction of minihaloes with $M_{\rm mh} \geq 10^{-12}\,{\rm M}_\odot$ is about 87% in terms of number and about 70% in terms of mass. The survival fraction will quickly diminish to $\lesssim 50\%$ at $M_{\rm mh} \gtrsim 10^{-6}\,{\rm M}_\odot$. Again the dominance of the stellar disruption is manifested.

In Figure 5.5.9, we show the post-disruption mass function of minihaloes at different galactocentric distances, $r_{\rm obs} = 4, 8, 16\,{\rm kpc}$, for the $m_{\rm a} = 25\,\mu{\rm eV}$ AMC model. Similar behaviour of the mass functions after disruptions is found at different target radii. In all cases, the massive end is more severely disrupted and the disruption is dominated by stellar disruption. The disruption at smaller galactocentric distances is stronger primarily due to enhanced stellar surface densities.

5.5.2 Disruption for different physics models

Here we explore the disruption of minihaloes in different physics models summarized in Section 5.2.1. These models feature different pre-disruption mass functions and mass-concentration relations.

In the top panel of Figure 5.5.10, we present the pre- and post-disruption mass functions of minihaloes in the AMC model with axion mass $m_{\rm a} = 1.25,\, 25,\, 500\,\mu{\rm eV}$. For the EMD case, we show the model with reheating temperature $T_{\rm rh} = 15,\, 30,\, 60\,{\rm MeV}$. The numeric sampling experiments are all conducted at $r_{\rm obs} = 8\,{\rm kpc}$. Since both the initial mass functions and mass-concentration relations are almost self-similar with a horizontal mass shift (and the relative mass change only depends on c and $\rho_{\rm mh}$), the post-disruption mass functions are also similar albeit with

a horizontal shift. The reduction of minihalo abundance from disruptions has very similar patterns between the AMC and the EMD models. In the bottom panel of Figure 5.5.10, we show the mass survival fraction of minihaloes. Regardless of the model choice, the overall (for minihaloes with $M_{\rm mh} > 10^{-12}\,{\rm M}_\odot$) survival fraction is about 70%. It is visible that the AMC (EMD) model with higher $m_{\rm a}$ ($T_{\rm rh}$) suffers from stronger disruption at the massive end. This is due to the lower minihalo concentration at the same mass in these models (as shown in Figure 5.2.1).

From the comparisons shown in this section, we can conclude that the model variations have little impact even quantitatively on the mass function and survival fraction of minihaloes up to the mass shift noted previously. The estimated mass survival fraction of minihaloes in the Solar neighborhood is 70%.

5.5.3 Galactic survival fraction

In Figure 5.5.11, we show the survival (mass) fraction of minihaloes after stellar and tidal disruption as a function of the radius of observation. We choose the fiducial AMC and EMD models ($m_{\rm a} = 25\,\mu$eV and $T_{\rm rh} = 30\,$MeV) for comparison here. The number of surviving minihaloes is evaluated by integrating the mass function in three mass bins: $\log(M/[{\rm M}_\odot]) \in [-12, 9], (-9, -6], (-6, +\infty)$. For both models, the survival fraction of minihaloes significantly drops with increasing minihalo mass and decreasing galactocentric distance. Quantitatively, more than 80% of the minihaloes in the mass range $\log(M/[{\rm M}_\odot]) \in [-12, -9]$ can survive at any radius of observation, as opposed to $\lesssim 30\%$ survival fraction of minihaloes with $\log(M/[{\rm M}_\odot]) > -6$ at $r_{\rm obs} \lesssim 5\,$kpc. Low mass minihaloes, being more concentrated structures, are less vulnerable to disruption, though the survival fraction would still decrease sharply at small galactocentric radii due to enhanced stellar surface density. The overall mass survival fraction closely follows the survival fraction of in the central mass bin ($\log(M/[{\rm M}_\odot]) \in [-9, -6]$) where the peak of the mass function is located for the two models studied here.

We expect a high overall survival fraction (dominated by the concentrated minihaloes with low masses). The survival fraction of the most massive QCD axion miniclusters or EMD minihaloes in the Solar neighborhood is $\lesssim 50\%$, because many of them have merged and formed more massive

and dilute minihaloes. In short, this is encouraging for the prospects of axion direct detection in the post-inflationary scenario, because

- Most of the surviving minihaloes are actually dense cores with very high densities. We have shown this in Figure 5.3.6 in Section 5.3 that the stellar disruption has limited impact of the central core but primarily destroys the outer shells of the minihalo. The density profile at the outskirt of the minihalo remains steeper than the NFW profile even after the minihalo has fully relaxed from the previous encounter. Local measurements like PTAs may still be sensitive to axion minihaloes after disruption since they can potentially probe a mass fraction well below $\sim 10\%$ [e.g., Dror et al., 2019, Ramani et al., 2020, Lee et al., 2020].

- We expect a non-negligible fraction of free axions in the Solar neighborhood, impacting direct detection signals in axion haloscope experiments.

We leave the calculations of astrophysical signals of dark matter minihaloes in the Milky Way for follow-up studies.

5.6 *Conclusions*

We systematically studied the stellar and tidal disruption of dark matter minihaloes with masses as small as $10^{-12}\,M_\odot$ in the Milky Way environment, which allows us to generically make predictions for the survival probability of dark matter minihaloes as a function of minihalo mass and concentration. Due to the large dynamic range, it is impossible to simultaneously track the evolution of minihaloes and the Milky Way galaxy in numerical simulations which resolve both. Therefore we developed a framework to combine small box N-body simulations with an analytic model of the Milky Way galaxy, to make these sorts of predictions tractable. In this paper, we focus on the miniclusters of post-inflationary axions and minihaloes in the Early Matter Domination, but the same framework can be easily applied to other types of dark matter substructure models.

We studied the stellar disruption and tidal forces separately: we first determined the profile change after the tidal disruption (as the minihalo orbit takes it towards the Milky Way disk) and

then studied the stellar disruption (encounters as a minihalo passes through the Galactic disk) using the appropriately tidally-modified minihalo profile.

Our N-body simulations found that tidal disruption effects can be predicted accurately by relatively simple analytic models. But the simulations of stellar disruption require some empirical adjustments to and calibration of analytic expressions in the literature in order to be reproduced. The density profile evolution after stellar encounters can only be determined by simulation, which is important when considering successive encounters. For the stellar disruption, we then tested our recalibrated analytic predictions with different halo concentrations, halo masses and impact parameters, suggesting that the calibrated analytic model works for a variety of halo parameters and impact parameters. Both tidal disruption and stellar disruption primarily strip away the halo outskirts, which makes the subsequent disruptions less efficient.

We show that there could be non-trivial nonlinear interactions/combined effects between these processes. For tidal disruption, we confirm the existence of a tidal radius outside of which minihaloes are largely stripped, even for minihaloes with a mass of $10^{-8}\,\mathrm{M}_{\odot}$. This means however that only the first tidal disruption will have a real impact on the density profile of haloes, since what is left behind will be the denser core (with a smaller relic tidal radius) of the original halo. Stellar disruption, on the other hand, can slightly reduce the halo central density, as shown in our simulations. Our analytic method uses the accumulated injected energy to compute the stellar disruption fraction, which accounts for the effects of many successive encounters. In future work, it may be possible to model these combined effects in more detail in the regime where both operate simultaneously. To connect to galactic scales, we apply an orbit model of minihaloes and run Monte Carlo simulations to model different minihalo trajectories. This allows us to systematically make predictions for the disruption fraction of minihaloes in the Milky Way as a function of galactic radius and halo parameters. We apply our methods to well-motivated models like post-inflationary AMC and EMD that lead to the formation of dark matter minihaloes at high redshifts and find a fairly stable mass disruption fraction of $\sim 70\%$ for models with various parameter choices. Regardless of the model choices, the disruption is dominated by stellar disruptions in the entire mass range. This disruption fraction tells us that a non-negligible fraction of the minihaloes have been disrupted, but

the remaining haloes are abundant enough to give direct detection signals in *e.g.* the upcoming PTA observations and the remaining haloes are very dense and could give rise to stronger signal.

In the future, the framework built in this paper can be applied to many interesting topics in particle astrophysics, such as the dark matter annihilation in minihaloes rate and axion minicluster-neutron star encounters.

5.7 *Appendix*: *The minihalo mass function and concentration in different models*

The minihalo mass function arising from an enhanced matter power spectrum at small scales can be considered separately from the adiabatic power spectrum. We use the Press-Schechter model to compute the minihalo mass function [Press and Schechter, 1974]

$$\frac{M^2 \mathrm{d}n/\mathrm{d}M}{\bar{\rho}} \frac{\mathrm{d}M}{M} = \nu f(\nu) \frac{\mathrm{d}\nu}{\nu}, \tag{5.36}$$

where $\bar{\rho}$ is the comoving density of dark matter and ν is a dimensionless parameter that defines the rareness of the halo. $f(\nu)$ and ν are defined as

$$\begin{aligned} \nu f(\nu) &= \sqrt{\frac{\nu}{2\pi}} \exp(-\nu/2), \\ \nu &\equiv \frac{\delta_{\mathrm{c}}^2(z)}{\sigma^2(M)}, \end{aligned} \tag{5.37}$$

where $\delta_{\mathrm{c}} = 1.686$ is the critical density required for the formation of collapsed haloes in spherical collapse models. $\sigma^2(M)$ is the variance of the initial perturbations smoothed with a top-hat filter of scale $R = (3M/4\pi\bar{\rho})^{1/3}$, which can be determined as

$$\sigma^2(M) \equiv \int \frac{\mathrm{d}k}{k} \frac{k^3 P(k)}{2\pi^2} D_1(z)^2 |W(kR)|^2, \tag{5.38}$$

where $W(x) = (3/x^3)[\sin(x) - x\cos(x)]$ is the spherical top-hat window function, $D_1(z)$ is the growth function normalized in the radiation era, and $P(k)$ is the primordial matter power spectrum introduced by new physics, such as axions. The variance of white-noise power spectrum from the axion in the post-inflationary scenario can be expressed as:

$$\sigma(M) = D_1(z) \sqrt{\frac{3A_{\mathrm{osc}}}{2\pi^2} \frac{M_0}{M}}, \tag{5.39}$$

where $A_{\rm osc}$ is the amplitude of the white-noise power spectrum, which is taken to be 0.1 in this work. M_0 can be determined from the QCD axion mass [Dai and Miralda-Escudé, 2020, Xiao et al., 2021]

$$M_0 = 2.3 \times 10^{-10} \left(\frac{50\mu\text{eV}}{m_a}\right)^{0.51} \text{M}_\odot \tag{5.40}$$

Given the value of M_0, one can obtain the minihalo mass function using the Press-Schechter model if the adiabatic fluctuations are neglected. It is worth noting that the variance is a function of M/M_0, therefore the shape of the mass function will remain the same when we change the model parameters but the characteristic mass will shift accordingly.

In the early matter domination scenario, the minihalo mass function can be calculated with a similar method. In this scenario, the primordial power spectrum remain the same as the adiabatic fluctuations but their growth is modified. Effectively, this is enhancing the primordial power spectrum at small scales. The reheating temperature $T_{\rm rh}$ is the only relevant physical parameter that determines the characteristic scale of the matter power spectrum, which correponds to a characteristic mass scale $M_{\rm rh}$. The variance is enhanced at small scales due to early matter domination, in a manner which scales as

$$\sigma(M \lesssim M_{\rm rh}) \propto D_1(z)(M/M_{\rm rh})^{-(n+3)/6}, \tag{5.41}$$

where $n = 0.963$ is the scalar spectral index [Erickcek and Sigurdson, 2011] and $M_{\rm rh} \approx 9.8 \times 10^{-5}\,\text{M}_\odot(10\text{MeV}/T_{\rm rh})^3$. Similar to the axion minicluster scenario, the variance is only a function of $M/M_{\rm rh}$ and the shape does not change with the reheating temperature. Thus we can compute the minihalo mass function based on the variance using Press-Schechter. We can further compute the mass function including minihaloes that have fallen into the massive CDM haloes by including the effect of adiabatic fluctuations, as shown in Figure 5.5.10.

5.8 *Appendix*: *Convergence testing on the simulation of stellar disruptions*

Briefly here we discuss numerical tests of the simulations of stellar disruptions. The fiducial simulations presented in the main text employ the constant gravitation softening length 10^{-9} kpc and dark matter particle mass resolution $10^{-16}\,\text{M}_\odot$ for minihaloes with a mass of $10^{-10}\,\text{M}_\odot$. We cap

the timestep at 10^{-8}Gyr during the stellar encounter to resolve the star trajectory since the stellar disruption is mostly relevant during the crossing. We justify those choices in more detail here.

5.8.1 Gravitational softening

The gravitational softening length must be chosen appropriately in the simulation otherwise we will not be able to resolve the relevant physical scales. In our idealized simulations of stellar disruptions, the minimum halo mass is $10^{-10}\,\mathrm{M}_\odot$ which corresponds to a scale radius of $r_\mathrm{s} = 9.6 \times 10^{-8}$ kpc at $z = 0$. With the fiducial particle mass resolution, the convergence radius of dark matter calculated using the [Power et al., 2003] criterion is $\sim 10^{-8}$ kpc. Therefore, the fiducial gravitational softening length, 10^{-9} kpc, and particle mass resolution should be sufficient to resolve the core profile of the halo. An additional run was performed with a gravitational softening length 2×10^{-9}kpc and the results of the disruption fraction and mass profile are robust. We have also verified that the results are robust to particle number at our fiducial resolution.

5.8.2 Time-stepping

Since the crossing time of a stellar encounter is orders-of-magnitude shorter than the internal dynamical time of the minihalo, we need sufficiently small timesteps to resolve the trajectory of the star at the vicinity of the minihalo. The time-stepping parameter in our fiducial simulations is capped at 10^{-8} Gyr, which is roughly $1/5\, R_\mathrm{mh}/v_*$, where R_mh is the minihalo radius and the corresponding minihalo mass is $10^{-10}\,\mathrm{M}_\odot$. In an additional run, the time-stepping parameter is changed to 2×10^{-8} Gyr while other parameters including the minihalo parameters are exactly the same. We obtain the same disruption fraction, mass profile, and energy change after the halo is fully relaxed. .

5.9 *Appendix*: *Orbital model of minihaloes*

The analytic calculation of accumulated energy in Equation 5.29 comes from only one encounter with the minihalo velocities perpendicular to the disk plane. In reality, minihaloes after infall to

the Milky Way halo will typically cross the stellar disks multiple times at various locations. To measure the accumulated energy input from a series of disk crossings, we need to evaluate the total number of passages through the disk, the stellar surface density where the encounter occurs and the angle of incidence, with an ensemble average over all possible orbits for the minihaloes eventually found at the observed radius.

For simplicity, we adopt a singular isothermal sphere model following the method in [van den Bosch et al., 1999] to estimate the uncertainties related to the orbits of minihaloes. The density and potential of the system are given by

$$\rho = \frac{V_c^2}{4\pi G r^2}, \quad \Phi = V_c^2 \ln(r/r_0), \tag{5.42}$$

where V_c is the constant circular velocity assumed to be 200 km/s and r_0 is the point of zero potential assumed to be 10 kpc. For a bound test particle in this potential, its halocentric distance r will oscillate between the peri and apocenter with the period

$$T = 2\int_{r_1}^{r_2} \frac{\mathrm{d}r}{\sqrt{2\left[E - \Phi(r)\right] - L^2/r^2}}, \tag{5.43}$$

where r_1 and r_2 are the peri and apocenter of the orbit, which can be determined by solving the equation

$$\frac{1}{r^2} + \frac{2\left[\Phi(r) - E\right]}{L^2} = 0. \tag{5.44}$$

Due to the scale-free nature of the singular isothermal profile, the equations can be simplified by defining the maximum angular momentum $L_c(E) = r_c(E)V_c$, where $r_c(E)$ is the radius of the circular orbit with energy E given by

$$r_c(E) = r_0 \exp\left(\frac{E}{V_c^2} - \frac{1}{2}\right) \tag{5.45}$$

Based on this, the circularity parameter is defined as $\eta = L/L_c(E)$ and Equation 5.44 is reduced to

$$\frac{1}{x^2} + \frac{2\ln(x)}{\eta^2} - \frac{1}{\eta^2} = 0, \tag{5.46}$$

where $x \equiv r/r_c$ and the two solutions correspond to the peri and apocenter distances, which are independent of the energy of the test particle if normalized by $r_c(E)$. Similarly, if normalized by

$r_c(E)/V_c$, T also becomes independent of E. The look-up tables of T, r_1 and r_2 with respect to η are computed numerically. Here we do not consider the scattering and mergers of minihaloes within the parent halo and treat their orbits as unperturbed from various relaxation mechanisms.

Assuming spherical symmetry, the ergodic phase-space distribution function $f(\epsilon)$ can be derived through the Eddington inversion method

$$f(\epsilon) = \frac{1}{\sqrt{8}\pi^2}\frac{\mathrm{d}}{\mathrm{d}\epsilon}\int_0^\epsilon \frac{\mathrm{d}\psi}{\sqrt{\epsilon-\psi}}\frac{\mathrm{d}\rho}{\mathrm{d}\psi}, \tag{5.47}$$

where $\psi \equiv -\Phi$ and $\epsilon \equiv -E$. For the singular isothermal profile, the solution is simply the Boltzmann distribution

$$g(E) = K\exp\left(-2E/V_c^2\right), \tag{5.48}$$

where K is a constant normalization factor. Given a target radius for observation $r_{\rm obs}$, the normalized phase-space probability density function (PDF) of dark matter particles localized around $r_{\rm obs}$ is

$$f(E,L)|_{r_{\rm obs}} = \frac{4\pi}{r_{\rm obs}^2\rho(r_{\rm obs})}\frac{g(E)\,L}{\sqrt{2(E-\Phi(r_{\rm obs}))-L^2/r_{\rm obs}}}, \tag{5.49}$$

where $E \geq \Phi(r_{\rm obs})$ and $L \leq 2r_{\rm obs}\sqrt{E-\Phi(r_{\rm obs})}$ are required. Replacing L as $\eta L_c(E)$, we obtain

$$f(E,\eta)|_{r_{\rm obs}} = \frac{4\pi}{r_{\rm obs}\rho(r_{\rm obs})}\,g(E)\,L_c(E)\,\frac{\eta}{\sqrt{\eta_{\rm max}^2-\eta^2}}, \tag{5.50}$$

where $\eta \leq \eta_{\rm max} = r_{\rm obs}\sqrt{2(E-\Phi(r_{\rm obs}))}/L_c(E)$. Following [van den Bosch et al., 1999], we perform a Monte Carlo sampling of particles in the phase space based on this distribution function. For each sample particle, we compute its orbital period T, pericenter and apocenter distances r_1 and r_2 based on the look-up table created earlier. We note that because of the self-similar nature of the isothermal sphere, the value of r_1 and r_2 with respect to $r_{\rm obs}$ is independent of $r_{\rm obs}$, similarly for $T/T_{\rm circ}(r_{\rm obs})$. In Figure 5.9.12, we show the probability distribution function (PDF) of eccentricities, pericenter and apocenter distances and orbital periods of sampled minihalo orbits. The distribution should be self-similar for any target radius of observation. In the left panel of Figure 5.9.12, we compare the distribution of eccentricity derived here with that from [van den Bosch et al., 1999] which match perfectly. In the right panel of Figure 5.9.12, we compute the mean value of $N_{\rm p}/N_{\rm p}^{\rm circ} = T_{\rm circ}/T$

which gives us the correction factor for the number of passages through the stellar disk (compared to the circular orbit case) as $f_{N_\mathrm{p}} \equiv \langle N_\mathrm{p}\rangle_\mathrm{o}/N_\mathrm{p}^\mathrm{circ} \simeq 1.3$. $\langle\rangle_\mathrm{o}$ denotes averaging over all possible minihalo orbits. This correction factor is independent of the target radius of observation.

Assuming spherical symmetry, the orbit of a test particle will be confined in a plane and the precession of the orbit will eventually lead to a rosette-like pattern. The phase of the precession when the orbit cross the disk plane is random. Considering a large ensemble of dark matter particles, the distribution of the radial location where the encounter with the stellar disk takes place will be the same as the probability of the presence of the particle at that distance, and thus equivalent to the time-averaged radial distance of the test particle. Therefore, we have the averaged surface density given the orbit parameter E, L as

$$\langle\Sigma_*\rangle_\mathrm{x}\,(E,L) = \frac{2}{T}\int_{r_1}^{r_2}\frac{\Sigma_*(r)\,\mathrm{d}r}{\sqrt{2\,[E-\Phi(r)]-L^2/r^2}}, \tag{5.51}$$

where $\langle\rangle_\mathrm{x}$ denotes averaging over all past disk crossings and the stellar surface density profile $\Sigma_*(r)$ is given below Equation 5.24 following the measurements in [McMillan, 2011, 2017]. The average of the second order term $\langle\Sigma_*^2\rangle_\mathrm{x}$ can be obtained in a similar fashion. In the top panel of Figure 5.9.13, we show the distribution of $\langle\Sigma_*\rangle_\mathrm{x}/\Sigma_*(r_\mathrm{obs})$ at the target radius 8 kpc and the correction factor $f_{\Sigma_*}(r_\mathrm{obs}) \equiv \left\langle\langle\Sigma_*\rangle_\mathrm{x}/\Sigma_*(r_\mathrm{obs})\right\rangle_\mathrm{o}$ (averaging over all possible orbits) is about 1.16. We compute the value of f_{Σ_*} and $f_{\Sigma_*^2}$ at several different r_obs from 2 to 16 kpc and find that both $f_{\Sigma_*}(r_\mathrm{obs})$ and $f_{\Sigma_*^2}(r_\mathrm{obs})$ can be fitted by the functional form $A\,e^{B+(r_\mathrm{obs}/r_\mathrm{c})^\alpha}$. The best-fit parameters are $A = 0.106, B = 2.03, r_\mathrm{c} = 12.961, \alpha = 2.048$ for f_{Σ_*} and $A = 0.318, B = 0.781, r_\mathrm{c} = 5.740, \alpha = 1.628$ for $f_{\Sigma_*^2}$.

An additional correction will come from the enhanced surface density when the minihalo trajectory is not perpendicular to the disk plane. To the leading order, the effective surface density along the trajectory of the incident minihalo (as well as the time duration the minihalo stays in the disk) should scale as $1/\cos\theta$. Assuming the velocities of dark matter particles are isotropic, the correction factor is

$$f_\theta = \left\langle\frac{1}{\cos\theta}\right\rangle = \int_{H/r_\mathrm{d}}^{1}\frac{\mathrm{d}\cos\theta}{\cos\theta} = \ln\left(r_\mathrm{d}/H_\mathrm{d}\right) \simeq 2, \tag{5.52}$$

where we have imposed a cut-off at $\cos\theta = H_\mathrm{d}/r_\mathrm{d}$ with H_d and r_d the scale height and length of the

disk, assuming to be 400 pc and 3 kpc, respectively. Particles with even smaller incidence angles stay in the disk and will become completely disrupted (see Equation 5.24) which will have no impact on the averaged energy imparted. Combine the two effects above, we obtain the correction factor for the effective stellar surface density.

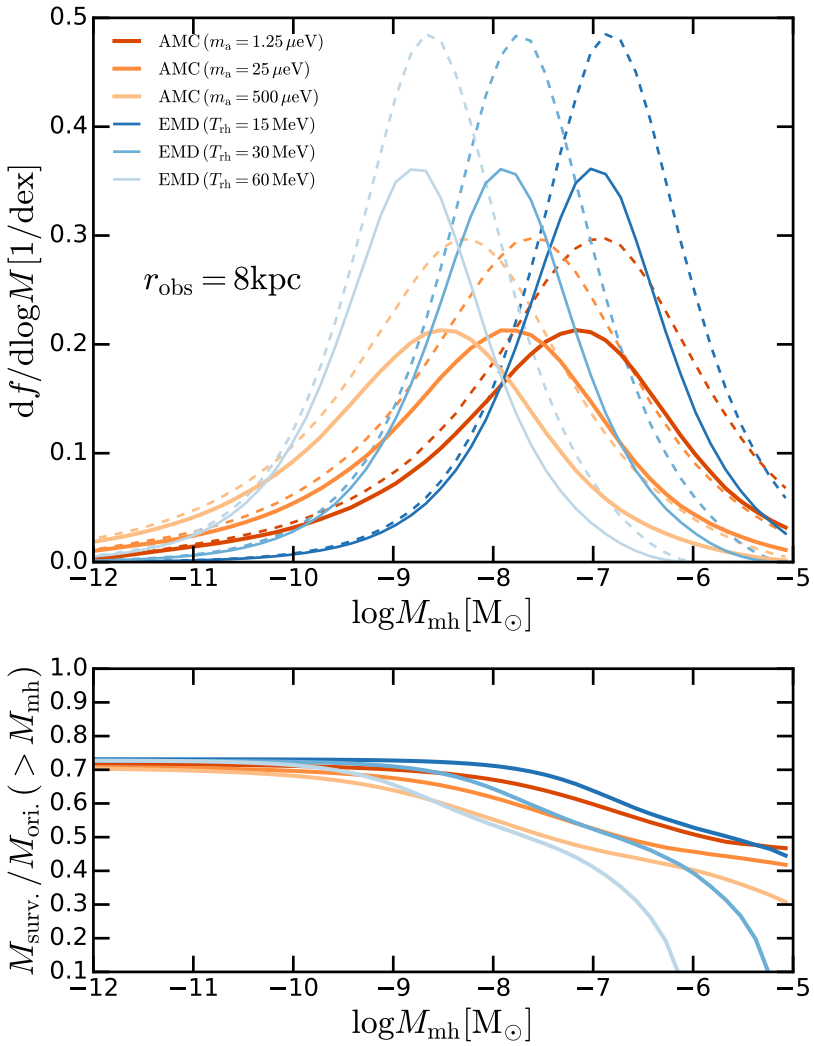

Figure 5.5.10: *Top:* Mass function of minihaloes in different models before (dashed) and after (solid) disruption. Two different models are studied: post-inflationary AMCs and EMD. The reheating temperature for the EMD era is $T_{\rm rh} = 15, 30, 60$ GeV while the axion mass in the post-inflationary AMC scenario is chosen as $m_a = 1.25, 25, 500\,\mu$eV. These parameters are purely chosen for illustrative purposes (especially for the EMD model) and one can use other parameters which will shift the mass range but the shape of the mass function will remain the same. *Bottom*: The integrated mass survival fraction of minihaloes for the models shown in the top panel. Regardless of the model choices, the overall survival fraction of minihaloes is around 70%.

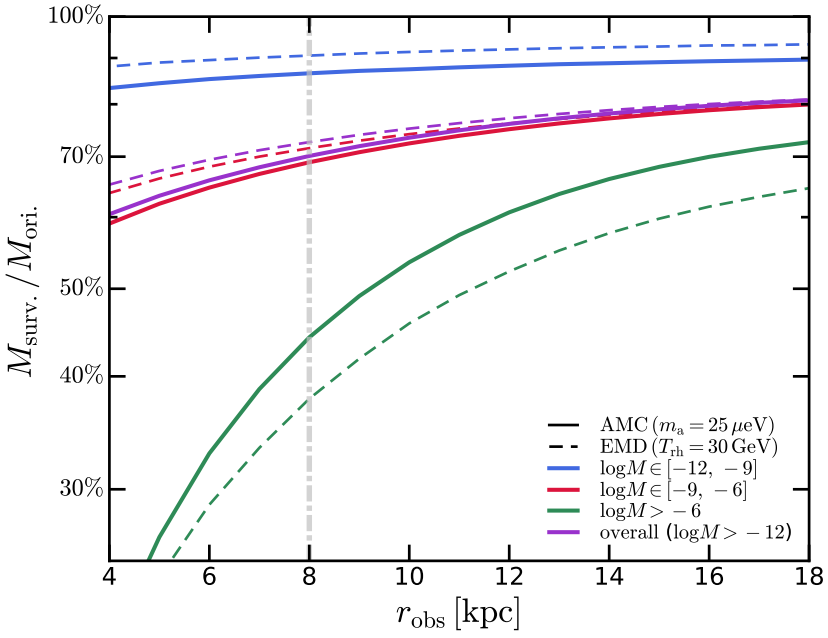

Figure 5.5.11: Mass survival fraction of minihaloes as a function of galactocentric distance. We show the survival (mass) fraction of minihaloes after stellar and tidal disruptions in three mass bins: $\log\left(M_{\rm mh}/[{\rm M}_\odot]\right) \in [-12, 9], (-9, -6], (-6, \infty)$.

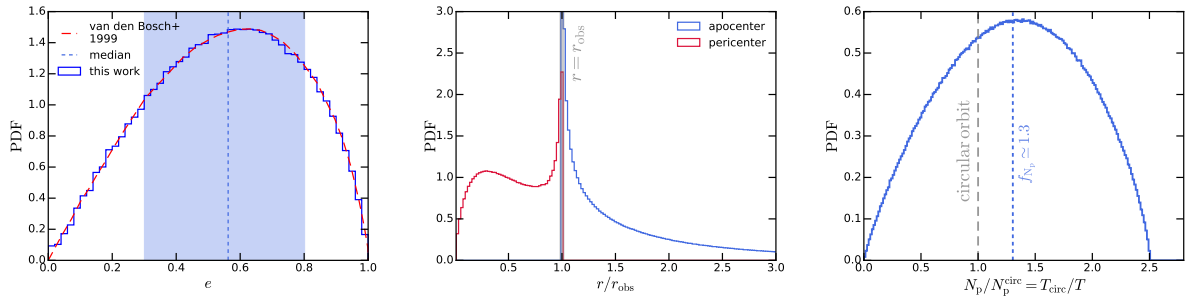

Figure 5.9.12: Distribution of eccentricities (left), pericenter and apocenter distances (middle) and orbital periods (or equivalently $N_{\rm p}$, right).

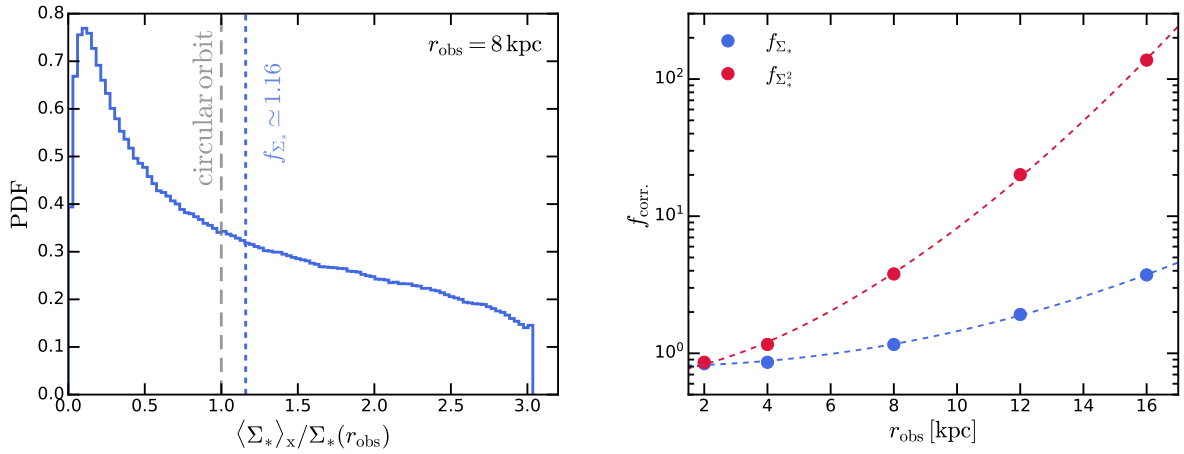

Figure 5.9.13: *Top*: Distribution of the surface density averaged over all past disk crossings. *Bottom*: The correction factor for Σ_* and Σ_*^2 as a function of $r_{\rm obs}$.

Chapter 6

RECURRENT AXINOVAE AND THEIR COSMOLOGICAL CONSTRAINTS

6.1 *Introduction*

The stars in our galaxy are made of $\sim 10^{57}$ fermions bound together by gravity and protected from collapse by thermal pressure or fermion degeneracy pressure. In the presence of a light, long-lived boson similar gravitationally bound states may exist, but in the absence of nuclear burning they are instead supported by gradient pressure, which is a result of the uncertainty principle. Axion stars are one such example of these bosonic objects.

In the Standard Model, stars convert approximately 0.1% of their mass energy into radiation over their lifetime. The small energy released (compared to rest mass) in the pp-chain, for instance, is due to the relatively small binding energy inside the star. Only very compact objects like neutron stars are relativistic in nature. Moreover, because of baryon number conservation, there is a limitation on overall energy release given the (approximately degenerate) neutrons and protons which must remain in the final state.

However, in the dark sector, there are reasons to expect the overall energy conversion could be much higher if a similar process were to occur. Complete conversion of rest mass from a $4 \rightarrow 2$ process is possible because there is no “baryon-number" conservation for bosonic dark matter. For example, axion stars will collapse and emit relativistic axions when they reach a critical mass. We call such processes that drastically convert dark matter to dark radiation as *Axinovae*. There is no mechanism to quench the axionovae if axion stars form ubiquitously in the Universe, as expected in the post-inflationary scenario where axion miniclusters form after matter-radiation equality. Therefore, a large formation rate of axion stars that lead to axinovae is very constraining. We take the formation of axion stars as a concrete example to study but the result can apply to

generic scalars whose self-interaction is attractive since the properties of axion stars do not depend on any interactions other than gravity and the axion self-couplings.

This paper is organized as follows: in Sec. 6.2, we discuss the formation of enhanced structures at small scales due to the axion perturbations and study the formation history of axion stars inside those structures. In Sec. 6.3, we study the constraints on axion parameter space by requiring the decay fraction of axion dark matter should not exceed an upper bound. In Sec. 6.4, we present our conclusions.

6.2 *Axions, Axion minihalos, and axion stars*

The axion is a well-motivated dark matter candidate, which can also leave unique fingerprint on the matter power spectrum at small scales if the PQ symmetry breaking occurs *after* inflation. In such scenarios, different horizon patches have different matter densities when the axion acquires its mass, leading to the formation of axion miniclusters or axion minihalos at matter-radiation equality. More interestingly, coherent objects called axion stars can form in the center of axion minihalos due to Bose-Einstein condensation, which may eventually accrete into a critical object and emit relativistic axions. We call such phenomenon axinovae, which occurs with an attractive axion self-coupling and the formation of axion minihalos at matter radiation equality.

Originally proposed to solve the strong CP problem Peccei and Quinn [1977], Weinberg [1978], Wilczek [1978], the present-day landscape of axions and axion-like particles (ALPs) is broad. One common feature across this landscape is that the axion, ϕ, is a pseudo-Goldstone boson of a global $U(1)_{PQ}$ symmetry broken at a scale f_a. The $U(1)_{PQ}$ is anomalous under a confining gauge group which means that the axion's potential is generated through instanton effects occurring at the compositeness scale of the gauge group, Λ, and takes the form

$$V(\phi) = \frac{\Lambda^4}{c_{ud}} \sqrt{1 - 4c_{ud}\, \sin^2\left(\frac{\phi}{f_a}\right)}\,. \tag{6.1}$$

In the case of the QCD axion $\Lambda \approx 200\,\mathrm{MeV}$ and $c_{ud} \approx m_u m_d/(m_u + m_d)^2 \approx 0.2$. In addition to the self couplings, coupling to gravity, and the anomaly-induced coupling to QCD (or QCD-like group), the axion may have model-dependent couplings to other SM gauge bosons and fermions.

We focus here on the self and gravitational couplings only, which can already lead to interesting dynamics such as axinovae.

6.2.1 Axion Minihalos

In the post-inflationary scenario, the present-day Universe contains a large number of patches which were causally disconnected at the time of QCD phase transition. In each causally disconnected patch of the Universe, axion field values are uncorrelated. Once the axion acquires a mass, and Hubble friction is small enough, axion behaves as cold dark matter and isocurvature fluctuations are present in the matter density. When the Universe becomes matter dominated this small-scale structure will start to collapse under gravity, leading to axion minihalos. Furthermore, there may be large overdensities of axions at even smaller scales arising from the evolution of the network of axion strings and domain walls [1] set up when the PQ symmetry breaks. Even for the much studied case of the QCD axion, there is controversy Gorghetto et al. [2018], Klaer and Moore [2017], Fleury and Moore [2016], Chang et al. [1999], Hagmann et al. [2001], Buschmann et al. [2022], Vaquero et al. [2019], Buschmann et al. [2020], Gorghetto et al. [2021], Kawasaki et al. [2018], Hiramatsu et al. [2011], Fleury and Moore [2016], Kawasaki et al. [2018], Klaer and Moore [2020], Vaquero et al. [2019], Buschmann et al. [2020], Gorghetto et al. [2021], Buschmann et al. [2022], Hindmarsh et al. [2020, 2021,] as to what fraction of the relic dark matter axions arose from misalignment or from the decay of topological defects. Along with those topological defects, objects called oscillons or axitons that can contribute to the small scale overdensities will form after the axion accquires its mass Buschmann et al. [2020], Vaquero et al. [2019]. Those objects can form when the axion self-interaction dominates over the Hubble expansion term, which is easily satisfied in the early Universe when the self-interaction is strong due to the high density. As the axion density drops, the formation of oscillons will be turned off and oscillons themselves will dissipate via emitting relativistic axions.

It is worth noting that the post-inflationary scenario is not essential for the axinovae. Any matter

[1] $N = 1$ for sanity

power spectrum which is enhanced at small scales can lead to the formation of axion minihalos around matter-radiation equality, but the post-inflationary scenario is a minimal realisation. We take a simple ansatz for the spectrum of initial fluctuations in the axion field, namely that the spectrum of isocurvature fluctuations in the axion field follow a white-noise spectrum, cut off at small scales *i.e.*

$$\frac{\delta\rho_a}{\rho_a} = A_0 \left(\frac{k}{k_0}\right)^3 \Theta(k_0 - k) \ . \tag{6.2}$$

Here $k_0 = a_{\rm osc} H_{\rm osc}$ is the (comoving) wavenumber determined by the horizon size at the time the axion starts to oscillate, *i.e.* $m_a(T_{\rm osc}) \sim 3H_{\rm osc}$. While here we consider a pure white noise spectrum we extend this analysis to a more general power law spectrum in Appendix 6.6. In reality one would expect a softening of the cutoff in the white noise power spectrum at small scales. The exact details of how this occurs is related to the dynamics of string network and axitons, and is unknown. It will not affect our conclusions, see Appendix 6.6 for details. As mentioned above, the contribution of strings and domain walls to the abundance of non-relativistic axions is uncertain and will impact the size of the power spectrum, we consider $A_0 = 0.1$ as a benchmark value Vaquero et al. [2019], Buschmann et al. [2020]. With this white noise power spectrum (6.2) the characteristic structure mass, defined as the peak in the distribution $dn/d\log M$, occurs at

$$M_{peak}(z) = \frac{A_0}{2\,\delta_c(z)^2} M_0 \ . \tag{6.3}$$

Where

$$M_0 = \frac{4\pi}{3}\overline{\rho}_0 \left(\frac{1}{k_0}\right)^3 \ , \tag{6.4}$$

is the co-moving mass in the horizon at the time the axion starts to roll and $\overline{\rho}_0$ is the present-day cosmological axion density. The subsequent evolution of the halo mass function is through the usual linear growth factor, encoded in $\delta_c(z) = 1.686(1+z)$. The minihalos have a distribution of masses but for simplicity we use the characteristic mass M_{peak} to provide a measure of the overall behavior. The growth continues till around $z \sim 10 - 20$ when the minihalos merge into standard CDM halos and their growth stalls Xiao et al. [2021].

We take the minihalos to have an NFW Navarro et al. [1996] density profile, defined by a scale

radius r_s and density ρ_s,

$$\rho(r) = \frac{\rho_s}{\frac{r}{r_s}\left(1+\frac{r}{r_s}\right)^2} \ . \tag{6.5}$$

At the scale radius the circular speed is given by

$$v_s^2 = 4\pi G_N \rho_s r_s^2 \left(\log 4 - 1\right) \ . \tag{6.6}$$

This speed will be relevant for the calculation of axion star formation rate. Numerical studies have shown that the dark matter halos at the characteristic mass will first rapidly grow to reach a concentration factor [2] $c \approx 4$ at the time of halo collapse Zhao et al. [2003]. For lighter halos that grow more through accretion than mergers, the halo concentration will grow linearly with the scale factor due to the decreasing background density. In the next subsections we discuss further structures that can develop in the core of these minihalos.

6.2.2 Lifecycle of an Axion Star

We now turn to the question of formation of axion stars at the core of the minihalos discussed above. The subsequent growth and explosion of axion stars (axinovae) will also be studied. As discussed in Appendix 6.5, there are two branches of axion star configurations: the dilute branch, which, below a certain mass, is stable and the dense branch which will blow up and emit relativistic axions. There is a critical star mass that separates the two branches. Therefore, if they continue to accrete mass, the lighter dilute axion stars will eventually become unstable in a minihalo environment. Axion minihalos are ideal environments for the axion star formation because they are dense and cold, owing to the high collapse redshifts and small virial masses. When the star formation rate is sufficiently large, stars will form in the minihalo center and grow to a critical mass star if the minihalo is massive enough. The critical star will contract under self-interaction and gravity, converting a large fraction of its mass to relativistic axions. Before the axinovae consume most of the minihalo mass, axion minihalos remain ideal environments for the axion star formation and

[2] The concentration is defined as the ratio $c = r_{200}/r_s$ where r_{200} is the radius at which the halos average density is 200 times the background DM density.

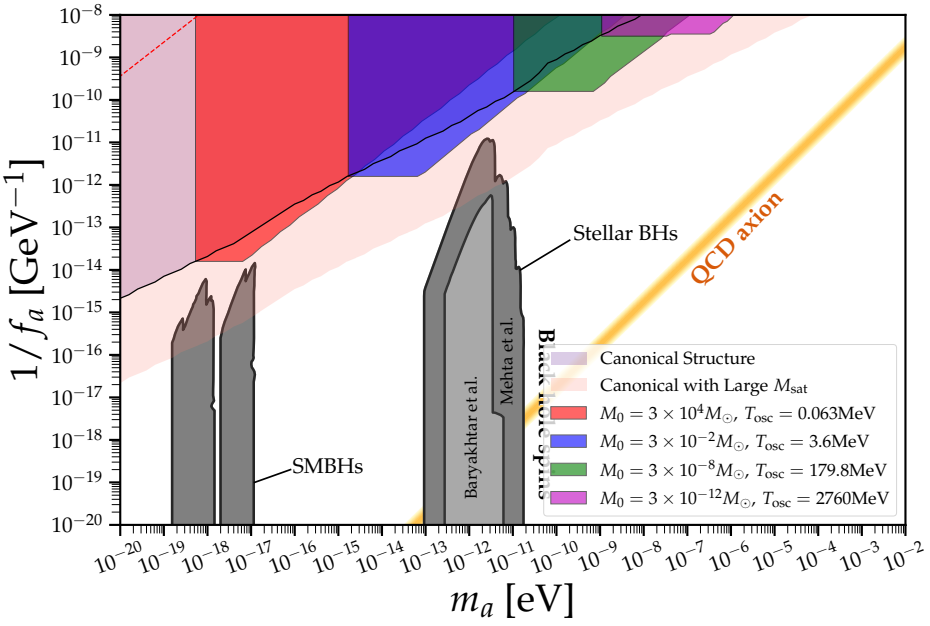

Figure 6.2.1: The exclusion plot of axion parameters in the scenario of enhanced small scale structures. The colored region represents the exclusion region with different characteristic structure masses while the light purple and pink region represents the canonical structure where the axion is at its zero-temperature mass when it starts to oscillate and imprint white-noise fluctuations between different horizon patches. Above the red dashed line, the Jeans scale is smaller than the size of dense axion stars at matter-radiation equality, leading to $O(1)$ formation of dense axion stars even without the enhanced structure formation on small scales. Our analysis is no longer applicable here but we still expect this region to be excluded for the same reason. Our constraints do not rely on non-gravitational couplings with the Standard Model sector. Therefore we only show the constraints from the black hole superradiance for comparison. The parameter space of QCD axion is also labeled for reference. This plot is generated with the Python notebooks in Ref. O'HARE [2020].

axinovae shall occur again within the same timescale. Thus there can be recurrent axinovae. The crucial calculation to determine the fate of axion stars is the formation rate in the minihalo center and the corresponding star mass.

Once minihalos exist, gravitational interactions or self-interactions can subsequently lead to the formation of Bose-Einstein condensed axion stars at their center. The timescale for this formation, and subsequent growth, in an environment where the axions being captured have typical number density n and speed v is determined Levkov et al. [2018], Eggemeier and Niemeyer [2019], Chen et al. [2021], Kirkpatrick et al. [2020] by

$$\tau \sim (f_{\rm BE} n \sigma v)^{-1} \ . \tag{6.7}$$

With σ the total scattering cross section. This formation rate is Bose-enhanced from the naive expectation due to the large phase space density, $f_{\rm BE} = 6\pi^2 n (m_a v)^{-3}$. The gravitational Rutherford transport cross section is $\sigma_{\rm gr} = 8\pi (G_N m_a v^{-2})^2 \log(m_a v R)$, where the Coulomb logarithm has been cutoff at a characteristic length scale of the minihalo, R. Attractive self-couplings can also lead to formation and the scattering cross section is $\sigma_{\rm self} = \lambda^2 m_a^{-2}/128\pi$. The total condensation time, considering both gravity and self-interaction, is

$$\tau_{\rm total} = \frac{\tau_{\rm self}\tau_{gr}}{\tau_{\rm gr} + \tau_{\rm self}}. \tag{6.8}$$

With each individual process having a timescale of

$$\tau_{\rm gr} = \frac{b}{48\pi^3} \frac{m_a v^6}{G_N^2 n^2 \log\left(m_a v R\right)} \ , \tag{6.9}$$

for gravity, and

$$\tau_{\rm self} = \frac{64 d m_a^5 v^2}{3\pi n^2 \lambda^2} \ . \tag{6.10}$$

The parameters $b, d \sim O(1)$ are numerical coefficients that are extracted from numerical simulations Chen et al. [2021]. Comparing these two timescales, (6.9) and (6.10), we see that the self interactions will determine the axion star formation rate if $f_a \lesssim M_{\rm pl} v$.

When determining the gravitational relaxation timescale for formation of axion stars in minihalos we take, as typical, the densities and speeds at the scale radius, see Eqs. (6.5) and (6.6). After their

initial condensation, axion stars can accrete axions from the surrounding minihalo and continue to grow in mass Levkov et al. [2018], Chen et al. [2021] with mass scaling as $M_* \propto \sqrt{t/\tau}$. However, since a dilute star shrinks in size as its mass grows (6.21) there will come a time when its radius is comparable to the de Broglie wavelength of the axions in the surrounding halo and the axions will no longer be able to effectively scatter off the axion star. For gradient pressure supported objects, which shrink in size as they grow in mass, there is an intrinsic tension in the capture process between the de Broglie wavelength and escape speed meaning that at some point the growth substantially slows. By equating the radius of the axion star to the de Broglie wavelength of axions in the minihalo, of mass M_h and density ρ_a, moving at the virial speed, the mass at which this growth saturates can be estimated Levkov et al. [2018], Eggemeier and Niemeyer [2019] to be

$$M_*^{\rm sat} \sim \rho_a^{1/6} G_N^{-1/2} m_a^{-1} M_h^{1/3} \,. \tag{6.11}$$

Growth beyond this mass can occur but at a considerably reduced rate. The scaling on the halo mass, axion mass, and halo density may depend on the central density profile while the above equation should hold for isothermal profiles Arvanitaki et al. [2020]. Assuming that power law growth still applies but with the speed of the captured axions now determined by the axion star's radius rather than the minihalo's virial speed *i.e.* $\tau \sim v^6 \sim M_*^6$ the growth is slowed to $M_* \propto (t/\tau_{\rm sat})^{1/8}$, where the saturation time is when the speed of captured axions becomes larger than the halo virial speed, $\tau_{\rm sat} = \tau_{\rm gr}(v_{\rm halo})$. Recently this predicted behavior of $t^{1/2}$ followed by $t^{1/8}$ growth, was confirmed in numerical simulations Chen et al. [2021]. Objects with the density profile of a minihalo containing an axion star in its core were identified in simulation and tracked from $t \sim \tau_{\rm sat}/10$ when their mass was to $M_* \sim M_*^{\rm sat}/\sqrt{10}$ to $t \geq \tau_{\rm sat}$. If the formation rate of axion stars is sufficiently large and axinovae are turned on, a single axion minihalo may form multiple stars within a Hubble time. This will require the critical mass to be smaller than the saturation mass. On the other hand, the timescale to form an axion star at critical mass is not as large as $\tau_{\rm gr}$ due to the growth behavior of axion stars that goes as $M \propto t^{1/2}$. Therefore, we expect the time we need to form a critical star is $t_{\rm crit} = \tau_{\rm gr}(M_*^{\rm max}/M_{\rm sat})^2$. The question arises as we evaluate the velocity in the expression of $\tau_{\rm gr}$ in Eq. (6.9): which radius to use? There are a few possible choices

here. One obvious option is the scale radius r_s, which can guarantee the majority of the axion minihalo can form a gravitational condensate and it is our choice for this work. The second option is to use the radius that can contain the saturation mass or the critical mass, which is mostly at a smaller radius than the scale radius because saturation mass is usually much smaller than the halo mass. This choice is valid when we only consider the depletion of one saturation star. However, we would like to study the recurrent axinovae and a significant fraction of the axion minihalo will convert to radiation. The third choice is the radius of a critical star, which can be very confusing when the critical star mass is much smaller than the saturation mass, in which case the star radius can be much greater than the halo size because the axion star radius is inversely proportional to its mass. However, that conclusion does not hold when a background gravitational potential is present. We still expect the star radius to be small at small masses if the gravitational potential is dominated by the minihalo. This is often the case that the minihalo provides most of the gravity because the condition of saturating the star growth is having the same virial velocity for both axion minihalos and axion stars, suggesting axion stars start to become self-gravitating at the moment of saturation.

Given that the majority of the dark matter has collapsed into axion minihalos with a characteristic mass $M_c(z)$, the rate of dark matter decay at any redshift can be calculated as

$$\frac{df_{\rm decay}}{dt} = \frac{\alpha_a}{\tau_{\rm total}(z)} \frac{M_*^{\rm sat}(z)^2}{M_*^{\rm max} M_c(z)} \Theta\left(M_*^{\rm sat}(z) - M_*^{\rm max}\right) \ , \tag{6.12}$$

where α_a is the fraction of axion stars that convert to relativistic axions during axinovae, which is take to be $\sim 10\%$ in this work. The total decay fraction is of course capped at $f_{\rm decay} = 1$ where all of the axion dark matter has been depleted. In realistic scenarios, this will not happen because our formulae are only valid when the conversion of dark matter to dark radiation is a small perturbation and there will be feedback effects. However, this is sufficient for the purpose of placing constraints because feedback effects are only relevant in situations where constraints would have excluded the parameter point already.

6.3 *Cosmological Constraints*

The fact that axions can generically form axion stars and lead to axinovae is constrained by cosmological observations if a significant fraction of energy in dark matter is converted to dark radiation in this scenario. This process is closely related to the scenario of decaying dark matter, which is well constrained by recent cosmological data Poulin et al. [2016], Bringmann et al. [2018], Nygaard et al. [2021]. For decaying dark matter which decays after recombination, the decrease of the dark matter fraction will increase the angular diameter distance to the last scattering surface over time. Furthermore, the amount of CMB lensing is reduced due to a smaller gravitational potential than expected. This scenario is constrained by a combination of CMB Aghanim et al. [2020] and, for very long lived dark matter, SDSS Dawson et al. [2013] data. If the decay of dark matter occurs well before recombination or even before matter-radiation equality, the primary effect of the decaying dark matter is to enhance $N_{\rm eff}$ since the decay products behave as dark radiation. In the short-lived situation the constraints are primarily from CMB measurements. We will be interested in the long-lived case, and in particular decays which occur after matter-radiation equality but are no longer ongoing. The equivalent bound Nygaard et al. [2021] for decaying dark matter on the fraction of the initial amount of dark matter that will decay is

$$f_{dDM} \equiv \frac{\Omega_{dDM}}{\Omega_{dDM} + \Omega_{DM}} \leq 2.62\% \quad (\text{at } 2\sigma) \ . \tag{6.13}$$

Although the cosmological evolution of the dark sectors for decaying dark matter and axinovae are not identical they will be similar and since the above constraint is independent of decaying dark matter lifetime over a wide range of lifetimes we will use it to constrain axions. We leave a more detailed `CLASS` Blas et al. [2011] based numerical analysis for future work.

In the scenario of axinovae, the decay of dark matter always occurs after matter-radiation equality when axion miniclusters start to form. To avoid the constraint of (6.13) requires either that the formation rate of axion stars is too small to be cosmologically relevant or that the formed axion star mass is smaller than the critical mass so there is no axinovae. There are three parameters that determine the amount of axion dark matter that is converted to dark radiation: the axion mass m_a, the decay constant f_a, and the structure mass M_0. Note that this does not rely upon a coupling to

photons, gluons, or SM fermions. However, our constraints do rely on the assumption that axions can produce the dark matter relic abundance. There are a few possible scenarios that will increase or decrease the relic abundance. If the dark phase transition that gives axion mass occurs at a sufficiently late time, the relic abundance can always be larger because the axion density during phase transition is always given by the axion potential. Decay from the string networks can increase the relic abundance by more than one order-of-magnitude Gorghetto et al. [2021]. On the other hand, entropy dump during the phase transition in nonstandard cosmological scenarios can decrease the axion relic density Nelson and Xiao [2018], Visinelli and Redondo [2020], Blinov et al. [2019]. Therefore, we assume the dark matter relic abundance can be produced with the axion parameters of interest in this work.

There are three parameters in the post-inflationary scenario of axions: axion mass m_a, decay constant f_a and the structure mass M_0. The critical axion star mass, above which dilute axion stars are unstable, is determined by the microphysics (m_a, f_a). Whether such objects have an opportunity to form in the Universe's evolution is determined by the history of structure formation (M_0). The amplitude A_0 might also affect axinovae by changing the structure mass. Also, the overall amplitude at the cutoff scale A_0/α^3 determines if the smallest structures can form at matter-radiation equality. When the overall amplitude decreases, axion minihalos will be less dense, leading to a smaller formation rate of axion stars. In this work, we discuss the scenario where axion minihalos form at matter-radiation equality, which is consistently to numerical studies on the axion perturbations induced by string networks in the early Universe Buschmann et al. [2020], Vaquero et al. [2019]. One could also consider other models and treat the amplitude as a free parameter. As discussed earlier (6.4), when the halos initially form their typical mass depends upon the horizon size when the axion starts to oscillate $m_a(T_{\rm osc}) = 3H(T_{\rm osc})$. For the QCD axion, where the temperature dependence of the axion mass is known, this oscillation time is uniquely determined. However, in more general axion scenarios the oscillation temperature, and therefore M_0, is a free parameter. In the radiation dominated era $H(T) = \pi\,(8\pi g_*(T)/90)^{1/2}\,T^2/M_{Pl}$ and the halos form with mass,

$$M_0 = \frac{4\pi}{3}\left(\frac{1}{a(T_{\rm osc})H(T_{\rm osc})}\right)^3 \overline{\rho}_0 \approx 0.1\left(\frac{M_{pl}}{T_0 T_{\rm osc}}\right)^3 \overline{\rho}_0\,. \tag{6.14}$$

The existence of DM structure down to small scales requires that the axions behave as dark matter by the time the temperature of the Universe is $\sim$ keV, *i.e.* $T_{\rm osc} \gtrsim 1\,{\rm keV}$. Thus, there is an upper bound on the initial halo mass

$$M_0 \lesssim 2 \times 10^8 \ . \tag{6.15}$$

Furthermore, assuming that $m_a(T) < m_a(0)$, which is the case for the QCD axion, the smallest object that can form is when the axion starts oscillating with its zero-temperatures mass, $T_{\rm osc} = \sqrt{m_a M_{pl}/3}$. We will plot constraints for axion parameters m_a, f_a under different assumptions for M_0.

As discussed above, rather than consider the whole distribution of minihalo masses we focus instead on the characteristic mass $M_{\rm c}(z)$, which evolves with redshift. This provides a good description to the overall behavior because the majority of the dark matter mass is contained in halos of mass M_c. As times evolves, the characteristic mass grows as $M_h \sim (1+z)^{-2}$ as minihalos merge with each other. Since a characteristic mass halo has concentration $c \approx 4$ its scale radius and density vary with redshift as $r_s \sim (1+z)^{-5/3}$, $\rho_s \sim (1+z)^3$. From Eqs. (6.6),(6.9), and (6.11) this implies that the time scale for collapse and the saturation mass in a halo scale as $\tau_{gr} \sim (1+z)^{-7}$, $M_*^{\rm sat} \sim (1+z)^{-1/6}$. This rapid lengthening of the axion star formation time as the Universe ages means that the dominant DM mass loss occurs as soon as the saturation mass is larger than the critical star mass, and the earlier that occurs the greater the fraction lost. This can be seen by keeping only the dependence on z and axion parameters in the decay rate (6.12)

$$\begin{aligned}\frac{df_{\rm decay}}{dz} &\sim 48\alpha_a\pi^2(1-f_{\rm decay})(1+z_{\rm eq})^{-26/3}(1+z)^{37/6} \\ &\times \frac{\rho_{\rm eq}^{4/3}M_{\rm pl}^3}{m_a^4 M_0^{7/3} f_a H_0}\left(1+\frac{1.06\times 10^4 M_0^{4/3}\rho_{\rm eq}^{2/3}(1+z)^2}{f_a^4(1+z_{\rm eq})^2}\right) \\ &\times \Theta\left(0.1\rho_{\rm eq}^{1/6}M_0^{1/3}((1+z)/(1+z_{\rm eq}))^{-1/6} - f_a\right) \ ,\end{aligned} \tag{6.16}$$

where we have suppressed the logarithmic corrections from the Rutherford cross section in (6.9). $\rho_{\rm eq}$ is the halo central density at matter-radiation equality.

This scaling means that for any initial halo mass M_0 there will always be an axion mass below which the timescale for star formation is shorter than the age of the Universe. Furthermore, since

both the star saturation mass (6.11) and the axion star critical mass (6.22) scale inversely with the axion mass once the timescale is short enough there will be maximal f_a below which the critical star is lighter than the saturation mass and thus the critical star can form. This region, bounded in $m_a - f_a$ space will be constrained by the cosmological data discussed above. In particular (6.12)

$$\int_{z_{\rm eq}}^{z=20} dz \, \frac{df_{\rm decay}}{dz} \leq 2.62\% \, . \tag{6.17}$$

The exclusions regions are show in Fig. 6.2.1. The shape of each excluded region with fixed M_0 is a combination of effects. The right-hand edge is due to the formation time $\tau_{\rm gr}$ becoming too long. The lower edge, which is independent of m_a, is due to the critical star mass (6.22) necessary for the instability to occur becoming larger than the saturation mass of the halo (6.11). Since both masses scale inversely with m_a the boundary only depends upon M_0 and f_a. There is however some uncertainty Mocz et al. [2017], Padilla et al. [2021] in the exact size of the $M_*^{\rm sat}$ so we also present results for the case of the saturation mass being increased by a factor of 200. The left edge of each excluded region arises because the lowest possible temperature at which the axion can start to oscillate, and therefore smallest possible M_0, occurs when $m_a(T_{\rm osc}) = m_a$. In Fig. 6.2.1, we also plotted a red dashed curve above which the Jeans scale is smaller than the dense axion star radius at matter-radiation equality. In such scenario, most of the axion dark matter will fragment to dense axion stars (or sometimes called oscillons in the early Universe) at that time even without the formation of axion miniclusters. Those objects are not cosmologically stable and will convert a large fraction of matter to radiation, which shall still be excluded. The main reason that the axionovae scenario is constraining the axion parameter space is because the formation history of axion stars is solely determined by the substructure formation while the explosion of axion stars is set by the self-coupling, which have distinct origins.

6.4 *Conclusions*

We obtain new bounds on axion dark matter parameters m_a, f_a assuming the formation of dense axion minihalos, motivated by the post-inflationary scenario. Axion perturbations in the post-inflationary scenario will lead to the formation of dense substructures known as axion miniclusters

or minihalos after matter-radiation equality, which can subsequently form coherent objects known as axion stars at the core of axion minihalos. The horizon size when axions start to oscillate k_0 determines the characteristic structure mass while the amplitude A_0 determines when the structures form. Dilute axion stars, supported by gradient pressure, can be cosmologically stable. However, they will accrete more axions from minihalos and continue to grow until the axion self-coupling turns on and the gradient pressure can not stop them from collapsing and emitting relativistic axions. The critical mass of axion stars depend on particle physics parameters m_a and f_a. It is cosmologically constraining if the formation rate is large enough and axinovae are turned on, which converts a significant fraction of matter to radiation. Our constraints only depend on the axion self-coupling and gravity, which can be mapped to axion-photon and axion-neutron couplings in specific models. Those constraints are obtained by requiring the population of dense axion stars formed in axion minihalos at high redshifts shall not dominate the mass of dark matter. If axion is only a fraction of dark matter or only a few percents of axion dark matter is decaying, the conversion to dark radiation may be cosmologically significant in future observations but consistent with the current data. A more sophisticated treatment on the cosmological evolution will be needed for future studies.

Appendix

6.5 *Axion Star Configurations*

The stable axion-field configuration for the gravitational bound-state of non-relativistic axions can be found by solving the Gross-Pitaevskii-Poisson equations, which must be done numerically. However, it has been shown that a good approximation of these solutions is obtained by using a Gaussian ansatz for the field profile Chavanis [2011], Chavanis and Delfini [2011], Chavanis [2016]. Doing so gives some insight into the competing effects driving the physicsVisinelli et al. [2018]. Expanding the axion potential (6.1) to quartic order one finds an attractive self interaction

$$V = \frac{1}{2}m_a^2\phi^2 - \frac{\lambda}{4!}\phi^4 \,, \tag{6.18}$$

with $\lambda = (1-3c)m_a^2/f_a^2$. An axion star of mass M_* and radius R_* has energy

$$E_* = -\frac{G_N M_*^2}{R_*} + c_1 \frac{M_*}{2\, m_a^2 R_*^2} - c_2 \frac{\lambda M_*^2}{12\, m_a^4 R_*^3} \,. \tag{6.19}$$

In order, these terms correspond to the gravitational self energy, the gradient pressure, and the internal energy from self interactions. The numerical coefficients, c_i, depend upon the details of the field profile and are found numerically Ruffini and Bonazzola [1969], Membrado et al. [1989], Visinelli et al. [2018] to be $c_1 = 9.9$, $c_2 = 0.85$. The mass-radius relation for axion stars, found by minimizing E_*, has two solutions

$$R_*^{\pm} = \frac{c_1}{2\, G_N M_* m_a^2} \left(1 \pm \sqrt{1 - \frac{c_2}{c_1^2}\lambda G_N M_*^2}\right) \,. \tag{6.20}$$

The R_*^+ root corresponds to the so-called dilute branch and the axion field value is small. On this branch gravitational attraction is balanced by gradient pressure leading to a stable configuration. As is typical for objects supported by uncertainty pressure the product of the radius and mass of the star is a constant

$$R_*^+ = 9.9 \frac{M_{\rm pl}^2}{m_a^2 M_*} \,. \tag{6.21}$$

However, as one moves to larger axion star mass the self interactions cannot be ignored and if they are attractive (as asummed above) they destabilise the star. There is a maximal mass, beyond which axion stars are no longer stable

$$M_*^{max} = \frac{10.7}{\sqrt{\lambda}} M_{\rm pl} \,. \tag{6.22}$$

The two solutions meet at this maximal mass. The second solution is one where gravity can be ignored and the gradient pressure and the axion's attractive self interactions are in unstable equilibrium. On this branch $R_* \sim M_*$.

The value of the axion field at the center of the star scales as $a_0^2 \sim M_*/(m_a^2 R_*^3)$ so that at the low mass end of the R_*^- branch $a_0 \sim 1$ and the axion field is not dilute. The axions can no longer be thought of as non-relativistic and the solution is approximately constant density ($\rho \sim m_\pi^2 f_\pi^2$) and thus $R_* \sim M_*^{1/3}$. However, it is believed that this field configuration is also unstable, with a lifetime $\sim 10^3 m_a^{-1}$ Visinelli et al. [2018], although alterations to the axion potential can make

these solutions long lived Cyncynates and Giurgica-Tiron [2021], Kawasaki et al. [2020], Olle et al. [2021].

The upshot of this is that if a dilute axion star with mass below $M_*^{\max}$ were to form and grow, by accumulation of additional axions, to the maximal mass it would then shrink in size and become a dense axion star which would survive for a short period. During this time the dense axion star goes through several oscillations and a density singularity develops in the central core and this dense region emits relativistic axions lowering the density Levkov et al. [2017]. This process repeats and $\sim 30\%$ of the initial star mass can be emitted, leaving a dilute remnant which may in turn grow to the maximal mass and emit more relativistic axions. Thus, maximal mass stars are an engine to turn substantial amounts of cold dark matter into radiation.

6.6 *Press-Schechter with White Noise-like power at short distances*

For simplicity we take the power spectrum to be scale invariant at large scales and power law at low scale, with a simple cut-off at very small scales. For the case of the axion it is believed the short-scale behavior is approximately white noise parametrize, corresponding to $n = 3$ below. Thus we parametrize the power spectrum as

$$\frac{k^3 P(k)}{2\pi^2} = \begin{cases} A_1 \,, & k \le k_1 \\ A_0 \left(\frac{k}{k_0}\right)^n \,, & k_1 < k \le k_0 \\ 0 \,, & k > k_0 \end{cases} . \tag{6.23}$$

Note that this only depends upon four parameters (A_0, A_1, k_0, n) and continuity requires

$$k_1 = \left(\frac{A_1}{A_0}\right)^{1/n} k_0 \,. \tag{6.24}$$

We will be interested in the regime $A_1 < A_0$ and thus require $n > 0$. An input to the Press-Schechter formalism is the variance of the density field which is given by

$$\sigma^2(R) = \int \frac{dk}{k} \frac{k^3 P(k)}{2\pi^2} \left|\widetilde{W}(kR)\right|^2 \,, \tag{6.25}$$

where $\widetilde{W}(kR)$ is the window function and can take various forms. For now we focus on the so-called sharp k-filter where $\widetilde{W}(z) = \Theta(1-z)$. For this choice of window function there is not a well defined mass, M, associated with a filter scale R, since the real space form of $\widetilde{W}$ does not have local support Maggiore and Riotto [2010]. However, we will follow the oft-used relation $M = 6\pi^2\rho R^3$ Lacey and Cole [1993], where in co-moving coordinates $\rho = \overline{\rho}_0$ the present day cosmological axion density. Note that for (6.25) to be well defined we have to introduce an IR cut-off k_{IR} and we define $M_0 = 6\pi^2\overline{\rho}k_0^{-3}$. Thus the variance is,

$$\sigma^2(M) = \begin{cases} c & M \leq M_0 \\ c - \frac{A_0}{n}\left(1 - \left(\frac{M_0}{M}\right)^{n/3}\right) & M_0 < M \leq \left(\frac{A_0}{A_1}\right)^{3/n} M_0 \\ c + \frac{A_1}{n}\left(\log\frac{A_0}{A_1} + 1\right) - \frac{A_0}{n} - \frac{A_1}{3}\log\frac{M}{M_0} & M > \left(\frac{A_0}{A_1}\right)^{3/n} M_0 \end{cases} . \tag{6.26}$$

where

$$c = \frac{A_1}{n}\left(\log\frac{A_1}{A_0} + n\log\frac{k_0}{k_{IR}}\right) + \frac{A_0 - A_1}{n} . \tag{6.27}$$

We are typically interested in $A_1 \ll 1$ and $A_0 \sim 0.1$ so $c \longrightarrow A_0/n$ and (6.26) also simplifies

$$\sigma^2(M) \sim \frac{A_0}{n} \times \begin{cases} 1 & M \leq M_0 \\ \left(\frac{M_0}{M}\right)^{n/3} & M > M_0 \end{cases} . \tag{6.28}$$

Recall that in PS formalism the halo mass function behaves as $dn/dM \sim \delta_c/\sigma(M)e^{-\delta_c^2/\sigma^2(M)}$ with $\delta_c(z) \sim 1.686(1+z)/(1+z_{\rm eq})$. Thus, the peak in the reweighted halo mass function $M^m dn/dM$ occurs at

$$M_{peak} = \left(\frac{n+6m}{2n^2}\frac{A_0}{\delta_c(z)^2}\right)^{3/n} M_0 . \tag{6.29}$$

Chapter 7

CONCLUSION

Our current theories about the Universe and particle physics have been very successful in many respects. The theory prediction largely agrees with experiments and observations from colliders to the sky. However, a few big puzzles still remain to be solved and dark matter is definitely one of most exciting ones. The axion, motivated from solving the strong CP problem, is also a solution to the dark matter problem. If the axion, either QCD axion or ALPs, is our dark matter candidate, future astrophysical observations can help us test this hypothesis. The axion Universe reveals an interesting possibility that enhanced substructures with planetary masses can form in the early Universe. This allows us to hunt for the axion dark matter in the sky. Moreover, axion substructures are also ideal environments for the axion star formation, which gives us rich phenomenology that might be detectable with future observations.

In the so called post-inflationary scenario, the Peccei-Quinn symmetry is broken after inflation and axion miniclusters are supposed to form due to the different axion field values in different horizon patches. However, axion miniclusters can also form with nonstandard thermal histories in the pre-inflationary scenario as we discussed in Chapter 2. We also found the story of axion cosmology, including the axion relic density and the characteristic mass of axion miniclusters will take different numbers in modified thermal histories.

In Chapter 3, We studied the evolution of axion minicluster and minihalos in the early Universe with N-body simulations, including its mass function and mass profiles, which will ultimately determine if those minihalos can be detectable. We found that while there are uncertainties at high k modes in the axion perturbations, the majority of the mass in minihalos will be at the massive end and therefore the overall behavior is dominated by relatively low k modes, which are well described by a white-noise power spectrum. The fluctuations are Gaussian at the lower k and we find that a

tweaked version of Sheth-Tormen mass function can well fit our simulation data. The mass profiles are well described by the NFW profile and we find that the mass-concentration relation agrees well with analytical predictions. These results will be important for the observability of axion minihalos as well as the axion star formation rate in these minihalo objects.

When we extend the axion models to a broader spectrum and consider axions motivated from other theories such as the string theory, ultralight axion-like particle can be a dark matter candidate that has interesting observational signatures. Similar to QCD axions, the post-inflationary scenario can lead to enhanced structure formation on small scales which can be constrained by existing observations such as the number of high-redshift dwarf galaxies, the reionization history, and the Lyα forest, as discussed in Chapter 4. We considered all these observables and found that the Lyα forest has the best sensitivity and constraining power. We also showed future $z \sim 20 - 30$ 21cm observations can improve these constraints further using that the supersonic motions of the axion minihalos with masses of $10^4 M_\odot$ would shock heat the baryons, sourcing large BAO features.

In Chapter 5, we studied the stellar disruption and tidal disruption of axion minihalos in the Milky Way environments. While we have established the cosmological simulations for the evolution of minihalos in the early Universe, the disruption effects in the Milky Way are crucial for local observations such as PTAs. However, this problem is also challenging due to the large dynamical range. The minihalo is as small as $10^{-12} M_\odot$, while the Milky Way dark matter halo has a mass of $10^{12} M_\odot$. We use N-body simulations to study the stellar disruption of minihalos encountering with individual stars and use the simulation results to calibrate the analytic formula. The same strategy is applied to the tidal stripping effect, which allows us to extend our prediction to larger scales. We also combine the tidal and stellar disruption nonlinearly and find that the stellar disruption is the dominating effect. The mass function of axion minihalos after disruption is predicted, which suggests that future PTA observations will still be sensitive to these minihalos as only $\sim 50\%$ of them have been disrupted. This method can easily be applied to generic models that can lead to enhanced substructures.

In Chapter 6, we studied the axion star formation rate and its cosmological constraints. The dense minihalos are ideal environments for the axion star formation since they are dense and cold.

Therefore, we expect axion stars to form inside those dense structures. The stable solution of axion field configurations show that axion stars above the critical mass will collapse and emit relativistic axions. Once these stars accrete to its critical mass, most of their mass will be converted into relativistic axions through self-couplings. We call this process axinova. The recurrerent axinovae will deplete the mass in axion minihalos and convert them to radiation, which should be constrained by cosmology. This will allow us to place constraint on axion parameters.

This thesis has been focused on the observational signatures of axion dark matter in cosmological and astrophysical observations, which are complementary to the direct detection experiments. The phenomenology of axion dark matter in the sky is rich and a lot of theoretical predictions have been made in this thesis. However, there are still exciting paths ahead that can lead us to interesting results. For example, the radio signals from axion minihalos or axion stars are not well understood yet. Moreover, the individual mass of each axion star inside each minihalo is also uncertain, which requires both numerical and analytical methods to help us understand the accretion process better. We expect the coming years will see more progress in these directions both on the theoretical and the observational sides. Such progress may lead even to evidence that axions are the dark matter.

BIBLIOGRAPHY

[1] Kevork Abazajian, Graeme Addison, Peter Adshead, Zeeshan Ahmed, Steven W. Allen, David Alonso, Marcelo Alvarez, Adam Anderson, Kam S. Arnold, Carlo Baccigalupi, Kathy Bailey, Denis Barkats, Darcy Barron, Peter S. Barry, James G. Bartlett, Ritoban Basu Thakur, Nicholas Battaglia, Eric Baxter, Rachel Bean, Chris Bebek, Amy N. Bender, Bradford A. Benson, Edo Berger, Sanah Bhimani, Colin A. Bischoff, Lindsey Bleem, Sebastian Bocquet, Kimberly Boddy, Matteo Bonato, J. Richard Bond, Julian Borrill, François R. Bouchet, Michael L. Brown, Sean Bryan, Blakesley Burkhart, Victor Buza, Karen Byrum, Erminia Calabrese, Victoria Calafut, Robert Caldwell, John E. Carlstrom, Julien Carron, Thomas Cecil, Anthony Challinor, Clarence L. Chang, Yuji Chinone, Hsiao-Mei Sherry Cho, Asantha Cooray, Thomas M. Crawford, Abigail Crites, Ari Cukierman, Francis-Yan Cyr-Racine, Tijmen de Haan, Gianfranco de Zotti, Jacques Delabrouille, Marcel Demarteau, Mark Devlin, Eleonora Di Valentino, Matt Dobbs, Shannon Duff, Adriaan Duivenvoorden, Cora Dvorkin, William Edwards, Joseph Eimer, Josquin Errard, Thomas Essinger-Hileman, Giulio Fabbian, Chang Feng, Simone Ferraro, Jeffrey P. Filippini, Raphael Flauger, Brenna Flaugher, Aurelien A. Fraisse, Andrei Frolov, Nicholas Galitzki, Silvia Galli, Ken Ganga, Martina Gerbino, Murdock Gilchriese, Vera Gluscevic, Daniel Green, Daniel Grin, Evan Grohs, Riccardo Gualtieri, Victor Guarino, Jon E. Gudmundsson, Salman Habib, Gunther Haller, Mark Halpern, Nils W. Halverson, Shaul Hanany, Kathleen Harrington, Masaya Hasegawa, Matthew Hasselfield, Masashi Hazumi, Katrin Heitmann, Shawn Henderson, Jason W. Henning, J. Colin Hill, Renée Hlozek, Gil Holder, William Holzapfel, Johannes Hubmayr, Kevin M. Huffenberger, Michael Huffer, Howard Hui, Kent Irwin, Bradley R. Johnson, Doug Johnstone, William C. Jones, Kirit Karkare, Nobuhiko Katayama, James Kerby, Sarah Kernovsky, Reijo Keskitalo, Theodore Kisner, Lloyd Knox, Arthur Kosowsky, John Kovac,

Ely D. Kovetz, Steve Kuhlmann, Chao-lin Kuo, Nadine Kurita, Akito Kusaka, Anne Lahteenmaki, Charles R. Lawrence, Adrian T. Lee, Antony Lewis, Dale Li, Eric Linder, Marilena Loverde, Amy Lowitz, Mathew S. Madhavacheril, Adam Mantz, Frederick Matsuda, Philip Mauskopf, Jeff McMahon, Matthew McQuinn, P. Daniel Meerburg, Jean-Baptiste Melin, Joel Meyers, Marius Millea, Joseph Mohr, Lorenzo Moncelsi, Tony Mroczkowski, Suvodip Mukherjee, Moritz Münchmeyer, Daisuke Nagai, Johanna Nagy, Toshiya Namikawa, Federico Nati, Tyler Natoli, Mattia Negrello, Laura Newburgh, Michael D. Niemack, Haruki Nishino, Martin Nordby, Valentine Novosad, Paul O'Connor, Georges Obied, Stephen Padin, Shivam Pandey, Bruce Partridge, Elena Pierpaoli, Levon Pogosian, Clement Pryke, Giuseppe Puglisi, Benjamin Racine, Srinivasan Raghunathan, Alexandra Rahlin, Srini Rajagopalan, Marco Raveri, Mark Reichanadter, Christian L. Reichardt, Mathieu Remazeilles, Graca Rocha, Natalie A. Roe, Anirban Roy, John Ruhl, Maria Salatino, Benjamin Saliwanchik, Emmanuel Schaan, Alessandro Schillaci, Marcel M. Schmittfull, Douglas Scott, Neelima Sehgal, Sarah Shandera, Christopher Sheehy, Blake D. Sherwin, Erik Shirokoff, Sara M. Simon, Anze Slosar, Rachel Somerville, David Spergel, Suzanne T. Staggs, Antony Stark, Radek Stompor, Kyle T. Story, Chris Stoughton, Aritoki Suzuki, Osamu Tajima, Grant P. Teply, Keith Thompson, Peter Timbie, Maurizio Tomasi, Jesse I. Treu, Matthieu Tristram, Gregory Tucker, Caterina Umiltà, Alexand er van Engelen, Joaquin D. Vieira, Abigail G. Vieregg, Mark Vogelsberger, Gensheng Wang, Scott Watson, Martin White, Nathan Whitehorn, Edward J. Wollack, W. L. Kimmy Wu, Zhilei Xu, Siavash Yasini, James Yeck, Ki Won Yoon, Edward Young, and Andrea Zonca. CMB-S4 Science Case, Reference Design, and Project Plan. *arXiv e-prints*, art. arXiv:1907.04473, Jul 2019.

[2] L. F. Abbott and P. Sikivie. A Cosmological Bound on the Invisible Axion. *Phys. Lett.*, B120:133–136, 1983. doi: 10.1016/0370-2693(83)90638-X. [,URL(1982)].

[3] Bobby Samir Acharya, Gordon Kane, and Eric Kuflik. Bounds on scalar masses in theories of moduli stabilization. *Int. J. Mod. Phys.*, A29:1450073, 2014. doi: 10.1142/S0217751X14500730.

[4] N. Afshordi, P. McDonald, and D. N. Spergel. Primordial Black Holes as Dark Matter: The Power Spectrum and Evaporation of Early Structures. Astrophysical Journal Letters, 594(2): L71–L74, Sep 2003. doi: 10.1086/378763.

[5] N. Aghanim et al. Planck 2018 results. VI. Cosmological parameters. *Astron. Astrophys.*, 641:A6, 2020. doi: 10.1051/0004-6361/201833910. [Erratum: Astron.Astrophys. 652, C4 (2021)].

[6] Prateek Agrawal, Gustavo Marques-Tavares, and Wei Xue. Opening up the QCD axion window. *JHEP*, 03:049, 2018. doi: 10.1007/JHEP03(2018)049.

[7] Andreas Albrecht, Paul J. Steinhardt, Michael S. Turner, and Frank Wilczek. Reheating an Inflationary Universe. *Phys. Rev. Lett.*, 48:1437, 1982. doi: 10.1103/PhysRevLett.48.1437.

[8] S. Andriamonje et al. An Improved limit on the axion-photon coupling from the CAST experiment. *JCAP*, 0704:010, 2007. doi: 10.1088/1475-7516/2007/04/010.

[9] G. W. Angus and HongSheng Zhao. Cold dark matter microhalo survival in the Milky Way. MNRAS, 375(4):1146–1156, March 2007. doi: 10.1111/j.1365-2966.2007.11400.x.

[10] Nima Arkani-Hamed, Hsin-Chia Cheng, Paolo Creminelli, and Lisa Randall. Extra natural inflation. *Phys. Rev. Lett.*, 90:221302, 2003. doi: 10.1103/PhysRevLett.90.221302.

[11] Asimina Arvanitaki, Savas Dimopoulos, Sergei Dubovsky, Nemanja Kaloper, and John March-Russell. String Axiverse. *Phys. Rev.*, D81:123530, 2010. doi: 10.1103/PhysRevD.81.123530.

[12] Asimina Arvanitaki, Masha Baryakhtar, and Xinlu Huang. Discovering the QCD axion with black holes and gravitational waves. *PRD*, 91(8):084011, April 2015. doi: 10.1103/PhysRevD.91.084011.

[13] Asimina Arvanitaki, Savas Dimopoulos, Marios Galanis, Luis Lehner, Jedidiah O. Thompson, and Ken Van Tilburg. Large-misalignment mechanism for the formation of compact

axion structures: Signatures from the QCD axion to fuzzy dark matter. *Phys. Rev. D*, 101 (8):083014, 2020. doi: 10.1103/PhysRevD.101.083014.

[14] Adrian Ayala, Inma Domínguez, Maurizio Giannotti, Alessandro Mirizzi, and Oscar Straniero. Revisiting the bound on axion-photon coupling from Globular Clusters. *Phys. Rev. Lett.*, 113(19):191302, 2014. doi: 10.1103/PhysRevLett.113.191302.

[15] Shant Baghram, Niayesh Afshordi, and Kathryn M. Zurek. Prospects for Detecting Dark Matter Halo Substructure with Pulsar Timing. *Phys. Rev. D*, 84:043511, 2011. doi: 10.1103/PhysRevD.84.043511.

[16] J. S. Bagla, Nishikanta Khandai, and Girish Kulkarni. Mass function of haloes: scale invariant models. *arXiv e-prints*, art. arXiv:0908.2702, August 2009.

[17] Yang Bai and Yuta Hamada. Detecting Axion Stars with Radio Telescopes. *Phys. Lett.*, B781:187–194, 2018. doi: 10.1016/j.physletb.2018.03.070.

[18] Yang Bai, Vernon Barger, and Joshua Berger. Hydrogen Axion Star: Metallic Hydrogen Bound to a QCD Axion BEC. *JHEP*, 12:127, 2016. doi: 10.1007/JHEP12(2016)127.

[19] C. A. Baker et al. An Improved experimental limit on the electric dipole moment of the neutron. *Phys. Rev. Lett.*, 97:131801, 2006. doi: 10.1103/PhysRevLett.97.131801.

[20] Tom Banks, David B. Kaplan, and Ann E. Nelson. Cosmological implications of dynamical supersymmetry breaking. *Phys. Rev.*, D49:779–787, 1994. doi: 10.1103/PhysRevD.49.779.

[21] Tom Banks, Michael Dine, Patrick J. Fox, and Elie Gorbatov. On the possibility of large axion decay constants. *JCAP*, 0306:001, 2003. doi: 10.1088/1475-7516/2003/06/001.

[22] Rennan Barkana. Possible interaction between baryons and dark-matter particles revealed by the first stars. *Nature*, 555(7694):71–74, Mar 2018. doi: 10.1038/nature25791.

[23] Rennan Barkana, Zoltán Haiman, and Jeremiah P. Ostriker. Constraints on Warm Dark Matter from Cosmological Reionization. *ApJ*, 558(2):482–496, Sep 2001. doi: 10.1086/322393.

[24] J. E. Barnes and L. Hernquist. Dynamics of interacting galaxies. *Ann. Rev. Astron.& Astrophys.* , 30:705–742, 1992. doi: 10.1146/annurev.aa.30.090192.003421.

[25] S. M. Barr and Jihn E. Kim. New Confining Force Solution of the QCD Axion Domain-Wall Problem. *Phys. Rev. Lett.*, 113(24):241301, 2014. doi: 10.1103/PhysRevLett.113.241301.

[26] Stephen M. Barr and D. Seckel. Planck scale corrections to axion models. *Phys. Rev. D*, 46: 539–549, 1992. doi: 10.1103/PhysRevD.46.539.

[27] J. Barranco and A. Bernal. Self-gravitating system made of axions. *Phys. Rev.*, D83:043525, 2011. doi: 10.1103/PhysRevD.83.043525.

[28] J. Barranco, A. Carrillo Monteverde, and D. Delepine. Can the dark matter halo be a collisionless ensemble of axion stars? *Phys. Rev.*, D87:103011, 2013. doi: 10.1103/PhysRevD.87.103011.

[29] Masha Baryakhtar, Robert Lasenby, and Mae Teo. Black hole superradiance signatures of ultralight vectors. *PRD*, 96(3):035019, August 2017. doi: 10.1103/PhysRevD.96.035019.

[30] Richard A. Battye, Bjoern Garbrecht, Jamie I. McDonald, Francesco Pace, and Sankarshana Srinivasan. Dark matter axion detection in the radio/mm-waveband. *Phys. Rev. D*, 102(2): 023504, 2020. doi: 10.1103/PhysRevD.102.023504.

[31] V. S. Berezinsky, V. I. Dokuchaev, and Yu. N. Eroshenko. Formation and internal structure of superdense dark matter clumps and ultracompact minihaloes. *JCAP*, 1311:059, 2013. doi: 10.1088/1475-7516/2013/11/059.

[32] V. S. Berezinsky, V. I. Dokuchaev, and Yu N. Eroshenko. Small-scale clumps of dark matter. *Physics Uspekhi*, 57(1):1-36, January 2014. doi: 10.3367/UFNe.0184.201401a.0003.

[33] V. S. Berezinsky, V. I. Dokuchaev, and Yu N. Eroshenko. Small-scale clumps of dark matter. *Phys. Usp.*, 57:1–36, 2014. doi: 10.3367/UFNe.0184.201401a.0003. [Usp. Fiz. Nauk184,3(2014)].

[34] Veniamin Berezinsky, Vyacheslav Dokuchaev, and Yury Eroshenko. Small-scale clumps in the galactic halo and dark matter annihilation. *PRD*, 68(10):103003, November 2003. doi: 10.1103/PhysRevD.68.103003.

[35] James Binney and Scott Tremaine. *Galactic dynamics*. 1987.

[36] James Binney and Scott Tremaine. *Galactic Dynamics: Second Edition*. 2008.

[37] Joss Bland-Hawthorn and Ortwin Gerhard. The Galaxy in Context: Structural, Kinematic, and Integrated Properties. *Ann. Rev. Astron.& Astrophys.* , 54:529–596, September 2016. doi: 10.1146/annurev-astro-081915-023441.

[38] Diego Blas, Julien Lesgourgues, and Thomas Tram. The Cosmic Linear Anisotropy Solving System (CLASS) II: Approximation schemes. *JCAP*, 07:034, 2011. doi: 10.1088/1475-7516/2011/07/034.

[39] Nikita Blinov, Matthew J Dolan, Patrick Draper, and Jonathan Kozaczuk. Dark matter targets for axionlike particle searches. *Phys. Rev. D*, 100(1):015049, 2019. doi: 10.1103/PhysRevD.100.015049.

[40] Nikita Blinov, Matthew J Dolan, and Patrick Draper. Imprints of the Early Universe on Axion Dark Matter Substructure. *Phys. Rev. D*, 101(3):035002, 2020. doi: 10.1103/PhysRevD.101.035002.

[41] Nikita Blinov, Matthew J. Dolan, Patrick Draper, and Jessie Shelton. Dark Matter Microhalos From Simplified Models. *Phys. Rev. D*, 103(10):103514, 2021. doi: 10.1103/PhysRevD.103.103514.

[42] Ana Bonaca, David W. Hogg, Adrian M. Price-Whelan, and Charlie Conroy. The Spur and the Gap in GD-1: Dynamical Evidence for a Dark Substructure in the Milky Way Halo. *ApJ*, 880(1):38, Jul 2019. doi: 10.3847/1538-4357/ab2873.

[43] J. R. Bond, S. Cole, G. Efstathiou, and N. Kaiser. Excursion Set Mass Functions for Hierarchical Gaussian Fluctuations. *ApJ*, 379:440, Oct 1991. doi: 10.1086/170520.

[44] H. Bondi and F. Hoyle. On the mechanism of accretion by stars. MNRAS, 104:273, Jan 1944. doi: 10.1093/mnras/104.5.273.

[45] R. J. Bouwens, G. D. Illingworth, P. A. Oesch, M. Trenti, I. Labbé, L. Bradley, M. Carollo, P. G. van Dokkum, V. Gonzalez, B. Holwerda, M. Franx, L. Spitler, R. Smit, and D. Magee. UV Luminosity Functions at Redshifts z
4 to z
10: 10,000 Galaxies from HST Legacy Fields. *ApJ*, 803:34, April 2015. doi: 10.1088/0004-637X/803/1/34.

[46] R. J. Bouwens, P. A. Oesch, I. Labbé, G. D. Illingworth, G. G. Fazio, D. Coe, B. Holwerda, R. Smit, M. Stefanon, P. G. van Dokkum, M. Trenti, M. L. N. Ashby, J. S. Huang, L. Spitler, C. Straatman, L. Bradley, and D. Magee. The Bright End of the z 9 and z 10 UV Luminosity Functions Using All Five CANDELS Fields*. *ApJ*, 830(2):67, Oct 2016. doi: 10.3847/0004-637X/830/2/67.

[47] R. J. Bouwens, P. A. Oesch, G. D. Illingworth, R. S. Ellis, and M. Stefanon. The z 6 Luminosity Function Fainter than -15 mag from the Hubble Frontier Fields: The Impact of Magnification Uncertainties. *ApJ*, 843(2):129, Jul 2017. doi: 10.3847/1538-4357/aa70a4.

[48] Jo Bovy, Carlos Allende Prieto, Timothy C. Beers, Dmitry Bizyaev, Luiz N. da Costa, Katia Cunha, Garrett L. Ebelke, Daniel J. Eisenstein, Peter M. Frinchaboy, Ana Elia García Pérez, Léo Girardi, Fred R. Hearty, David W. Hogg, Jon Holtzman, Marcio A. G. Maia, Steven R. Majewski, Elena Malanushenko, Viktor Malanushenko, Szabolcs Mészáros, David L. Nidever, Robert W. O'Connell, Christine O'Donnell, Audrey Oravetz, Kaike Pan, Helio J. Rocha-Pinto, Ricardo P. Schiavon, Donald P. Schneider, Mathias Schultheis, Michael Skrutskie, Verne V. Smith, David H. Weinberg, John C. Wilson, and Gail Zasowski. The Milky

Way's Circular-velocity Curve between 4 and 14 kpc from APOGEE data. *ApJ*, 759(2):131, November 2012. doi: 10.1088/0004-637X/759/2/131.

[49] Jo Bovy, Denis Erkal, and Jason L. Sanders. Linear perturbation theory for tidal streams and the small-scale CDM power spectrum. MNRAS, 466(1):628–668, Apr 2017. doi: 10.1093/mnras/stw3067.

[50] R. A. A. Bowler, J. S. Dunlop, R. J. McLure, and D. J. McLeod. Unveiling the nature of bright z 7 galaxies with the Hubble Space Telescope. MNRAS, 466(3):3612–3635, Apr 2017. doi: 10.1093/mnras/stw3296.

[51] Judd D. Bowman, Alan E. E. Rogers, Raul A. Monsalve, Thomas J. Mozdzen, and Nivedita Mahesh. An absorption profile centred at 78 megahertz in the sky-averaged spectrum. *Nature*, 555(7694):67–70, Mar 2018. doi: 10.1038/nature25792.

[52] M. Boylan-Kolchin, C.-P. Ma, and E. Quataert. Dissipationless mergers of elliptical galaxies and the evolution of the fundamental plane. MNRAS, 362:184–196, September 2005. doi: 10.1111/j.1365-2966.2005.09278.x.

[53] Eric Braaten, Abhishek Mohapatra, and Hong Zhang. Dense Axion Stars. *Phys. Rev. Lett.*, 117(12):121801, 2016. doi: 10.1103/PhysRevLett.117.121801.

[54] Eric Braaten, Abhishek Mohapatra, and Hong Zhang. Nonrelativistic Effective Field Theory for Axions. *Phys. Rev.*, D94(7):076004, 2016. doi: 10.1103/PhysRevD.94.076004.

[55] Eric Braaten, Abhishek Mohapatra, and Hong Zhang. Emission of Photons and Relativistic Axions from Axion Stars. *Phys. Rev.*, D96(3):031901, 2017. doi: 10.1103/PhysRevD.96.031901.

[56] R. Bradley, J. Clarke, D. Kinion, L. J. Rosenberg, K. van Bibber, S. Matsuki, M. Muck, and P. Sikivie. Microwave cavity searches for dark-matter axions. *Rev. Mod. Phys.*, 75:777–817, 2003. doi: 10.1103/RevModPhys.75.777.

[57] T. Braine, R. Cervantes, N. Crisosto, N. Du, S. Kimes, L. J. Rosenberg, G. Rybka, J. Yang, D. Bowring, A. S. Chou, R. Khatiwada, A. Sonnenschein, W. Wester, G. Carosi, N. Woollett, L. D. Duffy, R. Bradley, C. Boutan, M. Jones, B. H. LaRoque, N. S. Oblath, M. S. Taubman, J. Clarke, A. Dove, A. Eddins, S. R. O'Kelley, S. Nawaz, I. Siddiqi, N. Stevenson, A. Agrawal, A. V. Dixit, J. R. Gleason, S. Jois, P. Sikivie, J. A. Solomon, N. S. Sullivan, D. B. Tanner, E. Lentz, E. J. Daw, J. H. Buckley, P. M. Harrington, E. A. Henriksen, and K. W. Murch. Extended search for the invisible axion with the axion dark matter experiment. *Phys. Rev. Lett.*, 124:101303, Mar 2020. doi: 10.1103/PhysRevLett.124.101303. URL `https://link.aps.org/doi/10.1103/PhysRevLett.124.101303`.

[58] Torsten Bringmann, Felix Kahlhoefer, Kai Schmidt-Hoberg, and Parampreet Walia. Converting nonrelativistic dark matter to radiation. *Phys. Rev. D*, 98(2):023543, 2018. doi: 10.1103/PhysRevD.98.023543.

[59] Volker Bromm, Rolf P. Kudritzki, and Abraham Loeb. Generic Spectrum and Ionization Efficiency of a Heavy Initial Mass Function for the First Stars. *ApJ*, 552(2):464–472, May 2001. doi: 10.1086/320549.

[60] James H. Buckley, P.S. Bhupal Dev, Francesc Ferrer, and Fa Peng Huang. Fast radio bursts from axion stars moving through pulsar magnetospheres. 4 2020.

[61] James S. Bullock and Michael Boylan-Kolchin. Small-Scale Challenges to the ΛCDM Paradigm. *Ann. Rev. Astron.& Astrophys.* , 55(1):343–387, Aug 2017. doi: 10.1146/annurev-astro-091916-055313.

[62] James S. Bullock and Michael Boylan-Kolchin. Small-Scale Challenges to the ΛCDM Paradigm. *Ann. Rev. Astron.& Astrophys.* , 55(1):343–387, August 2017. doi: 10.1146/annurev-astro-091916-055313.

[63] Malte Buschmann, Joshua W. Foster, and Benjamin R. Safdi. Early-Universe Simulations of

the Cosmological Axion. *Phys. Rev. Lett.*, 124(16):161103, 2020. doi: 10.1103/PhysRevLett.124.161103.

[64] Malte Buschmann, Joshua W. Foster, Anson Hook, Adam Peterson, Don E. Willcox, Weiqun Zhang, and Benjamin R. Safdi. Dark matter from axion strings with adaptive mesh refinement. *Nature Commun.*, 13(1):1049, 2022. doi: 10.1038/s41467-022-28669-y.

[65] Andrea Caputo, Marco Regis, Marco Taoso, and Samuel J. Witte. Detecting the Stimulated Decay of Axions at RadioFrequencies. *JCAP*, 03:027, 2019. doi: 10.1088/1475-7516/2019/03/027.

[66] Pierluca Carenza, Alessandro Mirizzi, and Günter Sigl. Dynamical evolution of axion condensates under stimulated decays into photons. *Phys. Rev. D*, 101(10):103016, 2020. doi: 10.1103/PhysRevD.101.103016.

[67] B. J. Carr and M. Sakellariadou. Dynamical constraints on dark matter in compact objects. *The Astrophysical Journal*, 516(1):195–220, May 1999. doi: 10.1086/307071.

[68] Bernard Carr, Martti Raidal, Tommi Tenkanen, Ville Vaskonen, and Hardi Veermäe. Primordial black hole constraints for extended mass functions. *Phys. Rev. D*, 96(2):023514, 2017. doi: 10.1103/PhysRevD.96.023514.

[69] Renyue Cen, Jordi Miralda-Escudé, Jeremiah P. Ostriker, and Michael Rauch. Gravitational Collapse of Small-Scale Structure as the Origin of the Lyman-Alpha Forest. Astrophysical Journal Letters, 437:L9, Dec 1994. doi: 10.1086/187670.

[70] G. Chabrier. Galactic Stellar and Substellar Initial Mass Function. , 115:763–795, July 2003.

[71] Sanghyeon Chang, C. Hagmann, and P. Sikivie. Studies of the motion and decay of axion walls bounded by strings. *Phys. Rev. D*, 59:023505, 1999. doi: 10.1103/PhysRevD.59.023505.

[72] P. H. Chavanis and L. Delfini. Mass-Radius Relation of Newtonian Self-Gravitating Bose-Einstein Condensates with Short-Range Interactions: II. Numerical Results. *Phys. Rev. D*, 84:043532, 2011. doi: 10.1103/PhysRevD.84.043532.

[73] Pierre-Henri Chavanis. Mass-Radius Relation of Newtonian Self-Gravitating Bose-Einstein Condensates with Short-Range Interactions: I. Analytical Results. *Phys. Rev. D*, 84:043531, 2011. doi: 10.1103/PhysRevD.84.043531.

[74] Pierre-Henri Chavanis. Collapse of a Self-Gravitating Bose-Einstein Condensate with Attractive Self-Interaction. *Phys. Rev. D*, 94(8):083007, 2016. doi: 10.1103/PhysRevD.94.083007.

[75] Jiajun Chen, Xiaolong Du, Erik Lentz, and David J. E. Marsh. Relaxation times for Bose-Einstein condensation by self-interaction and gravity. 9 2021.

[76] Jiajun Chen, Xiaolong Du, Erik W. Lentz, David J. E. Marsh, and Jens C. Niemeyer. New Insights into the Formation and Growth of Boson Stars in Dark Matter Halos. *Phys. Rev. D*, 104(8):083022, 2021. doi: 10.1103/PhysRevD.104.083022.

[77] Wenlei Chen et al. Searching for Highly Magnified Stars at Cosmological Distances: Discovery of a Redshift 0.94 Blue Supergiant in Archival Images of the Galaxy Cluster MACS J0416.1-2403. 2 2019. doi: 10.3847/1538-4357/ab297d.

[78] Ki-woon Choi. A QCD axion from higher dimensional gauge field. *Phys. Rev. Lett.*, 92: 101602, 2004. doi: 10.1103/PhysRevLett.92.101602.

[79] Ki-Young Choi and Tomo Takahashi. New bound on low reheating temperature for dark matter in models with early matter domination. *Phys. Rev.*, D96(4):041301, 2017. doi: 10.1103/PhysRevD.96.041301.

[80] Joseph P. Conlon. The QCD axion and moduli stabilisation. *JHEP*, 05:078, 2006. doi: 10.1088/1126-6708/2006/05/078.

[81] Camila A. Correa, J. Stuart B. Wyithe, Joop Schaye, and Alan R. Duffy. The accretion history of dark matter haloes - I. The physical origin of the universal function. MNRAS, 450 (2):1514–1520, Jun 2015. doi: 10.1093/mnras/stv689.

[82] David Cyncynates and Tudor Giurgica-Tiron. Structure of the oscillon: The dynamics of attractive self-interaction. *Phys. Rev. D*, 103(11):116011, 2021. doi: 10.1103/PhysRevD.103.116011.

[83] Liang Dai and Jordi Miralda-Escudé. Gravitational Lensing Signatures of Axion Dark Matter Minihalos in Highly Magnified Stars. *Astron. J.*, 159(2):49, 2020. doi: 10.3847/1538-3881/ab5e83.

[84] Liang Dai, Tejaswi Venumadhav, Alexander A. Kaurov, and Jordi Miralda-Escudé. Probing Dark Matter Subhalos in Galaxy Clusters Using Highly Magnified Stars. *Astrophys. J.*, 867 (1):24, 2018. doi: 10.3847/1538-4357/aae478.

[85] Sacha Davidson. Axions: Bose Einstein Condensate or Classical Field? *Astropart. Phys.*, 65:101–107, 2015. doi: 10.1016/j.astropartphys.2014.12.007.

[86] Sacha Davidson and Martin Elmer. Bose Einstein condensation of the classical axion field in cosmology? *JCAP*, 1312:034, 2013. doi: 10.1088/1475-7516/2013/12/034.

[87] Sacha Davidson and Thomas Schwetz. Rotating Drops of Axion Dark Matter. *Phys. Rev.*, D93(12):123509, 2016. doi: 10.1103/PhysRevD.93.123509.

[88] Frederick B. Davies, Joseph F. Hennawi, Eduardo Bañados, Zarija Lukić, Roberto Decarli, Xiaohui Fan, Emanuele P. Farina, Chiara Mazzucchelli, Hans-Walter Rix, Bram P. Venemans, Fabian Walter, Feige Wang, and Jinyi Yang. Quantitative Constraints on the Reionization History from the IGM Damping Wing Signature in Two Quasars at z > 7. *ApJ*, 864(2): 142, Sep 2018. doi: 10.3847/1538-4357/aad6dc.

[89] M. Davis, G. Efstathiou, C. S. Frenk, and S. D. M. White. The evolution of large-scale structure in a universe dominated by cold dark matter. *ApJ*, 292:371–394, May 1985. doi: 10.1086/163168.

[90] Hooman Davoudiasl and Peter B. Denton. Ultralight Boson Dark Matter and Event Horizon Telescope Observations of M 87*. *PRL*, 123(2):021102, July 2019. doi: 10.1103/PhysRevLett.123.021102.

[91] Kyle S. Dawson et al. The Baryon Oscillation Spectroscopic Survey of SDSS-III. *Astron. J.*, 145:10, 2013. doi: 10.1088/0004-6256/145/1/10.

[92] B. de Carlos, J. A. Casas, F. Quevedo, and E. Roulet. Model independent properties and cosmological implications of the dilaton and moduli sectors of 4-d strings. *Phys. Lett.*, B318: 447–456, 1993. doi: 10.1016/0370-2693(93)91538-X.

[93] A. J. Deason, V. Belokurov, N. W. Evans, and J. An. Broken degeneracies: the rotation curve and velocity anisotropy of the Milky Way halo. MNRAS, 424(1):L44–L48, July 2012. doi: 10.1111/j.1745-3933.2012.01283.x.

[94] W. Dehnen. A Family of Potential-Density Pairs for Spherical Galaxies and Bulges. MNRAS, 265:250, November 1993. doi: 10.1093/mnras/265.1.250.

[95] M. Sten Delos. Evolution of dark matter microhalos through stellar encounters. *Phys. Rev. D*, 100(8):083529, 2019. doi: 10.1103/PhysRevD.100.083529.

[96] E. Di Valentino, T. Brinckmann, M. Gerbino, V. Poulin, F. R. Bouchet, J. Lesgourgues, A. Melchiorri, J. Chluba, S. Clesse, J. Delabrouille, C. Dvorkin, F. Forastieri, S. Galli, D. C. Hooper, M. Lattanzi, C. J. A. P. Martins, L. Salvati, G. Cabass, A. Caputo, E. Giusarma, E. Hivon, P. Natoli, L. Pagano, S. Paradiso, J. A. Rubiño-Martin, A. Achúcarro, P. Ade, R. Allison, F. Arroja, M. Ashdown, M. Ballardini, A. J. Banday, R. Banerji, N. Bartolo, J. G. Bartlett, S. Basak, D. Baumann, P. de Bernardis, M. Bersanelli, A. Bonaldi, M. Bonato, J. Borrill, F. Boulanger, M. Bucher, C. Burigana, A. Buzzelli, Z. Y. Cai, M. Calvo, C. S.

Carvalho, G. Castellano, A. Challinor, I. Charles, I. Colantoni, A. Coppolecchia, M. Crook, G. D'Alessandro, M. De Petris, G. De Zotti, J. M. Diego, J. Errard, S. Feeney, R. Fernandez-Cobos, S. Ferraro, F. Finelli, G. de Gasperis, R. T. Génova-Santos, J. González-Nuevo, S. Grandis, J. Greenslade, S. Hagstotz, S. Hanany, W. Handley, D. K. Hazra, C. Hernández-Monteagudo, C. Hervias-Caimapo, M. Hills, K. Kiiveri, T. Kisner, T. Kitching, M. Kunz, H. Kurki-Suonio, L. Lamagna, A. Lasenby, A. Lewis, M. Liguori, V. Lindholm, M. Lopez-Caniego, G. Luzzi, B. Maffei, S. Martin, E. Martinez-Gonzalez, S. Masi, S. Matarrese, D. McCarthy, J. B. Melin, J. J. Mohr, D. Molinari, A. Monfardini, M. Negrello, A. Notari, A. Paiella, D. Paoletti, G. Patanchon, F. Piacentini, M. Piat, G. Pisano, L. Polastri, G. Polenta, A. Pollo, M. Quartin, M. Remazeilles, M. Roman, C. Ringeval, A. Tartari, M. Tomasi, D. Tramonte, N. Trappe, T. Trombetti, C. Tucker, J. Väliviita, R. van de Weygaert, B. Van Tent, V. Vennin, G. Vermeulen, P. Vielva, N. Vittorio, K. Young, and M. Zannoni. Exploring cosmic origins with CORE: Cosmological parameters. J. Cosmology Astropart. Phys., 2018 (4):017, Apr 2018. doi: 10.1088/1475-7516/2018/04/017.

[97] P. Di Vecchia and G. Veneziano. Chiral Dynamics in the Large N Limit. *Nucl. Phys. B*, 171: 253–272, 1980. doi: 10.1016/0550-3213(80)90370-3.

[98] Jose M. Diego, Nick Kaiser, Tom Broadhurst, Patrick L. Kelly, Steve Rodney, Takahiro Morishita, Masamune Oguri, Timothy W. Ross, Adi Zitrin, Mathilde Jauzac, Johan Richard, Liliya Williams, Jesus Vega-Ferrero, Brenda Frye, and Alexei V. Filippenko. Dark Matter under the Microscope: Constraining Compact Dark Matter with Caustic Crossing Events. *ApJ*, 857(1):25, April 2018. doi: 10.3847/1538-4357/aab617.

[99] Benedikt Diemer and Andrey V. Kravtsov. Dependence of the Outer Density Profiles of Halos on Their Mass Accretion Rate. *ApJ*, 789(1):1, July 2014. doi: 10.1088/0004-637X/789/1/1.

[100] Benedikt Diemer, Surhud More, and Andrey V. Kravtsov. The Pseudo-evolution of Halo Mass. *ApJ*, 766(1):25, March 2013. doi: 10.1088/0004-637X/766/1/25.

[101] Tim Dietrich, Francesca Day, Katy Clough, Michael Coughlin, and Jens Niemeyer. Neutron

star–axion star collisions in the light of multimessenger astronomy. *Mon. Not. Roy. Astron. Soc.*, 483(1):908–914, 2019. doi: 10.1093/mnras/sty3158.

[102] Thomas van Dijk. An important paper. *QJRAS*, 2:202–207, 1902.

[103] Michael Dine and Willy Fischler. The Not So Harmless Axion. *Phys. Lett.*, B120:137–141, 1983. doi: 10.1016/0370-2693(83)90639-1. [,URL(1982)].

[104] Michael Dine, Patrick Draper, Laurel Stephenson-Haskins, and Di Xu. Axions, Instantons, and the Lattice. *Phys. Rev.*, D96(9):095001, 2017. doi: 10.1103/PhysRevD.96.095001.

[105] Elena D'Onghia, Volker Springel, Lars Hernquist, and Dusan Keres. Substructure Depletion in the Milky Way Halo by the Disk. *ApJ*, 709(2):1138–1147, February 2010. doi: 10.1088/0004-637X/709/2/1138.

[106] Jeff A. Dror, Harikrishnan Ramani, Tanner Trickle, and Kathryn M. Zurek. Pulsar Timing Probes of Primordial Black Holes and Subhalos. *Phys. Rev. D*, 100(2):023003, 2019. doi: 10.1103/PhysRevD.100.023003.

[107] S. Dye, A. Lawrence, M. A. Read, X. Fan, T. Kerr, W. Varricatt, K. E. Furnell, A. C. Edge, M. Irwin, N. Hambly, P. Lucas, O. Almaini, K. Chambers, R. Green, P. Hewett, M. C. Liu, I. McGreer, W. Best, Z. Zhang, E. Sutorius, D. Froebrich, E. Magnier, G. Hasinger, S. M. Lederer, M. Bold, and J. A. Tedds. The UKIRT Hemisphere Survey: definition and J-band data release. MNRAS, 473:5113–5125, February 2018. doi: 10.1093/mnras/stx2622.

[108] Joshua Eby, Madelyn Leembruggen, Peter Suranyi, and L. C. R. Wijewardhana. Collapse of Axion Stars. *JHEP*, 12:066, 2016. doi: 10.1007/JHEP12(2016)066.

[109] Joshua Eby, Madelyn Leembruggen, Joseph Leeney, Peter Suranyi, and L. C. R. Wijewardhana. Collisions of Dark Matter Axion Stars with Astrophysical Sources. *JHEP*, 04:099, 2017. doi: 10.1007/JHEP04(2017)099.

[110] Joshua Armstrong Eby. *Phenomenology and Astrophysics of Gravitationally-Bound Condensates of Axion-Like Particles*. PhD thesis, Cincinnati U., 2017. URL `http://lss.fnal.gov/archive/thesis/2000/fermilab-thesis-2017-19.pdf`.

[111] A. Edge, W. Sutherland, K. Kuijken, S. Driver, R. McMahon, S. Eales, and J. P. Emerson. The VISTA Kilo-degree Infrared Galaxy (VIKING) Survey: Bridging the Gap between Low and High Redshift. *The Messenger*, 154:32–34, December 2013.

[112] G. Efstathiou and J. R. Bond. Isocurvature cold dark matter fluctuations. MNRAS, 218: 103–121, Jan 1986. doi: 10.1093/mnras/218.1.103.

[113] Benedikt Eggemeier and Jens C. Niemeyer. Formation and Mass Growth of Axion Stars in Axion Miniclusters. *Phys. Rev. D*, 100(6):063528, 2019. doi: 10.1103/PhysRevD.100.063528.

[114] Benedikt Eggemeier, Javier Redondo, Klaus Dolag, Jens C. Niemeyer, and Alejandro Vaquero. First simulations of axion minicluster halos. 11 2019.

[115] Anna-Christina Eilers, David W. Hogg, Hans-Walter Rix, and Melissa K. Ness. The Circular Velocity Curve of the Milky Way from 5 to 25 kpc. *ApJ*, 871(1):120, January 2019. doi: 10.3847/1538-4357/aaf648.

[116] David Ellis, David J.E. Marsh, and Christoph Behrens. Axion Miniclusters Made Easy. 6 2020.

[117] Jonas Enander, Andreas Pargner, and Thomas Schwetz. Axion minicluster power spectrum and mass function. *JCAP*, 1712(12):038, 2017. doi: 10.1088/1475-7516/2017/12/038.

[118] Adrienne L. Erickcek. The Dark Matter Annihilation Boost from Low-Temperature Reheating. *Phys. Rev.*, D92(10):103505, 2015. doi: 10.1103/PhysRevD.92.103505.

[119] Adrienne L. Erickcek and Kris Sigurdson. Reheating Effects in the Matter Power Spectrum

and Implications for Substructure. *Phys. Rev.*, D84:083503, 2011. doi: 10.1103/PhysRevD.84.083503.

[120] Adrienne L. Erickcek, Kuver Sinha, and Scott Watson. Bringing Isolated Dark Matter Out of Isolation: Late-time Reheating and Indirect Detection. *Phys. Rev.*, D94(6):063502, 2016. doi: 10.1103/PhysRevD.94.063502.

[121] Raphaël Errani and Julio F. Navarro. The asymptotic tidal remnants of cold dark matter subhalos. *arXiv e-prints*, art. arXiv:2011.07077, November 2020.

[122] Gaétan Facchinetti, Martin Stref, and Julien Lavalle. Tidal stripping of dark matter subhalos by baryons from analytical perspectives: disk shocking and encounters with stars. *arXiv e-prints*, art. arXiv:2201.09788, January 2022.

[123] Malcolm Fairbairn, David J. E. Marsh, and Jérémie Quevillon. Searching for the QCD Axion with Gravitational Microlensing. *Phys. Rev. Lett.*, 119(2):021101, 2017. doi: 10.1103/PhysRevLett.119.021101.

[124] Malcolm Fairbairn, David J. E. Marsh, Jérémie Quevillon, and Simon Rozier. Structure formation and microlensing with axion miniclusters. *Phys. Rev.*, D97(8):083502, 2018. doi: 10.1103/PhysRevD.97.083502.

[125] JiJi Fan, Ogan Özsoy, and Scott Watson. Nonthermal histories and implications for structure formation. *Phys. Rev.*, D90(4):043536, 2014. doi: 10.1103/PhysRevD.90.043536.

[126] Martin Feix, Johann Frank, Andreas Pargner, Robert Reischke, Bjoern Malte Schäfer, and Thomas Schwetz. Isocurvature bounds on axion-like particle dark matter in the post-inflationary scenario. *JCAP*, 1905(05):021, 2019. doi: 10.1088/1475-7516/2019/05/021.

[127] Robert Feldmann, Eliot Quataert, Claude-André Faucher-Giguère, Philip F. Hopkins, Onur Çatmabacak, Dušan Kereš, Luigi Bassini, Mauro Bernardini, James S. Bullock, Elia Cenci,

Jindra Gensior, Lichen Liang, Jorge Moreno, and Andrew Wetzel. FIREbox: Simulating galaxies at high dynamic range in a cosmological volume. *arXiv e-prints*, art. arXiv:2205.15325, May 2022.

[128] Yu Feng, Simeon Bird, Lauren Anderson, Andreu Font-Ribera, and Chris Pedersen. Mp-gadget/mp-gadget: A tag for getting a doi, October 2018. URL `https://doi.org/10.5281/zenodo.1451799`.

[129] Anastasia Fialkov and Rennan Barkana. Signature of excess radio background in the 21-cm global signal and power spectrum. MNRAS, 486(2):1763–1773, Jun 2019. doi: 10.1093/mnras/stz873.

[130] Leesa Fleury and Guy D. Moore. Axion Dark Matter: Strings and Their Cores. *JCAP*, 01:004, 2016. doi: 10.1088/1475-7516/2016/01/004.

[131] Joshua W. Foster, Yonatan Kahn, Oscar Macias, Zhiquan Sun, Ralph P. Eatough, Vladislav I. Kondratiev, Wendy M. Peters, Christoph Weniger, and Benjamin R. Safdi. Green Bank and Effelsberg Radio Telescope Searches for Axion Dark Matter Conversion in Neutron Star Magnetospheres. *Phys. Rev. Lett.*, 125(17):171301, 2020. doi: 10.1103/PhysRevLett.125.171301.

[132] Paul Fournier. Not a real paper. *ApJ*, 1:101–111, 1901.

[133] Patrick Fox, Aaron Pierce, and Scott D. Thomas. Probing a QCD string axion with precision cosmological measurements. 2004.

[134] Steven R. Furlanetto, S. Peng Oh, and Frank H. Briggs. Cosmology at low frequencies: The 21 cm transition and the high-redshift Universe. Physics Reports, 433(4-6):181–301, Oct 2006. doi: 10.1016/j.physrep.2006.08.002.

[135] Steven R. Furlanetto, Jordan Mirocha, Richard H. Mebane, and Guochao Sun. A minimalist feedback-regulated model for galaxy formation during the epoch of reionization. MNRAS, 472(2):1576–1592, Dec 2017. doi: 10.1093/mnras/stx2132.

[136] A. Gardikiotis et al. Search for streaming dark matter axions or other exotica. 2018.

[137] O. E. Gerhard and S. M. Fall. Tidal interactions of disc galaxies. MNRAS, 203:1253–1268, June 1983. doi: 10.1093/mnras/203.4.1253.

[138] S. Ghigna, Maurizio Lusignoli, and M. Roncadelli. Instability of the invisible axion. *Phys. Lett. B*, 283:278–281, 1992. doi: 10.1016/0370-2693(92)90019-Z.

[139] Mark Gieles and Florent Renaud. If it does not kill them, it makes them stronger: collisional evolution of star clusters with tidal shocks. MNRAS, 463(1):L103–L107, November 2016. doi: 10.1093/mnrasl/slw163.

[140] Gian Francesco Giudice, Edward W. Kolb, and Antonio Riotto. Largest temperature of the radiation era and its cosmological implications. *Phys. Rev.*, D64:023508, 2001. doi: 10.1103/PhysRevD.64.023508.

[141] Oleg Y. Gnedin, Lars Hernquist, and Jeremiah P. Ostriker. Tidal Shocking by Extended Mass Distributions. *ApJ*, 514(1):109–118, March 1999. doi: 10.1086/306910.

[142] Tobias Goerdt, Oleg Y. Gnedin, Ben Moore, Jürg Diemand, and Joachim Stadel. The survival and disruption of cold dark matter microhaloes: implications for direct and indirect detection experiments. MNRAS, 375(1):191–198, February 2007. doi: 10.1111/j.1365-2966.2006.11281.x.

[143] Marco Gorghetto, Edward Hardy, and Giovanni Villadoro. Axions from Strings: the Attractive Solution. *JHEP*, 07:151, 2018. doi: 10.1007/JHEP07(2018)151.

[144] Marco Gorghetto, Edward Hardy, and Giovanni Villadoro. More Axions from Strings. *SciPost Phys.*, 10(2):050, 2021. doi: 10.21468/SciPostPhys.10.2.050.

[145] Peter W. Graham and Adam Scherlis. Stochastic axion scenario. *PRD*, 98(3):035017, August 2018. doi: 10.1103/PhysRevD.98.035017.

[146] Peter W. Graham, Igor G. Irastorza, Steven K. Lamoreaux, Axel Lindner, and Karl A. van Bibber. Experimental Searches for the Axion and Axion-Like Particles. *Ann. Rev. Nucl. Part. Sci.*, 65:485–514, 2015. doi: 10.1146/annurev-nucl-102014-022120.

[147] Peter W. Graham, Jeremy Mardon, and Surjeet Rajendran. Vector Dark Matter from Inflationary Fluctuations. *Phys. Rev. D*, 93(10):103520, 2016. doi: 10.1103/PhysRevD.93.103520.

[148] B. Graner, Y. Chen, E. G. Lindahl, and B. R. Heckel. Reduced Limit on the Permanent Electric Dipole Moment of Hg199. *Phys. Rev. Lett.*, 116(16):161601, 2016. doi: 10.1103/PhysRevLett.119.119901,10.1103/PhysRevLett.116.161601. [Erratum: Phys. Rev. Lett.119,no.11,119901(2017)].

[149] A. M. Green and S. P. Goodwin. On mini-halo encounters with stars. *Monthly Notices of the Royal Astronomical Society*, 375(3):1111–1120, Mar 2007. ISSN 1365-2966. doi: 10.1111/j.1365-2966.2007.11397.x. URL `http://dx.doi.org/10.1111/j.1365-2966.2007.11397.x`.

[150] Anne M. Green, Stefan Hofmann, and Dominik J. Schwarz. The first WIMPy halos. J. Cosmology Astropart. Phys., 2005(8):003, August 2005. doi: 10.1088/1475-7516/2005/08/003.

[151] Sheridan B. Green, Frank C. van den Bosch, and Fangzhou Jiang. The tidal evolution of dark matter substructure - II. The impact of artificial disruption on subhalo mass functions and radial profiles. MNRAS, 503(3):4075–4091, May 2021. doi: 10.1093/mnras/stab696.

[152] Bradley Greig, Andrei Mesinger, Zoltán Haiman, and Robert A. Simcoe. Are we witnessing the epoch of reionisation at z = 7.1 from the spectrum of J1120+0641? MNRAS, 466(4):4239–4249, Apr 2017. doi: 10.1093/mnras/stw3351.

[153] Bradley Greig, Andrei Mesinger, and Eduardo Bañados. Constraints on reionization from the z = 7.5 QSO ULASJ1342+0928. MNRAS, 484(4):5094–5101, Apr 2019. doi: 10.1093/mnras/stz230.

[154] Giovanni Grilli di Cortona, Edward Hardy, Javier Pardo Vega, and Giovanni Villadoro. The QCD axion, precisely. *JHEP*, 01:034, 2016. doi: 10.1007/JHEP01(2016)034.

[155] Daniel Grin, Tristan L. Smith, and Marc Kamionkowski. Axion constraints in non-standard thermal histories. *Phys. Rev.*, D77:085020, 2008. doi: 10.1103/PhysRevD.77.085020.

[156] David J. Gross, Robert D. Pisarski, and Laurence G. Yaffe. QCD and Instantons at Finite Temperature. *Rev. Mod. Phys.*, 53:43, 1981. doi: 10.1103/RevModPhys.53.43.

[157] Michael Y Grudić and Philip F Hopkins. A general-purpose time-step criterion for simulations with gravity. *Monthly Notices of the Royal Astronomical Society*, 495(4):4306–4313, may 2020. doi: 10.1093/mnras/staa1453. URL https://doi.org/10.1093%2Fmnras%2Fstaa1453.

[158] Simon de la Guarde. A last unreal paper. *MNRAS*, 4:404–481, 1904.

[159] Alan H. Guth, Mark P. Hertzberg, and C. Prescod-Weinstein. Do Dark Matter Axions Form a Condensate with Long-Range Correlation? *Phys. Rev.*, D92(10):103513, 2015. doi: 10.1103/PhysRevD.92.103513.

[160] Francesco Haardt and Piero Madau. Radiative Transfer in a Clumpy Universe. IV. New Synthesis Models of the Cosmic UV/X-Ray Background. *ApJ*, 746(2):125, Feb 2012. doi: 10.1088/0004-637X/746/2/125.

[161] C. Hagmann and P. Sikivie. Computer simulations of the motion and decay of global strings. *Nucl. Phys.*, B363:247–280, 1991. doi: 10.1016/0550-3213(91)90243-Q.

[162] C. Hagmann, Sanghyeon Chang, and P. Sikivie. Axion radiation from strings. *Phys. Rev. D*, 63:125018, 2001. doi: 10.1103/PhysRevD.63.125018.

[163] Zoltán Haiman, Martin J. Rees, and Abraham Loeb. Destruction of Molecular Hydrogen during Cosmological Reionization. *ApJ*, 476(2):458–463, Feb 1997. doi: 10.1086/303647.

[164] Zoltán Haiman, Tom Abel, and Martin J. Rees. The Radiative Feedback of the First Cosmological Objects. *ApJ*, 534(1):11–24, May 2000. doi: 10.1086/308723.

[165] Steen Hannestad. What is the lowest possible reheating temperature? *Phys. Rev.*, D70: 043506, 2004. doi: 10.1103/PhysRevD.70.043506.

[166] Edward Hardy. Miniclusters in the Axiverse. *JHEP*, 02:046, 2017. doi: 10.1007/JHEP02(2017)046.

[167] Chen He Heinrich, Vinicius Miranda, and Wayne Hu. Complete reionization constraints from Planck 2015 polarization. *PRD*, 95(2):023513, Jan 2017. doi: 10.1103/PhysRevD.95.023513.

[168] Thomas Helfer, David J. E. Marsh, Katy Clough, Malcolm Fairbairn, Eugene A. Lim, and Ricardo Becerril. Black hole formation from axion stars. *JCAP*, 1703(03):055, 2017. doi: 10.1088/1475-7516/2017/03/055.

[169] Xavier Hernandez, Tonatiuh Matos, Roberto A Sussman, and Yosef Verbin. Scalar field mini-machos: A New explanation for galactic dark matter. *Phys. Rev.*, D70:043537, 2004. doi: 10.1103/PhysRevD.70.043537.

[170] L. Hernquist and P. J. Quinn. Shells and dark matter in elliptical galaxies. *ApJ*, 312:1–16, January 1987. doi: 10.1086/164844.

[171] L. Hernquist and D. N. Spergel. Formation of shells in major mergers. Astrophysical Journal Letters, 399:L117–L120, November 1992. doi: 10.1086/186621.

[172] L. Hernquist, D. N. Spergel, and J. S. Heyl. Structure of Merger Remnants. III. Phase-Space Constraints. *ApJ*, 416:415–+, October 1993. doi: 10.1086/173247.

[173] Lars Hernquist. An Analytical Model for Spherical Galaxies and Bulges. *ApJ*, 356:359, June 1990. doi: 10.1086/168845.

[174] Lars Hernquist and P. J. Quinn. Formation of Shell Galaxies. I. Spherical Potentials. *ApJ*, 331:682, August 1988. doi: 10.1086/166592.

[175] Lars Hernquist, Neal Katz, David H. Weinberg, and Jordi Miralda-Escudé. The Lyman-Alpha Forest in the Cold Dark Matter Model. Astrophysical Journal Letters, 457:L51, Feb 1996. doi: 10.1086/309899.

[176] J. Herpich, G. S. Stinson, H. W. Rix, M. Martig, and A. A. Dutton. How to bend galaxy disc profiles - II. Stars surfing the bar in Type-III discs. MNRAS, 470(4):4941–4955, October 2017. doi: 10.1093/mnras/stx1511.

[177] Mark P. Hertzberg and Enrico D. Schiappacasse. Dark Matter Axion Clump Resonance of Photons. 2018.

[178] Mark P Hertzberg, Max Tegmark, and Frank Wilczek. Axion Cosmology and the Energy Scale of Inflation. *Phys. Rev.*, D78:083507, 2008. doi: 10.1103/PhysRevD.78.083507.

[179] Mark P. Hertzberg, Yao Li, and Enrico D. Schiappacasse. Merger of Dark Matter Axion Clumps and Resonant Photon Emission. *JCAP*, 07:067, 2020. doi: 10.1088/1475-7516/2020/07/067.

[180] Mark Hindmarsh, Joanes Lizarraga, Asier Lopez-Eiguren, and Jon Urrestilla. Scaling Density of Axion Strings. *Phys. Rev. Lett.*, 124(2):021301, 2020. doi: 10.1103/PhysRevLett.124.021301.

[181] Mark Hindmarsh, Joanes Lizarraga, Asier Lopez-Eiguren, and Jon Urrestilla. Approach to Scaling in Axion String Networks. *Phys. Rev. D*, 103(10):103534, 2021. doi: 10.1103/PhysRevD.103.103534.

[182] Mark Hindmarsh, Joanes Lizarraga, Asier Lopez-Eiguren, and Jon Urrestilla. Comment on "More Axions from Strings". 9 2021.

[183] Takashi Hiramatsu, Masahiro Kawasaki, Toyokazu Sekiguchi, Masahide Yamaguchi, and Jun'ichi Yokoyama. Improved Estimation of Radiated Axions from Cosmological Axionic Strings. *Phys. Rev. D*, 83:123531, 2011. doi: 10.1103/PhysRevD.83.123531.

[184] A. Hoag, M. Bradač, K. Huang, C. Mason, T. Treu, K. B. Schmidt, M. Trenti, V. Strait, B. C. Lemaux, E. Q. Finney, and M. Paddock. Constraining the Neutral Fraction of Hydrogen in the IGM at Redshift 7.5. *ApJ*, 878(1):12, Jun 2019. doi: 10.3847/1538-4357/ab1de7.

[185] Stefan Hofmann, Dominik J. Schwarz, and Horst Stöcker. Damping scales of neutralino cold dark matter. *PRD*, 64(8):083507, October 2001. doi: 10.1103/PhysRevD.64.083507.

[186] C. J. Hogan and M. J. Rees. AXION MINICLUSTERS. *Phys. Lett.*, B205:228–230, 1988. doi: 10.1016/0370-2693(88)91655-3.

[187] Anson Hook. TASI Lectures on the Strong CP Problem and Axions. *PoS*, TASI2018:004, 2019.

[188] Anson Hook, Yonatan Kahn, Benjamin R. Safdi, and Zhiquan Sun. Radio Signals from Axion Dark Matter Conversion in Neutron Star Magnetospheres. *Phys. Rev. Lett.*, 121(24): 241102, 2018. doi: 10.1103/PhysRevLett.121.241102.

[189] P. F. Hopkins, L. Hernquist, T. J. Cox, J. D. Younger, and G. Besla. The Radical Consequences of Realistic Satellite Orbits for the Heating and Implied Merger Histories of Galactic Disks. *ApJ*, 688:757–769, December 2008. doi: 10.1086/592087.

[190] P. F. Hopkins, T. R. Lauer, T. J. Cox, L. Hernquist, and J. Kormendy. Dissipation and Extra Light in Galactic Nuclei. III. "Core" Ellipticals and "Missing" Light. *ApJS*, 181:486–532, April 2009. doi: 10.1088/0067-0049/181/2/486.

[191] Philip F. Hopkins. A new class of accurate, mesh-free hydrodynamic simulation methods. MNRAS, 450(1):53–110, June 2015. doi: 10.1093/mnras/stv195.

[192] Philip F. Hopkins, Dušan Kereš, José Oñorbe, Claude-André Faucher-Giguère, Eliot Quataert, Norman Murray, and James S. Bullock. Galaxies on FIRE (Feedback In Realistic Environments): stellar feedback explains cosmologically inefficient star formation. MNRAS, 445(1):581–603, November 2014. doi: 10.1093/mnras/stu1738.

[193] Philip F. Hopkins, Andrew Wetzel, Dušan Kereš, Claude-André Faucher-Giguère, Eliot Quataert, Michael Boylan-Kolchin, Norman Murray, Christopher C. Hayward, Shea Garrison-Kimmel, Cameron Hummels, Robert Feldmann, Paul Torrey, Xiangcheng Ma, Daniel Anglés-Alcázar, Kung-Yi Su, Matthew Orr, Denise Schmitz, Ivanna Escala, Robyn Sanderson, Michael Y. Grudić, Zachary Hafen, Ji-Hoon Kim, Alex Fitts, James S. Bullock, Coral Wheeler, T. K. Chan, Oliver D. Elbert, and Desika Narayanan. FIRE-2 simulations: physics versus numerics in galaxy formation. MNRAS, 480(1):800–863, October 2018. doi: 10.1093/mnras/sty1690.

[194] Philip F Hopkins et al. FIRE-2 Simulations: Physics versus Numerics in Galaxy Formation. *Mon. Not. Roy. Astron. Soc.*, 480(1):800–863, 2018. doi: 10.1093/mnras/sty1690.

[195] Cullan Howlett, Antony Lewis, Alex Hall, and Anthony Challinor. CMB power spectrum parameter degeneracies in the era of precision cosmology. J. Cosmology Astropart. Phys., 1204:027, 2012. doi: 10.1088/1475-7516/2012/04/027.

[196] Wayne Hu and Gilbert P. Holder. Model-independent reionization observables in the CMB. *PRD*, 68(2):023001, Jul 2003. doi: 10.1103/PhysRevD.68.023001.

[197] Lam Hui, Jeremiah P. Ostriker, Scott Tremaine, and Edward Witten. Ultralight scalars as cosmological dark matter. *PRD*, 95(4):043541, February 2017. doi: 10.1103/PhysRevD.95.043541.

[198] Kazuhide Ichikawa, Masahiro Kawasaki, and Fuminobu Takahashi. The Oscillation effects on thermalization of the neutrinos in the Universe with low reheating temperature. *Phys. Rev.*, D72:043522, 2005. doi: 10.1103/PhysRevD.72.043522.

[199] Derek Inman and Yacine Ali-Haïmoud. Early structure formation in primordial black hole cosmologies. *PRD*, 100(8):083528, October 2019. doi: 10.1103/PhysRevD.100.083528.

[200] Vid Iršič and Matthew McQuinn. Absorber Model: the Halo-like model for the Lyman-α forest. J. Cosmology Astropart. Phys., 2018(4):026, Apr 2018. doi: 10.1088/1475-7516/2018/04/026.

[201] Vid Iršič, Matteo Viel, Martin G. Haehnelt, James S. Bolton, and George D. Becker. First Constraints on Fuzzy Dark Matter from Lyman-α Forest Data and Hydrodynamical Simulations. *PRL*, 119(3):031302, Jul 2017. doi: 10.1103/PhysRevLett.119.031302.

[202] Vid Iršič, Huangyu Xiao, and Matthew McQuinn. Early structure formation constraints on the ultralight axion in the postinflation scenario. *Phys. Rev. D*, 101(12):123518, 2020. doi: 10.1103/PhysRevD.101.123518.

[203] A. Iwazaki. Axion stars and fast radio bursts. *Phys. Rev. D*, 91(2):023008, 2015. doi: 10.1103/PhysRevD.91.023008.

[204] Aiichi Iwazaki. Radiations from axion miniclusters and axion boson stars in galactic magnetic fields. 1997.

[205] Aiichi Iwazaki. Fast Radio Bursts from Axion Stars. 2014.

[206] Aiichi Iwazaki. Axion Stars and Repeating Fast Radio Bursts with Finite Bandwidths. 2017.

[207] D. F. Jackson Kimball, D. Budker, J. Eby, M. Pospelov, S. Pustelny, T. Scholtes, Y. V. Stadnik, A. Weis, and A. Wickenbrock. Searching for axion stars and Q-balls with a terrestrial magnetometer network. *Phys. Rev.*, D97(4):043002, 2018. doi: 10.1103/PhysRevD.97.043002.

[208] A. Jenkins, C. S. Frenk, S. D. M. White, J. M. Colberg, S. Cole, A. E. Evrard, H. M. P. Couchman, and N. Yoshida. The mass function of dark matter haloes. MNRAS, 321(2): 372–384, February 2001. doi: 10.1046/j.1365-8711.2001.04029.x.

[209] Jarrett L. Johnson, Thomas H. Greif, and Volker Bromm. Local Radiative Feedback in the Formation of the First Protogalaxies. *ApJ*, 665(1):85–95, Aug 2007. doi: 10.1086/519212.

[210] G. Jungman, M. Kamionkowski, and K. Griest. Supersymmetric dark matter. Physics Reports, 267:195–373, Mar 1996. doi: 10.1016/0370-1573(95)00058-5.

[211] Marc Kamionkowski and John March-Russell. Planck scale physics and the Peccei-Quinn mechanism. *Phys. Lett. B*, 282:137–141, 1992. doi: 10.1016/0370-2693(92)90492-M.

[212] Gordon Kane, Kuver Sinha, and Scott Watson. Cosmological Moduli and the Post-Inflationary Universe: A Critical Review. *Int. J. Mod. Phys.*, D24(08):1530022, 2015. doi: 10.1142/S0218271815300220.

[213] David B. Kaplan and Ann E. Nelson. Inflationary Axion Cosmology Beyond Our Horizon. 2008.

[214] Andrey Katz, Joachim Kopp, Sergey Sibiryakov, and Wei Xue. Femtolensing by dark matter revisited. J. Cosmology Astropart. Phys., 2018(12):005, December 2018. doi: 10.1088/1475-7516/2018/12/005.

[215] Alexander A. Kaurov, Liang Dai, Tejaswi Venumadhav, Jordi Miralda-Escudé, and Brenda Frye. Highly Magnified Stars in Lensing Clusters: New Evidence in a Galaxy Lensed by MACS J0416.1-2403. 2 2019. doi: 10.3847/1538-4357/ab2888.

[216] Bradley J. Kavanagh, Thomas D.P. Edwards, Luca Visinelli, and Christoph Weniger. Stellar Disruption of Axion Miniclusters in the Milky Way. 11 2020.

[217] M. Kawasaki, Kazunori Kohri, and Naoshi Sugiyama. Cosmological constraints on late time entropy production. *Phys. Rev. Lett.*, 82:4168, 1999. doi: 10.1103/PhysRevLett.82.4168.

[218] M. Kawasaki, Kazunori Kohri, and Naoshi Sugiyama. MeV scale reheating temperature and thermalization of neutrino background. *Phys. Rev.*, D62:023506, 2000. doi: 10.1103/PhysRevD.62.023506.

[219] Masahiro Kawasaki, Toyokazu Sekiguchi, Masahide Yamaguchi, and Jun'ichi Yokoyama. Long-Term Dynamics of Cosmological Axion Strings. *PTEP*, 2018(9):091E01, 2018. doi: 10.1093/ptep/pty098.

[220] Masahiro Kawasaki, Wakutaka Nakano, and Eisuke Sonomoto. Oscillon of Ultra-Light Axion-like Particle. *JCAP*, 01:047, 2020. doi: 10.1088/1475-7516/2020/01/047.

[221] Patrick L. Kelly, Jose M. Diego, Steven Rodney, Nick Kaiser, Tom Broadhurst, Adi Zitrin, Tommaso Treu, Pablo G. Pérez-González, Takahiro Morishita, Mathilde Jauzac, Jonatan Selsing, Masamune Oguri, Laurent Pueyo, Timothy W. Ross, Alexei V. Filippenko, Nathan Smith, Jens Hjorth, S. Bradley Cenko, Xin Wang, D. Andrew Howell, Johan Richard, Brenda L. Frye, Saurabh W. Jha, Ryan J. Foley, Colin Norman, Marusa Bradac, Weikang Zheng, Gabriel Brammer, Alberto Molino Benito, Antonio Cava, Lise Christensen, Selma E. de Mink, Or Graur, Claudio Grillo, Ryota Kawamata, Jean-Paul Kneib, Thomas Matheson, Curtis McCully, Mario Nonino, Ismael Pérez-Fournon, Adam G. Riess, Piero Rosati, Kasper Borello Schmidt, Keren Sharon, and Benjamin J. Weiner. Extreme magnification of an individual star at redshift 1.5 by a galaxy-cluster lens. *Nature Astronomy*, 2(4):334–342, Apr 2018. ISSN 2397-3366. doi: 10.1038/s41550-018-0430-3. URL https://doi.org/10.1038/s41550-018-0430-3.

[222] Thomas W. Kephart and Thomas J. Weiler. Stimulated radiation from axion cluster evolution. *Phys. Rev.*, D52:3226–3238, 1995. doi: 10.1103/PhysRevD.52.3226.

[223] M. Yu. Khlopov and A. G. Polnarev. SUPERHEAVY PARTICLES IN COSMOLOGY AND EVOLUTION OF INHOMOGENEITIES IN THE EARLY UNIVERSE. In *Nuffield Workshop on the Very Early Universe Cambridge, England, June 21-July 9, 1982*, pages 407–447, 1982.

[224] M. Yu. Khlopov, A. S. Sakharov, and D. D. Sokoloff. The large scale modulation of the density distribution in standard axionic CDM and its cosmological and physical impact. In

2nd International Workshop on Birth of the Universe and Fundamental Physics Rome, Italy, May 19-24, 1997, 1998.

[225] T. W. B. Kibble. Topology of Cosmic Domains and Strings. *J. Phys.*, A9:1387–1398, 1976. doi: 10.1088/0305-4470/9/8/029.

[226] T.W.B. Kibble. Some implications of a cosmological phase transition. *Physics Reports*, 67 (1):183 – 199, 1980. ISSN 0370-1573. doi: https://doi.org/10.1016/0370-1573(80)90091-5. URL http://www.sciencedirect.com/science/article/pii/0370157380900915.

[227] Jihn E. Kim. Weak-interaction singlet and strong CP invariance. *Phys. Rev. Lett.*, 43:103–107, Jul 1979. doi: 10.1103/PhysRevLett.43.103. URL https://link.aps.org/doi/10.1103/PhysRevLett.43.103.

[228] Jihn E. Kim and Gianpaolo Carosi. Axions and the Strong CP Problem. *Rev. Mod. Phys.*, 82:557–602, 2010. doi: 10.1103/RevModPhys.82.557.

[229] Ivan King. The structure of star clusters. I. an empirical density law. Astronomical Journal, 67:471, October 1962. doi: 10.1086/108756.

[230] Kay Kirkpatrick, Anthony E. Mirasola, and Chanda Prescod-Weinstein. Relaxation Times for Bose-Einstein Condensation in Axion Miniclusters. *Phys. Rev. D*, 102(10):103012, 2020. doi: 10.1103/PhysRevD.102.103012.

[231] Vincent B. Klaer and Guy D. Moore. The dark-matter axion mass. *JCAP*, 11:049, 2017. doi: 10.1088/1475-7516/2017/11/049.

[232] Vincent B. Klaer and Guy D. Moore. Global Cosmic String Networks as a Function of Tension. *JCAP*, 06:021, 2020. doi: 10.1088/1475-7516/2020/06/021.

[233] Anatoly Klypin, HongSheng Zhao, and Rachel S. Somerville. ΛCDM-based Models for the Milky Way and M31. I. Dynamical Models. *ApJ*, 573(2):597–613, July 2002. doi: 10.1086/340656.

[234] Alexander Knebe, Steffen R. Knollmann, Stuart I. Muldrew, Frazer R. Pearce, Miguel Angel Aragon-Calvo, Yago Ascasibar, Peter S. Behroozi, Daniel Ceverino, Stephane Colombi, Juerg Diemand, Klaus Dolag, Bridget L. Falck, Patricia Fasel, Jeff Gardner, Stefan Gottlöber, Chung-Hsing Hsu, Francesca Iannuzzi, Anatoly Klypin, Zarija Lukić, Michal Maciejewski, Cameron McBride, Mark C. Neyrinck, Susana Planelles, Doug Potter, Vicent Quilis, Yann Rasera, Justin I. Read, Paul M. Ricker, Fabrice Roy, Volker Springel, Joachim Stadel, Greg Stinson, P. M. Sutter, Victor Turchaninov, Dylan Tweed, Gustavo Yepes, and Marcel Zemp. Haloes gone MAD: The Halo-Finder Comparison Project. MNRAS, 415(3):2293–2318, August 2011. doi: 10.1111/j.1365-2966.2011.18858.x.

[235] Takeshi Kobayashi, Riccardo Murgia, Andrea De Simone, Vid Iršič, and Matteo Viel. Lyman-α constraints on ultralight scalar dark matter: Implications for the early and late universe. *PRD*, 96(12):123514, Dec 2017. doi: 10.1103/PhysRevD.96.123514.

[236] Hideo Kodama and Misao Sasaki. Cosmological Perturbation Theory. *Prog. Theor. Phys. Suppl.*, 78:1–166, 1984. doi: 10.1143/PTPS.78.1.

[237] Lev Kofman, Andrei D. Linde, and Alexei A. Starobinsky. Reheating after inflation. *Phys. Rev. Lett.*, 73:3195–3198, 1994. doi: 10.1103/PhysRevLett.73.3195.

[238] Lev Kofman, Andrei Linde, and Alexei A. Starobinsky. Nonthermal Phase Transitions after Inflation. *PRL*, 76(7):1011–1014, Feb 1996. doi: 10.1103/PhysRevLett.76.1011.

[239] Edward W. Kolb and Igor I. Tkachev. Axion miniclusters and Bose stars. *Phys. Rev. Lett.*, 71:3051–3054, 1993. doi: 10.1103/PhysRevLett.71.3051.

[240] Edward W. Kolb and Igor I. Tkachev. Nonlinear axion dynamics and formation of cosmological pseudosolitons. *Phys. Rev.*, D49:5040–5051, 1994. doi: 10.1103/PhysRevD.49.5040.

[241] Edward W. Kolb and Igor I. Tkachev. Femtolensing and picolensing by axion miniclusters. *Astrophys. J.*, 460:L25–L28, 1996. doi: 10.1086/309962.

[242] Edward W. Kolb and Michael S. Turner. *The early universe*, volume 69. 1990.

[243] Edward W. Kolb, Alessio Notari, and Antonio Riotto. Reheating stage after inflation. *PRD*, 68(12):123505, Dec 2003. doi: 10.1103/PhysRevD.68.123505.

[244] E. Komatsu et al. Seven-Year Wilkinson Microwave Anisotropy Probe (WMAP) Observations: Cosmological Interpretation. *Astrophys. J. Suppl.*, 192:18, 2011. doi: 10.1088/0067-0049/192/2/18.

[245] P. Kroupa. On the variation of the initial mass function. MNRAS, 322:231–246, April 2001. doi: 10.1046/j.1365-8711.2001.04022.x.

[246] Pavel Kroupa. The initial mass function of stars: Evidence for uniformity in variable systems. *Science*, 295(5552):82–91, 2002. ISSN 0036-8075. doi: 10.1126/science.1067524. URL https://science.sciencemag.org/content/295/5552/82.

[247] Pavel Kroupa, Christopher A. Tout, and Gerard Gilmore. The Distribution of Low-Mass Stars in the Galactic Disc. MNRAS, 262:545–587, June 1993. doi: 10.1093/mnras/262.3.545.

[248] Cedric Lacey and Shaun Cole. Merger rates in hierarchical models of galaxy formation. *Monthly Notices of the Royal Astronomical Society*, 262(3):627–649, 06 1993. ISSN 0035-8711. doi: 10.1093/mnras/262.3.627. URL https://doi.org/10.1093/mnras/262.3.627.

[249] Anne de Laguarde. Another unreal paper. *Nat*, 3:303–304, 1903.

[250] Muhammad A. Latif and Andrea Ferrara. Formation of Supermassive Black Hole Seeds. Publications of the Astronomical Society of Australia, 33:e051, October 2016. doi: 10.1017/pasa.2016.41.

[251] A. Lawrence, S. J. Warren, O. Almaini, A. C. Edge, N. C. Hambly, R. F. Jameson, P. Lucas, M. Casali, A. Adamson, S. Dye, J. P. Emerson, S. Foucaud, P. Hewett, P. Hirst, S. T. Hodgkin, M. J. Irwin, N. Lodieu, R. G. McMahon, C. Simpson, I. Smail, D. Mortlock, and M. Folger.

The UKIRT Infrared Deep Sky Survey (UKIDSS). MNRAS, 379:1599–1617, August 2007. doi: 10.1111/j.1365-2966.2007.12040.x.

[252] George Lazarides and Q. Shafi. Axion Models with No Domain Wall Problem. *Phys. Lett.*, 115B:21–25, 1982. doi: 10.1016/0370-2693(82)90506-8.

[253] George Lazarides, Robert K. Schaefer, D. Seckel, and Q. Shafi. Dilution of Cosmological Axions by Entropy Production. *Nucl. Phys.*, B346:193–212, 1990. doi: 10.1016/0550-3213(90)90244-8.

[254] T. D. Lee and C. N. Yang. Question of parity conservation in weak interactions. *Phys. Rev.*, 104:254–258, Oct 1956. doi: 10.1103/PhysRev.104.254. URL https://link.aps.org/doi/10.1103/PhysRev.104.254.

[255] Vincent S. H. Lee, Stephen R. Taylor, Tanner Trickle, and Kathryn M. Zurek. Bayesian Forecasts for Dark Matter Substructure Searches with Mock Pulsar Timing Data. *JCAP*, 08: 025, 2021. doi: 10.1088/1475-7516/2021/08/025.

[256] Vincent S.H. Lee, Andrea Mitridate, Tanner Trickle, and Kathryn M. Zurek. Probing Small-Scale Power Spectra with Pulsar Timing Arrays. 12 2020.

[257] Martin Lemoine and Jerome Martin. Neutralino Dark Matter and the Curvaton. *Phys. Rev.*, D75:063504, 2007. doi: 10.1103/PhysRevD.75.063504.

[258] D. G. Levkov, A. G. Panin, and I. I. Tkachev. Relativistic Axions from Collapsing Bose Stars. *Phys. Rev. Lett.*, 118(1):011301, 2017. doi: 10.1103/PhysRevLett.118.011301.

[259] D. G. Levkov, A. G. Panin, and I. I. Tkachev. Gravitational Bose-Einstein Condensation in the Kinetic Regime. *Phys. Rev. Lett.*, 121(15):151301, 2018. doi: 10.1103/PhysRevLett.121.151301.

[260] Antony Lewis. CAMB Notes. https://cosmologist.info/notes/CAMB.pdf.

[261] Antony Lewis and Sarah Bridle. Cosmological parameters from CMB and other data: A Monte Carlo approach. *PRD*, 66:103511, 2002. doi: 10.1103/PhysRevD.66.103511.

[262] Antony Lewis, Anthony Challinor, and Anthony Lasenby. Efficient computation of CMB anisotropies in closed FRW models. *ApJ*, 538:473–476, 2000. doi: 10.1086/309179.

[263] Andrei D. Linde. Generation of Isothermal Density Perturbations in the Inflationary Universe. *Phys. Lett.*, 158B:375–380, 1985. doi: 10.1016/0370-2693(85)90436-8.

[264] Andrei D. Linde and Viatcheslav F. Mukhanov. Nongaussian isocurvature perturbations from inflation. *Phys. Rev.*, D56:R535–R539, 1997. doi: 10.1103/PhysRevD.56.R535.

[265] Abraham Loeb and Matias Zaldarriaga. Small-scale power spectrum of cold dark matter. *PRD*, 71(10):103520, May 2005. doi: 10.1103/PhysRevD.71.103520.

[266] Zarija Lukić, Katrin Heitmann, Salman Habib, Sergei Bashinsky, and Paul M. Ricker. The Halo Mass Function: High-Redshift Evolution and Universality. *ApJ*, 671(2):1160–1181, Dec 2007. doi: 10.1086/523083.

[267] David H. Lyth. A Limit on the Inflationary Energy Density From Axion Isocurvature Fluctuations. *Phys. Lett.*, B236:408–410, 1990. doi: 10.1016/0370-2693(90)90374-F.

[268] David H. Lyth and Ewan D. Stewart. Constraining the inflationary energy scale from axion cosmology. *Phys. Lett.*, B283:189–193, 1992. doi: 10.1016/0370-2693(92)90006-P.

[269] David H. Lyth and David Wands. Generating the curvature perturbation without an inflaton. *Phys. Lett.*, B524:5–14, 2002. doi: 10.1016/S0370-2693(01)01366-1.

[270] Marie E. Machacek, Greg L. Bryan, and Tom Abel. Simulations of Pregalactic Structure Formation with Radiative Feedback. *ApJ*, 548(2):509–521, Feb 2001. doi: 10.1086/319014.

[271] Michele Maggiore and Antonio Riotto. The Halo Mass Function from Excursion Set Theory. I. Gaussian fluctuations with non-Markovian dependence on the smoothing scale. *Astrophys. J.*, 711:907–927, 2010. doi: 10.1088/0004-637X/711/2/907.

[272] Karim A. Malik, David Wands, and Carlo Ungarelli. Large scale curvature and entropy perturbations for multiple interacting fluids. *Phys. Rev.*, D67:063516, 2003. doi: 10.1103/PhysRevD.67.063516.

[273] David J. E. Marsh. Axion Cosmology. *Phys. Rept.*, 643:1–79, 2016. doi: 10.1016/j.physrep.2016.06.005.

[274] David J. E. Marsh, Daniel Grin, Renée Hlozek, and Pedro G. Ferreira. Axiverse cosmology and the energy scale of inflation. *PRD*, 87(12):121701, Jun 2013. doi: 10.1103/PhysRevD.87.121701.

[275] Charlotte A. Mason, Tommaso Treu, Mark Dijkstra, Andrei Mesinger, Michele Trenti, Laura Pentericci, Stephane de Barros, and Eros Vanzella. The Universe Is Reionizing at z 7: Bayesian Inference of the IGM Neutral Fraction Using Lyα Emission from Galaxies. *ApJ*, 856(1):2, Mar 2018. doi: 10.3847/1538-4357/aab0a7.

[276] Charlotte A. Mason, Adriano Fontana, Tommaso Treu, Kasper B. Schmidt, Austin Hoag, Louis Abramson, Ricardo Amorin, Maruša Bradač, Lucia Guaita, Tucker Jones, Alaina Henry, Matthew A. Malkan, Laura Pentericci, Michele Trenti, and Eros Vanzella. Inferences on the timeline of reionization at z 8 from the KMOS Lens-Amplified Spectroscopic Survey. MNRAS, 485(3):3947–3969, May 2019. doi: 10.1093/mnras/stz632.

[277] Eduard Masso and Ramon Toldra. On a light spinless particle coupled to photons. *Phys. Rev. D*, 52:1755–1763, 1995. doi: 10.1103/PhysRevD.52.1755.

[278] James McBride, Onsi Fakhouri, and Chung-Pei Ma. Mass accretion rates and histories of dark matter haloes. MNRAS, 398(4):1858–1868, Oct 2009. doi: 10.1111/j.1365-2966.2009.15329.x.

[279] Ian D. McGreer, Andrei Mesinger, and Valentina D'Odorico. Model-independent evidence in favour of an end to reionization by z $\approx$ 6. MNRAS, 447(1):499–505, Feb 2015. doi: 10.1093/mnras/stu2449.

[280] Christopher F. McKee, Antonio Parravano, and David J. Hollenbach. Stars, Gas, and Dark Matter in the Solar Neighborhood. *ApJ*, 814(1):13, November 2015. doi: 10.1088/0004-637X/814/1/13.

[281] R. J. McLure, J. S. Dunlop, R. A. A. Bowler, E. Curtis-Lake, M. Schenker, R. S. Ellis, B. E. Robertson, A. M. Koekemoer, A. B. Rogers, Y. Ono, M. Ouchi, S. Charlot, V. Wild, D. P. Stark, S. R. Furlanetto, M. Cirasuolo, and T. A. Targett. A new multifield determination of the galaxy luminosity function at z = 7-9 incorporating the 2012 Hubble Ultra-Deep Field imaging. MNRAS, 432(4):2696–2716, Jul 2013. doi: 10.1093/mnras/stt627.

[282] R. G. McMahon, M. Banerji, E. Gonzalez, S. E. Koposov, V. J. Bejar, N. Lodieu, R. Rebolo, and VHS Collaboration. First Scientific Results from the VISTA Hemisphere Survey (VHS). *The Messenger*, 154:35–37, December 2013.

[283] Paul J. McMillan. Mass models of the Milky Way. MNRAS, 414(3):2446–2457, July 2011. doi: 10.1111/j.1365-2966.2011.18564.x.

[284] Paul J. McMillan. The mass distribution and gravitational potential of the Milky Way. MNRAS, 465(1):76–94, February 2017. doi: 10.1093/mnras/stw2759.

[285] M. McQuinn. *Autobiography: The Great Quotations of Matthew McQuinn*. 2020.

[286] Matthew McQuinn. The Evolution of the Intergalactic Medium. *Ann. Rev. Astron.& Astrophys.* , 54:313–362, Sep 2016. doi: 10.1146/annurev-astro-082214-122355.

[287] Matthew McQuinn and Ryan M. O'Leary. The Impact of the Supersonic Baryon-Dark Matter Velocity Difference on the z $\backsim$20 21 cm Background. *ApJ*, 760(1):3, Nov 2012. doi: 10.1088/0004-637X/760/1/3.

[288] Richard H. Mebane, Jordan Mirocha, and Steven R. Furlanetto. The Persistence of Population III Star Formation. MNRAS, 479(4):4544–4559, Oct 2018. doi: 10.1093/mnras/sty1833.

[289] Avery A. Meiksin. The physics of the intergalactic medium. *Reviews of Modern Physics*, 81 (4):1405–1469, Oct 2009. doi: 10.1103/RevModPhys.81.1405.

[290] M. Membrado, J. Abad, A. F. Pacheco, and J. Sanudo. Newtonian Boson Spheres. *Phys. Rev. D*, 40:2736–2738, 1989. doi: 10.1103/PhysRevD.40.2736.

[291] Florent Michel and Ian G. Moss. Relativistic collapse of axion stars. 2018.

[292] Jordi Miralda-Escudé, Renyue Cen, Jeremiah P. Ostriker, and Michael Rauch. The Ly alpha Forest from Gravitational Collapse in the Cold Dark Matter + Lambda Model. *ApJ*, 471: 582, Nov 1996. doi: 10.1086/177992.

[293] Vinicius Miranda, Adam Lidz, Chen He Heinrich, and Wayne Hu. CMB signatures of metal-free star formation and Planck 2015 polarization data. MNRAS, 467(4):4050–4056, Jun 2017. doi: 10.1093/mnras/stx306.

[294] H J Mo, Shude Mao, and Simon D.M. White. The formation of galactic discs. *Monthly Notices of the Royal Astronomical Society*, 295(2):319–336, 1998. ISSN 00358711. doi: 10.1046/j.1365-8711.1998.01227.x.

[295] Philip Mocz, Mark Vogelsberger, Victor H. Robles, Jesús Zavala, Michael Boylan-Kolchin, Anastasia Fialkov, and Lars Hernquist. Galaxy formation with BECDM – I. Turbulence and relaxation of idealized haloes. *Mon. Not. Roy. Astron. Soc.*, 471(4):4559–4570, 2017. doi: 10.1093/mnras/stx1887.

[296] Philip Mocz, Anastasia Fialkov, Mark Vogelsberger, Fernando Becerra, Mustafa A. Amin, Sownak Bose, Michael Boylan-Kolchin, Pierre-Henri Chavanis, Lars Hernquist, Lachlan Lancaster, Federico Marinacci, Victor H. Robles, and Jesús Zavala. First star-forming structures in fuzzy cosmic filaments. *Phys. Rev. Lett.*, 123:141301, Oct 2019. doi: 10.1103/PhysRevLett.123.141301. URL https://link.aps.org/doi/10.1103/PhysRevLett.123.141301.

[297] Silvia Mollerach. Isocurvature Baryon Perturbations and Inflation. *Phys. Rev.*, D42:313–325, 1990. doi: 10.1103/PhysRevD.42.313.

[298] Paulo Montero-Camacho, Xiao Fang, Gabriel Vasquez, Makana Silva, and Christopher M. Hirata. Revisiting constraints on asteroid-mass primordial black holes as dark matter candidates. J. Cosmology Astropart. Phys., 2019(8):031, August 2019. doi: 10.1088/1475-7516/2019/08/031.

[299] Ben Moore. An Upper Limit to the Mass of Black Holes in the Halo of the Galaxy. Astrophysical Journal Letters, 413:L93, August 1993. doi: 10.1086/186967.

[300] Surhud More, Benedikt Diemer, and Andrey V. Kravtsov. The Splashback Radius as a Physical Halo Boundary and the Growth of Halo Mass. *ApJ*, 810(1):36, September 2015. doi: 10.1088/0004-637X/810/1/36.

[301] Takeo Moroi and Tomo Takahashi. Effects of cosmological moduli fields on cosmic microwave background. *Phys. Lett.*, B522:215–221, 2001. doi: 10.1016/S0370-2693(02)02070-1,10.1016/S0370-2693(01)01295-3. [Erratum: Phys. Lett.B539,303(2002)].

[302] Benjamin P. Moster, Thorsten Naab, and Simon D. M. White. Galactic star formation and accretion histories from matching galaxies to dark matter haloes. MNRAS, 428(4):3121–3138, February 2013. doi: 10.1093/mnras/sts261.

[303] Kyohei Mukaida, Masahiro Takimoto, and Masaki Yamada. On Longevity of I-ball/Oscillon. *JHEP*, 03:122, 2017. doi: 10.1007/JHEP03(2017)122.

[304] Riccardo Murgia, Giulio Scelfo, Matteo Viel, and Alvise Raccanelli. Lyman-α forest constraints on Primordial Black Holes as Dark Matter. *arXiv e-prints*, art. arXiv:1903.10509, Mar 2019.

[305] Yasusada Nambu and Misao Sasaki. Quantum Treatment of Cosmological Axion Perturbations. *Phys. Rev.*, D42:3918–3924, 1990. doi: 10.1103/PhysRevD.42.3918.

[306] Julio F. Navarro, Carlos S. Frenk, and Simon D.M. White. The Structure of cold dark matter halos. *Astrophys. J.*, 462:563–575, 1996. doi: 10.1086/177173.

[307] Julio F. Navarro, Carlos S. Frenk, and Simon D. M. White. A Universal Density Profile from Hierarchical Clustering. *ApJ*, 490(2):493–508, December 1997. doi: 10.1086/304888.

[308] Ann E. Nelson and Jakub Scholtz. Dark Light, Dark Matter and the Misalignment Mechanism. *Phys. Rev. D*, 84:103501, 2011. doi: 10.1103/PhysRevD.84.103501.

[309] Ann E. Nelson and Huangyu Xiao. Axion Cosmology with Early Matter Domination. *Phys. Rev. D*, 98(6):063516, 2018. doi: 10.1103/PhysRevD.98.063516.

[310] Toshifumi Noumi, Ken'ichi Saikawa, Ryosuke Sato, and Masahide Yamaguchi. Effective gravitational interactions of dark matter axions. *Phys. Rev.*, D89(6):065012, 2014. doi: 10.1103/PhysRevD.89.065012.

[311] Andreas Nygaard, Thomas Tram, and Steen Hannestad. Updated constraints on decaying cold dark matter. *JCAP*, 05:017, 2021. doi: 10.1088/1475-7516/2021/05/017.

[312] P. A. Oesch, R. J. Bouwens, G. D. Illingworth, I. Labbé, M. Franx, P. G. van Dokkum, M. Trenti, M. Stiavelli, V. Gonzalez, and D. Magee. Probing the Dawn of Galaxies at z ˜ 9-12: New Constraints from HUDF12/XDF and CANDELS data. *ApJ*, 773:75, August 2013. doi: 10.1088/0004-637X/773/1/75.

[313] Masamune Oguri and Jounghun Lee. A realistic model for spatial and mass distributions of dark halo substructures: An analytic approach. MNRAS, 355(1):120–128, November 2004. doi: 10.1111/j.1365-2966.2004.08304.x.

[314] Ciaran O'Hare. cajohare/axionlimits: Axionlimits. `https://cajohare.github.io/AxionLimits/`, July 2020.

[315] Ciaran O'HARE. cajohare/axionlimits: Axionlimits, July 2020. URL `https://doi.org/10.5281/zenodo.3932430`.

[316] Ciaran A. J. O'Hare, Giovanni Pierobon, Javier Redondo, and Yvonne Y. Y. Wong. Simulations of axion-like particles in the post-inflationary scenario. 12 2021.

[317] Chiamaka Okoli. Dark matter halo concentrations: a short review. *arXiv e-prints*, art. arXiv:1711.05277, November 2017.

[318] Ryan M. O'Leary and Matthew McQuinn. The Formation of the First Cosmic Structures and the Physics of the z ∼20 Universe. *ApJ*, 760(1):4, Nov 2012. doi: 10.1088/0004-637X/760/1/4.

[319] Jan Olle, Oriol Pujolas, and Fabrizio Rompineve. Recipes for oscillon longevity. *JCAP*, 09: 015, 2021. doi: 10.1088/1475-7516/2021/09/015.

[320] Eve C. Ostriker. Dynamical Friction in a Gaseous Medium. *ApJ*, 513(1):252–258, Mar 1999. doi: 10.1086/306858.

[321] Jeremiah P. Ostriker, Jr. Spitzer, Lyman, and Roger A. Chevalier. On the Evolution of Globular Clusters. Astrophysical Journal Letters, 176:L51, September 1972. doi: 10.1086/181018.

[322] F. Pacucci, A. Mesinger, and Z. Haiman. Focusing on warm dark matter with lensed high-redshift galaxies. MNRAS, 435:L53–L57, Aug 2013. doi: 10.1093/mnrasl/slt093.

[323] Luis E. Padilla, Tanja Rindler-Daller, Paul R. Shapiro, Tonatiuh Matos, and J. Alberto Vázquez. Core-halo mass relation in scalar field dark matter models and its consequences for the formation of supermassive black holes. *PRD*, 103(6):063012, March 2021. doi: 10.1103/PhysRevD.103.063012.

[324] R. D. Peccei. The Strong CP problem and axions. *Lect. Notes Phys.*, 741:3–17, 2008. doi: 10.1007/978-3-540-73518-2_1. [,3(2006)].

[325] R. D. Peccei and Helen R. Quinn. CP Conservation in the Presence of Instantons. *Phys. Rev. Lett.*, 38:1440–1443, 1977. doi: 10.1103/PhysRevLett.38.1440.

[326] J. M. Pendlebury et al. Revised experimental upper limit on the electric dipole moment of the neutron. *Phys. Rev.*, D92(9):092003, 2015. doi: 10.1103/PhysRevD.92.092003.

[327] Planck Collaboration, P. A. R. Ade, N. Aghanim, M. Arnaud, M. Ashdown, J. Aumont, C. Baccigalupi, A. J. Banday, R. B. Barreiro, J. G. Bartlett, N. Bartolo, E. Battaner, R. Battye, K. Benabed, A. Benoît, A. Benoit-Lévy, J. P. Bernard, M. Bersanelli, P. Bielewicz, J. J. Bock, A. Bonaldi, L. Bonavera, J. R. Bond, J. Borrill, F. R. Bouchet, F. Boulanger, M. Bucher, C. Burigana, R. C. Butler, E. Calabrese, J. F. Cardoso, A. Catalano, A. Challinor, A. Chamballu, R. R. Chary, H. C. Chiang, J. Chluba, P. R. Christensen, S. Church, D. L. Clements, S. Colombi, L. P. L. Colombo, C. Combet, A. Coulais, B. P. Crill, A. Curto, F. Cuttaia, L. Danese, R. D. Davies, R. J. Davis, P. de Bernardis, A. de Rosa, G. de Zotti, J. Delabrouille, F. X. Désert, E. Di Valentino, C. Dickinson, J. M. Diego, K. Dolag, H. Dole, S. Donzelli, O. Doré, M. Douspis, A. Ducout, J. Dunkley, X. Dupac, G. Efstathiou, F. Elsner, T. A. Enßlin, H. K. Eriksen, M. Farhang, J. Fergusson, F. Finelli, O. Forni, M. Frailis, A. A. Fraisse, E. Franceschi, A. Frejsel, S. Galeotta, S. Galli, K. Ganga, C. Gauthier, M. Gerbino, T. Ghosh, M. Giard, Y. Giraud-Héraud, E. Giusarma, E. Gjerløw, J. González-Nuevo, K. M. Górski, S. Gratton, A. Gregorio, A. Gruppuso, J. E. Gudmundsson, J. Hamann, F. K. Hansen, D. Hanson, D. L. Harrison, G. Helou, S. Henrot-Versillé, C. Hernández-Monteagudo, D. Herranz, S. R. Hildebrand t, E. Hivon, M. Hobson, W. A. Holmes, A. Hornstrup, W. Hovest, Z. Huang, K. M. Huffenberger, G. Hurier, A. H. Jaffe, T. R. Jaffe, W. C. Jones, M. Juvela, E. Keihänen, R. Keskitalo, T. S. Kisner, R. Kneissl, J. Knoche, L. Knox, M. Kunz, H. Kurki-Suonio, G. Lagache, A. Lähteenmäki, J. M. Lamarre, A. Lasenby, M. Lattanzi, C. R. Lawrence, J. P. Leahy, R. Leonardi, J. Lesgourgues, F. Levrier, A. Lewis, M. Liguori, P. B. Lilje, M. Linden-Vørnle, M. López-Caniego, P. M. Lubin, J. F. Macías-Pérez, G. Maggio, D. Maino, N. Mandolesi, A. Mangilli, A. Marchini, M. Maris, P. G. Martin, M. Martinelli, E. Martínez-González, S. Masi, S. Matarrese, P. McGehee, P. R. Meinhold, A. Melchiorri, J. B. Melin, L. Mendes, A. Mennella, M. Migliaccio, M. Millea, S. Mitra, M. A. Miville-Deschênes, A. Moneti, L. Montier, G. Morgante, D. Mortlock, A. Moss, D. Munshi, J. A.

Murphy, P. Naselsky, F. Nati, P. Natoli, C. B. Netterfield, H. U. Nørgaard-Nielsen, F. Noviello, D. Novikov, I. Novikov, C. A. Oxborrow, F. Paci, L. Pagano, F. Pajot, R. Paladini, D. Paoletti, B. Partridge, F. Pasian, G. Patanchon, T. J. Pearson, O. Perdereau, L. Perotto, F. Perrotta, V. Pettorino, F. Piacentini, M. Piat, E. Pierpaoli, D. Pietrobon, S. Plaszczynski, E. Pointecouteau, G. Polenta, L. Popa, G. W. Pratt, G. Prézeau, S. Prunet, J. L. Puget, J. P. Rachen, W. T. Reach, R. Rebolo, M. Reinecke, M. Remazeilles, C. Renault, A. Renzi, I. Ristorcelli, G. Rocha, C. Rosset, M. Rossetti, G. Roudier, B. Rouillé d'Orfeuil, M. Rowan-Robinson, J. A. Rubiño-Martín, B. Rusholme, N. Said, V. Salvatelli, L. Salvati, M. Sandri, D. Santos, M. Savelainen, G. Savini, D. Scott, M. D. Seiffert, P. Serra, E. P. S. Shellard, L. D. Spencer, M. Spinelli, V. Stolyarov, R. Stompor, R. Sudiwala, R. Sunyaev, D. Sutton, A. S. Suur-Uski, J. F. Sygnet, J. A. Tauber, L. Terenzi, L. Toffolatti, M. Tomasi, M. Tristram, T. Trombetti, M. Tucci, J. Tuovinen, M. Türler, G. Umana, L. Valenziano, J. Valiviita, F. Van Tent, P. Vielva, F. Villa, L. A. Wade, B. D. Wandelt, I. K. Wehus, M. White, S. D. M. White, A. Wilkinson, D. Yvon, A. Zacchei, and A. Zonca. Planck 2015 results. XIII. Cosmological parameters. A&A, 594:A13, Sep 2016. doi: 10.1051/0004-6361/201525830.

[328] Planck Collaboration, Y. Akrami, F. Arroja, M. Ashdown, J. Aumont, C. Baccigalupi, M. Ballardini, A. J. Banday, R. B. Barreiro, N. Bartolo, S. Basak, K. Benabed, J. P. Bernard, M. Bersanelli, P. Bielewicz, J. J. Bock, J. R. Bond, J. Borrill, F. R. Bouchet, F. Boulanger, M. Bucher, C. Burigana, R. C. Butler, E. Calabrese, J. F. Cardoso, J. Carron, A. Challinor, H. C. Chiang, L. P. L. Colombo, C. Combet, D. Contreras, B. P. Crill, F. Cuttaia, P. de Bernardis, G. de Zotti, J. Delabrouille, J. M. Delouis, E. Di Valentino, J. M. Diego, S. Donzelli, O. Doré, M. Douspis, A. Ducout, X. Dupac, S. Dusini, G. Efstathiou, F. Elsner, T. A. Enßlin, H. K. Eriksen, Y. Fantaye, J. Fergusson, R. Fernandez-Cobos, F. Finelli, F. Forastieri, M. Frailis, E. Franceschi, A. Frolov, S. Galeotta, S. Galli, K. Ganga, C. Gauthier, R. T. Génova-Santos, M. Gerbino, T. Ghosh, J. González-Nuevo, K. M. Górski, S. Gratton, A. Gruppuso, J. E. Gudmundsson, J. Hamann, W. Handley, F. K. Hansen, D. Herranz, E. Hivon, D. C. Hooper, Z. Huang, A. H. Jaffe, W. C. Jones, E. Keihänen, R. Keskitalo,

K. Kiiveri, J. Kim, T. S. Kisner, N. Krachmalnicoff, M. Kunz, H. Kurki-Suonio, G. Lagache, J. M. Lamarre, A. Lasenby, M. Lattanzi, C. R. Lawrence, M. Le Jeune, J. Lesgourgues, F. Levrier, A. Lewis, M. Liguori, P. B. Lilje, V. Lindholm, M. Lpez-Caniego, P. M. Lubin, Y. Z. Ma, J. F. Macías-Pérez, G. Maggio, D. Maino, N. Mandolesi, A. Mangilli, A. Marcos-Caballero, M. Maris, P. G. Martin, E. Martínez-González, S. Matarrese, N. Mauri, J. D. McEwen, P. D. Meerburg, P. R. Meinhold, A. Melchiorri, A. Mennella, M. Migliaccio, S. Mitra, M. A. Miville-Deschênes, D. Molinari, A. Moneti, L. Montier, G. Morgante, A. Moss, M. Münchmeyer, P. Natoli, H. U. Nørgaard-Nielsen, L. Pagano, D. Paoletti, B. Partridge, G. Patanchon, H. V. Peiris, F. Perrotta, V. Pettorino, F. Piacentini, L. Polastri, G. Polenta, J. L. Puget, J. P. Rachen, M. Reinecke, M. Remazeilles, A. Renzi, G. Rocha, C. Rosset, G. Roudier, J. A. Rubiño-Martín, B. Ruiz-Granados, L. Salvati, M. Sandri, M. Savelainen, D. Scott, E. P. S. Shellard, M. Shiraishi, C. Sirignano, G. Sirri, L. D. Spencer, R. Sunyaev, A. S. Suur-Uski, J. A. Tauber, D. Tavagnacco, M. Tenti, L. Toffolatti, M. Tomasi, T. Trombetti, J. Valiviita, B. Van Tent, P. Vielva, F. Villa, N. Vittorio, B. D. Wandelt, I. K. Wehus, S. D. M. White, A. Zacchei, J. P. Zibin, and A. Zonca. Planck 2018 results. X. Constraints on inflation. *arXiv e-prints*, art. arXiv:1807.06211, Jul 2018.

[329] Vivian Poulin, Pasquale D. Serpico, and Julien Lesgourgues. A fresh look at linear cosmological constraints on a decaying dark matter component. *JCAP*, 08:036, 2016. doi: 10.1088/1475-7516/2016/08/036.

[330] C. Power, J. F. Navarro, A. Jenkins, C. S. Frenk, S. D. M. White, V. Springel, J. Stadel, and T. Quinn. The inner structure of ΛCDM haloes - I. A numerical convergence study. MNRAS, 338(1):14–34, January 2003. doi: 10.1046/j.1365-8711.2003.05925.x.

[331] Anirudh Prabhu. Optical Lensing by Axion Stars: Observational Prospects with Radio Astrometry. 6 2020.

[332] Anirudh Prabhu and Nicholas M. Rapidis. Resonant Conversion of Dark Matter Oscillons in Pulsar Magnetospheres. 5 2020.

[333] John Preskill, Mark B. Wise, and Frank Wilczek. Cosmology of the Invisible Axion. *Phys. Lett.*, B120:127–132, 1983. doi: 10.1016/0370-2693(83)90637-8. [,URL(1982)].

[334] William H. Press and Paul Schechter. Formation of Galaxies and Clusters of Galaxies by Self-Similar Gravitational Condensation. *ApJ*, 187:425–438, Feb 1974. doi: 10.1086/152650.

[335] Anthony R. Pullen, Andrew J. Benson, and Leonidas A. Moustakas. Nonlinear Evolution of Dark Matter Subhalos and Applications to Warm Dark Matter. *ApJ*, 792(1):24, September 2014. doi: 10.1088/0004-637X/792/1/24.

[336] Georg G. Raffelt. Astrophysical axion bounds. *Lect. Notes Phys.*, 741:51–71, 2008. doi: 10.1007/978-3-540-73518-2_3. [,51(2006)].

[337] Harikrishnan Ramani, Tanner Trickle, and Kathryn M. Zurek. Observability of Dark Matter Substructure with Pulsar Timing Correlations. 5 2020.

[338] Lisa Randall. Composite axion models and Planck scale physics. *Phys. Lett. B*, 284:77–80, 1992. doi: 10.1016/0370-2693(92)91928-3.

[339] Massimo Ricotti, Nickolay Y. Gnedin, and J. Michael Shull. Feedback from Galaxy Formation: Production and Photodissociation of Primordial H_2. *ApJ*, 560(2):580–591, Oct 2001. doi: 10.1086/323051.

[340] Tanja Rindler-Daller and Paul R. Shapiro. Vortices and Angular Momentum in Bose-Einstein-Condensed Cold Dark Matter Halos. *ASP Conf. Ser.*, 432:244, 2010.

[341] Tanja Rindler-Daller and Paul R. Shapiro. Angular Momentum and Vortex Formation in Bose-Einstein-Condensed Cold Dark Matter Haloes. *Mon. Not. Roy. Astron. Soc.*, 422: 135–161, 2012. doi: 10.1111/j.1365-2966.2012.20588.x.

[342] Tanja Rindler-Daller, Tanja Rindler-Daller, Paul R. Shapiro, and Paul R. Shapiro. Finding New Signature Effects on Galactic Dynamics to Constrain Bose–Einstein-Condensed Cold Dark Matter. In *6th International Meeting on Gravitation and Cosmology Guadalajara,*

Jalisco, Mexico, May 21-25, 2012, pages 163–182, 2012. doi: 10.1007/978-3-319-02063-1_12. URL http://inspirehep.net/record/1184893/files/arXiv:1209.1835.pdf. [,163(2014)].

[343] Pablo A. Rosado, Alberto Sesana, and Jonathan Gair. Expected properties of the first gravitational wave signal detected with pulsar timing arrays. *Mon. Not. Roy. Astron. Soc.*, 451(3):2417–2433, 2015. doi: 10.1093/mnras/stv1098.

[344] Remo Ruffini and Silvano Bonazzola. Systems of selfgravitating particles in general relativity and the concept of an equation of state. *Phys. Rev.*, 187:1767–1783, 1969. doi: 10.1103/PhysRev.187.1767.

[345] Benjamin R. Safdi, Zhiquan Sun, and Alexander Y. Chen. Detecting Axion Dark Matter with Radio Lines from Neutron Star Populations. *Phys. Rev. D*, 99(12):123021, 2019. doi: 10.1103/PhysRevD.99.123021.

[346] Ken'ichi Saikawa and Masahide Yamaguchi. Evolution and thermalization of dark matter axions in the condensed regime. *Phys. Rev.*, D87(8):085010, 2013. doi: 10.1103/PhysRevD.87.085010.

[347] A. D. Sakharov. Violation of CP Invariance, C asymmetry, and baryon asymmetry of the universe. *Pisma Zh. Eksp. Teor. Fiz.*, 5:32–35, 1967. doi: 10.1070/PU1991v034n05ABEH002497.

[348] A. S. Sakharov and M. Yu. Khlopov. The Nonhomogeneity problem for the primordial axion field. *Phys. Atom. Nucl.*, 57:485–487, 1994. [Yad. Fiz.57,514(1994)].

[349] Edwin E. Salpeter. The Luminosity Function and Stellar Evolution. *ApJ*, 121:161, January 1955. doi: 10.1086/145971.

[350] J. M. Scalo. The stellar initial mass function. *Fundamentals of Cosmic Physics*, 11:1–278, May 1986.

[351] Hsi-Yu Schive, Tzihong Chiueh, and Tom Broadhurst. Cosmic structure as the quantum interference of a coherent dark wave. *Nature Physics*, 10(7):496–499, Jul 2014. doi: 10.1038/nphys2996.

[352] Aurel Schneider, Lawrence Krauss, and Ben Moore. Impact of dark matter microhalos on signatures for direct and indirect detection. *PRD*, 82(6):063525, September 2010. doi: 10.1103/PhysRevD.82.063525.

[353] D. Seckel and Michael S. Turner. Isothermal Density Perturbations in an Axion Dominated Inflationary Universe. *Phys. Rev.*, D32:3178, 1985. doi: 10.1103/PhysRevD.32.3178.

[354] Edward Seidel and Wai-Mo Suen. Formation of bosonic compact objects. In *On recent developments in theoretical and experimental general relativity, gravitation, and relativistic field theories. Proceedings, 7th Marcel Grossmann Meeting, Stanford, USA, July 24-30, 1994. Pt. A + B*, pages 1067–1069, 1994.

[355] Uroš Seljak, Alexey Makarov, Patrick McDonald, and Hy Trac. Can Sterile Neutrinos Be the Dark Matter? *PRL*, 97(19):191303, Nov 2006. doi: 10.1103/PhysRevLett.97.191303.

[356] Xuejian Shen, Huangyu Xiao, Philip F. Hopkins, and Kathryn M. Zurek. Disruption of Dark Matter Minihaloes in the Milky Way environment: Implications for Axion Miniclusters and Early Matter Domination. 7 2022.

[357] Ravi K. Sheth and Giuseppe Tormen. Large-scale bias and the peak background split. MNRAS, 308(1):119–126, September 1999. doi: 10.1046/j.1365-8711.1999.02692.x.

[358] Ravi K. Sheth and Giuseppe Tormen. An excursion set model of hierarchical clustering: ellipsoidal collapse and the moving barrier. MNRAS, 329(1):61–75, Jan 2002. doi: 10.1046/j.1365-8711.2002.04950.x.

[359] J. Michael Shull, Anthony Harness, Michele Trenti, and Britton D. Smith. Critical Star Formation Rates for Reionization: Full Reionization Occurs at Redshift z $\approx$ 7. *ApJ*, 747(2):100, Mar 2012. doi: 10.1088/0004-637X/747/2/100.

[360] Ethan R. Siegel, M. P. Hertzberg, and J. N. Fry. Probing Dark Matter Substructure with Pulsar Timing. *Mon. Not. Roy. Astron. Soc.*, 382:879, 2007. doi: 10.1111/j.1365-2966.2007.12435.x.

[361] P. Sikivie. Of Axions, Domain Walls and the Early Universe. *Phys. Rev. Lett.*, 48:1156–1159, 1982. doi: 10.1103/PhysRevLett.48.1156.

[362] P. Sikivie and Q. Yang. Bose-Einstein Condensation of Dark Matter Axions. *Phys. Rev. Lett.*, 103:111301, 2009. doi: 10.1103/PhysRevLett.103.111301.

[363] Pierre Sikivie. Axion Cosmology. *Lect. Notes Phys.*, 741:19–50, 2008. doi: 10.1007/978-3-540-73518-2_2. [,19(2006)].

[364] Tracy R. Slatyer, Nikhil Padmanabhan, and Douglas P. Finkbeiner. CMB constraints on WIMP annihilation: Energy absorption during the recombination epoch. *PRD*, 80(4): 043526, Aug 2009. doi: 10.1103/PhysRevD.80.043526.

[365] Renske Smit, Rychard J. Bouwens, Marijn Franx, Garth D. Illingworth, Ivo Labbé, Pascal A. Oesch, and Pieter G. van Dokkum. The Star Formation Rate Function for Redshift z $\sim$4-7 Galaxies: Evidence for a Uniform Buildup of Star-forming Galaxies during the First 3 Gyr of Cosmic Time. *ApJ*, 756(1):14, September 2012. doi: 10.1088/0004-637X/756/1/14.

[366] A. Sollima. The stellar initial mass function of the solar neighbourhood revealed by Gaia. MNRAS, 489(2):2377–2394, October 2019. doi: 10.1093/mnras/stz2093.

[367] Rachel S. Somerville, Peter Behroozi, Viraj Pandya, Avishai Dekel, S. M. Faber, Adriano Fontana, Anton M. Koekemoer, David C. Koo, P. G. Pérez-González, Joel R. Primack, Paola Santini, Edward N. Taylor, and Arjen van der Wel. The relationship between galaxy and dark matter halo size from z $\sim$ 3 to the present. MNRAS, 473(2):2714–2736, January 2018. doi: 10.1093/mnras/stx2040.

[368] Jr. Spitzer, Lyman. Disruption of Galactic Clusters. *ApJ*, 127:17, January 1958. doi: 10.1086/146435.

[369] Volker Springel. The cosmological simulation code GADGET-2. MNRAS, 364(4):1105–1134, December 2005. doi: 10.1111/j.1365-2966.2005.09655.x.

[370] Matthew J. Stott and David J. E. Marsh. Black hole spin constraints on the mass spectrum and number of axionlike fields. *PRD*, 98(8):083006, October 2018. doi: 10.1103/PhysRevD.98.083006.

[371] Martin Stref and Julien Lavalle. Modeling dark matter subhalos in a constrained galaxy: Global mass and boosted annihilation profiles. *Phys. Rev. D*, 95:063003, Mar 2017. doi: 10.1103/PhysRevD.95.063003. URL https://link.aps.org/doi/10.1103/PhysRevD.95.063003.

[372] G. Sun and S. R. Furlanetto. Constraints on the star formation efficiency of galaxies during the epoch of reionization. MNRAS, 460(1):417–433, Jul 2016. doi: 10.1093/mnras/stw980.

[373] Sichun Sun and Yun-Long Zhang. Gravitational Waves and Possible Fast Radio Bursts from Axion Clumps. 3 2020.

[374] Peter Svrcek and Edward Witten. Axions In String Theory. *JHEP*, 06:051, 2006. doi: 10.1088/1126-6708/2006/06/051.

[375] Gerard 't Hooft. Computation of the Quantum Effects Due to a Four-Dimensional Pseudoparticle. *Phys. Rev.*, D14:3432–3450, 1976. doi: 10.1103/PhysRevD.18.2199.3,10.1103/PhysRevD.14.3432. [,70(1976)].

[376] Gerard 't Hooft. How Instantons Solve the U(1) Problem. *Phys. Rept.*, 142:357–387, 1986. doi: 10.1016/0370-1573(86)90117-1.

[377] Giuliano Taffoni, Lucio Mayer, Monica Colpi, and Fabio Governato. On the life and death of satellite haloes. MNRAS, 341(2):434–448, May 2003. doi: 10.1046/j.1365-8711.2003.06395.x.

[378] James E. Taylor and Arif Babul. The Dynamics of Sinking Satellites around Disk Galaxies: A Poor Man's Alternative to High-Resolution Numerical Simulations. *ApJ*, 559(2):716–735, October 2001. doi: 10.1086/322276.

[379] Peter Tinyakov, Igor Tkachev, and Konstantin Zioutas. Tidal streams from axion miniclusters and direct axion searches. *JCAP*, 1601(01):035, 2016. doi: 10.1088/1475-7516/2016/01/035.

[380] I. I. Tkachev. Coherent scalar field oscillations forming compact astrophysical objects. *Sov. Astron. Lett.*, 12:305–308, 1986. [Pisma Astron. Zh.12,726(1986)].

[381] I. I. Tkachev. Phase transitions at preheating. *Physics Letters B*, 376:35–40, Feb 1996. doi: 10.1016/0370-2693(96)00297-3.

[382] I. I. Tkachev. Fast Radio Bursts and Axion Miniclusters. *JETP Lett.*, 101(1):1–6, 2015. doi: 10.1134/S0021364015010154. [Pisma Zh. Eksp. Teor. Fiz.101,no.1,3(2015)].

[383] J. Towns, T. Cockerill, M. Dahan, I. Foster, K. Gaither, A. Grimshaw, V. Hazlewood, S. Lathrop, D. Lifka, G. D. Peterson, R. Roskies, J. R. Scott, and N. Wilkins-Diehr. Xsede: Accelerating scientific discovery. *Computing in Science & Engineering*, 16 (5):62–74, Sept.-Oct. 2014. ISSN 1521-9615. doi: 10.1109/MCSE.2014.80. URL doi.ieeecomputersociety.org/10.1109/MCSE.2014.80.

[384] Hy Trac, Renyue Cen, and Philip Mansfield. SCORCH I: The Galaxy-Halo Connection in the First Billion Years. *ApJ*, 813(1):54, Nov 2015. doi: 10.1088/0004-637X/813/1/54.

[385] Jennie H. Traschen and Robert H. Brandenberger. Particle Production During Out-of-equilibrium Phase Transitions. *Phys. Rev.*, D42:2491–2504, 1990. doi: 10.1103/PhysRevD.42.2491.

[386] Scott Tremaine, Douglas O. Richstone, Yong-Ik Byun, Alan Dressler, S. M. Faber, Carl Grillmair, John Kormendy, and Tod R. Lauer. A Family of Models for Spherical Stellar Systems. Astronomical Journal, 107:634, February 1994. doi: 10.1086/116883.

[387] Michele Trenti and Massimo Stiavelli. Formation Rates of Population III Stars and Chemical Enrichment of Halos during the Reionization Era. *ApJ*, 694(2):879–892, Apr 2009. doi: 10.1088/0004-637X/694/2/879.

[388] Dmitriy Tseliakhovich and Christopher Hirata. Relative velocity of dark matter and baryonic fluids and the formation of the first structures. *PRD*, 82(8):083520, Oct 2010. doi: 10.1103/PhysRevD.82.083520.

[389] Michael S. Turner. Coherent Scalar Field Oscillations in an Expanding Universe. *Phys. Rev.*, D28:1243, 1983. doi: 10.1103/PhysRevD.28.1243.

[390] Michael S. Turner and Frank Wilczek. Inflationary axion cosmology. *Phys. Rev. Lett.*, 66: 5–8, 1991. doi: 10.1103/PhysRevLett.66.5.

[391] Frank C. van den Bosch, Geraint F. Lewis, George Lake, and Joachim Stadel. Substructure in Dark Halos: Orbital Eccentricities and Dynamical Friction. *ApJ*, 515(1):50–68, April 1999. doi: 10.1086/307023.

[392] Frank C. van den Bosch, Go Ogiya, Oliver Hahn, and Andreas Burkert. Disruption of dark matter substructure: fact or fiction? MNRAS, 474(3):3043–3066, March 2018. doi: 10.1093/mnras/stx2956.

[393] Ludovic van Waerbeke and Ariel Zhitnitsky. Fast Radio Bursts and the Axion Quark Nugget Dark Matter Model. *Phys. Rev. D*, 99(4):043535, 2019. doi: 10.1103/PhysRevD.99.043535.

[394] Alejandro Vaquero, Javier Redondo, and Julia Stadler. Early Seeds of Axion Miniclusters. *JCAP*, 04:012, 2019. doi: 10.1088/1475-7516/2019/04/012.

[395] Jan Veltmaat, Jens C. Niemeyer, and Bodo Schwabe. Formation and structure of ultralight bosonic dark matter halos. *PRD*, 98(4):043509, Aug 2018. doi: 10.1103/PhysRevD.98.043509.

[396] Tejaswi Venumadhav, Liang Dai, and Jordi Miralda-Escudé. Microlensing of Extremely Magnified Stars near Caustics of Galaxy Clusters. *ApJ*, 850(1):49, November 2017. doi: 10.3847/1538-4357/aa9575.

[397] Matteo Viel, Julien Lesgourgues, Martin G. Haehnelt, Sabino Matarrese, and Antonio Riotto. Constraining warm dark matter candidates including sterile neutrinos and light gravitinos with WMAP and the Lyman-α forest. *PRD*, 71(6):063534, Mar 2005. doi: 10.1103/PhysRevD.71.063534.

[398] A. Vilenkin and A. E. Everett. Cosmic Strings and Domain Walls in Models with Goldstone and PseudoGoldstone Bosons. *Phys. Rev. Lett.*, 48:1867–1870, 1982. doi: 10.1103/PhysRevLett.48.1867.

[399] Eli Visbal and Matthew McQuinn. The Impact of Neutral Intergalactic Gas on Lyα Intensity Mapping during Reionization. Astrophysical Journal Letters, 863(1):L6, Aug 2018. doi: 10.3847/2041-8213/aad5e6.

[400] Eli Visbal, Zoltán Haiman, and Greg L. Bryan. Limits on Population III star formation in minihaloes implied by Planck. MNRAS, 453(4):4456–4466, Nov 2015. doi: 10.1093/mnras/stv1941.

[401] Eli Visbal, Zoltán Haiman, and Greg L. Bryan. Self-consistent semi-analytic models of the first stars. MNRAS, 475(4):5246–5256, Apr 2018. doi: 10.1093/mnras/sty142.

[402] Luca Visinelli. Light axion-like dark matter must be present during inflation. *Phys. Rev.*, D96(2):023013, 2017. doi: 10.1103/PhysRevD.96.023013.

[403] Luca Visinelli and Paolo Gondolo. Dark matter axions revisited. *Phys. Rev. D*, 80:035024, Aug 2009. doi: 10.1103/PhysRevD.80.035024. URL `https://link.aps.org/doi/10.1103/PhysRevD.80.035024`.

[404] Luca Visinelli and Paolo Gondolo. Axion cold dark matter in non-standard cosmologies. *Phys. Rev.*, D81:063508, 2010. doi: 10.1103/PhysRevD.81.063508.

[405] Luca Visinelli and Javier Redondo. Axion Miniclusters in Modified Cosmological Histories. *Phys. Rev. D*, 101(2):023008, 2020. doi: 10.1103/PhysRevD.101.023008.

[406] Luca Visinelli, Sebastian Baum, Javier Redondo, Katherine Freese, and Frank Wilczek. Dilute and Dense Axion Stars. *Phys. Lett.*, B777:64–72, 2018. doi: 10.1016/j.physletb.2017.12.010.

[407] M. I. Vysotsky, Ya. B. Zeldovich, M. Yu. Khlopov, and V. M. Chechetkin. Some Astrophysical Limitations on Axion Mass. *Pisma Zh. Eksp. Teor. Fiz.*, 27:533–536, 1978. [JETP Lett.27,502(1978)].

[408] D. J. Watts, G. A. Addison, C. L. Bennett, and J. L. Weiland. Beyond optical depth: Future determination of ionization history from the CMB. 2019.

[409] Risa H. Wechsler, James S. Bullock, Joel R. Primack, Andrey V. Kravtsov, and Avishai Dekel. Concentrations of Dark Halos from Their Assembly Histories. *ApJ*, 568(1):52–70, March 2002. doi: 10.1086/338765.

[410] Steven Weinberg. Gauge and Global Symmetries at High Temperature. *Phys. Rev.*, D9: 3357–3378, 1974. doi: 10.1103/PhysRevD.9.3357.

[411] Steven Weinberg. The U(1) Problem. *Phys. Rev.*, D11:3583–3593, 1975. doi: 10.1103/PhysRevD.11.3583.

[412] Steven Weinberg. A New Light Boson? *Phys. Rev. Lett.*, 40:223–226, 1978. doi: 10.1103/PhysRevLett.40.223.

[413] Steven Weinberg. The Cosmological Constant Problem. *Rev. Mod. Phys.*, 61:1–23, 1989. doi: 10.1103/RevModPhys.61.1.

[414] Frank Wilczek. Problem of Strong P and T Invariance in the Presence of Instantons. *Phys. Rev. Lett.*, 40:279–282, 1978. doi: 10.1103/PhysRevLett.40.279.

[415] Frank Wilczek. A Model of Anthropic Reasoning, Addressing the Dark to Ordinary Matter Coincidence. *arXiv e-prints*, art. hep-ph/0408167, August 2004.

[416] Nancy Wilkins-Diehr, Sergiu Sanielevici, Jay Alameda, John Cazes, Lonnie Crosby, Marlon Pierce, and Ralph Roskies. An overview of the xsede extended collaborative support program. 1 2016. doi: 10.1007/978-3-319-32243-8_1.

[417] John H. Wise and Tom Abel. Suppression of H_2 Cooling in the Ultraviolet Background. *ApJ*, 671(2):1559–1567, Dec 2007. doi: 10.1086/522876.

[418] C. S. Wu, E. Ambler, R. W. Hayward, D. D. Hoppes, and R. P. Hudson. Experimental Test of Parity Conservation in β Decay. *Phys. Rev.*, 105:1413–1414, 1957. doi: 10.1103/PhysRev.105.1413.

[419] Huangyu Xiao, Ian Williams, and Matthew McQuinn. Simulations of axion minihalos. *Phys. Rev. D*, 104(2):023515, 2021. doi: 10.1103/PhysRevD.104.023515.

[420] Weichen Winston Yin, Liang Dai, and Simone Ferraro. Probing cosmic strings by reconstructing polarization rotation of the cosmic microwave background. 11 2021.

[421] Andrew R. Zentner and James S. Bullock. Halo Substructure and the Power Spectrum. *ApJ*, 598(1):49–72, November 2003. doi: 10.1086/378797.

[422] Andrew R. Zentner, Andreas A. Berlind, James S. Bullock, Andrey V. Kravtsov, and Risa H. Wechsler. The Physics of Galaxy Clustering. I. A Model for Subhalo Populations. *ApJ*, 624 (2):505–525, May 2005. doi: 10.1086/428898.

[423] D. H. Zhao, Y. P. Jing, H. J. Mo, and G. Brner. Mass and redshift dependence of dark halo structure. *The Astrophysical Journal*, 597(1):L9–L12, oct 2003. doi: 10.1086/379734. URL `https://doi.org/10.1086/379734`.

[424] D. H. Zhao, H. J. Mo, Y. P. Jing, and G. Börner. The growth and structure of dark matter haloes. MNRAS, 339(1):12–24, February 2003. doi: 10.1046/j.1365-8711.2003.06135.x.

[425] Hongsheng Zhao. Analytical models for galactic nuclei. MNRAS, 278(2):488–496, January 1996. doi: 10.1093/mnras/278.2.488.

[426] HongSheng Zhao, Dan Hooper, Garry W. Angus, James E. Taylor, and Joseph Silk. Tidal Disruption of the First Dark Microhalos. *ApJ*, 654(2):697–701, January 2007. doi: 10.1086/509649.

[427] Kathryn M. Zurek, Craig J. Hogan, and Thomas R. Quinn. Astrophysical Effects of Scalar Dark Matter Miniclusters. *Phys. Rev.*, D75:043511, 2007. doi: 10.1103/PhysRevD.75.043511.